Development of a Two-Parameter Model (K_{max}, ΔK) for Fatigue Crack Growth Analysis

by

Amir Hossein NoroozíSani

A thesis

presented to the University of Waterloo

in fulfillment of the

thesis requirement for the degree of

Doctor of Philosophy

in

Mechanical Engineering

Waterloo, Ontario, Canada, 2007

I hereby declare that I am the sole author of this thesis. This is a true copy of the thesis, including any required final revisions, as accepted by my examiners.

I understand that my thesis may be made electronically available to the public.

Abstract

It is generally accepted that the fatigue crack growth depends on the stress intensity factor range (ΔK) and the maximum stress intensity factor (K_{max}). Numerous driving forces were introduced to analyze fatigue crack growth for a wide range of stress ratios. However, it appears that the effect of the crack tip stresses and strains need to be included into the fatigue crack growth analysis as well. Such an approach can be successful as long as the stress intensity factors are correlated with the actual elastic-plastic crack tip stress-strain field. Unfortunately, the correlation between the stress intensity factors and the crack tip stress-strain field is often altered by residual stresses induced by reversed plastic deformations.

A two-parameter model (ΔK_{tot}, $K_{max,tot}$) based on the elastic-plastic crack tip stress-strain history has been proposed. The applied stress intensity factors (ΔK_{appl}, $K_{max,appl}$) were modified and converted into the total stress intensity factors (ΔK_{tot}, $K_{max,tot}$) in order to account for the effect of local crack tip stresses and strains on the fatigue crack growth. The fatigue crack growth was regarded as a process of successive crack re-initiations in the crack tip region and predicted by simulating the stress-strain response in the material volume adjacent to the crack tip and estimating the accumulated fatigue damage. The model was developed to predict the mean stress effect for steady-state fatigue crack growth and to determine the fatigue crack growth under simple variable amplitude loading histories. Moreover, the influence of the applied compressive stress on fatigue crack growth can be explained with the proposed two-parameter model. A two-parameter driving force in the form of: $\Delta\kappa = K_{max,tot}^{p} \Delta K_{tot}^{(1-p)}$ was derived based on the local stresses and strains at the crack

tip using the Smith-Watson-Topper (SWT) fatigue damage parameter: $D = \sigma_{max}\Delta\varepsilon/2$. The parameter p is a function of material cyclic stress-strain properties and varies from 0 to 0.5 depending on the fatigue crack growth rate. The effects of the internal (residual) stress induced by the reversed cyclic plasticity manifested themselves in the change of the resultant (total) stress intensity factors driving the crack.

Experimental fatigue crack growth data sets for two aluminum alloys (7075-T6 and 2024-T351), two steel alloys (4340 and 4140), and one titanium alloy (Ti-6Al-4V) were used for the verification of the model under constant amplitude loading. This model was also capable of predicting variable-amplitude fatigue crack growth. Experimental fatigue crack growth data sets after single overloads for the aluminum alloy 7075-T6, steel alloy 4140, and titanium alloy Ti-6Al-4V were also used for the verification of the model. The results indicate that the driving force $\Delta\kappa$ can successfully predict the stress ratio R effect and also the load-interaction effect on fatigue crack growth.

Acknowledgements

I would like to thank my supervisors, Professor Grzegorz Glinka and Professor Stephen B. Lambert for their guidance, technical support, and helpful discussions during the course of this project.

Financial support from the Office of Naval Research, USA in the form of a research grant to Professor Grzegorz Glinka is gratefully acknowledged.

I would also like to thank all my fellow graduate students for their support and encouragement. In particular, I am grateful to Javad Gholipour, Semen Mikheevskiy, Shahid Malik, Ramtin Kahvaie-Zad, and Siamak Nazari for their help and friendship.

Finally, I would like to express my profound gratitude to my family especially my sister for their support and encouragement throughout my education and professional career.

Table of Contents

List of Tables

List of Figures

Nomenclature

a	crack length
b	fatigue strength exponent
c	fatigue ductility exponent
C	fatigue crack growth constant
C*	fatigue crack growth equation constant for plane strain
da/dN	crack growth rate
D	fatigue damage
E	modulus of elasticity
FCG	fatigue crack growth
$f(\sigma^a_{eq})$	plastic strain expression (function)
K	stress intensity factor
K'	cyclic strength coefficient
$K_{max,appl}$	maximum applied stress intensity factor
$K_{max,th}$	maximum threshold stress intensity factor
$K_{max,tot}$	total maximum stress intensity factor
$K_{min,appl}$	minimum applied stress intensity factor
$K_{max,net}$	maximum net stress intensity factor
$K_{min,net}$	minimum net stress intensity factor
K_{net}	net stress intensity factor
$K_{min,tot}$	total minimum stress intensity factor
K_r	residual stress intensity factor

ΔK_{appl}	applied stress intensity range
ΔK^{+}	tensile part of the stress intensity range
ΔK_{net}	net stress intensity range
ΔK_{th}	threshold stress intensity range
ΔK_{tot}	total stress intensity range
ΔK_{BL}	base line stress intensity factor range
ΔK_{IC}	fracture toughness
$\Delta\kappa$	two parameter driving force
m	Paris' equation exponent
m(x,a)	weight function
M_1, M_2, M_3	weight function parameters
N	number of cycle
N_f	number of cycle to fail the first element
N_{BL}	number of base-line cycles
n'	cyclic strain hardening exponent
p	driving force constant
r	radial polar coordinate
r_p	plastic zone size
r_{pc}	corrected plastic zone for the crack tip plasticity
OLR	overload ratio
OCR	occurrence ratio
ULR	underload ratio

R	stress ratio
R_{appl}	applied stress ratio
SIF	stress intensity factor
$S_{max,appl}$	maximum applied nominal (remote) stress
$S_{min,appl}$	minimum applied nominal (remote) stress
SWT	Smith-Watson-Topper fatigue damage parameter
x	distance from the crack tip
Y	geometrical stress intensity correction factor
ε	strain
ε'_f	fatigue ductility coefficient
$\tilde{\varepsilon}^a_m$	maximum actual strain over the first elementary block
$\tilde{\varepsilon}^e_i$	average elastic strain over the i-th elementary material block
$\tilde{\varepsilon}^a_i$	average actual strain over the i-th elementary material block
$\Delta\varepsilon$	strain range ahead of the crack tip
$\Delta\tilde{\varepsilon}^a$	actual strain range over the first elementary block
γ	fatigue crack growth equation exponent
ρ^*	notch tip radius or elementary material block size
ν	Poisson's coefficient
σ	stress
σ'_f	fatigue strength coefficient
σ_{max}	maximum stress ahead of the crack tip
$\tilde{\sigma}^a_{max,th}$	actual maximum threshold stress over the first elementary block

σ_x, $\sigma_{y,}$ τ_{xy}	stress components
$\tilde{\sigma}^a_i$	average actual stress over the i-th elementary block
σ^a_{eq}	equivalent actual stress
$\tilde{\sigma}^a_m$	mean actual stress over the first elementary block
$\tilde{\sigma}^e_i$	average pseudo-elastic stress over the i-th elementary block
$\tilde{\sigma}^e_{max,net}$	maximum net pseudo-elastic stress over the first elementary block
$\tilde{\sigma}^e_{min,net}$	minimum net pseudo-elastic stress over the first elementary block
$\sigma^e_{min,net}$	minimum net pseudo-elastic stress at the crack tip
σ_r	residual stress distribution
$\Delta\tilde{\sigma}^a$	actual stress range over the first elementary block
$\Delta\tilde{\sigma}^e_{net}$	net elastic stress range over the first elementary block
$\Delta\sigma_{th}$	threshold stress range
$\Delta\tilde{\sigma}^a_{th}$	actual threshold stress range over the first elementary block
ψ_i	the averaging constant corresponding to the i-th elementary block

Chapter 1
Introduction and Research Objectives

Throughout their service life, machines, equipment, vehicles, buildings and aircraft are subjected to loads, the majority of which fluctuates with time. This kind of loading may cause small cracks to grow during the life of a component and lead to fatigue failure. The cracks either pre-exist at the time of manufacturing or are created by in-service conditions. Therefore, the growth of the crack should be predictable to provide guidelines for inspection programs, which ensure that cracks will never propagate and fail prior to detection. Therefore, fatigue crack growth prediction models must be developed.

During the last five decades, a lot of research effort has focused on fatigue crack growth and prediction models. The most successful and popular model has been Paris' law [1], based on the applied stress intensity range, ΔK_{appl}, as the only governing parameter for fatigue crack growth. The Paris equation initiated widespread research aiming at possible improvements to its original form and at the analytical modeling of fatigue crack growth, in general. One of the fundamental problems concerning the Paris expression and all other fatigue damage accumulation models is the quantification of the mean stress effect. In other words, the apparent effectiveness of the applied stress intensity range, ΔK_{appl}, is influenced by the load ratio R (min. load/max. load).

In 1971, Elber [2] modified the applied stress intensity factor range, ΔK_{appl}, introducing a closure mechanism in order to quantify the effect of the load ratio, R, on fatigue crack growth. The closure model has been also used to account for interaction effects under variable amplitude loading [3,4,5,6,7]. The contemporary belief is that the crack tip closure concept can explain both mean stress and variable amplitude effects on fatigue crack

growth. However, mounting evidence suggests that this may not be true; the model is difficult to use, and it requires experimental calibrations [8,9,10,11]. Therefore, fatigue research has attempted [11,12,13,14,15] to use alternative methods, for example by assuming a new two-parameter driving force combining the applied maximum stress intensity factor, $K_{max,appl}$, and the applied stress intensity range, ΔK_{appl}, in order to analyze fatigue crack growth behavior. The two-parameter driving forces are capable of explaining the R-ratio effect on fatigue crack growth behavior. However, the available two-parameter driving force models [11, 12, 14, 15] tend to be suitable only for high stress ratios. In general, they can not explain the influence of the compressive part of the load history on fatigue crack growth; also they can not predict fatigue crack growth under variable amplitude loading.

The main goal of the current research is to develop a two-parameter model accounting for mean stress and load interaction effects for fatigue crack growth analysis. More specifically, the following research objectives were undertaken:

- To investigate and understand mechanisms controlling fatigue crack growth in terms of local stresses and strains near the crack tip,
- To predict the effect of mean and minimum compressive stresses on fatigue crack growth at different stress ratios for a variety of engineering materials,
- To investigate load-interaction or load-history effects on fatigue crack growth response, and
- To develop a fatigue crack growth prediction methodology appropriately accounting for mean stress and load interaction effects.

To accomplish these objectives, a two-parameter fatigue crack propagation model based on the elastic-plastic stress-strain history at the crack tip has been proposed. In the

proposed model the applied stress intensity factors, $K_{max,appl}$ and ΔK_{appl}, are modified to account for the effect of residual stresses induced by reversed plasticity at the crack tip. Therefore, an original mathematical formulation of the model has been developed to represent the residual stress effect in terms of the residual stress intensity factor, K_r, which can be used to modify the applied stress intensity factors. A fatigue crack growth equation in terms of the two-parameter driving force, $K_{max,tot}^{p}\Delta K_{tot}^{0.5}$, was derived based on local stresses and strains at the crack tip and the Smith-Watson-Topper (SWT) [16] fatigue damage parameter, $D = \sigma_{max}\cdot\Delta\varepsilon/2$, for both plane stress and plane strain conditions. The parameter "p" is a function of cyclic stress-strain material properties and varies from 0 to 0.5 depending on the fatigue crack growth rate. Then, three two-parameter driving forces, $K_{max,tot}^{p}\Delta K_{tot}^{1-p}$, $K_{max,tot}^{0.5}\Delta K_{tot}^{0.5}$, and $K_{max,tot}^{p}\Delta K_{tot}^{0.5}$, have been introduced to predict the mean stress effect on fatigue crack growth in different growth rate regimes. It was found that the driving force in the form of $K_{max,tot}^{p}\Delta K_{tot}^{0.5}$ could be used for fatigue crack growth predictions under a wide range of load ratios, and fatigue crack growth rates spanning from the near threshold to the high growth rate regime.

The dissertation is structured to first review pertinent literature of linear elastic fracture mechanics (LEFM) principles. In the second part of the literature review, a brief review of fatigue crack growth predictive methodologies for fatigue crack growth under constant and variable amplitude loading is included. The background and literature review is followed by fatigue crack propagation modeling including the formulation of a model: analysis of strains and stresses at the crack tip, residual stress intensity factor calculation, K_r, and consequently the calculation of the total stress intensity factors, $K_{max,tot}$ and ΔK_{tot}. This section also contains the analytical derivation of the two-parameter driving force,

$K_{max,tot}^{p}\Delta K_{tot}^{(1-p)}$, for predominantly elastic, plastic and elastic-plastic behavior of the material at the crack tip. The fatigue crack propagation modeling section ends by describing different methods for the determination of the elementary material block size, ρ*. The verification section presents the experimental fatigue crack growth data at different R-ratios for a variety of materials under constant amplitude loading. It ties together the experimental and analytical results as necessary to demonstrate and illustrate the mean stress effect and the capability of the proposed model for the steady-state fatigue crack growth prediction. The validation section also includes the experimental data and analytical results demonstrating load-interaction effects on fatigue crack growth. In both cases, the analytical results are obtained by the predictive methodologies theorized. The dissertation finishes with a brief summary of the conclusions and recommendations for future research activities.

Chapter 2
Literature Review

2.1 Linear Elastic Fracture Mechanics

Linear elastic fracture mechanics (LEFM) principles are used to correlate the stress magnitude and the stress distribution near the crack tip to the remote stresses/loads, crack shape, crack size, and material properties of a component. The crack tip stress field can be determined using the stress intensity factor for mode I loading, K_I.

2.1.1 Ideal Sharp Crack

In the mid-1950s, Irwin [17] showed that the local elastic stresses near the crack tip in an isotropic linear elastic material are a function of "r" and "θ" coordinates, as shown in Figure 2-1 [18]:

$$\sigma_x = \frac{K_I}{\sqrt{2\pi r}}\cos\frac{\theta}{2}\left[1-\sin\frac{\theta}{2}\sin\frac{3\theta}{2}\right]+\psi_x(r,\theta) \quad \text{(a)}$$

$$\sigma_y = \frac{K_I}{\sqrt{2\pi r}}\cos\frac{\theta}{2}\left[1+\sin\frac{\theta}{2}\sin\frac{3\theta}{2}\right]+\psi_y(r,\theta) \quad \text{(b)}$$

$$\tau_{xy} = \frac{K_I}{\sqrt{2\pi r}}\cos\frac{\theta}{2}\sin\frac{\theta}{2}\cos\frac{3\theta}{2}+\psi_{xy}(r,\theta) \quad \text{(c)} \qquad (2.1)$$

$$\sigma_z = 0 \qquad \text{plane stress} \quad \text{(d)}$$

$$\sigma_z = \nu(\sigma_x+\sigma_y) \qquad \text{plane strain} \quad \text{(e)}$$

$$\tau_{yz} = \tau_{zx} = 0 \quad \text{(f)}$$

The terms ψ_x, ψ_y and ψ_{xy} are higher-order terms from the series expansion of the complete stress field solution, and they are insignificant in the close vicinity of the crack tip. The stress components in the potential plane of the crack ($\theta = 0$) can be expressed as follows:

$$\sigma_x = \sigma_y = \frac{K_I}{\sqrt{2\pi x}} \tag{2.2}$$

All non-zero stress components in Eq set (2.1) tend to infinity as the distance from the crack tip, r, tends to zero (crack tip). Thus, a mathematical singularity exists at the crack tip and no specific value of the stress can be given at the crack tip.

2.1.2 Blunted Crack

The distribution of stress components ahead of a blunt crack tip with the tip radius ρ^*, as shown in Figure 2-2, can be obtained from the Creager and Paris [19] solution:

$$\sigma_x = -\frac{K_I}{\sqrt{2\pi r}}\frac{\rho^*}{2r}\cos\frac{3\theta}{2} + \frac{K_I}{\sqrt{2\pi r}}\cos\frac{\theta}{2}\left[1 - \sin\frac{\theta}{2}\sin\frac{3\theta}{2}\right] + \cdots \quad \text{(a)}$$

$$\sigma_y = \frac{K_I}{\sqrt{2\pi r}}\frac{\rho^*}{2r}\cos\frac{3\theta}{2} + \frac{K_I}{\sqrt{2\pi r}}\cos\frac{\theta}{2}\left[1 + \sin\frac{\theta}{2}\sin\frac{3\theta}{2}\right] + \cdots \quad \text{(b)}$$

$$\tau_{xy} = -\frac{K_I}{\sqrt{2\pi r}}\frac{\rho^*}{2r}\sin\frac{3\theta}{2} + \frac{K_I}{\sqrt{2\pi r}}\sin\frac{\theta}{2}\cos\frac{\theta}{2}\cos\frac{3\theta}{2} + \cdots \quad \text{(c)} \tag{2.3}$$

$$\sigma_z = 0 \qquad \text{Plane stress} \qquad \text{(d)}$$

$$\sigma_z = \nu(\sigma_x + \sigma_y) \qquad \text{Plane strain} : \varepsilon_z = 0 \qquad \text{(e)}$$

The elastic stresses near the crack tip in the potential crack plane ($\theta = 0$) are

$$\sigma_x = \frac{K_I}{\sqrt{2\pi x}}\left(1 - \frac{\rho^*}{2x}\right) + \cdots \quad \text{(a)}$$

$$\sigma_y = \frac{K_I}{\sqrt{2\pi x}}\left(1 + \frac{\rho^*}{2x}\right) + \cdots \quad \text{(b)} \tag{2.4}$$

$$\tau_{xy} = 0 \qquad \text{(c)}$$

2.1.3 Crack Tip Plasticity and Plastic Zone Corrections

It is obvious that from Eqs. (2.1), in the case of a sharp crack, stresses tend to infinity when r, the distance from the crack tip, tends toward zero. Therefore, most materials deform plastically in the crack tip region. The plastically deformed region is called the crack tip plastic zone. To use LEFM principles, the plastic zone size must not be excessively large compared with the overall dimensions of the crack and the cracked body.

Irwin [20] was the first one to develop a model for the modification of the linear-elastic crack tip solution in order to account for the elastic-plastic behavior of material near the crack tip. He replaced the actual crack length by a longer equivalent crack length, as shown in Figure 2-3. For the first approximation, Irwin assumed that the stress over the plastic zone was equal to the yield stress and calculated the plastic zone size under plane stress condition as:

$$r_p = \frac{1}{2\pi}\left(\frac{K_I}{\sigma_{ys}}\right)^2 \qquad (2.5)$$

When yielding occurs, stresses must redistribute themselves in order to satisfy equilibrium. Consequently, the plastic zone size will increase. A simple force balance, $F_1 = F_2$, leads to a more accurate estimation of the plastic zone size (corrected plastic zone), r_{pc}, as shown in Figure 2-3:

$$F_1 = F_2 \Rightarrow \Delta r_p = \frac{1}{2\pi}\left(\frac{K_I}{\sigma_{ys}}\right)^2 \qquad (2.6)$$

$$r_{pc} = r_p + \Delta r_p = 2r_p = \frac{1}{\pi}\left(\frac{K_I}{\sigma_{ys}}\right)^2 \tag{2.7}$$

The equations above are valid only for plane stress and an ideal elastic-plastic material.

Dugdale [21] and Barenblatt [22] introduced another model, called the strip yield model, in order to determine the plastic zone size near the crack tip. The Dugdale crack was assumed to be in a thin elastic plate of infinite length and width, for a non-hardening material in plane stress. The plastic zone was modeled by assuming a crack of length $2a + 2r_p$, where r_p is the length of the plastic zone, with the yield stress, σ_{ys}, tending to close the crack, as shown in Figure 2-4 [23]. The size of the plastic zone, r_p, was determined based on the condition that the stress singularity at the crack tip of the Dugdale crack must disappear. In other words, the stress intensity factor due to the nominal stress, S, must be balanced out by the stress intensity factor due to the compressive yield stress, σ_{ys}, acting in the plastic zone. The stress intensity factor caused by the nominal stress is given as

$$K_S = S\sqrt{\pi(a + r_p)} \tag{2.8}$$

and the stress intensity factor due to the compressive yield stress is given as [24]

$$K_{\sigma_{ys}} = -2\sigma_{ys}\sqrt{\frac{a + r_p}{\pi}}\cos^{-1}\left(\frac{a}{a + r_p}\right) \tag{2.9}$$

From the condition $K_S + K_{\sigma_{ys}} = 0$ it follows that

$$\frac{a}{a + r_p} = \cos\left(\frac{\pi S}{2\sigma_{ys}}\right) \tag{2.10}$$

By expanding the right side of equation (2.10) using a Taylor series and neglecting higher-order terms, one can determine the plastic zone size, r_p:

$$r_p = \frac{\pi^2 S^2 a}{8\sigma_{ys}^2} = \frac{\pi}{8}\left(\frac{K_I}{\sigma_{ys}}\right)^2 \tag{2.11}$$

A comparison between equation (2.7) and equation (2.11) shows that the Irwin and Dugdale's models predict similar plastic zone sizes [25].

The plastic zone correction proposed by Irwin or Dugdale can be used only for a crack. In 1985, Glinka [26] determined the plastic zone size and plastic zone adjustment in a notch body for both tension and bending loads. The first approximation of the plastic zone size, r_p, ahead of a notch tip was calculated from the Hencky-Mises-Huber criterion on the basis of the elastic stress distribution near a blunt crack tip. For plane stress, the plastic yielding criterion takes the following form:

$$\sigma_{eq} = \sqrt{\sigma_x^2 - \sigma_x \sigma_y + \sigma_y^2} \tag{2.12}$$

Substituting equations (2.4) into equation (2.12) results in

$$\sigma_{eq} = \frac{K_I}{\sqrt{2\pi r}}\left(\sqrt{1 + \frac{3}{4}\left(\frac{\rho^*}{r}\right)^2}\right) \tag{2.13}$$

The first approximation to the plastic zone size can be obtained from equation (2.13) if the value of the equivalent stress at $r = r_p$ is assumed equal to the yield stress, $\sigma_{eq} = \sigma_{ys}$.

$$\sigma_{ys} = \frac{K_I}{\sqrt{2\pi r_p}}\left(\sqrt{1 + \frac{3}{4}\left(\frac{\rho^*}{r_p}\right)^2}\right) \tag{2.14}$$

Glinka also adjusted the plastic zone size by adding the increment Δr_p to the first estimation, r_p. The adjustment results from the stress redistribution caused by plastic yielding. Because of plastic yielding, the real stresses in the plastic zone are lower than those derived on the basis of linear-elastic analysis. To satisfy equilibrium conditions, stress redistribution occurs

and results in an increase in the plastic zone, as shown in Figure 2-5. Such an increase in the plastic zone can be interpreted, analogously with Irwin [27], as an increase in the hypothetical elastic stresses. The forces F_1 and F_2 represented by area F_1 and F_2 in Figure 2-5 must be equal, and the plastic zone increment, Δr_p, can be calculated as:

$$F_1 = F_2 \Rightarrow \int_{\rho^*/2}^{r_p} \sigma_y dr - [\sigma_y(r_p) \times (r_p - \frac{\rho^*}{2})] = \sigma_y(r_p) \times \Delta r_p \tag{2.15}$$

where

$$\sigma_y(r_p) = \frac{K_I}{\sqrt{2\pi r_p}} \left(1 + \frac{\rho^*}{2r_p}\right) \tag{2.16}$$

Substituting Eqs. (2.4)-b and (2.16) into Eq. (2.15) and solving for Δr_p results in

$$\Delta r_p = \rho^* \frac{\left[2\left(\frac{r_p}{\rho^*}\right)^{1/2} - \left(\frac{\rho^*}{r_p}\right)^{1/2}\right]}{\left[\left(\frac{\rho^*}{r_p}\right)^{1/2} + \frac{1}{2}\left(\frac{\rho^*}{r_p}\right)^{3/2}\right]} - \rho^*\left(\frac{r_p}{\rho^*} - \frac{1}{2}\right) \tag{2.17}$$

Therefore, the elastic stress increases near the notch tip due to the presence of the plastic zone. The corrected (increased) stress can be determined, at a given point ahead of the crack tip, from the following equation:

$$C_p = \frac{\sigma(\text{corrected})}{\sigma(\text{elastic})} \tag{2.18}$$

The correction factor, C_p, can be calculated from expressions (2.19) or (2.20), as discussed in Appendix A.

$$\Rightarrow C_p = \sqrt{1 + \frac{\Delta r_p}{r_p}} \times \sqrt{\frac{1 + \frac{3}{4}\left[\frac{\rho^*}{r} \times \left(1 + \frac{\Delta r_p}{r_p}\right)\right]^2}{1 + \frac{3}{4}\left(\frac{\rho^*}{r}\right)^2}} \tag{2.19}$$

or

$$\Rightarrow C_p = \sqrt{1+\frac{\Delta r_p}{r_p}} \times \sqrt{\frac{1+\frac{3}{4}\left[\frac{\rho^*}{x+\frac{\rho^*}{2}} \times \left(1+\frac{\Delta r_p}{r_p}\right)\right]^2}{1+\frac{3}{4}\left(\frac{\rho^*}{x+\frac{\rho^*}{2}}\right)^2}} \tag{2.20}$$

The correction factor, C_p, depends on the distance "x" from the crack tip, and its decay can be finally written in the form of expression (2.21):

$$C_p^* = 1+(C_p-1)\left(\frac{r_p+\Delta r_p}{r-\frac{\rho^*}{2}+r_p+\Delta r_p}\right)^{\alpha} = 1+(C_p-1)\left(\frac{r_p+\Delta r_p}{x+r_p+\Delta r_p}\right)^{\alpha} \quad \text{where} \quad \alpha = \frac{3}{2} \tag{2.21}$$

The correction factor, C_p^*, was verified by Glinka [28] using elasto-plastic FE data.

2.2 Elasto-Plastic Stress-Strain Material Response at Notches and Cracks

Elastic stress-strain analysis can not be directly used for the calculation of stresses and strains in the vicinity of the crack tip due to plasticity. Unfortunately, no closed-form analytical solutions exist for elastic-plastic stresses and strains at notches and cracks. Therefore, several approximate methods are used [29]. The most frequently used is Neuber's rule [30], which is generalized by Barkey et al. [31] for multi-axial loading and by Seeger and Heuler [32].

Neuber's rule states that the theoretical stress concentration factor, K_t, is the geometric mean of the local stress concentration factor, K_σ, and the local strain concentration

factor, K_ε. The theoretical stress concentration factor, K_t, is the relation between the nominal elastic stress, S, the local elasto-plastic stress, σ_{22}^a, and strain, ε_{22}^a, near the notch tip.

$$K_t^2 = K_\sigma K_\varepsilon = \frac{\sigma_{22}^a}{S}\frac{\varepsilon_{22}^a}{e} \tag{2.22}$$

For nominally elastic behavior, the remote (nominal) strain, e, can be related to the remote stress, S, using Hooke's law. Neuber's rule, Eq. (2.22), then takes the following form:

$$\frac{(K_t S)^2}{E} = \sigma_{22}^e \varepsilon_{22}^e = \sigma_{22}^a \varepsilon_{22}^a \tag{2.23}$$

Superscript "e" represents the elastic strain and stress while superscript "a" shows the local (actual) stress and strain at the notch tip. Neuber's rule can also be represented in terms of the equality of the total strain energy (the strain energy and the complement of the strain energy density) at the notch tip, as shown in Figure 2-6(a) by the rectangles A and B.

It has been observed [30, 33] that Eq. (2.23) overestimates the local strain at the notch tip. Therefore, in 1985, Glinka [34] introduced another equation based on the equivalence of the strain energy density (ESED). The ESED method can be interpreted in terms of the equality between the strain energy density at the notch tip of a linear elastic body (superscript "e" in Eq. (2.24)) and that of a geometrically identical, elastic-plastic body (superscript "a" Eq. (2.24)), both subjected to the same loading.

$$\int_0^{\varepsilon_{22}^e} \sigma_{22}^e d\varepsilon_{22}^e = \int_0^{\varepsilon_{22}^a} \sigma_{22}^a d\varepsilon_{22}^a \tag{2.24}$$

Relationship (2.24) can be illustrated based on the equality of the area under the linear-elastic curve and the area under the actual elastic-plastic material stress-strain response, as shown in Figure 2-6(b).

Both methods consist of two parts, namely the constitutive equation and the relationship linking the fictitious linear elastic stress-strain state $(\sigma_{ij}^{e}, \varepsilon_{ij}^{e})$ at the notch tip with the actual stresses and strains $(\sigma_{ij}^{a}, \varepsilon_{ij}^{a})$, as shown in Figure 2-7. By solving appropriate simultaneous equations, the constitutive equation and either the Neuber or ESED equation, the local strains and stresses can be estimated at the notch tip.

2.3 Fatigue Crack Growth Predictive Methodologies

A goal in fatigue design is to develop reliable models that predict fatigue crack growth. The models allow the calculation of fatigue life of a component in terms of number of cycles, N, for growing a crack from an initial size, a_i, to a final size, a_f.

$$N = N_f - N_i = \int_{a_i}^{a_f} \frac{da}{\left(\frac{da}{dN}\right)} \tag{2.25}$$

In Eq. (2.25), N_i is the number of cycles required to create the initial crack and N_f is the number of cycles required to grow the crack to a_f. The term $\frac{da}{dN}$ represents the fatigue crack growth increments, depending on loading conditions, crack geometry, and specimen geometry.

With the advent of fracture mechanics in the 1960s, Paris et al. [35] were the first to recognize fracture mechanics as a powerful tool for characterizing the behavior of fatigue cracks. They postulated that the rate of crack growth per cycle, $\frac{da}{dN}$, is a function of the stress intensity factor range, ΔK. Later, different expressions were introduced to show the

relationship between $\frac{da}{dN}$ and ΔK, and several models were developed to predict fatigue life under constant and variable amplitude loadings.

2.3.1 Fatigue Crack Growth Prediction under Constant Amplitude Loading

Constant amplitude crack growth data normally can be presented as plots of the fatigue crack growth rate, $\frac{da}{dN}$, versus the stress intensity range, ΔK. A schematic plot of log (da/dN) versus log (ΔK), a sigmoidal curve, is shown in Figure 2-8. The stress intensity range, ΔK, is influenced by the applied stress range, Δσ, the crack length, a, and the geometry factor, Y, which depends upon the geometry and the relative crack length, α = a/W.

$$\Delta K = K_{max} - K_{min} = Y\Delta\sigma\sqrt{\pi a} = Y(\sigma_{max} - \sigma_{min})\sqrt{\pi a} \tag{2.26}$$

Several regions can be identified in such diagrams. In region I, there is a threshold stress intensity range, ΔK_{th}, below which the crack does not grow. The crack growth rate in the near threshold region is sensitive to the microstructure and mean stress.

Most parts of the fatigue crack growth are associated with the intermediate range II. One of the most successful models for FCG prediction under constant amplitude loading in region II is the Paris law relationship [1].

$$\frac{da}{dN} = C(\Delta K)^m \tag{2.27}$$

The material constants "C" and "m" can be found in the literature and data books for a number of metals [36, 37, 38]. They depend on mean stress, test temperature, load frequency, and the environment. ASTM E647 provides guidelines and procedures for the measurement of these parameters.

Fatigue life, number of cycles to failure, may be calculated by integrating Eq. (2.27).

$$N = \int_{a_i}^{a_f} \frac{da}{C(\Delta K)^m} = \int_{a_i}^{a_f} \frac{da}{C\left(Y\Delta\sigma\sqrt{\pi a}\right)^m} \tag{2.28}$$

In the case of where "Y" is constant, a small edge crack in a semi-infinite plate or a through crack in an infinite plate, a closed form solution exist for the integration of fatigue life under constant amplitude loading.

$$\begin{aligned} N &= \frac{2}{(m-2)C(\Delta\sigma Y)^m \pi^{m/2}}\left[\frac{1}{a_i^{(m-2)/2}} - \frac{1}{a_f^{(m-2)/2}}\right] \quad \text{for} \quad m \neq 2 \\ N &= \frac{1}{C\Delta\sigma^2\pi Y^2}\ln\frac{a_f}{a_i} \quad \text{for} \quad m = 2 \end{aligned} \tag{2.29}$$

In the case of a variable geometry factor, numerical integration becomes necessary. To perform the integration, the first step is to assume the crack increment, Δa_j. It is necessary that the crack increment be sufficiently small for accurate representation of the fatigue life curve, "a" versus "N". For any material, geometry, and load, ΔK_j can be calculated for each crack increment from the following equation.

$$\Delta K_j = Y_j\Delta\sigma\sqrt{\pi a_j} \qquad \text{(a)} \tag{2.30}$$

where $$a_j = a_{j-1} + \Delta a_j \qquad \text{(b)}$$

Then, the crack growth rate, da/dN, is estimated by using any mathematical form of the ΔK and da/dN equations. Finally, the number of cycles, ΔN_j, for each constant crack increment, Δa_j, may be determined by the following equations:

$$\begin{aligned} &\left(\frac{da}{dN}\right)_j = C\left(\Delta K_j\right)^m && \text{(a)} \\ &\frac{\Delta a_j}{\Delta N_j} = C\left(\Delta K_j\right)^m \Rightarrow \Delta N_j = \frac{\Delta a_j}{C\left(\Delta K_j\right)^m} && \text{(b)} \\ &N_j = N_{j-1} + \Delta N_j && \text{(c)} \end{aligned} \tag{2.31}$$

The calculated a_j and N_j after each increment can be used to create the "a" versus "N" curve, which in turn can be utilized to predict fatigue life.

In region III, the fatigue crack growth rate increases rapidly as the stress intensity range, ΔK, increases. The fraction of fatigue life corresponding to this region is negligible due to very fast crack growth rates, and therefore region III is generally less important in fatigue analysis.

2.3.1.1 The R-ratio Effect on Fatigue Crack Growth

For a wide range of materials, experimental FCG data shows that by increasing the R-ratio, fatigue crack growth will increase for a given ΔK. A qualitative picture of the R-ratio effect is shown in Figure 2-9 [39]. Because the Paris equation cannot show the R-ratio effect on fatigue crack growth, two kinds of models have been developed to characterize the mean stress effect on FCG.

2.3.1.1.1 Crack Closure Model

In 1970, Elber [2] proposed the crack closure mechanism in order to explain the stress ratio effect on fatigue crack growth. He observed that a fatigue crack is closed during unloading, even though the load is still in tension; and, during the next loading, it is open only if the load is sufficiently high. Crack closure occurs as a result of crack-tip plasticity, and the plastically deformed material left in the wake of a propagating crack, as shown in Figure 2-10. From this observation, Elber also postulated that fatigue crack growth occurs only during that portion of the cyclic loading in which the crack is completely open. The load level at which the crack opens is called the crack opening load level, P_{op}, and corresponds to the opening stress intensity factor, K_{op}. The crack opening load, P_{op}, is defined as the load

associated with a 2% deviation from linearity on the load-displacement curve. The methods for the calculation of the crack opening load are described in ASTM-E647. The portion of the load cycle that is below K_{op} does not contribute to fatigue crack growth, and the effective stress intensity factor range, ΔK_{eff}, smaller than the applied stress intensity factor range should be used for fatigue crack growth prediction.

$$\frac{da}{dN} = C(\Delta K_{eff})^m \tag{2.32}$$

$$\begin{aligned} \Delta K_{eff} &= K_{max,appl} - K_{op} < \Delta K_{appl} \quad \text{if} \quad K_{op} > K_{min,appl} \\ \Delta K_{eff} &= K_{max,appl} - K_{min,appl} = \Delta K_{appl} \quad \text{if} \quad K_{op} < K_{min,appl} \end{aligned} \tag{2.33}$$

Thus, the effective stress intensity factor range, ΔK_{eff}, is used to explain the R-ratio effect on fatigue crack growth rates. However, at high stress ratios, due to the absence of the crack closure, the effective driving force, which is close to the applied value, can not show the R-ratio effect on fatigue crack growth. Therefore, the empirical parameter U is used to modify the effective stress intensity factor range, ΔK_{eff}, at high stress ratios.

$$\Delta K_{eff} = U\Delta K_{appl} \tag{2.34}$$

Elber proposed the following relationship for a range of $R > 0$.

$$U = 0.4R + 0.5 \tag{2.35}$$

Schijve [40] also proposed an alternative equation for the U parameter to show the mean stress effect on fatigue crack growth at a wide range of R-ratios varying from -1 to 0.54 for 2024-T3 aluminum alloy:

$$U = 0.55 + 0.33R + 0.12R^2 \tag{2.36}$$

In general, the U parameter depends on R-ratio as well as the stress state, specimen geometry, the stress intensity factor range, and environment.

The crack closure mechanism is referred to as "plasticity-induced" crack closure or the Elber mechanism. It is recognized that other mechanisms may be responsible for crack closure effects. Suresh and Ritchie [41] proposed five mechanisms for fatigue crack closure to explain closure effects, especially in the behavior of fatigue cracks in the near-threshold region: (1) plasticity, (2) roughness or asperity, (3) oxide, (4) phase transformation, and (5) viscous fluids. Due to the importance of the first three, the following discussion is limited to plasticity, roughness, and oxide mechanisms.

Plasticity-induced crack closure results from the residual deformation left in the wake of a propagating crack. During one cycle of crack growth, the plastically deformed material, the cyclic plastic zone, builds in front of the crack tip. As the crack grows into the plastic zone, this plastically deformed material is left on the flanks of the propagating crack, leading to crack closure at positive stress levels [39]. During crack propagation, the increased stress intensity range and consequently enlarged cyclic plastic zone result in an envelope of plastically deformed material in the wake of the growing crack, as shown in Figure 2-10 and Figure 2-11(b).

Oxide-induced closure depends on the stress ratio and environmental effects. During the propagation of a fatigue crack in a moist atmosphere, the freshly formed fracture surfaces oxidize. The oxide debris and other corrosion products can become wedged between the crack faces, as shown in Figure 2-11(c). At low R-ratios and in a moist atmosphere, oxide-induced closure is significant in the near threshold regime where the crack opening is small. This phenomenon can be seen in the experiments done by Suresh et al. [42]. They found that

the addition of moisture to hydrogen or helium atmosphere led to crack growth retardation at low ΔK levels and low R-ratios due to this oxide formation in a steel alloy. Moreover, they found that at high stress ratios (R = 0.75) there was no oxide-induced crack closure effect in either wet or dry environments in a martensitic $2\frac{1}{4}$Cr-1Mo steel. Consequently, the ΔK_{th} values were almost the same in moist air, dry helium, and dry hydrogen for high stress ratios.

Asperity or roughness-induced crack closure results from micro-structural effects. On a global scale, fatigue cracks propagate in Mode I. However, on a microscopic scale, because of micro-structural heterogeneity, crack deflections can lead to local mixed modes. Crack deflections and the associated Mode II and/or Mode III plastic displacements cause crack surface offsets with peaks on the mating surfaces interfering with each other. This surface roughness induces crack closure at positive applied loads, as shown in Figure 2-11(d). Coarse-grained materials usually produce a surface with more roughness in fatigue compared to fine-grained materials, and consequently the closure effects are higher [43].

Despite a large amount of crack closure data generated during the last 30 years, there are still significant difficulties correlating crack closure measurement with crack growth behavior. Experimental results indicate that the crack-opening load, P_{op}, depends on the measurement location relative to the crack tip and the technique employed [8, 9]. Generally, measurements taken at points far away from the crack tip give lower opening loads compared to measurements taken close to the crack tip. In 1992, Ling and Schijve [44] proposed that heat treatment can change the crack-opening load, P_{op}. Furthermore, the crack-opening load, P_{op}, depends on the crack length [45].

Garrett and Knott [46] showed that crack closure has little effect on FCG rates in plane strain conditions in the air and cannot explain the relation between the stress ratio and

fatigue crack growth. Moreover, crack closure cannot be used to explain some overload-induced crack delays and arrests measured under plane strain at high R ratios, because the experimental measurements of the opening load for A542-2 steel after 100% overload (ΔK_{BL}= 10 MPa$\sqrt{m}$, R = 0.05) show an increase of the ΔK_{eff} [47]. The FE data proposed by Wei and James [48] showed that the crack-opening load depends on the stress state, plane stress or plane strain, at the crack tip. The data also demonstrated that larger crack closure opening loads are predicted for plane stress conditions.

Recently, Donald and Paris [15, 49] observed that by using the crack closure model, fatigue crack growth curves cannot be correlated in the near threshold regime for aluminum alloys. Therefore, an estimation of the effective stress intensity range at the crack tip should take into account the additional cyclic crack tip strain below the opening load. They proposed a new partial crack closure model. Using the proposed model, they modified the opening stress intensity factor, K_{op}, and introduced new driving forces, $\Delta K_{2/\pi}$ and $\Delta K_{2/\pi 0}$, for fatigue crack growth prediction.

$$\Delta K_{2/\pi 0} = K_{max} - \frac{2}{\pi} K_{op} \tag{2.37}$$

$$\Delta K_{2/\pi} = K_{max} - \frac{2}{\pi} K_{op} - \left(1 - \frac{2}{\pi}\right) K_{min} = \Delta K_{appl} - \frac{2}{\pi}\left(K_{op} - K_{min}\right) \tag{2.38}$$

The $\Delta K_{2/\pi}$ gives an overestimate of the effective SIF and the $\Delta K_{2/\pi 0}$ gives an underestimate of the effective SIF. An improved correlation of fatigue crack growth rates results from the driving forces in five aluminum alloys at load ratios, R, from -1.0 to 0.7. Since most cycles of crack growth accumulate to threshold, this discovery was very important for improving life prediction. However, the model requires measurement and prediction of opening loads.

Kujawski [13, 14] also showed that the crack closure model can not predict fatigue crack growth behavior near the threshold for aluminum alloys. For many materials, for example, 7017-T6 aluminum alloy and Ti-24Al-11Nb titanium aluminide, it was found that the correction for closure is not sufficient to collapse the fatigue crack growth curves into a single curve at different R-ratios [50, 51]. In 1974, Shih and Wei [52] showed crack closure was likely to be only one of several factors that contributed to observed R effects. Their experimental results in Ti-6Al-4V titanium alloy showed that crack closure is observed only at stress ratios less than 0.3. However, FitzGernald and Wei [53] indicated that the R-ratio affects fatigue crack growth in Ti-6Al-4V titanium alloy for $0.05 < R < 0.9$. They also showed [52] that under variable-amplitude loading (single tensile overload) at $R_{OL} > 0.3$ crack closure is absent; however, fatigue crack growth is significantly retarded. Therefore, crack closure is not the only factor that needs to be considered to account for the stress ratio and variable amplitude loading effects.

In 1994, Sadananda and Vasudevan [11] showed that the closure contribution from asperities resulting from oxides or corrosion products, or surface roughness is only 20% of the estimate based on a change in the slope of load-displacement curves near the threshold. Moreover, it was shown that plasticity-induced closure is insignificant at the near threshold. Therefore, the closure mechanism can not describe the stress ratio effect on fatigue crack growth for the threshold regime. They postulated that there are two load parameters, ΔK^*_{th} and $K^*_{max,th}$, that must be exceeded simultaneously if fatigue crack growth is to occur. They also proposed a new model based on two parameters, ΔK and K_{max}, to describe variations in the fatigue crack threshold with the load ratio.

Clerivet and Bathias [54] proposed that the crack closure model can not fully explain the R-ratio and environment effects on fatigue crack growth for 7175 T651 aluminum alloy. They showed that the effective stress intensities determined in laboratory air and in a salt water environment are the same. Therefore, the closure model can not explain the environmental effect on FCG. In other words, the experimental results can not show the effect of oxide- or corrosion-induced closure on FCG. They also concluded that the measured closure loads have no relevance to fatigue processes.

In a vacuum test, where closure is absent, the FCG should be faster than the air test, but experimental results contradict such a belief [55]. Therefore, the possibility of other factors on FCG behavior must be addressed.

A comparison of predictions by the closure model and the observed crack growth rates for BS4360 50B structural steel, Figure 2-12, following a single tensile overload show that the predicted growth rates are less than the experimental measurements from the minimum point to the stabilized FCG rate for both plane strain and plane stress conditions. The discrepancy between predicted and measured growth rates is due to discontinuous closure, first identified experimentally by Fleck [10, 56]. The phenomenon of discontinuous closure refers to the point at which the crack surfaces are first closed behind the crack tip and is induced by a residual hump of stretched material due to a single overload, as shown in Figure 2-13. As a result, the opening load obtained from the closure measurements when the crack flanks first come into contact is greater than the actual opening load when the crack tip is closed. The measured stress intensity factor range is less than that experienced at the crack tip, and consequently, the predicted FCG rates are less than the measured values, as shown in Figure 2-12.

2.3.1.1.2 Two-Parameter Models

The above stated observations show that the possible role of other factors on FCG prediction must be considered. Therefore, numerous research activities [11, 12, 13, 14, 15] have attempted to modify the general form of the Paris equation by introducing a two-parameter driving force in the form of a combination of the maximum SIF, K_{max}, and the stress intensity range, ΔK. The first form of the fatigue crack growth equation in terms of a two-parameter driving force was proposed by Walker in 1970 [12].

$$\frac{da}{dN} = C_1 \left[\frac{\Delta K_{appl}}{(1-R)^{1-p}} \right]^m = C_1 \left[K_{max,appl}^{(1-p)} \Delta K_{appl}^{\ p} \right]^m \tag{2.39}$$

where: $C_1 = C(1-R)^{m(1-p)}$

The constants "C" and "m" are the Paris coefficient and slope for R = 0, respectively, and the "p" parameter is a material constant. However, the Walker equation is valid only for $R \geq 0$ and for region II crack growth.

In 1963, Broek, Schijve and Erdogan [57] proposed another combination of the two-parameter driving force to show the mean stress effect on FCG for region II.

$$\frac{da}{dN} = C K_{max}^2 \Delta K \tag{2.40}$$

Forman, Kearny and Engle [58] observed that the crack growth rate tends to infinity when K_{max} approaches K_{IC}. They suggested the following equation for regions II and III in terms of a two-parameter driving force.

$$\frac{da}{dN} = \frac{A(\Delta K)^n}{(1-R)(K_{IC} - K_{max})} \tag{2.41}$$

where “A” and “n” are empirical material constants.

Another empirical equation for regions II and III was introduced by Weertman [59].

$$\frac{da}{dN} = \frac{C\Delta K^4}{K_{IC}^2 - K_{max}^2} \tag{2.42}$$

None of the above equations addresses the fatigue crack growth behavior at threshold. To predict FCG behavior in the threshold regime, Klesnil and Lukas [60] modified the Paris equation:

$$\frac{da}{dN} = C(\Delta K^m - \Delta K_{th}^m) \tag{2.43}$$

Later, Donahue et al. [61] introduced a similar relationship:

$$\frac{da}{dN} = C(\Delta K - \Delta K_{th})^m \tag{2.44}$$

Priddle [57] proposed an empirical relationship to describe the entire crack growth curve, taking into account both K_{IC} and ΔK_{th}:

$$\frac{da}{dN} = C\left(\frac{\Delta K - \Delta K_{th}}{K_{IC} - K_{max}}\right)^m \tag{2.45}$$

McEvily [62] developed another equation that can be fitted to the entire crack growth rate region.

$$\frac{da}{dN} = C(\Delta K - \Delta K_{th})^2\left(1 + \frac{\Delta K}{K_{IC} - K_{max}}\right) \tag{2.46}$$

Parida and Nicholas [51] introduced a two parameter driving force in terms of the mean stress intensity factor, K_{mean}, and the stress intensity range, ΔK, to consolidate fatigue crack growth data into a single curve for different R-ratios, $0.1 < R < 0.8$, in titanium aluminide, Ti-24Al-11Nb. They modified the Paris equation as follows:

$$\frac{da}{dN} = C\left[\left(K_{mean}\right)^{m}\left(\Delta K\right)^{1-m}\right]^{n} \tag{2.47}$$

where: $$K_{mean} = \frac{K_{max} + K_{min}}{2}$$

For this material, m = 0.5 provides the best driving force to represent the experimental data as a single curve, based on regression analysis. For other materials, the magnitude of the exponent "m" can be determined from regression analysis of the experimental data. However, this driving force can be used only for positive stress ratios.

Recently, Dinda and Kujawski [14] proposed a two-parameter fatigue crack driving force, $K_{max}{}^{\alpha}(\Delta K^{+})^{(1-\alpha)}$, to show the effect of R-ratios on fatigue crack growth behavior in different materials. The parameter α is an empirical fitting parameter. He also demonstrated that for α = 0.5, a good correlation of FCG data with the driving force, $(\Delta K^{+}.K_{max})^{0.5}$, can be obtained in six aluminum alloys, especially in the threshold region [13]. FCG data for different R-ratios can then be correlated when the data is shown in terms of the proposed driving force without the necessity of the concept of crack closure. Kujawski [13] also compared the correlating ability of the two-parameter driving force to the closure-based ΔK_{eff} approach. It was found that the two-parameter model is as effective as the crack closure model to show the R-ratio effect on fatigue crack growth [14]. However, this model can not predict the effect of the compressive part of loading on FCG. Moreover, the correlation of experimental FCG data for positive stress ratios was better than for negative ones.

Donald and Paris [15] postulated that fatigue crack growth depends not only on the stress intensity range, ΔK, but also on the maximum stress intensity factor, K_{max}. To show the K_{max} contribution to stress ratio effects, they did two tests, one at the constant R-ratio of 0.7 and the other at a constant K_{max} of 22 MPa√m with a decreasing ΔK ($0.5 < R < 0.95$) for two

aluminum alloys, 6061-T6 and 2024-T3. Figure 2-14 shows the experimental results for the two tests in 2024-T3 aluminum alloy. Although both curves were closure free, the discrepancy between the two curves, especially at near-threshold fatigue crack growth rates, could be observed due to differences in K_{max}, as shown in Figure 2-14. Therefore, they introduced a two-parameter driving force in the form of $\Delta K_{eff}^{(1-n)} K_{max}^{n}$ to account for the K_{max} effect on FCG prediction. In the proposed two-parameter driving force, the exponent "n" is an experimental fitting parameter. Using the proposed driving force, $\Delta K_{eff}^{(1-n)} K_{max}^{n}$, provided a single curve of the FCG data for 2024-T3 aluminum alloy, as shown in Figure 2-15.

2.3.2 Fatigue Crack Growth Prediction under Variable Amplitude Loading

Most fatigue loaded components and structures experience a spectrum of stresses under typical operating conditions. Under constant amplitude loading, fatigue crack growth depends on crack size and applied load. However, under variable amplitude loading, it also depends on the preceding cyclic loading history as a consequence of load interaction. The complexity of fatigue crack growth predictions under variable amplitude loading was highlighted in the literature review done by Skorupa [63, 64], from which the following lines are taken.

> "The reviewed data suggest that, depending on a particular combination of load parameters, material, geometry and environment, variable-amplitude load sequences of the same type can produce either retardation or acceleration in fatigue crack growth [63]."
>
> "Mechanisms linked to plastic straining at the crack tip enable an interpretation of the majority of the experimental results. Some observations, however, which cannot be understood in terms of plasticity-induced crack closure, or which are even in

contradiction with the crack closure approach, indicates a possible role of other factors. A general conclusion is that conditions under which various phenomena can affect variable-amplitude fatigue crack growth and interactions between them are insufficiently recognized [64]."

Therefore, fatigue life prediction under variable-amplitude loading must be estimated with excessive safety factors for design and proper prediction models used. Various types of load sequences—over-loads, under-loads, and combinations of overloads and under-loads—induce different load-interaction effects, which can cause significant acceleration or retardation of fatigue crack growth rate. Therefore, a more complete understanding of interaction and sequence effects is essential for developing crack growth prediction models under variable amplitude loading. Due to the beneficial effect of overloads on fatigue life prediction, the main focus of this study is to show the effect of overloads on subsequent fatigue crack growth.

2.3.2.1 Overload Effects on Fatigue Crack Growth

Overloads can retard fatigue crack growth rates; therefore, most load-interaction studies have concentrated on overload effects. The typical retardation of the crack growth following a single overload is presented schematically in Figure 2-16. The number of delay cycles, N_D, is a measure of the magnitude and extent of retardation, as shown in Figure 2-16.

Numerous researchers have demonstrated fatigue crack growth retardation following a single overload for various metals. Representative crack growth retardation following a single overload, analogous to Figure 2-16 , has been reported in 7075-T6 aluminum [82, 65], 7075-T651 aluminum [66], 2024-T3 aluminum [65, 67], 2024-T351 aluminum [68, 69], D16Cz aluminum [70], 4340 steel [71], 4140 steel [72], 18G2A steel [73], FV520B steel

[74], A514F steel [75], Ti-6Al-4V [67], and Ti-6222 [76]. The crack growth retardation induced by a single overload increases with an increase of the overload-ratio, OLR, which also results in an increase of the number of delay cycles, N_D, and a decrease of the minimum fatigue crack growth rate [65, 77, 78, 79, 80]. Moreover, as the number of overload cycles increases, the amount of the retardation following single overloads is more pronounced [67, 79].

Initial acceleration was not observed for any materials, especially for high overload ratios as shown in the publications by Shin et al. [80] for stainless steel at OLR of 2, by Damri et al. [81] for mild steel at OLR of 2.5, and Chanani [82] for the 7075-T6 aluminum alloy at OLR of 1.8. However, Tsukuda et al. [83] showed that initial acceleration depends not only on the overload ratio but also on the R ratio ($R = \frac{K_{min,BL}}{K_{max,BL}}$). The 2017-T3 aluminum alloy, they [83] found that at R = 0 for overload ratios of 1.5 and 2, there was an initial acceleration; however, at R-ratios of 0.5 and 0.7, with the same overload ratios, the initial acceleration was absent. It was found that FCG retardation decreases with an increase of the R-ratio [80, 83].

Results from the literature [63, 80, 84, 85] show that FCG retardation, following a single overload, is not consistent with the change in baseline loading, ΔK_{BL}, as shown in Figure 2-17. The experimental results for aluminum alloys [85, 86], aluminum-lithium alloy [87], steel alloys [85], and a Ti alloy [84] indicated a U-shaped plot of the delay cycles, N_D, versus ΔK_{BL} with significantly less delay occurring at some intermediate baseline loading. However, other experimental results for stainless steel [80] and structural steel [88] showed different plots of N_D versus ΔK_{BL}, in total contrast to the U-shape curves, as illustrated in Figure 2-17.

For single-periodic overloads, as shown in Figure 2-18, Yildirim and Vardar [89, 90, 91] showed that fatigue crack growth rate depends on the number of constant amplitude cycles between tensile overloads, N_{CA}. Their experiments on Al 7075-T6 and Al 2024-T3 specimens demonstrated that retardation increases and then decreases as the number of constant amplitude cycles between single tensile overloads increases. However, the maximum retardation occurs when tensile overloads are applied at $N_D/2$, where N_D is the number of delay cycles in the case of a single overload (Figure 2-18). For Al-alloy 7075-T6, they [89] also proposed that the crack growth rate for different occurrence ratios ($OCR = \frac{1}{N_{CA}}$) follows constant amplitude loading behavior, with a parallel shift such that it can be modeled as a pseudo-constant-amplitude crack growth. Hence, fatigue crack growth rates can be predicted using the Paris equation without changing the exponent. In other words, single-periodic overloads can be treated as pseudo-constant-amplitude loading in developing fatigue crack growth prediction models.

Mills and Hertzberg [92] showed that in periodic overloads, interaction effects of tensile overloads in the 2024-T3 aluminum alloy can be related to the increment of crack extension separating overloads. Maximum interaction between two single or block overloads (minimum fatigue crack growth rate) was obtained when the increment of crack extension separating peak loads or the distance between two tensile overloads was almost $\frac{r_{OL}}{4}$, where r_{OL} is the plastic zone size resulting from a single overload. It was noted that the interaction effect can be eliminated only if the amount of crack extension is approximately three times the plastic zone size resulting from a single overload $(= 3r_{OL})$. These observations contrast with the fact that crack growth returns to the normal growth rate when the crack propagates

through r_{OL} rather than $3r_{OL}$. In addition, the fatigue crack growth retardation resulting from periodic overload blocks was found to be greater than that associated with single-periodic overloads.

2.3.2.2 Prediction Models

Several predictive models have been formulated since the 1970s to account for load interaction effects and to estimate quantitatively fatigue crack growth lives under variable amplitude loading conditions. Because of the complexity of mechanisms governing FCG under variable amplitude loading, only semi-empirical models can provide reasonable FCG predictions. The earliest models, the Wheeler [93] and Willenborg [94] models, were based on the compressive residual stresses ahead of crack tip induced by overloads. The second generation of the models, i.e. the crack closure models [3, 4, 5, 6, 7] were based on the plastic deformation left in the wake of a propagating crack. These models are still used in different computer programs and codes for fatigue life estimation. A description of the models follows.

2.3.2.2.1 Crack-Tip Plasticity Models

The most popular crack-tip plasticity or yield zone models were proposed by Wheeler [93] and Willenborg [94] in the early 1970s. Due to the simplicity of the models, they have been used widely in different fatigue crack growth computer programs such as AFGROW and CRCAKS2000. Both models can predict FCG retardation as long as the fatigue crack propagates through the overload plastic zone.

The Wheeler model [39, 93] predicts crack growth retardation by modifying the Paris equation as follows:

$$\frac{da}{dN_i} = (Cp)_i \left[C(\Delta K_i)^m \right] \tag{2.48}$$

where, the retardation parameter, $(Cp)_i$, ranging from 0 to 1 depends on the current plastic zone, $r_{p,i}$, and the overload plastic zone, $r_{p,OL}$.

$$(Cp)_i = \left(\frac{r_{p,i}}{r_{p,OL} - \Delta a_i} \right)^p \tag{2.49}$$

The Wheeler exponent "p" is a fitting empirical parameter depending upon the loading history. Other terms in Eq. (2.49) are defined graphically in Figure 2-19. The model predicts that the maximum retardation occurs immediately after the overload and it decreases by growing the crack through the overload plastic zone. The retardation effect ceases as soon as the current plastic zone touches the boundary of the overload plastic zone, $(Cp)_i = 1$.

A major limitation of the Wheeler model is the shaping factor, p, which must be determined experimentally for loading history. Moreover, the observed phenomenon of the delayed retardation, and also crack growth acceleration, cannot be predicted with the Wheeler model.

The Willenborg model [39, 94] predicts that crack retardation will occur due to the compressive residual stresses induced by the overload at the crack tip. The compressive stresses can be expressed in terms of the reduced stress intensity factor, K_{red}, to modify the applied stress intensity factors. To calculate compressive stresses at the crack tip, Willenborg et al. introduced the required stress, σ_{req}, which is required to produce a yield zone, $r_{p,req}$, whose boundary just touches the overload plastic zone boundary, $r_{p,OL}$, as shown in Figure 2-20. The required stress can be expressed in terms of the required maximum stress intensity factor, $K_{max,req}$, which is determined as follows:

$$a_i + (r_{p,req})_i = a_{OL} + r_{p,OL} \tag{2.50}$$

$$K_{max,req} = K_{max,OL}\sqrt{1 - \frac{(a_i - a_{OL})}{r_{p,OL}}} \tag{2.51}$$

The compressive residual stress is the difference between the maximum stress, σ_{max}, and the required stress, σ_{req}. In terms of the stress intensity factor, the difference between the required maximum stress intensity factor, $K_{max,req}$, and the maximum stress intensity factor, $K_{max,i}$, is then defined as the reduced stress intensity factor, K_{red}.

$$K_{red} = K_{max,req} - K_{max,i} \tag{2.52}$$

Subsequently the effective stress intensity factors can be obtained.

$$K_{max,eff})_i = K_{max,i} - K_{red} \tag{2.53}$$

$$K_{min,eff})_i = K_{min,i} - K_{red} \tag{2.54}$$

Fatigue crack growth in each cycle can then be calculated from the Paris Eq. (2.27), Walker Eq. (2.39), or Forman Eq. (2.41) based on effective stress intensity factors. The Willenborg model cannot predict delayed retardation; the maximum retardation occurs immediately after an overload. Moreover, similar to the Wheeler model, FCG accelerations can not be predicted with this model. A major advantage of the Willenborg model is that only the constant-amplitude crack growth data is used to predict fatigue crack growth retardation without using the empirical shaping factor.

2.3.2.2.2 Crack Closue Model

Crack closure models based on the crack closure phenomenon can predict the effects of load interactions, such as acceleration and retardation of the fatigue crack growth. Several crack closure models such as PREFFAS [3], ONERA [4], and CORPUS [5] have been

developed recently to account for load interaction effects under variable amplitude loading [39]. A detailed description of theses models can be found in reference [39]. Among them, the most successful finite element model has been developed by Newman [6,7]. The Newman model was based on the strip yield plastic zone that is left in the wake of the advancing crack. The plastically deformed material can induce crack closure even at positive stress levels. According to this model, the fatigue crack growth rate for highly irregular loading, should be calculated on a cycle by cycle basis.

However, the crack opening load, P_{op}, changes in a variable amplitude loading history; and consequently, the effective stress intensity, ΔK_{eff}, can vary with each cycle. Therefore, the determination of the crack opening load and the corresponding crack opening stress intensity factor, K_{op}, is the main problem in the crack closure models in the case of variable amplitude loading. The Newman model [6,7] assumed that the crack opening load, P_{op}, remains constant during a small crack increment and does not change after each load cycle. In engineering approaches, for simplicity, it was assumed that the crack opening stress intensity factor, K_{op}, is constant during a given block of variable amplitude loading. It can be calculated from the constant amplitude fatigue test with an equivalent stress intensity range defined as $\Delta K = K_{max,VA} - K_{min,VA}$, where $K_{max,VA}$ is the maximum stress intensity factor and $K_{min,VA}$ is the minimum stress intensity factor in the block of variable amplitude loading [42]. However, the fatigue crack growth rate is predicted for each cycle using the Paris law.

$$\frac{da}{dN_i} = A(\Delta K_{eff,i})^m \tag{2.55}$$

where: $$\Delta K_{eff,i} = K_{max,i} - K_{op}$$

The constant "A" is not the same as constant "C" used in the Paris equation. The constant "C" in the Paris equation was calculated based on the applied stress intensity factor, ΔK_{appl}.

However, the constant "A" should be estimated based on the effective stress intensity factor, ΔK_{eff}, at each cycle. The constant "C" can be corrected for a new closure level with the following equation [95].

$$A = \frac{C}{(U_i)^m} \tag{2.56}$$

where:

$$U_i = \frac{\Delta K_{eff,i}}{\Delta K_{appl,i}}$$

Eq. (2.55) should be solved using a numerical integration method to obtain cycle-by-cycle fatigue crack growth and consequently the fatigue life from an initial crack size to a final crack size. A number of computer programs, such as NASGRO, FASTRAN-II, MODGRO, and FLAGRO have been developed to estimate fatigue life under variable amplitude loading.

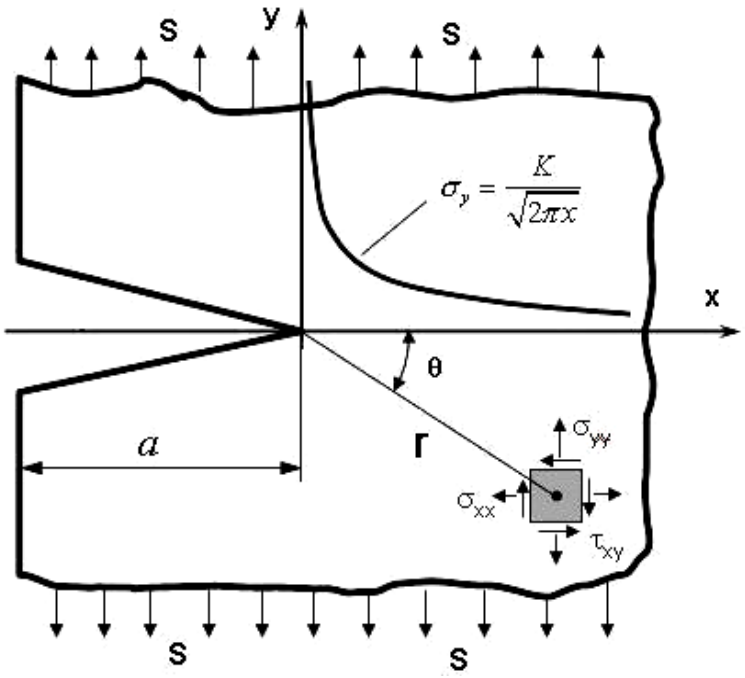

Figure 2-1: Stress distribution and the system of coordinates at the sharp crack tip [18].

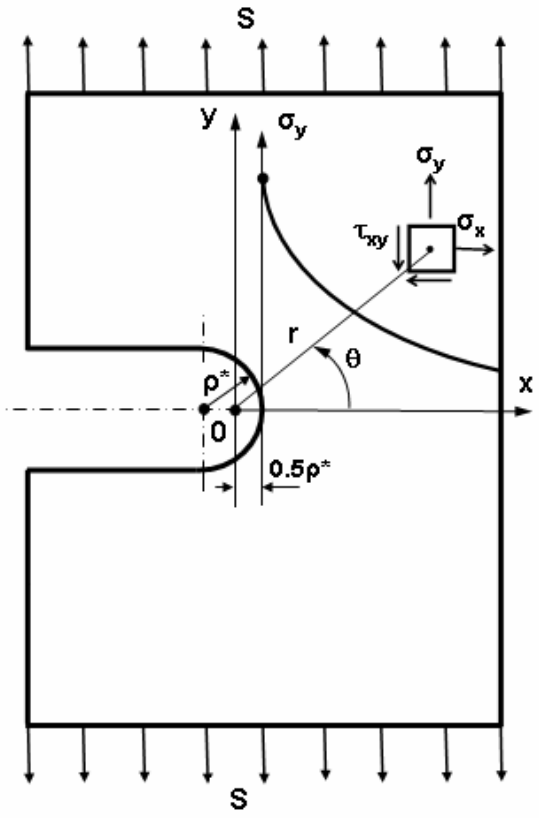

Figure 2-2: The stress distribution and the system of coordinates used for at the blunt crack tip.

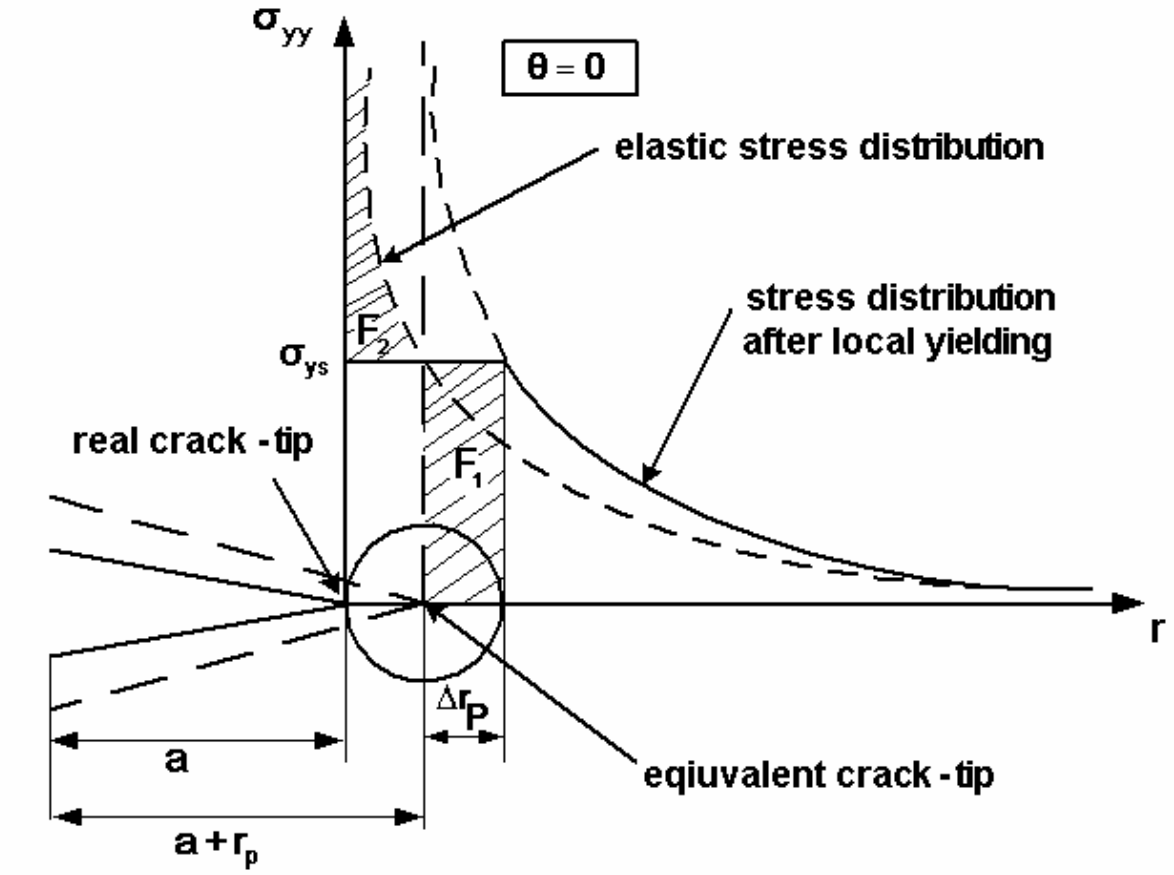

Figure 2-3: Irwin's plastic zone size, the equivalent crack size and the original and corrected stress distribution.

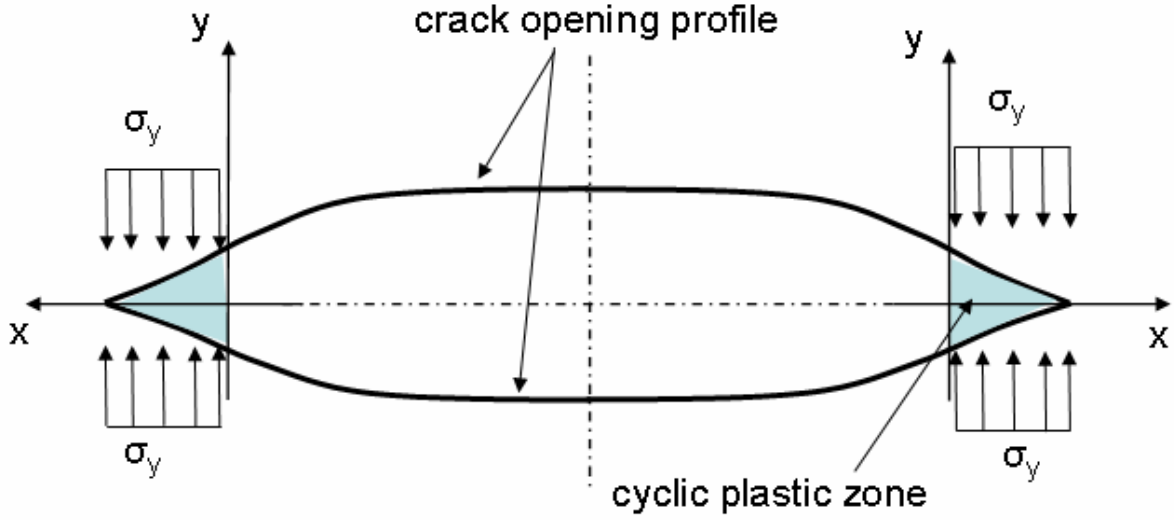

Figure 2-4: The Dugdale crack model and plastic zone size [23].

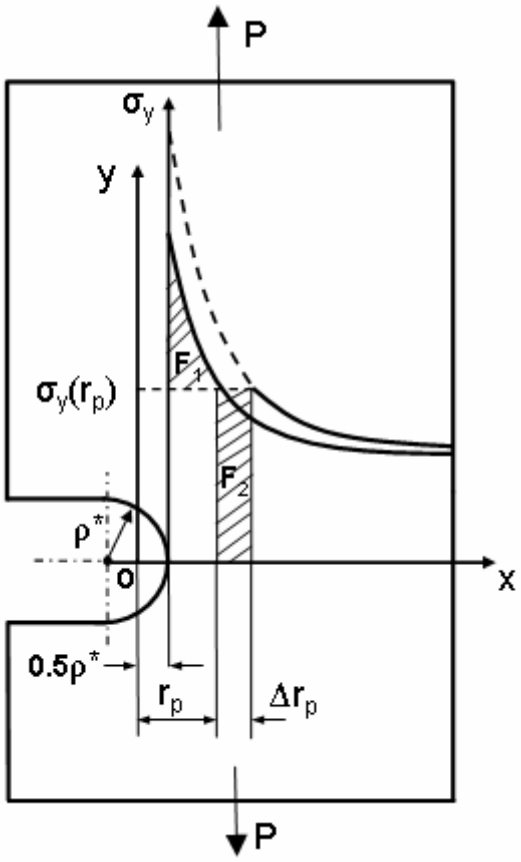

Figure 2-5: Plastic yielding and redistribution of the elastic stress field ahead of a notch tip [26].

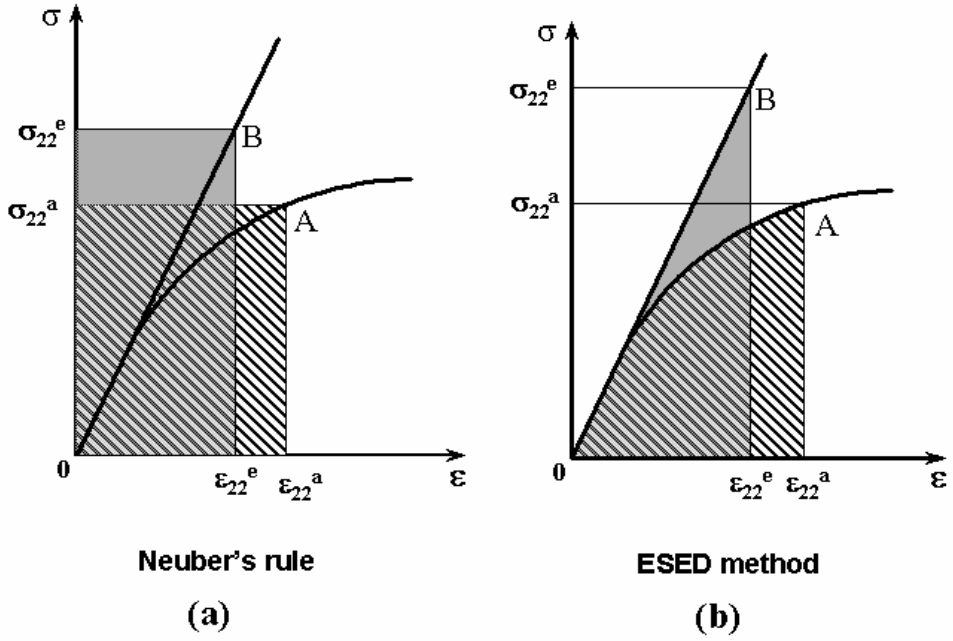

Figure 2-6: Graphical representation of Neuber's rule and the equivalent strain energy density (ESED) method: a) Neuber's rule b) ESED method [18].

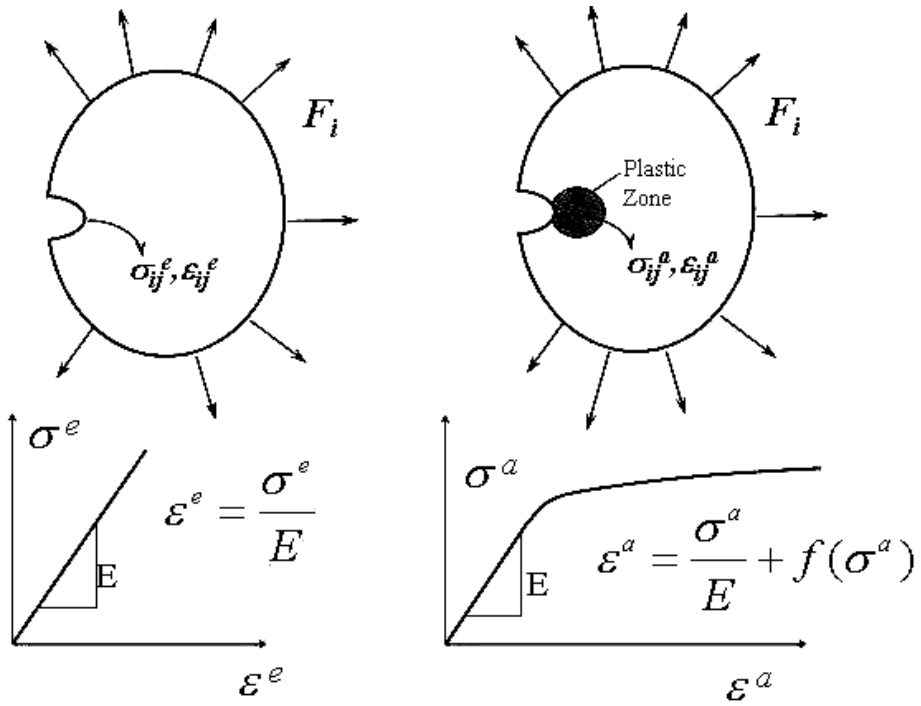

Figure 2-7: Stress states in geometrically identical elastic and elastic-plastic bodies subjected to identical boundary conditions [18].

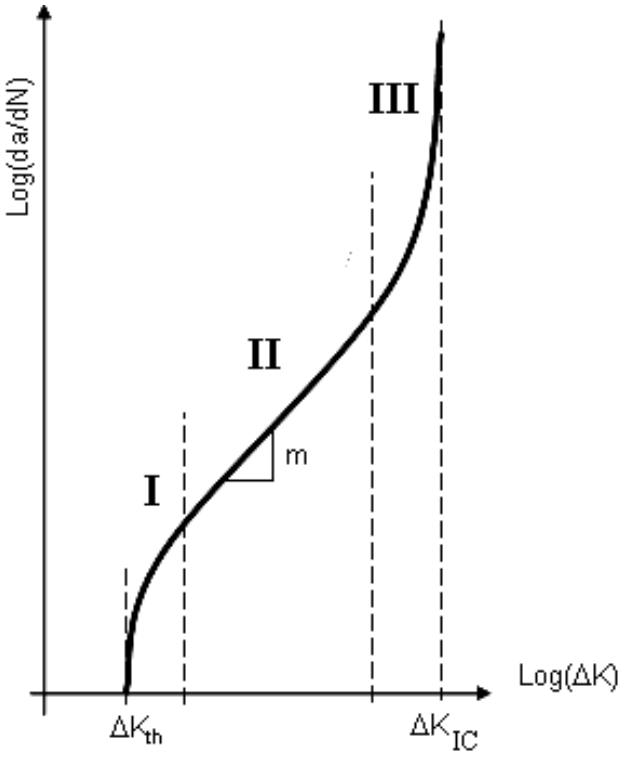

Figure 2-8: Typical fatigue crack growth rate in metals [18].

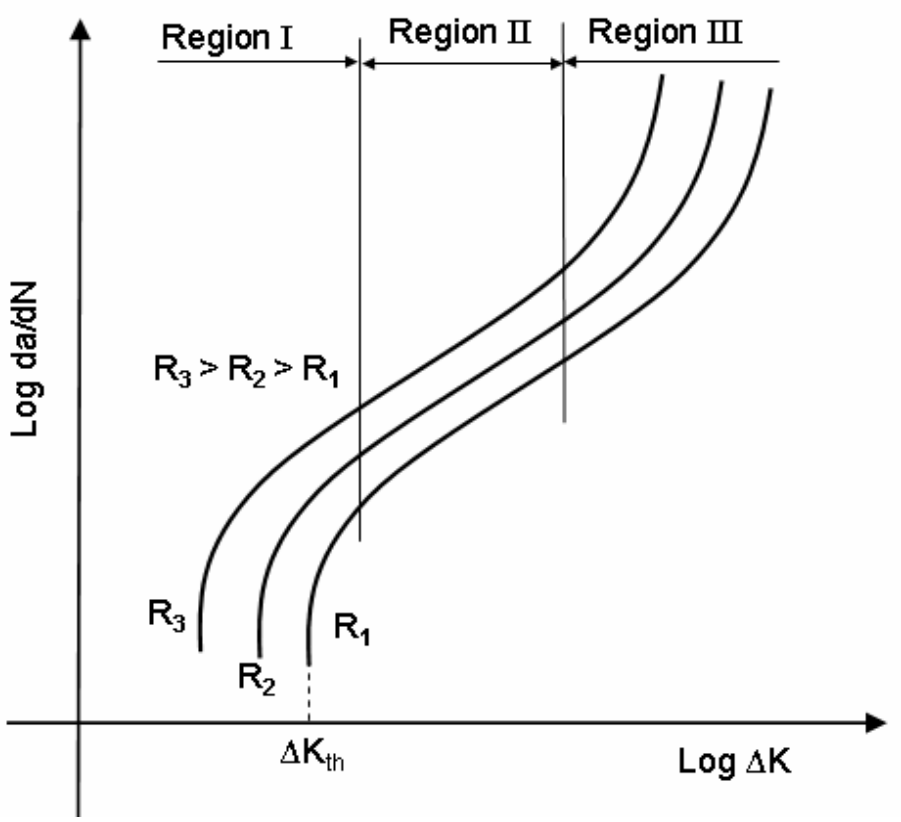

Figure 2-9: The R-ratio effect on the fatigue crack growth [39].

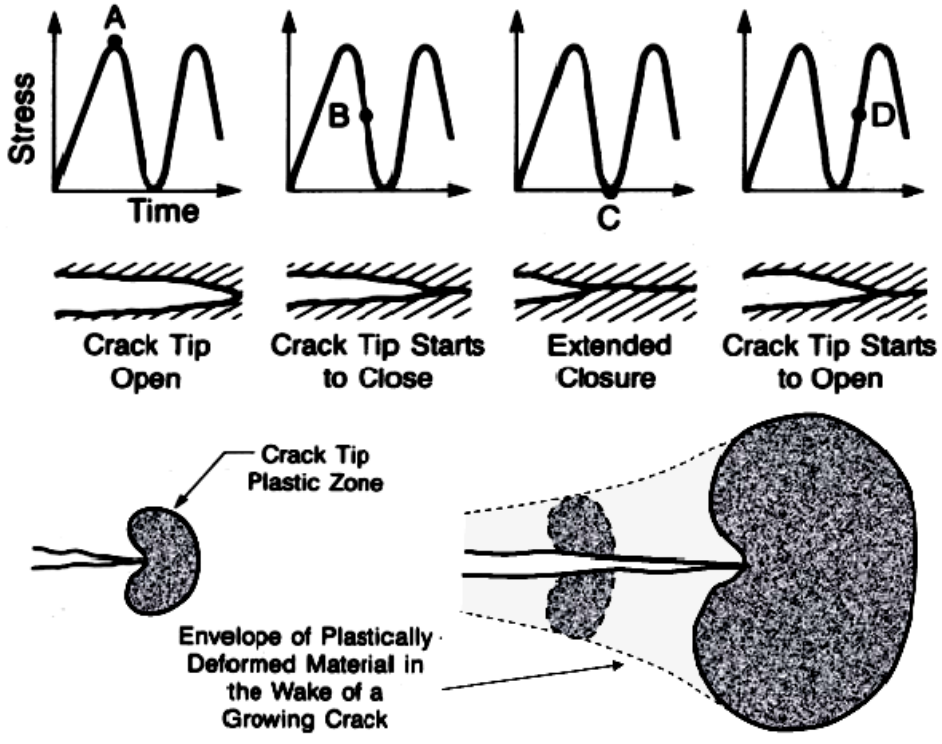

Figure 2-10: Evolution of the crack tip plastic zone ahead of a fatigue crack and crack tip closure [18].

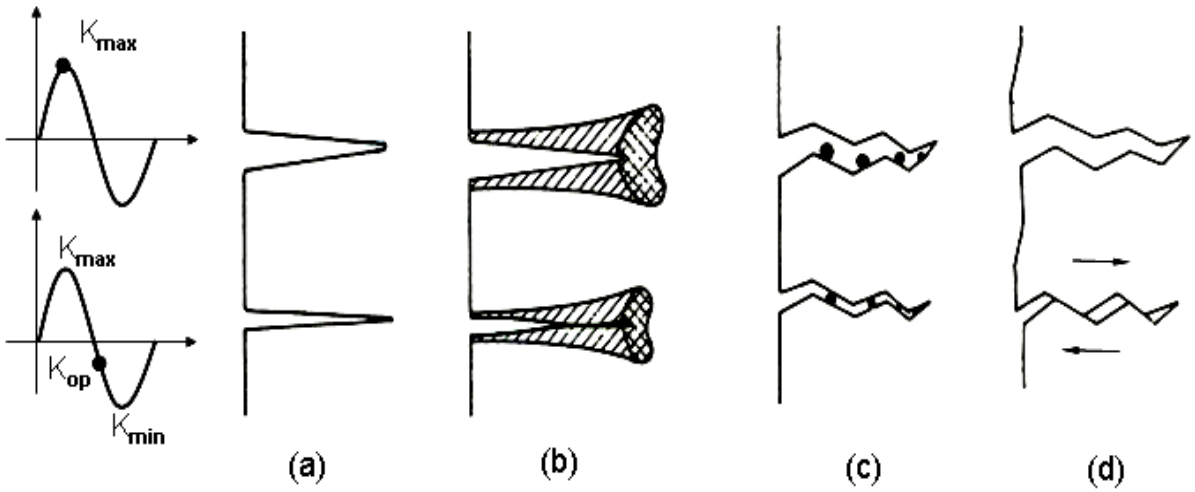

Figure 2-11: Mechanisms of fatigue crack closure: a) no closure; b) plasticity-induced closure; c) oxide-induced closure; d) roughness-induced closure [41].

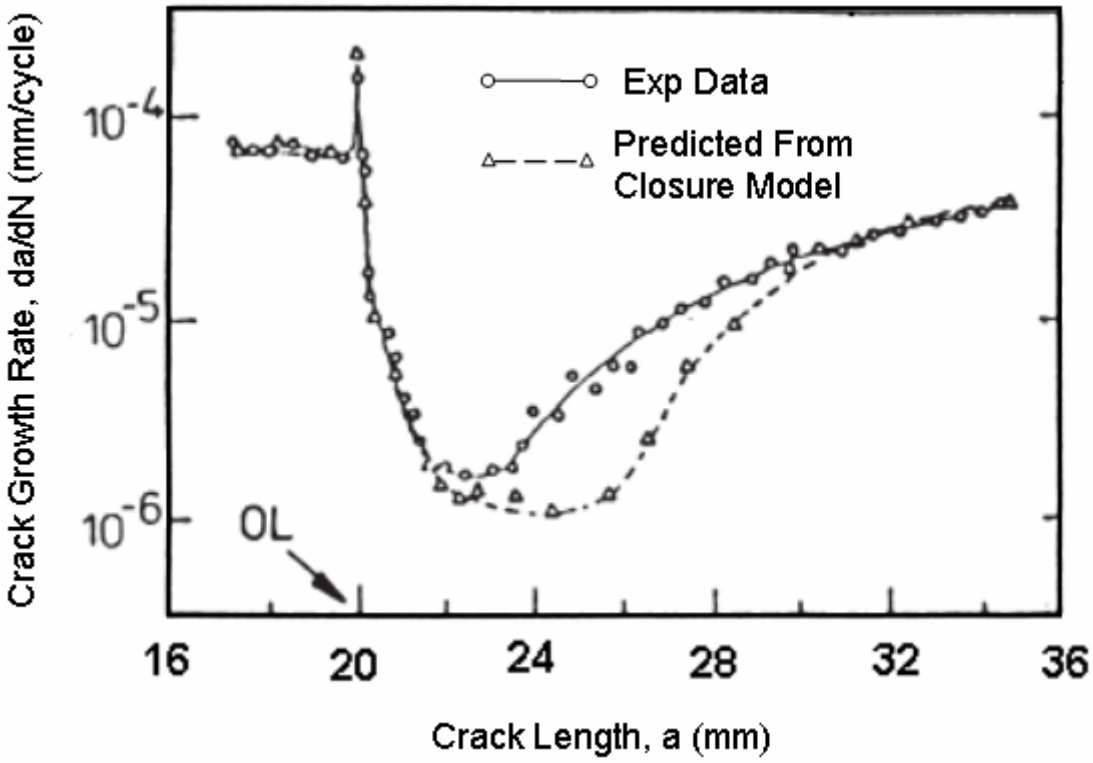

Figure 2-12: Comparison of measured and predicted fatigue crack growth rates after a single overload (R = 0.05, OLR = 2, ΔK_{BL} = 25 MPa√m) on a 3 mm CT specimen in BS4360 50B structural steel [64].

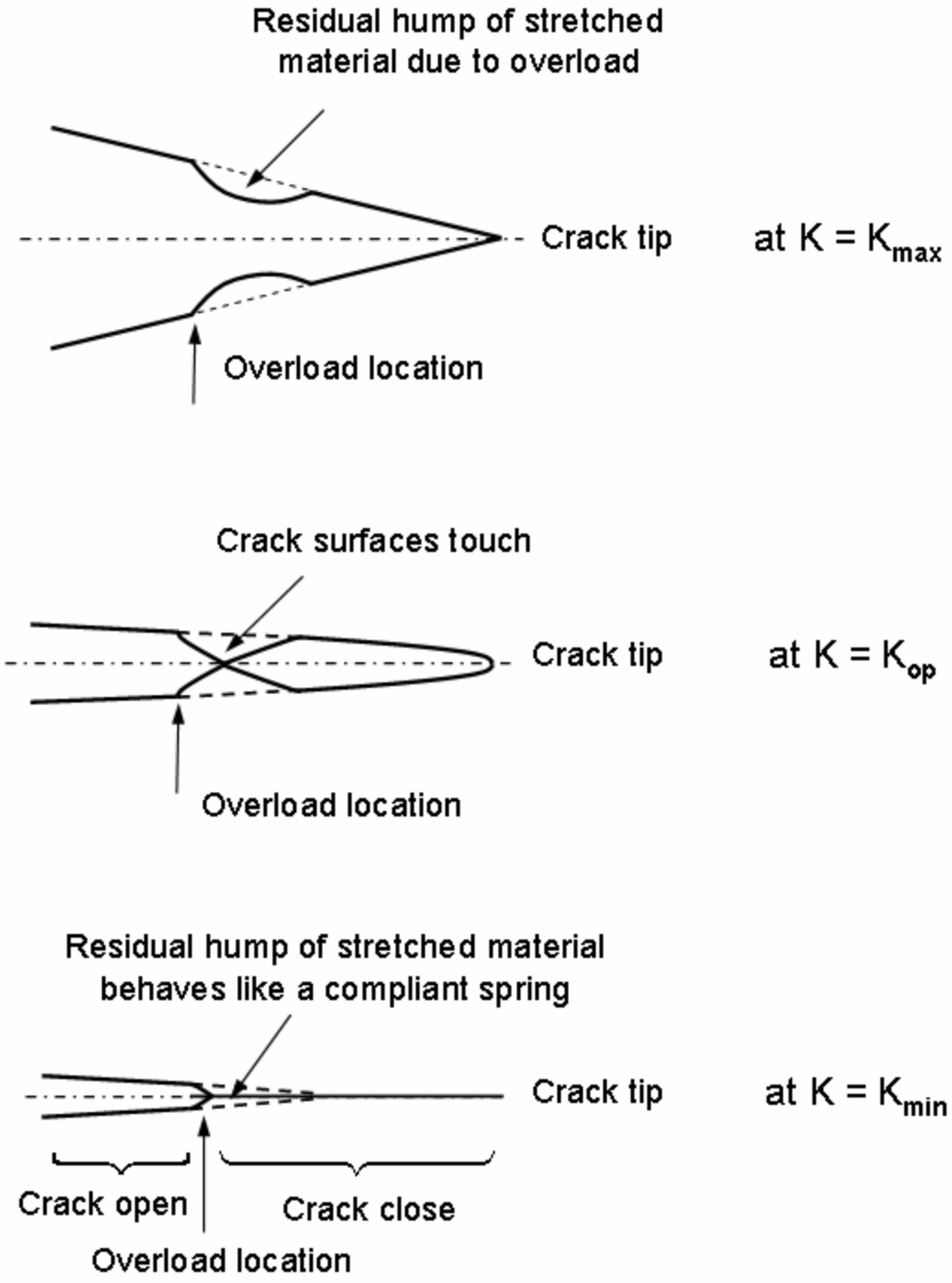

Figure 2-13: The phenomenon of discontinues closure [10].

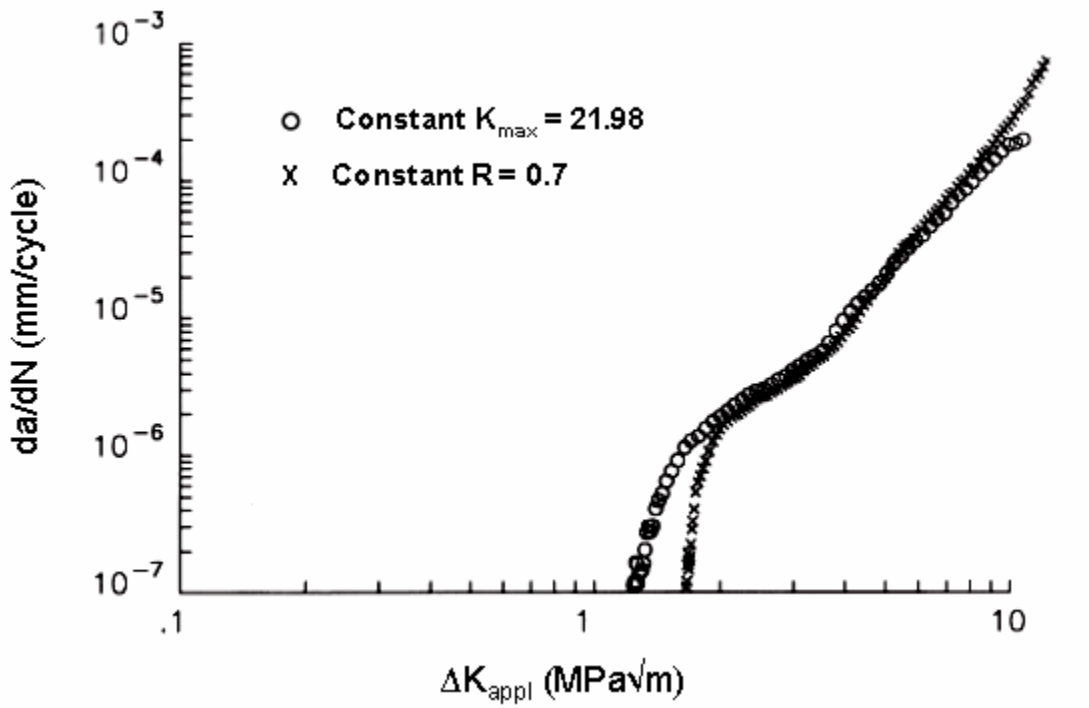

Figure 2-14: Fatigue crack growth rates as a function of ΔK_{appl} for two different tests: constant K_{max} (K_{max} = 22 MPa√m), and constant R (R = 0.7) in Al 2024-T3 [15].

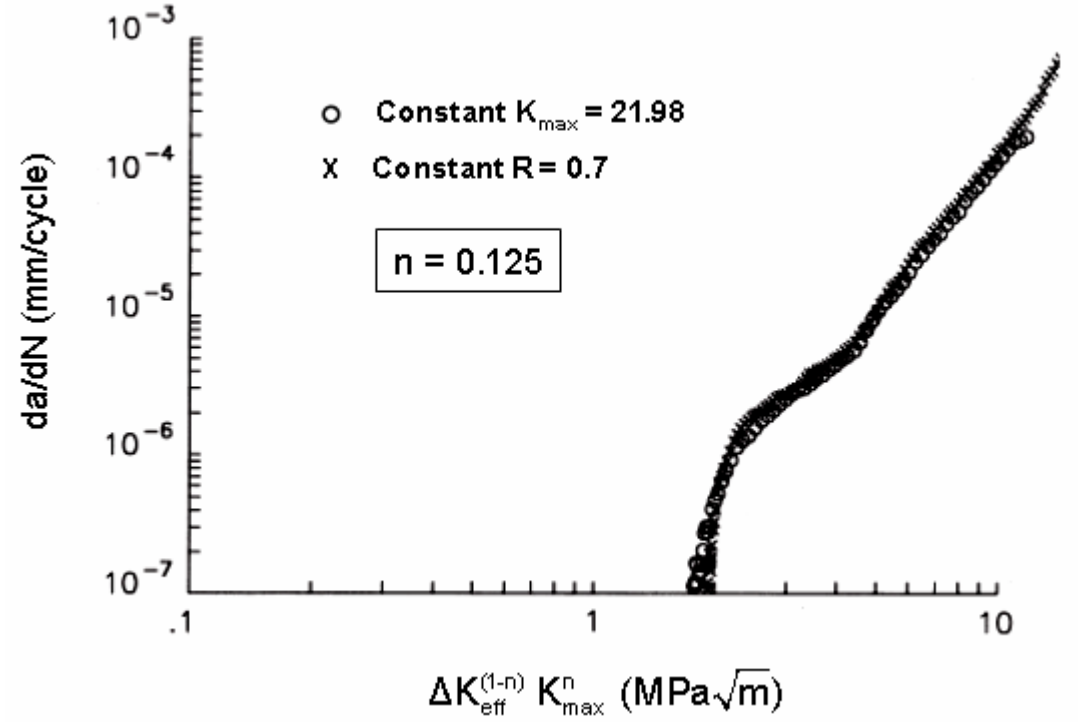

Figure 2-15: Fatigue crack growth rates as a function of the two-parameter driving force, $\Delta K_{eff}{}^{(1-n)} K_{max}{}^{n}$, for two different tests, constant K_{max} (K_{max} = 22 MPa√m) and constant R (R = 0.7) in Al 2024-T3 [15].

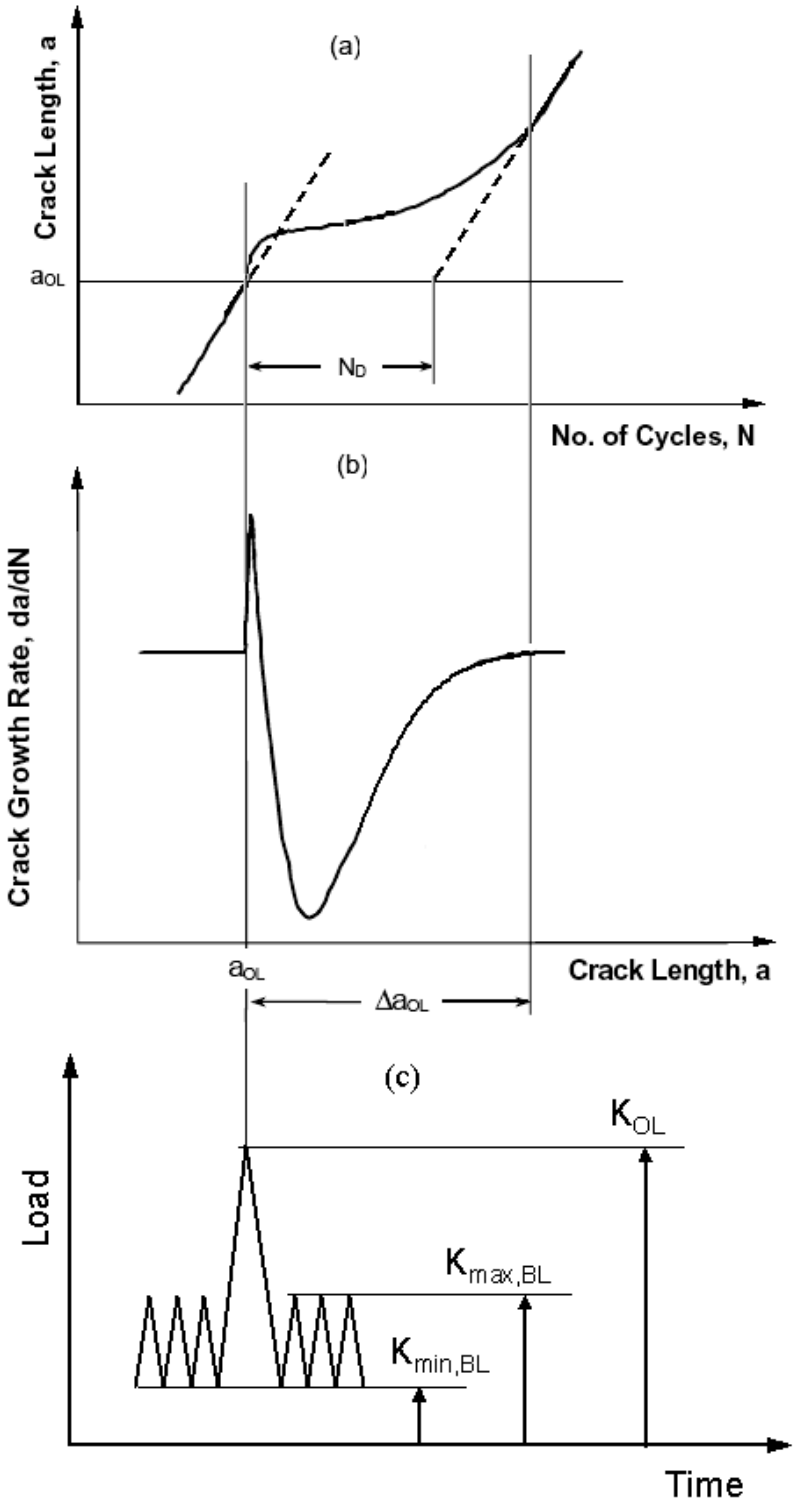

Figure 2-16: Schematic of typical overload retardation in a K-controlled test: a) crack length versus number of cycles; b) crack growth rate versus crack length; c) single overload and associated terminologies.

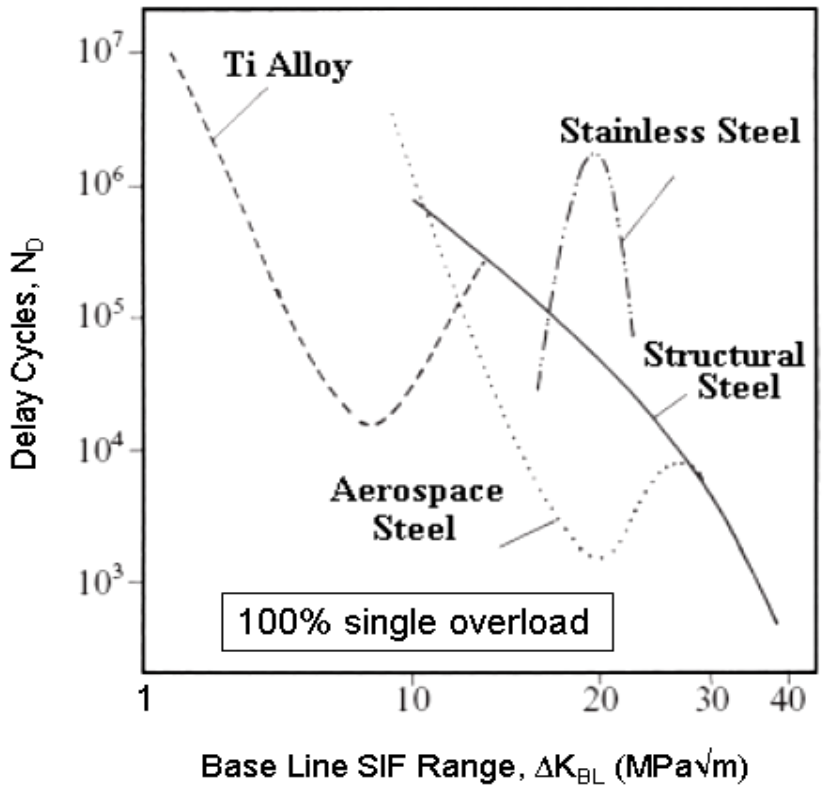

Figure 2-17: Effect of ΔK_{BL} on the amount of retardation following a single overload [63].

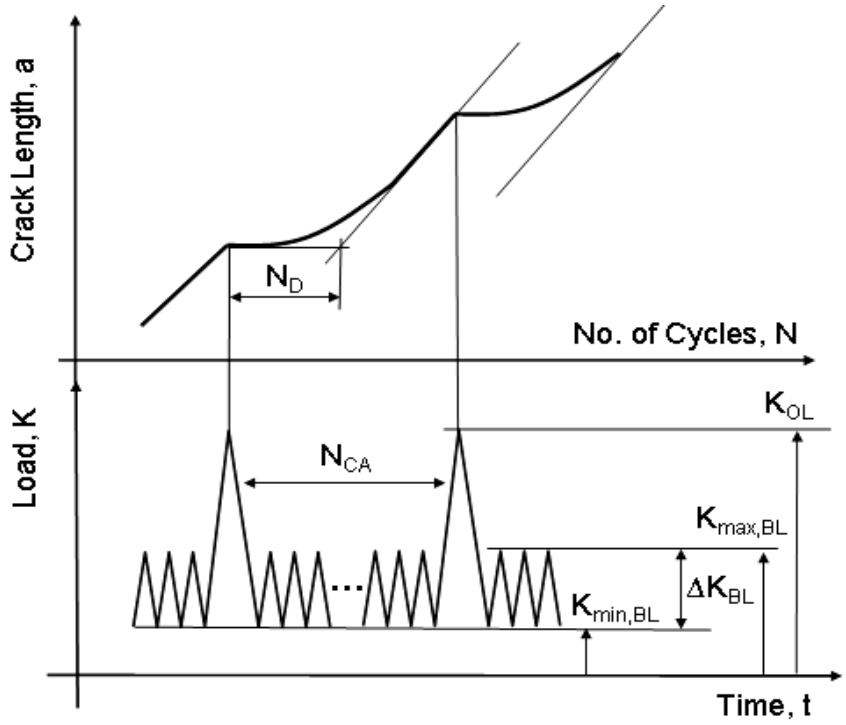

Figure 2-18: Schematic of the crack growth retardation after a single periodic-tensile overload [91].

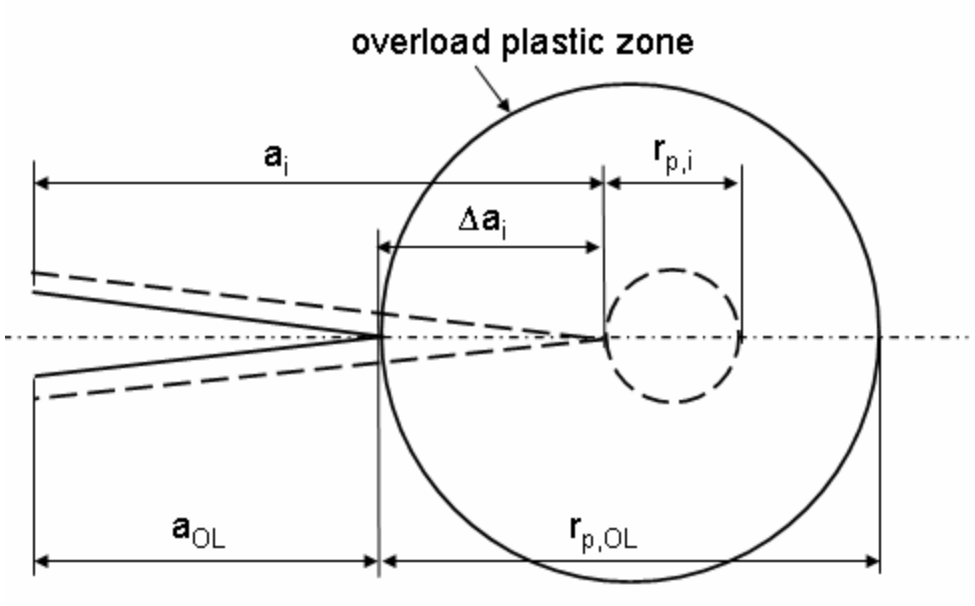

Figure 2-19: Schematic of the Wheeler model [39].

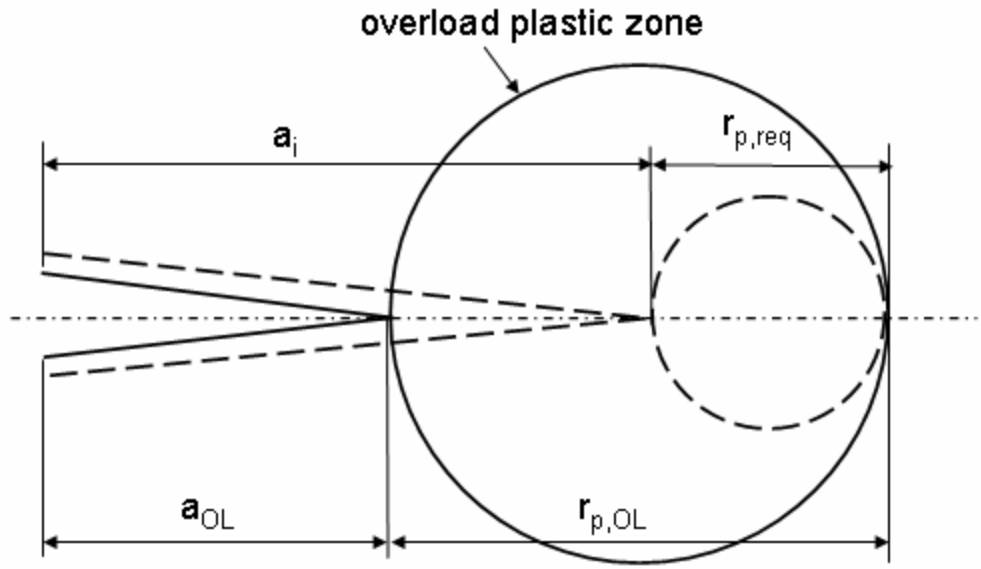

Figure 2-20: Schematic of the Willenborg model [39].

Chapter 3
Modeling of Fatigue Crack Growth

3.1 Formulation of the Proposed Model

It is generally accepted that the local stresses and strains near the crack tip control the fatigue crack growth process. Unfortunately, determination of the crack tip stress and strain in the case of elastic-plastic behavior is difficult and it is strongly dependent on the theoretical and numerical method used for the analysis. Therefore, fracture mechanics principles are often used in order to defocus attention from the local crack tip stress-strain field and to express all necessary quantities in terms of global parameters such as the nominal stress, crack size, geometry, etc., which are combined into one parameter called the stress intensity factor (SIF). Such approaches are successful as long as the SIF is uniquely correlated with the actual elastic-plastic crack tip stress-strain field. Unfortunately, the correlation between the SIF and the crack tip stress-strain filed is often altered by residual stresses induced by reversed plastic deformations.

There are also several difficulties in defining the crack tip geometry on the basis of the mechanics of continua. The classical fracture mechanics solutions [96, 97] concerning stresses and strains at the crack tip were derived for a sharp crack having tip radius $\rho^* = 0$. Such a crack-tip geometry leads to a singular solution resulting in unrealistically high strains and stresses in the vicinity of the crack tip. In spite of the importance of these fundamental fracture mechanics solutions, they unfortunately cannot be directly used for the determination of the actual stresses and strains in the vicinity of the crack tip. Therefore, several attempts were made in the past [98, 99, 100] to model the crack as a notch with a small but finite tip radius $\rho^* > 0$. The advantage of using the blunt crack model lies in the fact that notch

theories can be applied and the calculated crack tip stresses and strains become more realistic. There are two important implications resulting from such a model: the crack tip radius is assumed to be finite ($\rho^* > 0$) and the crack region just behind the tip remains open, as shown in Figure 3-1.

In the case of pure elastic behavior, the crack subjected to tensile loading behaves like a notch of length/depth 2a with tip radius equal to ρ^*, as shown in Figure 3-1(a). However, under compressive loading, as shown in Figure 3-1b, the opposite crack surfaces come into contact with each other except for the region just behind the crack tip. In Figure 3-1(b), the crack induces the same local stress field as two circular notches under compressive loading. The argument for using such a crack model comes from the Neuber micro-support concept [101] applied for calculating the fatigue notch factor. Neuber suggested that there is a limit to the smallest notch tip radius the material can 'feel' as a notch. The minimum effective notch tip radius, ρ^*, was considered to be a material property, determining the maximum stress concentration which can be generated in the material.

Due to the Bauschinger effect, the plastic deformations induced by the first reversal of the cyclic load are greater than those generated during a subsequent unloading reversal, even if both reversals are of the same magnitude. The plastically deformed material volume near the crack tip resists deformation during subsequent reversals of cyclic loading. Therefore, cyclic deformations near the tip of a propagating fatigue crack may be smaller than deformations induced during the first reversal applied to a virgin crack without any previous history. Thus, the plastic zone created during loading can not disappear and a small portion of the plastic zone is deformed again in the reversed direction. This re-deformed part of the plastic zone is called the cyclic plastic zone (Figure 3-2(c) and load level 4). This

plastically deformed material is left at the crack tip like an obstacle or a small 'ball' for subsequent reversals (Figure 3-2(c)). The plastically deformed material prevents the region behind the crack tip from being closed. In other words, the fatigue crack surfaces come into contact with each other but not just behind the crack tip, even if compressive loads are applied. Very small or no change in the opening displacement behind the crack tip during the unloading part of a cycle can be interpreted, based on global macro-measurements, as crack tip closure, even if there is no physical contact between crack surfaces. Schematically, this effect is illustrated in Figure 3-2(a) and Figure 3-2(b), showing the applied load history and qualitative variations in the stress and strain at the crack tip.

The possibility of the existence of "empty" or stress-free space behind the crack tip was found experimentally by Bowels [102] and Zhang [103]. The "empty" stress-free region appearing just behind the crack tip was also found by carrying out thorough Finite Element analyses [104, 105]. The plastic zone effect on the crack tip displacements can be modeled by assuming the displacement field behind the crack tip in the form of an opening shown in Figure 3-3(a). From a superposition point of view, the plastic zone deformations and the displacement field behind the crack tip, shown in Figure 3-3(a), can be replaced by an equivalent stress field as illustrated in Figure 3-3(b). It is assumed that the residual stresses, $\sigma_r(x)$, in the plastic zone are generated by reversed plastic deformations ahead of the crack tip, and that they can be determined by solving the elastic-plastic notched body boundary problem. A symmetric compressive residual stress field is added in order to simulate the effect of the opening behind the physical crack tip. The resultant model of the crack tip region, accounting for the plastic zone deformation resistance and the opening behind the crack tip, is shown in Figure 3-3(b).

The effect of the plastic zone and the crack tip opening behind the crack tip can be subsequently quantified by estimating the residual stress contribution to the applied stress intensity factors. Two effects need to be considered: the difference in the stress/strain concentration at the crack tip associated with the tensile and compressive part of the loading cycle (Figure 3-1), and the effect of the plasticity-induced residual stress around the crack tip.

A real engineering material, according to the Neuber [101] micro-support concept, can be modeled (Figure 3-4) as a medium made of elementary blocks of dimension ρ^*. The elementary material block can be considered as the smallest material volume to which the mechanics of continuum and bulk material properties such as modulus of elasticity, E, Poisson's ratio, ν, strength coefficient, K' and strain hardening exponent, n', apply. The same idea, but from the material science point of view, was discussed by Forsyth [106], who stated that "the micro-structural features in metals cause break up of the crack front into segments that relate to elementary blocks operating with some degree of independence from their neighbors but under the general influence of the macroscopic crack of which they are part". Therefore, it is anticipated that the dimension ρ^* can be indirectly dependent on the micro-structural features of the analyzed material, but cannot be uniquely associated with any specific micro-structural particle size. The elementary material block size, ρ^*, can be understood rather as an average dimension of an inhomogeneous material block which still behaves like the bulk material. The resolution of the mechanics of continua is not sufficient to determine a meaningful stress and strain field within the elementary blocks of size ρ^*. Therefore, only the average continuum mechanics stresses and strains can be assigned to those elementary blocks of material.

Based on the observations discussed above, the following fatigue crack model has been proposed:

- The material is assumed to be composed of identical elementary material blocks of a finite linear dimension ρ^* (Figure 3-4).
- The fatigue crack can be analyzed as a notch with tip radius ρ^*.
- Fatigue crack growth is regarded as successive crack re-initiations over the distance ρ^*.
- The material properties used in the proposed model are the Ramberg-Osgood cyclic stress strain curve [107]

$$\varepsilon = \frac{\sigma}{E} + \left(\frac{\sigma}{K'}\right)^{\frac{1}{n'}} \tag{3.1}$$

and the strain-life (Manson-Coffin) fatigue curve [108].

$$\frac{\Delta\varepsilon}{2} = \frac{\sigma'_f}{E}(2N)^b + \varepsilon'_f(2N)^c \tag{3.2}$$

- The number of cycles "N" to failure of the first elementary block of the material at the crack tip can be determined from the strain-life (Manson-Coffin) fatigue curve (3.2), by accounting for the stress-strain history and by using the Smith-Watson-Topper (SWT) fatigue damage parameter [16].

$$D = \sigma_{max}\frac{\Delta\varepsilon}{2} \tag{3.3}$$

- The fatigue crack growth rate can be determined as the average fatigue crack propagation rate over the elementary material block of size ρ^*.

$$\frac{da}{dN} = \frac{\rho^*}{N} \tag{3.4}$$

The simulation of the crack tip stress-strain history includes the effect of the cyclic elastic-plastic stress-strain material behavior and the effect of local residual stresses induced by the reversed cyclic plastic deformations in the crack tip region.

3.2 Analysis of Strains and Stresses at the Crack Tip

The calculation of elastic–plastic strains and stresses at the crack tip requires solving the elastic-plastic stress-strain boundary problem of a cracked body. Analytical solutions of such complex problems are seldom attainable. Numerical Finite Element solutions are feasible but not very convenient in practice due to the complexity of the FE model. Moreover, they are lengthy in the case of cyclic loading. Therefore, a simplified method based on the Neuber [30] or the ESED [34] rule was applied. The method requires a two-step approach: first the linear elastic stress-strain analysis needs to be carried out and second the actual elastic-plastic crack tip strains and stresses must be determined from the Neuber [30] or ESED [34] rules for which the linear elastic stress data is the input.

3.2.1 The Linear Elastic Analysis of Stresses and Strains near the Blunt Crack Tip

The fatigue crack growth expressions are most often formulated in terms of the stress intensity factor range, ΔK. Therefore, the analysis below is carried out wherever possible using the stress intensity factor and fracture mechanics principles. The linear elastic stress-strain analysis must also be carried out using a two-step approach because the stress response at the crack tip to the tensile load (no contact between crack surfaces) is different than the compressive one.

– Crack Tip Stresses Induced by Tensile Loading ($K_{min,appl} > 0$)

The calculations of linear elastic stresses and strains induced by tensile loading are in essence reduced to the analysis of a notch of depth "a" and having tip radius ρ^* (Figure 3-5a).

The Creager-Paris solution [19] was used assuming that the crack tip radius, ρ^*, would always be small in comparison with the crack depth, a.

$$\sigma_x = -\frac{K}{\sqrt{2\pi r}}\frac{\rho^*}{2r}\cos\frac{3\theta}{2} + \frac{K}{\sqrt{2\pi r}}\cos\frac{\theta}{2}\left[1 - \sin\frac{\theta}{2}\sin\frac{3\theta}{2}\right] + \cdots \quad \text{(a)}$$

$$\sigma_y = \frac{K}{\sqrt{2\pi r}}\frac{\rho^*}{2r}\cos\frac{3\theta}{2} + \frac{K}{\sqrt{2\pi r}}\cos\frac{\theta}{2}\left[1 + \sin\frac{\theta}{2}\sin\frac{3\theta}{2}\right] + \cdots \quad \text{(b)} \qquad (3.5)$$

$$\tau_{xy} = -\frac{K}{\sqrt{2\pi r}}\frac{\rho^*}{2r}\sin\frac{3\theta}{2} + \frac{K}{\sqrt{2\pi r}}\sin\frac{\theta}{2}\cos\frac{\theta}{2}\cos\frac{3\theta}{2} + \cdots \quad \text{(c)}$$

The linear-elastic stress components along the crack plane ($\theta = 0$, $r = x$) are:

$$\sigma_x = \frac{K}{\sqrt{2\pi x}}\left(1 - \frac{\rho^*}{2x}\right) + \cdots \quad \text{(a)}$$

$$\sigma_y = \frac{K}{\sqrt{2\pi x}}\left(1 + \frac{\rho^*}{2x}\right) + \cdots \quad \text{(b)} \qquad (3.6)$$

$$\tau_{xy} = 0 \quad \text{(c)}$$

The maximum stress at the crack tip can be determined from the applied stress intensity factor, assuming $x = \rho^*/2$.

$$\sigma_y = \frac{2K}{\sqrt{\pi\rho^*}} \qquad (3.7)$$

However, the calculations need to be carried out for elementary material blocks of the size ρ^* . Therefore the average stress over each elementary block was used in the analysis.

$$\tilde{\sigma}^{e}_{y,i} = \frac{1}{x_{i+1} - x_i} \int_{x_i}^{x_{i+1}} \frac{K}{\sqrt{2\pi x}} \left(\frac{\rho^*}{2x} + 1 \right) dx \tag{3.8}$$

After integrating expression (3.8), the average stress over elementary block 'i' can be written in the form:

$$\tilde{\sigma}^{e}_{y,i} = \frac{K \times \psi_{y,i}}{\sqrt{2\pi\rho^*}} \tag{3.9}$$

where: $\psi_{y,1} = 1.633,\ \psi_{y,2} = 0.8967,\ \psi_{y,3} = 0.6773,\ \psi_{y,4} = 0.5641$ for the first four blocks.

A similar expression can be derived for the stress component σ_x.

$$\tilde{\sigma}^{e}_{x,i} = \frac{K \times \psi_{x,i}}{\sqrt{2\pi\rho^*}} \tag{3.10}$$

where: $\psi_{x,1} = 0.4376,\ \psi_{x,2} = 0.5287,\ \psi_{x,3} = 0.4814,\ \psi_{x,4} = 0.4378$

Based on Eq. (3.9), the maximum and minimum linear elastic stresses and the stress range over the first elementary material block induced by the applied maximum nominal tensile stress, $S_{max,appl} > 0$, (or the maximum stress intensity factor $K_{max,appl}$) and the applied minimum tensile stress, $S_{min,appl} > 0$, can be calculated as:

$$\tilde{\sigma}^{e}_{max,net} = \frac{\psi_{y,1} K_{max,appl}}{\sqrt{2\pi\rho^*}} = \frac{\psi_{y,1} S_{max,appl} Y\sqrt{\pi a}}{\sqrt{2\pi\rho^*}} = S_{max,appl} Y \sqrt{\frac{a}{2\rho^*}} \psi_{y,1} \tag{3.11}$$

$$\tilde{\sigma}^{e}_{min,net} = \frac{\psi_{y,1} K_{min,appl}}{\sqrt{2\pi\rho^*}} = \frac{\psi_{y,1} S_{min,appl} Y\sqrt{\pi a}}{\sqrt{2\pi\rho^*}} = S_{min,appl} Y \sqrt{\frac{a}{2\rho^*}} \psi_{y,1} \tag{3.12}$$

$$\Delta\tilde{\sigma}^{e}_{net} = \frac{\psi_{y,1} K_{max,appl}}{\sqrt{2\pi\rho^*}} - \frac{\psi_{y,1} K_{min,appl}}{\sqrt{2\pi\rho^*}} = \frac{\psi_{y,1}}{\sqrt{2\pi\rho^*}} \Delta K_{appl} = \Delta S_{appl} Y \sqrt{\frac{a}{2\rho^*}} \psi_{y,1} \tag{3.13}$$

where: $S_{min,appl} = \frac{K_{min,appl}}{Y\sqrt{\pi a}}, \quad S_{max,appl} = \frac{K_{max,appl}}{Y\sqrt{\pi a}}, \quad \Delta S_{appl} = \frac{\Delta K_{appl}}{Y\sqrt{\pi a}}$

The nominal or reference stress ($S_{max,appl}$ or $S_{min,appl}$) in the stress intensity factor expression is easy to identify in the case of a simple loading configuration such as uniform tension or bending. However, any stress/load parameter can be chosen as the reference in the case of complex stress fields, such as residual stress distributions or thermally induced stress fields. As long as the stress intensity factor is used as the load parameter, the choice of the reference stress is not important. Therefore, for consistency reasons, the nominal stresses are used wherever possible. Expressions (3.11) - (3.13) are valid only for tensile loading, i.e. for $K > 0$. The net stress components are needed as input into the Neuber rule equations.

– Crack Tip Stresses Induced by Compressive Loading ($K_{min,appl} < 0$)

The crack tip stress concentration under compressive loading is much less than in tension. This is due to the fact that under the compressive minimum nominal stress, $S_{min,appl} < 0$, the contact pressure is transferred through the contacting crack surfaces. In such a case the crack should be treated according to the model in Figure 3-5(b) as a single or two identical circular holes. The stress at the edge of a circular hole ($\theta = 0$ and $x = \rho^*$) of diameter, $2\rho^*$, in a wide plate can be estimated from the well known classical solution [101] for the circular notch problem in an infinite plate (for $\theta = 0$ and $x = \rho^*$).

$$\sigma_x = S\left[1 - 2.5\left(\frac{\rho^*}{x}\right)^2 + 1.5\left(\frac{\rho^*}{x}\right)^4\right] \tag{3.14}$$

$$\sigma_y = S\left[1 + 0.5\left(\frac{\rho^*}{x}\right)^2 + 1.5\left(\frac{\rho^*}{x}\right)^4\right] \tag{3.15}$$

The stress concentration factor at the edge of the hole $(x = \rho^*)$, according to Eq. (3.15), is $K_t = 3$ and the minimum compressive stress at that point can be calculated as:

$$\sigma^e_{min,net} = 3S_{min,appl} \tag{3.16}$$

The applied nominal minimum stress, $S_{min,appl}$, can also be related to a pseudo minimum applied stress intensity factor:

$$S_{min,appl} = \frac{K_{min,appl}}{Y\sqrt{\pi a}} \tag{3.17}$$

Thus, the minimum local stress at the edge of the notch can finally be related to the minimum applied stress intensity factor, $K_{min,appl}$.

$$\sigma^e_{min,net} = \frac{3K_{min,appl}}{Y\sqrt{\pi a}} \tag{3.18}$$

However, the Creager-Paris solution (3.7) would suggest that if the problem is treated as a blunt crack a certain net minimum stress intensity factor, $K_{min,net}$, needs to be applied in order to generate the same stress at the crack tip as determined from Eq. (3.18).

$$\sigma^e_{min,net} = \frac{2K_{min,net}}{\sqrt{\pi\rho^*}} \tag{3.19}$$

A combination of Eqs. (3.18) and (3.19) makes it possible to determine the net stress intensity factor, $K_{min,net}$, which will give the same crack tip stress as that calculated from Eq. (3.18) when substituted into the Creager-Paris expression (3.19).

$$K_{min,net} = K_{min,appl}\frac{3}{2Y}\sqrt{\frac{\rho^*}{a}} \qquad \text{or} \qquad \frac{K_{min,net}}{K_{min,appl}} = \frac{3}{2Y}\sqrt{\frac{\rho^*}{a}} \tag{3.20}$$

In order to determine the fluctuations of the linear elastic stress near the crack tip, it is necessary to account for the differences in the tensile and compressive parts of the cycle, i.e.

$$\tilde{\sigma}^{e}_{max,net} = \frac{\psi_{y,1} K_{max,appl}}{\sqrt{2\pi\rho^{*}}} = \frac{\psi_{y,1} S_{max,appl} Y\sqrt{\pi a}}{\sqrt{2\pi\rho^{*}}} = S_{max,appl} Y \sqrt{\frac{a}{2\rho^{*}}} \psi_{y,1} \tag{3.21}$$

$$\tilde{\sigma}^{e}_{min,net} = \frac{\psi_{y,1} K_{min,net}}{\sqrt{2\pi\rho^{*}}} = \frac{3\psi_{y,1}}{2\sqrt{2}} \frac{K_{min,appl}}{Y\sqrt{\pi a}} = S_{min,appl} \frac{3\psi_{y,1}}{2\sqrt{2}} \tag{3.22}$$

$$\begin{aligned} \Delta\tilde{\sigma}^{e}_{net} &= \tilde{\sigma}^{e}_{max,net} - \tilde{\sigma}^{e}_{min,net} \\ &= \frac{\psi_{y,1} K_{max,appl}}{\sqrt{2\pi\rho^{*}}} - \frac{3\psi_{y,1}}{2\sqrt{2}} \frac{K_{min,appl}}{Y\sqrt{\pi a}} = \frac{\psi_{y,1}}{\sqrt{2\pi\rho^{*}}} \left(K_{max,appl} - \frac{3}{2Y} \sqrt{\frac{\rho^{*}}{a}} K_{min,appl} \right) \end{aligned} \tag{3.23}$$

It can be seen from Eq. (3.23) that the contribution of the compressive part of the applied stress reversal (from 0 to $K_{min,appl}$) to the local crack tip stress range is relatively small and depends on the crack tip radius, ρ^{*}, and crack size, a. It is possible that the circular hole approximation (Figure 3-5(b)) might be non-conservative, but this will be discussed later. The maximum crack tip stress, $\tilde{\sigma}^{e}_{max,net}$, and the stress range, $\Delta\tilde{\sigma}^{e}_{net}$, over the first elementary material block obtained from the linear elastic analysis are the input for calculating the elastic-plastic stress-strain response.

3.2.2 Elastic-Plastic Analysis of Stresses and Strains near the Crack Tip

The purpose of the elastic-plastic stress-strain analysis is to determine the actual stress-strain history over the first (i = 1) elementary material block and the residual stress induced by reversed plastic yielding in the crack tip region.

In order to avoid solving the complete but unfortunately very complex elastic-plastic cracked body boundary problem, the well known Neuber's rule [30] was used for each load/stress reversal. Neuber's rule was originally derived for a uni-axial stress state (i.e. pure shear) but it has been recently expanded for multi-axial proportional and non-proportional loading conditions [109, 110]. Neuber's rule is based on the equivalence of the strain energy

density at the notch tip between the linear elastic and elastic-plastic behavior of geometrically identical notched bodies subjected to identical external loads. In the case of a uni-axial stress state at the notch tip, Neuber's rule provides the relationship between the hypothetical linear elastic notch tip stress-strain input data and the actual elastic-plastic stress-strain response.

$$\tilde{\sigma}^{e}_{y,i}\tilde{\varepsilon}^{e}_{y,i} = \tilde{\sigma}^{a}_{y,i}\tilde{\varepsilon}^{a}_{y,i} \tag{3.24}$$

For cracked bodies in plane stress, the stress state near the crack tip is bi-axial. In the case of bodies in plane strain, the near tip stress state is tri-axial but the third principal stress is a function of the other two, and in both situations the modified bi-axial Neuber's rule [109] can be used. In addition, the elastic stress tensor used as input does not rotate during loading, and all stress components change proportionally. Therefore, the Hencky equations [111] of total deformation theory of plasticity can be applied.

In the case of a bi-axial stress state, the Hencky stress-strain relationships, the Ramberg-Osgood stress-strain constitutive Eq. (3.1) and the multi-axial Neuber rule [109] can be combined to obtain a set of five equations from which all elastic-plastic crack tip strains and stresses can be determined over each material block ahead of the crack tip.

$$\begin{cases} \tilde{\varepsilon}^{a}_{x,i} = \dfrac{1}{E}\left(\tilde{\sigma}^{a}_{x,i} - \nu\tilde{\sigma}^{a}_{y,i}\right) + \dfrac{f(\sigma^{a}_{eq})}{\sigma^{a}_{eq}}\left(\tilde{\sigma}^{a}_{x,i} - \dfrac{1}{2}\tilde{\sigma}^{a}_{y,i}\right) \\ \tilde{\varepsilon}^{a}_{y,i} = \dfrac{1}{E}\left(\tilde{\sigma}^{a}_{y,i} - \nu\tilde{\sigma}^{a}_{x,i}\right) + \dfrac{f(\sigma^{a}_{eq})}{\sigma^{a}_{eq}}\left(\tilde{\sigma}^{a}_{y,i} - \dfrac{1}{2}\tilde{\sigma}^{a}_{x,i}\right) \\ \tilde{\varepsilon}^{a}_{z,i} = \dfrac{1}{E}\left[-\nu\left(\tilde{\sigma}^{a}_{x,i} + \tilde{\sigma}^{a}_{y,i}\right)\right] + \dfrac{f(\sigma^{a}_{eq})}{\sigma^{a}_{eq}}\left[-\dfrac{1}{2}\left(\tilde{\sigma}^{a}_{x,i} + \tilde{\sigma}^{a}_{y,i}\right)\right] \\ \tilde{\sigma}^{e}_{x,i}\tilde{\varepsilon}^{e}_{x,i} = \tilde{\sigma}^{a}_{x,i}\tilde{\varepsilon}^{a}_{x,i} \\ \tilde{\sigma}^{e}_{y,i}\tilde{\varepsilon}^{e}_{y,i} = \tilde{\sigma}^{a}_{y,i}\tilde{\varepsilon}^{a}_{y,i} \end{cases} \tag{3.25}$$

where: $\sigma_{eq}^{a} = \sqrt{\left(\tilde{\sigma}_{x,i}^{a}\right)^2 - \tilde{\sigma}_{x,i}^{a}\tilde{\sigma}_{y,i}^{a} + \left(\tilde{\sigma}_{y,i}^{a}\right)^2}$ and $f(\sigma_{eq}^{a}) = \left(\frac{\sigma_{eq}^{a}}{K'}\right)^{\frac{1}{n'}}$

In the case of cracked bodies in plane stress, the stress state over the first elementary material block reduces to one normal stress component. Therefore, the equation set (3.25) reduces to the classical uni-axial Neuber rule associated with the Ramberg-Osgood equation.

$$\begin{cases} \tilde{\varepsilon}_{x,1}^{a} = -\frac{\nu}{E}\tilde{\sigma}_{y,1}^{a} - \frac{1}{2}\left(\frac{\tilde{\sigma}_{y,1}^{a}}{K'}\right)^{\frac{1}{n'}} \\ \tilde{\varepsilon}_{y,1}^{a} = \frac{\tilde{\sigma}_{y,1}^{a}}{E} + \left(\frac{\tilde{\sigma}_{y,1}^{a}}{K'}\right)^{\frac{1}{n'}} \\ \tilde{\varepsilon}_{z,1}^{a} = -\frac{\nu}{E}\tilde{\sigma}_{y,1}^{a} - \frac{1}{2}\left(\frac{\tilde{\sigma}_{y,1}^{a}}{K'}\right)^{\frac{1}{n'}} \\ \tilde{\sigma}_{y,1}^{e}\tilde{\varepsilon}_{y,1}^{e} = \tilde{\sigma}_{y,1}^{a}\tilde{\varepsilon}_{y,1}^{a} \end{cases} \tag{3.26}$$

Neuber's Eq. (3.24) can also be written in terms of the nominal stress or the stress intensity factor over the first elementary material block.

$$\tilde{\sigma}_{y,1}^{e}\tilde{\varepsilon}_{y,1}^{e} = \frac{\left(\tilde{\sigma}_{y,1}^{e}\right)^2}{E} = \frac{1}{E}\left(\frac{\psi_{y,1}K_{net}}{\sqrt{2\pi\rho^{*}}}\right)^2 = \tilde{\sigma}_{y,1}^{a}\tilde{\varepsilon}_{y,1}^{a} \tag{3.27}$$

The maximum stress and starin at the crack tip induced by the first reversal can be determined from the Neuber rule (3.27) and the Ramberg-Osgood strain-stress curve (3.1).

$$\begin{cases} \frac{1}{E}\left(\frac{K_{max,net}\times\psi_{y,1}}{\sqrt{2\pi\rho^{*}}}\right)^2 = \frac{(\tilde{\sigma}_{max}^{a})^2}{E} + \tilde{\sigma}_{max}^{a}\left(\frac{\tilde{\sigma}_{max}^{a}}{K'}\right)^{\frac{1}{n'}} \\ \tilde{\varepsilon}_{max}^{a} = \frac{\tilde{\sigma}_{max}^{a}}{E} + \left(\frac{\tilde{\sigma}_{max}^{a}}{K'}\right)^{\frac{1}{n'}} \end{cases} \tag{3.28}$$

The crack tip strain and stress ranges can be determined from Neuber's equation but written in terms of ranges, for the hysteresis loop, according to Massing's hypothesis stress-strain curve.

$$\begin{cases} \dfrac{1}{E}\left(\dfrac{\Delta K_{net}\times\psi_{y,1}}{\sqrt{2\pi\rho^{*}}}\right)^{2} = \dfrac{(\Delta\tilde{\sigma}^{a})^{2}}{E} + 2(\Delta\tilde{\sigma}^{a})\left(\dfrac{\Delta\tilde{\sigma}^{a}}{2K'}\right)^{\frac{1}{n'}} \\ \dfrac{\Delta\tilde{\varepsilon}^{a}}{2} = \dfrac{\Delta\tilde{\sigma}^{a}}{2E} + \left(\dfrac{\Delta\tilde{\sigma}^{a}}{2K'}\right)^{\frac{1}{n'}} \end{cases} \tag{3.29}$$

The equations above enable the determination of elastic-plastic strains and stresses at the crack tip induced by two reversals of the load history, represented by fluctuations in the stress intensity factors, i.e. $K_{max,net}$ and ΔK_{net}. After calculating the elastic-plastic strains and stresses at various locations, the residual stress distribution $\sigma_r(x)$ induced by the application of the loading and unloading stress reversals can be determined.

Schematic diagrams showing stress distributions ahead of the crack tip corresponding to the maximum and minimum load levels respectively generated at three different stress ratios, $R_{appl} > 0.5$, $0 \le R_{appl} \le 0.5$ and $R < 0$, are presented in Figure 3-6. Both stress distributions, i.e. those corresponding to the maximum and minimum loads, are most often tensile at high applied stress ratios ($R_{appl} > 0.5$), as illustrated in Figure 3-6(a). In such a case the crack tip displacement field and the crack tip stress field are only dependent on the applied stress intensity factors. However, compressive residual stresses might be generated at the minimum load level for low stress ratios ($R_{appl} < 0.5$), as shown in Figure 3-6(b) and Figure 3-6(c). The residual stresses remain present in the crack tip region even at zero applied load level. Therefore, residual stresses have to be included in the relationship correlating the applied load, the crack tip stress-strain response, and the displacement field

for subsequent stress/load reversals. It is assumed that the compressive stress ahead of the crack tip is acting as a clamp over the crack tip region and its action has to be overcome before the increments of the applied (or the net) stress intensity range can be fully effective as stated in Eqs. (3.28) and (3.29). Again, the residual compressive stress effect needs to be expressed in terms of the stress intensity factor before it could be included in any fatigue crack growth expression.

Neuber's rule makes it possible to determine the residual stress distribution throughout the plastic zone ahead of the crack tip. However, in order to simulate the character of the displacement field around the crack tip, shown in Figure 3-3(a), the compressive part of the residual stress field from ahead of the crack tip was symmetrically added over the region behind the crack tip, as shown in Figure 3-3(b). The residual stress field shown in Figure 3-3(b) was subsequently used for calculating the residual stress intensity factor, K_r.

3.3 Calculation of the Residual Stress Intensity Factor, K_r

The compressive residual stress ahead of the crack tip prevents deformation and opening displacement behind the crack tip. Therefore, it was assumed, analogously to the well-know Dugdale [112] model, that the effect of residual stress $\sigma_r(x)$ can be expressed in terms of the stress intensity factor calculated for a crack tip (Figure 3-3(b)) surrounded by the compressive stress applied to the crack surface. Calculation of the residual stress intensity factor, K_r, was carried out using the weight function method. The following universal weight function expression (3.30) was used in the analysis [113, 114].

$$m(x,a) = \frac{2P}{\sqrt{2\pi(a-x)}}\left[1 + M_1\left(1-\frac{x}{a}\right)^{\frac{1}{2}} + M_2\left(1-\frac{x}{a}\right)^{1} + M_3\left(1-\frac{x}{a}\right)^{\frac{3}{2}}\right] \qquad (3.30)$$

The geometry factors, M_1, M_2 and M_3, for edge and through cracks in a finite width plate can be found in Appendix B. Additional M_1, M_2 and M_3 factors for various geometrical configurations are given in references [115, 116].

The stress intensity factor was calculated by integrating the product of the residual stress $\sigma_r(x)$ and the weight function m(x,a) over the crack surface area.

$$K_r = \int_0^a \sigma_r(x) m(x,a) dx \tag{3.31}$$

The physical crack tip location at "x = a" is chosen as the upper limit for the integration of expression (3.31). It was also found that region "r_p" was close to the cyclic plastic zone size. A special numerical procedure was developed for calculating the integral (3.31) [117].

The residual stress intensity factor can be calculated from Eq. (3.31) for any stress ratio and any load magnitude. When the calculated residual stress intensity factors for any constant stress ratio are plotted against the applied maximum stress intensity factor, a linear relationship of the K_r versus $K_{max,appl}$ can be obtained. The typical linear K_r-$K_{max,appl}$ relationship can be shown for any material in Figure 3-7. Moreover, the slope of the K_r versus $K_{max,appl}$ line decreases with increasing stress ratio, R. Knowing the linear relationship of the K_r versus $K_{max,appl}$, the residual stress intensity factor, K_r, can be obtained for any load magnitude without using Eq. (3.31). Application of the linear relation between the residual stress intensity factor and the applied maximum stress intensity factor can significantly decrease the computational time required for the fatigue crack growth analysis.

3.4 Calculation of Total (resultant) Stress Intensity Factors

The residual stress effect cannot be assessed by simple superposition of stress intensity factors because the nature of the crack opening displacement field needs to be

accounted for. The residual stress at the crack tip is induced by the first two loading reversals (0 -1 and 1-4, Figure 3-2(a)) even when the minimum load is tensile. Because of the residual stress created by the first two loading reversals, the maximum stress at the crack tip corresponding to the maximum load at the end of the third reversal (at point 8 in Figure 3-2(a)) can not reach the same level as the one at the end of the first loading reversal (at point 1, Figure 3-2(a)). This effect can be modeled by using the resultant maximum stress intensity factor, $K_{max,tot}$, obtained be decreasing the applied maximum stress intensity factor, $K_{max,appl}$, by the residual stress intensity factor, K_r. The interactions of the stress intensity factor, the plastic zone and the residual stress manifest themselves mainly in the change (decrease) in the resultant maximum stress intensity factor, $K_{max,tot}$, without significant changes in the resultant minimum stress intensity factor, $K_{min,tot}$. It is assumed that the minimum stress intensity factor is not affected by the crack tip residual stress. As a result of such a correction, both the resultant maximum stress intensity factor, $K_{max,tot}$, and the resultant stress intensity range, ΔK_{tot}, are affected by the plasticity-induced crack tip residual stresses. However, the magnitude of the residual stress effect depends on the applied stress ratio and it has to be treated differently for positive and negative stress ratios, R.

– Calculation of Total Stress Intensity Factors at Positive Stress Ratios, $R_{appl} \geq 0$

The reversed plastic deformations around the crack tip induced at relatively high stress ratios ($R_{appl} > 0.5$) and relatively small stress intensity ranges (near threshold FCG), are usually not sufficient to produce compressive residual stresses (Figure 3-6(a)). Therefore, the residual stress intensity factor is close to zero ($K_r = 0$) and the total SIFs are the same as the applied ones:

$$K_{min,tot} = K_{min,net} = K_{min,appl} \tag{3.32}$$

$$K_{max,tot} = K_{max,net} = K_{max,appl} \tag{3.33}$$

$$\Delta K_{tot} = K_{max,tot} - K_{min,tot} = \Delta K_{net} = \Delta K_{appl} \tag{3.34}$$

However, either for other positive stress ratios ($0 \leq Rappl \leq 0.5$) or for relatively high stress ratios ($Rappl > 0.5$) and high stress intensity ranges (medium range FCG rates), the residual stresses at the crack tip can change the effectiveness of applied SIFs. The maximum total stress intensity factor, $K_{max,tot}$, is calculated in such a case by adding the negative residual stress intensity factor, K_r, to the maximum applied stress intensity factor, $K_{max,appl}$. However, the minimum total SIF is assumed to be unaffected by the residual stress and equals the applied minimum SIF, $K_{min,appl}$. In such a case, the total SIFs are calculated as:

$$K_{min,tot} = K_{min,net} = K_{min,appl} \tag{3.35}$$

$$K_{max,tot} = K_{max,net} + K_r = K_{max,appl} + K_r \tag{3.36}$$

$$\Delta K_{tot} = K_{max,tot} - K_{min,tot} = K_{max,appl} + K_r - K_{min,appl} = \Delta K_{appl} + K_r \tag{3.37}$$

– Calculation of Total Stress Intensity Factors at Negative Stress Ratios, $R_{appl} < 0$

In the case of negative stress ratios $R_{appl} < 0$, the maximum total (resultant) stress intensity factor, $K_{max,tot}$, is calculated analogously as in the case of $R_{appl} > 0$, i.e. the $K_{max,tot}$ is the algebraic sum of the maximum net, $K_{max,net}$, and the negative K_r residual stress intensity factor. However, the compressive part of the loading cycle is not entirely effective as far as FCG is concerned. Therefore, the minimum net stress intensity factor $K_{min,net}$, is not equal to the applied one and needs to be determined according to Eq. (3.20). Thus, all the stress intensity quantities at negative stress ratios can be determined from Eqs. (3.38) - (3.40).

$$K_{min,tot} = K_{min,net} = K_{min,appl} \frac{3}{2Y}\sqrt{\frac{\rho^*}{a}} \tag{3.38}$$

$$K_{max,tot} = K_{max,net} + K_r = K_{max,appl} + K_r \tag{3.39}$$

$$\Delta K_{tot} = K_{max,tot} - K_{min,tot} = K_{max,appl} + K_r - K_{min,appl} \frac{3}{2Y}\sqrt{\frac{\rho^*}{a}} = \Delta K_{net} + K_r \tag{3.40}$$

The resultant maximum stress intensity factor, $K_{max,tot}$, and the resultant stress intensity range, ΔK_{tot}, are the two main parameters governing fatigue crack growth rate. However, they need to be combined into one driving force expression analogous to the fatigue damage parameter used in classical fatigue theories.

3.5 Analytical Derivation of the Two-Parameter Fatigue Crack Driving Force $\Delta\kappa$ and the Fatigue Crack Growth Expression da/dN-$\Delta\kappa$

Expressions (3.28), (3.29) and Neuber's rule provide the link between the stress-strain response at the crack tip and the applied stress intensity factor history. Therefore, the fatigue crack growth expression can be derived providing that an appropriate fatigue damage accumulation parameter is employed. The Smith-Watson-Topper (SWT) damage parameter [16] was chosen in the analysis to determine the fatigue damage accumulation at the crack tip:

$$D = \tilde{\sigma}^a_{max} \frac{\Delta\tilde{\varepsilon}^a}{2} \tag{3.41}$$

After including the SWT damage parameter into the Manson-Coffin strain-life material fatigue curve, the following expression is obtained, relating the SWT damage parameter to the number of cycles to failure.

$$\tilde{\sigma}^a_{max} \frac{\Delta\tilde{\varepsilon}^a}{2} = \frac{\left(\sigma'_f\right)^2}{E}\left(2N_f\right)^{2b} + \sigma'_f\varepsilon'_f\left(2N_f\right)^{b+c} \tag{3.42}$$

Eqs. (3.28) and (3.29) provide a unique relationship between the applied stress intensity factor and the actual strains and stresses at the crack tip, providing there are no additional effects altering those equations. Unfortunately, this is true only in the case of cracks subjected to cyclic loads applied at relatively high stress ratios, R > 0.5. At low stress ratios, a compressive residual stress field is generated ahead of the crack tip and Eqs. (3.28) and (3.29) can be used only when the net maximum stress intensity factor, $K_{max,net}$, and the net stress intensity range ΔK_{net} are corrected for the effect of the residual stress σ_r. In other words, the resultant maximum SIF, $K_{max,tot}$, and the resultant SIF range, ΔK_{tot}, discussed below must be used in those equations.

The actual maximum stress at the crack tip can be obtained from the set of two equations involving the resultant stress intensity factor, $K_{max,tot}$, the Nueber rule, and the cyclic stress-strain material curve.

$$\begin{cases} \dfrac{1}{E}\left(\dfrac{K_{max,tot}\times\psi_{y,1}}{\sqrt{2\pi\rho^*}}\right)^2 = \dfrac{\left(\tilde{\sigma}^a_{max}\right)^2}{E} + \tilde{\sigma}^a_{max}\left(\dfrac{\tilde{\sigma}^a_{max}}{K'}\right)^{\frac{1}{n'}} \\ \tilde{\varepsilon}^a_{max} = \dfrac{\tilde{\sigma}^a_{max}}{E} + \left(\dfrac{\tilde{\sigma}^a_{max}}{K'}\right)^{\frac{1}{n'}} \end{cases} \tag{3.43}$$

The actual crack tip strain range can be determined from the set of two equations involving the resultant stress intensity range, ΔK_{tot}, the Nueber rule, and the cyclic stress-strain material curve, expanded by a factor of two.

$$\begin{cases} \dfrac{1}{E}\left(\dfrac{\Delta K_{tot}\times\psi_{y,1}}{\sqrt{2\pi\rho^*}}\right)^2 = \dfrac{\left(\Delta\tilde{\sigma}^a\right)^2}{E} + 2\left(\Delta\tilde{\sigma}^a\right)\left(\dfrac{\Delta\tilde{\sigma}^a}{2K'}\right)^{\frac{1}{n'}} \\ \dfrac{\Delta\tilde{\varepsilon}^a}{2} = \dfrac{\Delta\tilde{\sigma}^a}{2E} + \left(\dfrac{\Delta\tilde{\sigma}^a}{2K'}\right)^{\frac{1}{n'}} \end{cases} \tag{3.44}$$

Unfortunately, derivation of closed form solutions for $\tilde{\sigma}^{a}_{max}$ and $\Delta\tilde{\varepsilon}^{a}$ are not feasible. However, approximate closed form solutions can be obtained if some terms in Eqs. (3.43) and (3.44) are neglected. At high applied loads, i.e. at high maximum stress intensity factors and high stress intensity factor ranges, the strains at the crack tip are predominantly plastic. Therefore, the elastic terms in Eqs. (3.43) and (3.44) can be neglected. In the near threshold fatigue crack growth region, the strains at the crack tip are predominantly elastic; therefore, the plastic terms in Eqs. (3.43) and (3.44) can be neglected. However, it is often observed for notched machine components subjected to service cyclic loading that the maximum notch tip strains are predominantly plastic but the subsequent strain ranges are predominantly elastic. For each material behavior, the fatigue crack growth equation, in terms of the two-parameter driving force, can be derived in a closed form as follows.

3.5.1 Predominantly Plastic Material Behavior at the Crack Tip

Eqs. (3.43) and (3.44) take a simpler form after neglecting the elastic terms.

$$\begin{cases} \dfrac{1}{E}\left(\dfrac{K_{max,tot}\times\psi_{y,1}}{\sqrt{2\pi\rho^{*}}}\right)^{2} = \tilde{\sigma}^{a}_{max}\left(\dfrac{\tilde{\sigma}^{a}_{max}}{K'}\right)^{\frac{1}{n'}} \\ \tilde{\varepsilon}^{a}_{max} = \left(\dfrac{\tilde{\sigma}^{a}_{max}}{K'}\right)^{\frac{1}{n'}} \end{cases} \tag{3.45}$$

$$\begin{cases} \dfrac{1}{E}\left(\dfrac{\Delta K_{tot}\times\psi_{y,1}}{\sqrt{2\pi\rho^{*}}}\right)^{2} = 2\left(\Delta\tilde{\sigma}^{a}\right)\left(\dfrac{\Delta\tilde{\sigma}^{a}}{2K'}\right)^{\frac{1}{n'}} \\ \dfrac{\Delta\tilde{\varepsilon}^{a}}{2} = \left(\dfrac{\Delta\tilde{\sigma}^{a}}{2K'}\right)^{\frac{1}{n'}} \end{cases} \tag{3.46}$$

Therefore, the maximum stress and the strain range at the crack tip can be subsequently determined in closed form.

$$\begin{cases} \tilde{\sigma}_{max}^{a} = \left(\dfrac{\left(K^{'}\right)^{\frac{1}{n^{'}}} \left(\psi_{y,1}\right)^{2}}{2\pi E \rho^{*}} \right)^{\frac{n^{'}}{n^{'}+1}} \left(K_{max,tot}^{2}\right)^{\frac{n^{'}}{n^{'}+1}} \\ \Delta\tilde{\varepsilon}^{a} = \left(\dfrac{2^{n^{'}} \left(\psi_{y,1}\right)^{2}}{4\pi E K^{'} \rho^{*}} \right)^{\frac{1`}{n^{'}+1}} \left(\Delta K_{tot}^{2}\right)^{\frac{1}{n^{'}+1}} \end{cases} \tag{3.47}$$

For consistency, the elastic term in the strain-life expression (3.42) should be neglected as well, resulting in:

$$\tilde{\sigma}_{max}^{a} \frac{\Delta\tilde{\varepsilon}^{a}}{2} = \sigma_{f}^{'} \varepsilon_{f}^{'} \left(2N_{f}\right)^{b+c} \tag{3.48}$$

After substituting for the maximum stress and the strain range in Eq. (3.48), one can write the expression relating the number of cycles to failure to the two stress intensity factor parameters.

$$\left(\frac{\left(\psi_{y,1}\right)^{2}}{2^{\frac{n'+3}{n'+1}} \pi E \rho^{*}} \right) \left(K_{max,tot}^{2}\right)^{\frac{n'}{n'+1}} \left(\Delta K_{tot}^{2}\right)^{\frac{1}{n'+1}} = \sigma_{f}^{'} \varepsilon_{f}^{'} \left(2N_{f}\right)^{b+c} \tag{3.49}$$

Thus, the number of cycles N_f needed to fail the elementary material block, ρ^*, at the crack tip is:

$$N_{f} = \frac{1}{2} \left[\frac{1}{\sigma_{f}^{'} \varepsilon_{f}^{'}} \times \frac{\left(\psi_{y,1}\right)^{2}}{2^{\frac{n'+3}{n'+1}} \pi E \rho^{*}} \left(K_{max,tot}^{2}\right)^{\frac{n'}{n'+1}} \left(\Delta K_{tot}^{2}\right)^{\frac{1}{n'+1}} \right]^{\frac{1}{b+c}} \tag{3.50}$$

The fatigue crack growth rate (3.4) can be subsequently calculated as:

$$\frac{da}{dN} = \frac{\rho^{*}}{N_{f}} = 2\rho^{*} \left[\frac{1}{\sigma_{f}^{'} \varepsilon_{f}^{'}} \times \frac{\left(\psi_{y,1}\right)^{2}}{2^{\frac{n'+3}{n'+1}} \pi E \rho^{*}} \left(K_{max,tot}^{2}\right)^{\frac{n'}{n'+1}} \left(\Delta K_{tot}^{2}\right)^{\frac{1}{n'+1}} \right]^{-\left(\frac{1}{b+c}\right)} \tag{3.51}$$

Because the only variables in Eq. (3.51) are the maximum stress intensity factor and the stress intensity factor range, the fatigue crack growth expression can be written in a short form.

$$\frac{da}{dN} = C\left[\left(K_{max,tot}\right)^{p}\left(\Delta K_{tot}\right)^{1-p}\right]^{\gamma} \tag{3.52}$$

where: $$C = 2\rho^{*}\left[\frac{\left(\psi_{y,1}\right)^{2}}{2^{\frac{n'+3}{n'+1}}\sigma_f'\varepsilon_f'\pi E\rho^{*}}\right]^{-\left(\frac{1}{b+c}\right)}; \quad p = \frac{n'}{n'+1}; \quad \gamma = -\frac{2}{b+c}$$

Eq. (3.52) indicates how the two stress intensity factor parameters, i.e. $K_{max,tot}$ and ΔK_{tot}, should be combined into one fatigue crack driving force. However, The plastic driving force, $K_{max,tot}^{\frac{n'}{1+n'}}\Delta K_{tot}^{\frac{1}{1+n'}}$, can be used to predict FCG only in the high and medium FCG-rate regime where plastic strains dominate at the crack tip. In these regimes, the parameter "p" is almost constant and depends mainly on the cyclic strain hardening exponent of the cyclic stress-strain material curve, n′. The plastic driving force, $K_{max,tot}^{\frac{n'}{1+n'}}\Delta K_{tot}^{\frac{1}{1+n'}}$, enables the analysis of FCG for various stress ratios "R" without the necessity of changing any of the constants (Eq. (3.52)). In other words, Eq. (3.52) represents a master da/dN-ΔK curve valid for all R-ratios.

3.5.2 Predominantly Elastic Material Behavior at the Crack Tip

Similar analysis can be carried out while neglecting the plastic terms in Eqs. (3.43) and (3.44). This is supposed to be an approximation of the crack tip material stress-strain behaviour in the near threshold fatigue crack growth regime. The final fatigue crack growth expression derived for the near threshold fatigue crack growth regime has taken the following form:

$$\frac{da}{dN} = C\left[\left(K_{max,tot}\right)^{p}\left(\Delta K_{tot}\right)^{1-p}\right]^{\gamma} \tag{3.53}$$

where: $$C = 2\rho^{*}\left[\frac{\left(\psi_{y,1}\right)^{2}}{4\pi\rho\sigma_{f}'^{2}}\right]^{-\frac{1}{2b}}; \quad p = 0.5; \quad \gamma = -\frac{1}{b}$$

The elastic driving force, $K_{max,tot}^{0.5}\Delta K_{tot}^{0.5}$, can be subsequently used to predict FCG for the near threshold region (at low FCG rates) where elastic strains dominate at the crack tip. In this region, the parameter "p" is almost constant and equal to 0.5 (p = 0.5).

As mentioned earlier, the elastic (p = 0.5) and plastic ($p = \frac{n'}{n'+1}$) driving forces can be used only for one of the two FCG regimes. In other words, these solutions (Eqs. (3.52) and (3.53)) become less accurate in the FCG regions where both elastic and plastic strains are equally important. To predict the fatigue crack growth at any FCG rate, in the region spanning from the near threshold to the high fatigue crack growth rate regime, the concept of approximate elasto-plastic driving force with one constant "p" has been introduced. It has been observed that the maximum notch tip strains are predominantly plastic, but the subsequent strain ranges are often dominated by elastic strains. Therefore, analogous expression such as those derived above can be used but with the "p" exponent valid over the entire range of fatigue crack growth rates, i.e. from threshold up to final fracture.

3.5.3 Elastic-Plastic Material Behavior at the Crack Tip

It was assumed that the crack tip strain, $\tilde{\varepsilon}_{max}^{a}$, induced by the loading reversal was predominantly plastic, and during unloading the strain, $\Delta\tilde{\varepsilon}^{a}$, was predominantly elastic. Considering only the plastic terms of the Ramberg-Osgood and Neuber equations for the

loading reversal and only the elastic terms for the unloading reversal, Eqs. (3.43) and (3.44) take the following forms:

$$\begin{cases} \dfrac{1}{E}\left(\dfrac{K_{max,tot}\times\psi_{y,1}}{\sqrt{2\pi\rho^{*}}}\right)^{2} = \tilde{\sigma}^{a}_{max}.\tilde{\varepsilon}^{a}_{max} \\ \tilde{\varepsilon}^{a}_{max} = \left(\dfrac{\tilde{\sigma}^{a}_{max}}{K'}\right)^{\frac{1}{n'}} \end{cases} \tag{3.54}$$

$$\begin{cases} \dfrac{1}{E}\left(\dfrac{\Delta K_{tot}\times\psi_{y,1}}{\sqrt{2\pi\rho^{*}}}\right)^{2} = \dfrac{\left(\Delta\tilde{\sigma}^{a}\right)^{2}}{E} \\ \dfrac{\Delta\tilde{\varepsilon}^{a}}{2} = \dfrac{\Delta\tilde{\sigma}^{a}}{2E} \end{cases} \tag{3.55}$$

The maximum stress and the strain range at the crack tip can be subsequently determined in a closed form given by expression (3.56).

$$\begin{cases} \tilde{\sigma}^{a}_{max} = \left(\dfrac{\left(K'\right)^{\frac{1}{n'}}\left(\psi_{y,1}\right)^{2}}{2\pi E\rho^{*}}\right)^{\frac{n'}{n'+1}}\left(K^{2}_{max,tot}\right)^{\frac{n'}{n'+1}} \\ \Delta\tilde{\varepsilon}^{a} = \dfrac{1}{E}\left(\dfrac{\Delta K_{tot}\times\psi_{y,1}}{\sqrt{2\pi\rho^{*}}}\right) \end{cases} \tag{3.56}$$

The plastic term in the Manson-Coffin together with the SWT parameter (Eq. (3.42)) was also omitted.

$$\tilde{\sigma}^{a}_{max}\,\frac{\Delta\tilde{\varepsilon}^{a}}{2} = \frac{\left(\sigma'_{f}\right)^{2}}{E}\left(2N_{f}\right)^{2b} \tag{3.57}$$

By substituting Eq. set (3.56) into Eq. (3.57), the number of cycles N_f needed to fail the elementary material block at the crack tip can be calculated:

$$N_f = \frac{1}{2}\left[\frac{\psi_{y,1}}{2(\sigma_f')^2\sqrt{2\pi\rho^*}} \times \left(\frac{\left(\psi_{y,1}\right)^2 (K')^{\frac{1}{n'}}}{2\pi E\rho^*}\right)^{\frac{n'}{n'+1}} \left(K_{max,tot}^2\right)^{\frac{n'}{n'+1}} \left(\Delta K_{tot}\right)\right]^{\frac{1}{2b}} \tag{3.58}$$

The fatigue crack growth rate can be subsequently calculated as:

$$\frac{da}{dN} = \frac{\rho^*}{N_f} = 2\rho^*\left[\frac{\psi_{y,1}}{2(\sigma_f')^2\sqrt{2\pi\rho^*}} \times \left(\frac{\left(\psi_{y,1}\right)^2 (K')^{\frac{1}{n'}}}{2\pi E\rho^*}\right)^{\frac{n'}{n'+1}} \left(K_{max,tot}^2\right)^{\frac{n'}{n'+1}} \left(\Delta K_{tot}\right)\right]^{\frac{-1}{2b}} \tag{3.59}$$

Because the only variables in Eq. (3.59) are the maximum stress intensity factor and the stress intensity range, the fatigue crack growth expression can be written in the following short form:

$$\frac{da}{dN} = C\left[\left(K_{max,tot}\right)^p \left(\Delta K_{tot}\right)^{0.5}\right]^\gamma \tag{3.60}$$

where: $$C = 2\rho^*\left[\frac{1}{2(\sigma_f')^2} \times \left[\left(\frac{\psi_{y,1}}{\sqrt{2\pi\rho^*}}\right)^{3n'+1} \times \frac{K'}{E^{n'}}\right]^{\frac{1}{n'+1}}\right]^{\frac{-1}{2b}}; \quad p = \frac{n'}{n'+1}; \quad \gamma = -\frac{1}{b}$$

The FCG expression (3.60) indicates how the two SIF parameters, ΔK_{tot} and $K_{max,tot}$, characterizing the loading cycle, should be combined into one driving force, over the entire range of fatigue crack growth rates, in the form of:

$$\Delta\kappa = K_{max,tot}^p \Delta K_{tot}^{0.5} \tag{3.61}$$

The crack growth expressions (3.52), (3.60) and (3.53) are formally the same as those proposed by Walker [12], Donald and Paris [15] and Kujawski [14], except that the resultant maximum stress intensity factor $K_{max,tot}$ and the resultant stress intensity range ΔK_{tot}, accounting for the compressive residual stress effect, are used.

A similar analysis was carried out assuming plane strain at the crack tip, by modifying the stress-strain relationship as proposed in references [118, 119]. The form of the fatigue crack driving force (3.61) derived for the plane strain at the crack tip was the same as in the case of plane stress. The only difference found was the constant "C*" in the fatigue crack growth expression.

$$\frac{da}{dN} = C^{*}\left[\left(K_{max,tot}\right)^{p}\left(\Delta K_{tot}\right)^{1-p}\right]^{\gamma} \tag{3.62}$$

The constants "C^{*}" derived for the crack tip in plane strain state are:

– for predominantly plastic plane strain state at the crack tip

$$C^{*} = \frac{C}{(1-\nu^{2})^{\frac{1}{b+c}}} = \frac{2\rho^{*}}{(1-\nu^{2})^{\frac{1}{b+c}}}\left[\frac{\left(\psi_{y,1}\right)^{2}}{2^{\frac{n'+3}{n'+1}}\sigma_{f}'\varepsilon_{f}'\pi E\rho^{*}}\right]^{-\left(\frac{1}{b+c}\right)} \tag{3.63}$$

– for predominantly elastic plane strain state at the crack tip

$$C^{*} = \frac{C}{(1-\nu^{2})^{\frac{1}{2b}}} = \frac{2\rho^{*}}{(1-\nu^{2})^{\frac{1}{2b}}}\left[\frac{\left(\psi_{y,1}\right)^{2}}{4\pi\rho\sigma_{f}'^{2}}\right]^{-\frac{1}{2b}} \tag{3.64}$$

– for elastic-plastic plane strain state at the crack tip

$$C^{*} = \frac{C}{\left[\frac{2\left(1-\nu^{2}\right)^{\frac{2n'+1}{n'+1}}}{\sqrt{3}}\right]^{\frac{1}{2b}}} = \frac{2\rho^{*}}{\left[\frac{2\left(1-\nu^{2}\right)^{\frac{2n'+1}{n'+1}}}{\sqrt{3}}\right]^{\frac{1}{2b}}}\left[\frac{1}{2(\sigma_{f}')^{2}}\times\left[\left(\frac{\psi_{y,1}}{\sqrt{2\pi\rho^{*}}}\right)^{3n'+1}\times\frac{K'}{E^{n'}}\right]^{\frac{1}{n'+1}}\right]^{\frac{-1}{2b}} \tag{3.65}$$

3.5.4 The Effect of "Stabilized" Fatigue Damage Accumulation on Fatigue Crack Growth

The fatigue crack growth equations derived above make it possible to predict FCG based on the number of cycles required to fracture the first elementary material block of a virgin material ahead of the crack tip. However, for the current elementary material block at the crack tip, the number of cycles changes because the fatigue damage has already accumulated in this elementary material block. Glinka [100] assumed that only four elements ahead of the crack tip can accumulate damage simultaneously because of the high strain gradient in the vicinity of the crack tip. By using the four-element model, he showed that the number of cycles stabilizes after the fatigue crack grows over a few elements. Using the Miner fatigue damage summation rule [120, 121], the number of cycles to fracture any elements ahead of the crack tip, N_j, can be expressed in terms of the number of cycles to fracture the first element, N_f, and the fatigue damage accumulation parameter, Φ_j.

$$N^* = N_j = N_f \Phi_j = N_f \Phi \tag{3.66}$$

where:
$$\Phi_j = 1 - \Phi_{j-3}\left(\frac{x_1}{x_4}\right)^{\frac{2}{c(n'+1)}} - \Phi_{j-2}\left(\frac{x_1}{x_3}\right)^{\frac{2}{c(n'+1)}} - \Phi_{j-1}\left(\frac{x_1}{x_2}\right)^{\frac{2}{c(n'+1)}} \tag{3.67}$$

The parameter Φ is the stabilized value of the parameter Φ_j and can be calculated from several iterations of Eq. (3.67), where $\Phi_j = 0$ for $j \leq 0$. Eq. (3.67) also shows that the fatigue damage accumulation in the elements far away from the crack tip depends on the cyclic and fatigue properties of the material. However, the calculated stabilized fatigue damage accumulation parameter, Φ, ($\Phi \geq 0.7$) for different materials shows that this parameter can not be more than 30% of the critical accumulated damage in the first elementary material block [100]. In other words, the fatigue crack growth increases up to 30% after the failure of

a few elementary material blocks ahead of the crack tip but it stabilizes later over the next elements [100]. Therefore, the fatigue crack growth rate (3.4) should be expressed in terms of the number of cycles after stabilization, N^*.

$$\frac{da}{dN} = \frac{\rho^*}{N^*} = \frac{\rho^*}{\Phi N_f} \tag{3.68}$$

After substituting for the number of cycles, N_f, in Eq. (3.68), the two-parameter fatigue crack growth equation accounting for the effect of fatigue damage accumulation can then be derived.

$$\frac{da}{dN} = C_d \left[\left(K_{max,tot} \right)^p \left(\Delta K_{tot} \right)^{1-p} \right]^\gamma \tag{3.69}$$

$$C_d = \frac{C}{\Phi} \quad \text{for plane stress and}$$

$$C_d = \frac{C^*}{\Phi} \quad \text{for plane strain}$$

The constant "C" can be determined from Eqs. (3.52), (3.60), and (3.53); and the constant "C^*" can be determined from Eqs. (3.63) - (3.65) depending on the material behavior at the crack tip.

All constants in the fatigue crack growth expressions derived above can be determined analytically if the material properties in the form of the cyclic stress-strain curve (3.1) and the fatigue strain-life expression (3.2) are available. The only unknown parameter which needs to be determined is the size of the elementary material block, ρ^*.

3.6 Determination of the Elementary Material Block Size, ρ*

In order to determine the elementary material block size, ρ^*, a limited fatigue crack growth data is necessary. The obvious material properties are the threshold stress intensity

factor ΔK_{th} and the fatigue limit $\Delta\sigma_{th}$. For the fatigue crack not to grow at the threshold stress intensity range, ΔK_{th}, the local stress at the crack tip must be equal to the fatigue limit, $\Delta\sigma_{th}$. Due to the fact that the fatigue limit is less than the material yield limit, only the elastic stress-strain analysis can be carried out. Thus, according to the Creager–Paris solution, the two material properties can be related using the relationship below:

$$\Delta\tilde{\sigma}_{th}^{a} = \frac{\Delta K_{th} \times \psi_{y,l}}{\sqrt{2\pi\rho^{*}}} \tag{3.70}$$

Eq. (3.71) may subsequently be used for the determination of the elementary material block size, ρ^{*} :

$$\rho^{*} = \frac{\left(\psi_{y,l}\right)^{2}}{2\pi}\left(\frac{\Delta K_{th}}{\Delta\tilde{\sigma}_{th}^{a}}\right)^{2} \tag{3.71}$$

The elementary material block size (3.71) is in such a case close to the well-known parameter resulting from the Kitagawa diagram [122]. However, care must be taken in order to make sure that the fatigue limit $\Delta\tilde{\sigma}_{th}^{a}$ was obtained at the same stress ratio R as the stress ratio at the crack tip induced by the threshold stress intensity range ΔK_{th}. Further, some care needs to be taken while determining the threshold stress intensity factors. Namely, the fatigue crack may not grow due to one of the following [11]: the applied maximum stress intensity factor is less than the maximum threshold stress intensity factor ($K_{max,\ appl} < K_{max,\ th}$), or the applied stress intensity range is less than the threshold stress intensity range ($\Delta K_{appl} < \Delta K_{th}$). If the crack ceases to grow at the stress ratio R = 0 it is not certain whether the maximum stress intensity or the stress intensity range has reached the threshold level. Therefore, the optimum stress ratio at which the threshold stress range ΔK_{th} can be determined, without producing

significant plasticity at maximum stress intensity factor, is $0.2 < R < 0.3$ and in such a case the "elastic" solution, Eq. (3.71), can be used.

Because of the difficulties with using Eq. (3.71), discussed above, the estimation of the crack tip radius, ρ*, can be carried out by using the experimental fatigue crack growth data and solving simultaneously the complete set of Eqs. (3.43), (3.44), and (3.72).

$$\tilde{\sigma}_{max}^{a}\frac{\Delta\tilde{\varepsilon}^{a}}{2}=\frac{\left(\sigma_f^{'}\right)^2}{E}\left(\frac{2\rho^{*}}{da/dN}\right)^{2b}+\sigma_f^{'}\varepsilon_f^{'}\left(\frac{2\rho^{*}}{da/dN}\right)^{b+c} \tag{3.72}$$

Depending on the nature of available experimental fatigue crack growth data, various methods for estimating the ρ* can be suggested.

If the near threshold fatigue crack growth data at high stress ratios $R_{appl} > 0.5$ is available, the determination of the crack-tip radius, ρ*, can be found by using the applied stress intensity factors. At high stress ratios and close to the threshold, the total stress intensity factors, $K_{max,tot}$ and ΔK_{tot}, have the same magnitudes as the applied ones. Therefore, the applied SIFs can be used in Eqs. (3.43), (3.44) and consequently the ρ* parameter can be estimated from Eqs (3.43), (3.44) and (3.72) by using the iteration technique. Due to the scatter of fatigue crack growth data, it is recommended that several near threshold FCG data points are selected. The ρ* parameter can then be calculated for each FCG data point. The average of the calculated ρ* parameters is considered as the ρ* parameter for the analyzed material.

In order to determine the elementary material block size ρ* in the absence of the near threshold fatigue crack growth data, one set of fatigue crack growth data obtained at any stress ratio is sufficient. The ρ* parameter can be obtained by using an iteration technique. First, the residual SIF, K_r, can be determined for the assumed ρ* magnitude followed by the

determination of the total stress intensity factors, $K_{max,tot}$ and ΔK_{tot}, corresponding to given experimental FCG reference data points. The total stress intensity factors are used to calculate the magnitude of the two-parameter driving force, $\Delta\kappa = K_{max,tot}^{p}\Delta K_{tot}^{(1-p)}$. Second, the experimental fatigue crack growth data points can be plotted in terms of the two parameter driving force, da/dN vs. $\Delta\kappa$. Finally, by using Eqs. (3.43), (3.44), (3.72) and the assumed ρ* parameter, the analytically derived FCG curve (exact solution) can be drawn (Figure 3-8) in the same system of coordinates, da/dN vs. $\Delta\kappa$. If the analytically derived FCG curve is in a good agreement with the experimental FCG data points, the initial assumption concerning the ρ* parameter was correct. Otherwise, the entire process needs to be iterated until the correct ρ* is determined. In this method, the estimation of the ρ* parameter needs several iterations which are time consuming. Therefore, instead of using the exact solution, the approximate solution resulting from Eq. (3.52) can be used for the comparison with the experimental FCG reference data points. However, it is recommended to use in this case the high fatigue crack growth data as the reference because the high-rate FCG is governed predominantly by plastic strains and the use of Eq. (3.52) is justified. Moreover, at high fatigue crack growth rates, the approximate solution is the same as the exact solution.

In summary, the ρ* parameter may be regarded as an empirical parameter, even though it has some physical meaning as well. Its value for a given material can be determined by fitting the theoretical solution into experimental set of fatigue crack growth data by solving the complete set of Eqs. (3.43), (3.44), and (3.72) discussed above. The magnitude of the parameter ρ* decreases with the increase of the strain hardening exponent, n′.

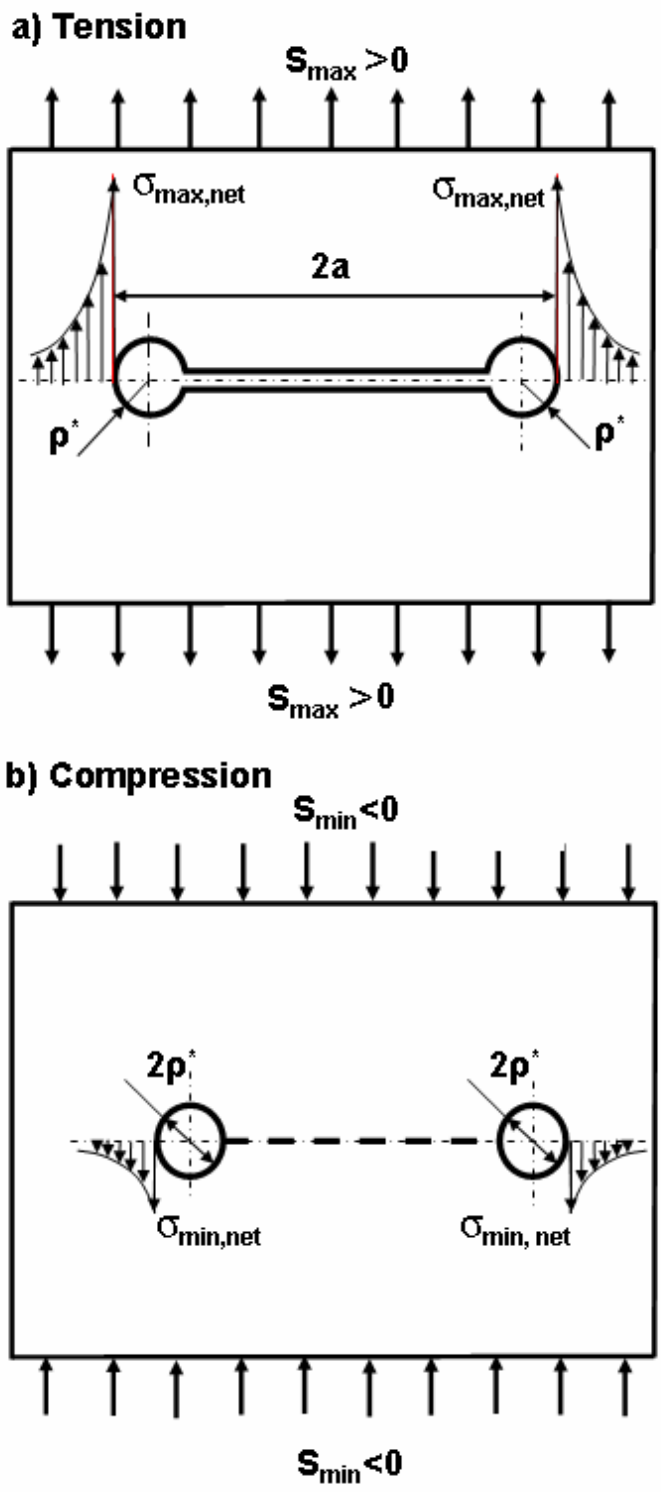

Figure 3-1: A crack model for linear elastic analysis of stresses and strains near the crack tip; a) stress concentration near the crack tip according to Creager-Paris solution b) stress concentration for a circular notch simulating the crack under compressive loading.

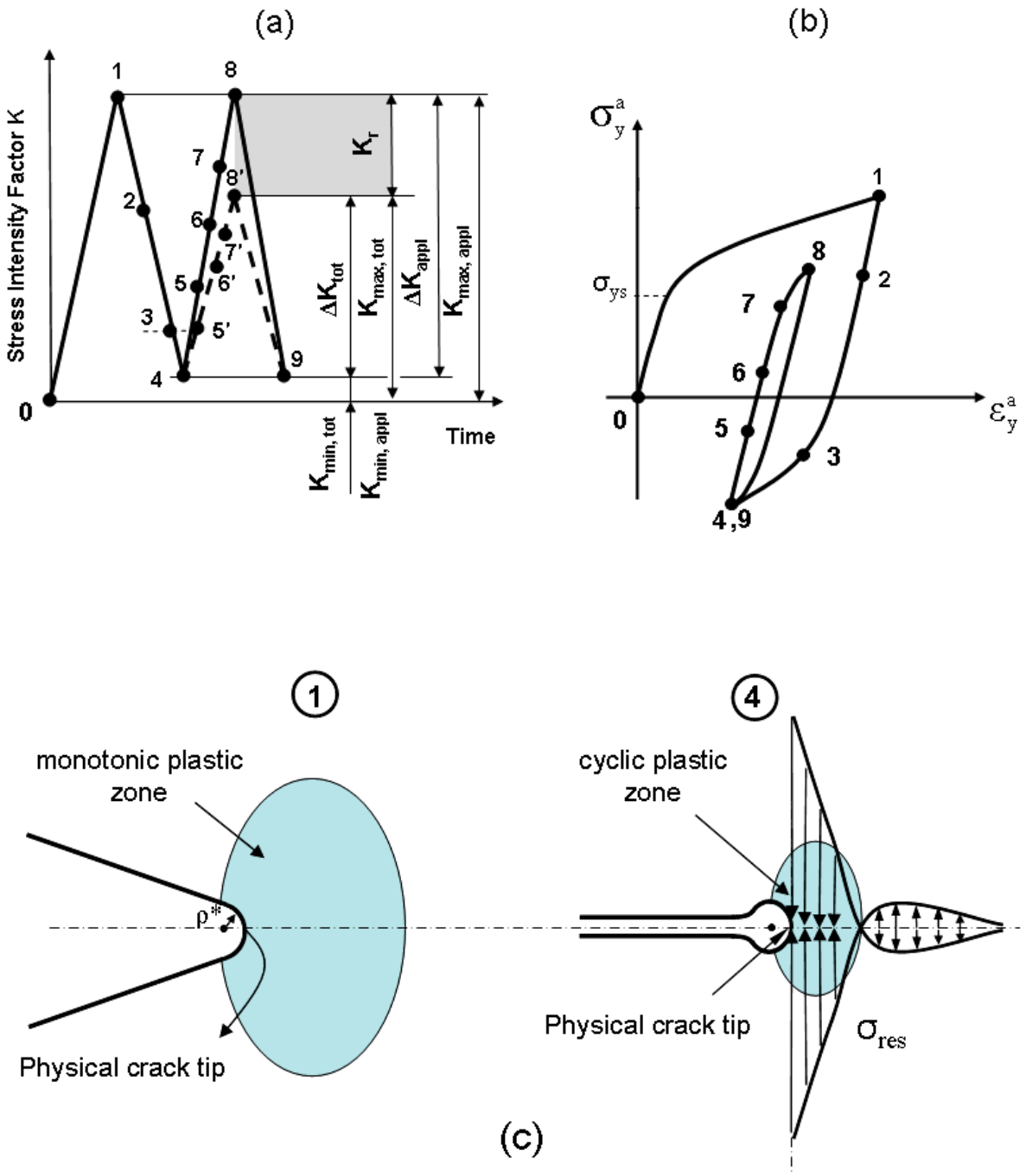

Figure 3-2: Schematic of the crack tip geometry, the cyclic plastic zone and the crack tip stress-strain response; a) applied load (stress intensity factor) history, b) qualitative stress-strain response at the crack tip, c) evolution of the crack opening displacements in the crack tip region.

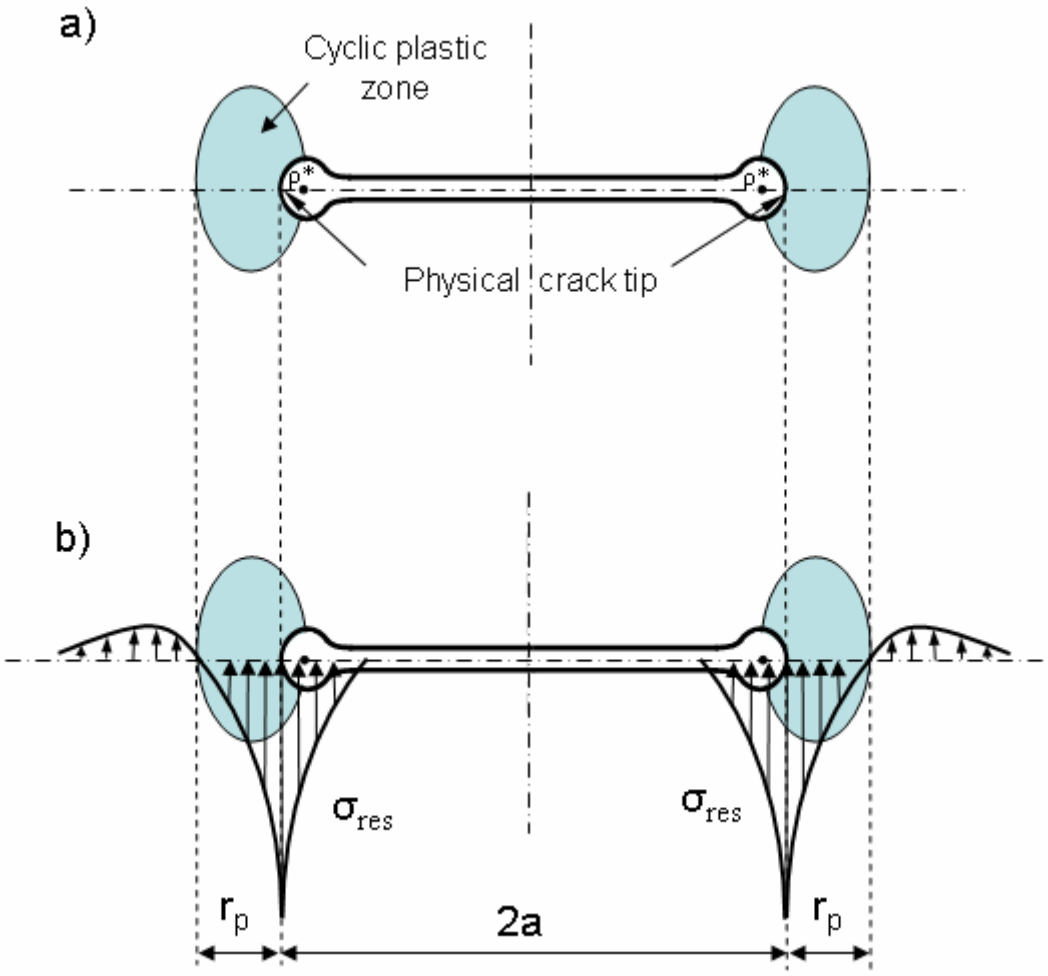

Figure 3-3: Approximate crack tip displacement field and corresponding residual stress distribution; a) illustration of the displacement field around the plastic zone, b) residual stress distribution required for generating the displacement field.

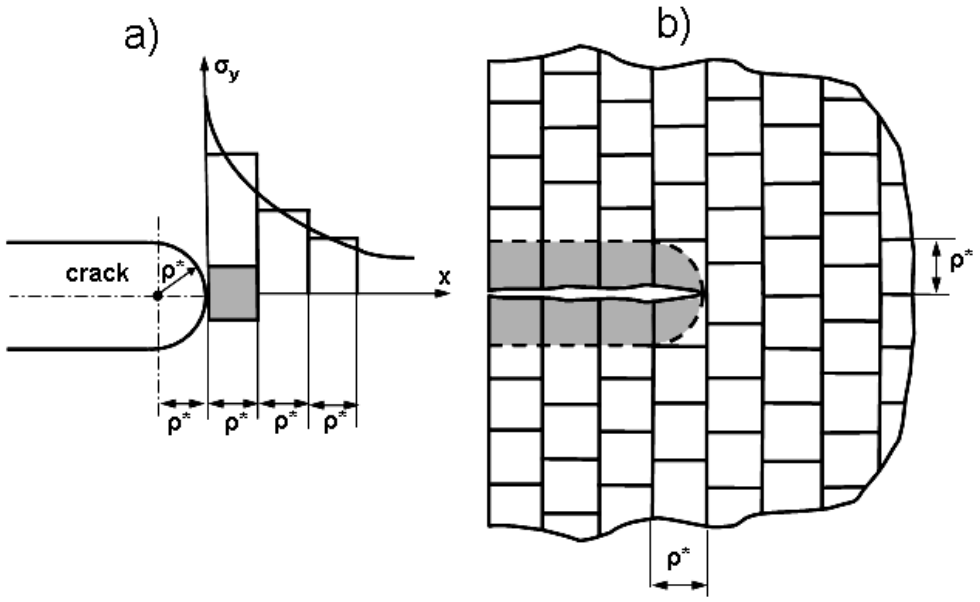

Figure 3-4: The idealized crack tip geometry and the discrete structure of the material; a) the crack tip geometry and averaged stresses over individual elementary material blocks, b) the crack and the discrete elementary material blocks.

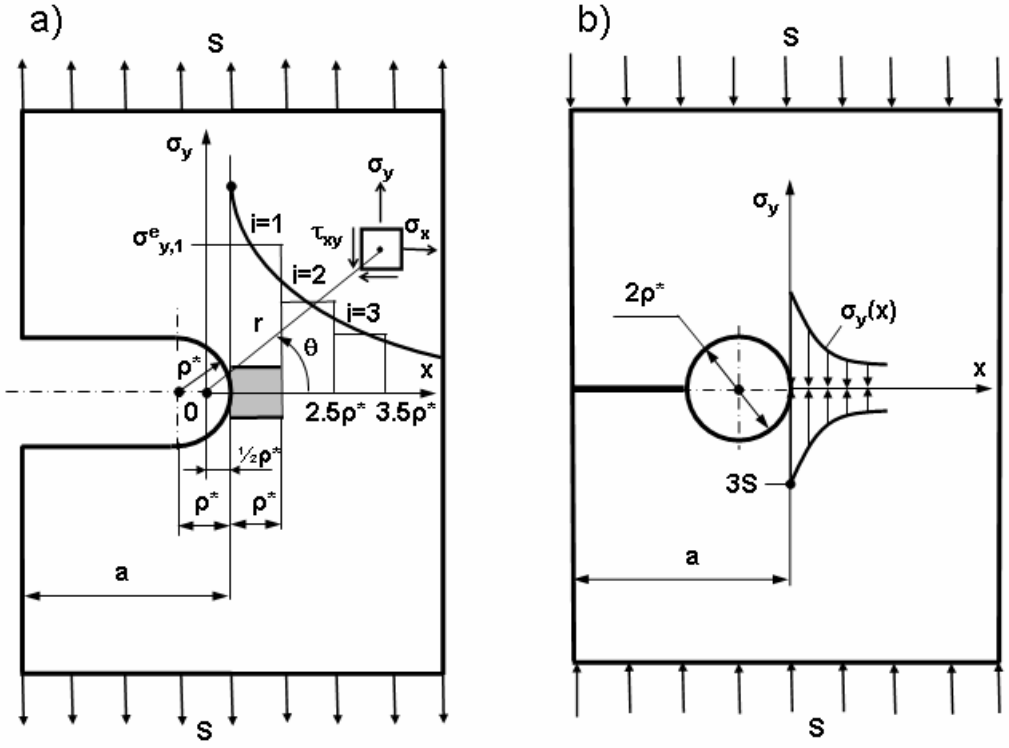

Figure 3-5: Schematic of stress distributions ahead of the crack tip induced by tensile and compressive loading; a) stress concentration and the nomenclature for the Creager-Paris notch tip stress expressions, b) stress concentration and stress distribution induced by compressive loading.

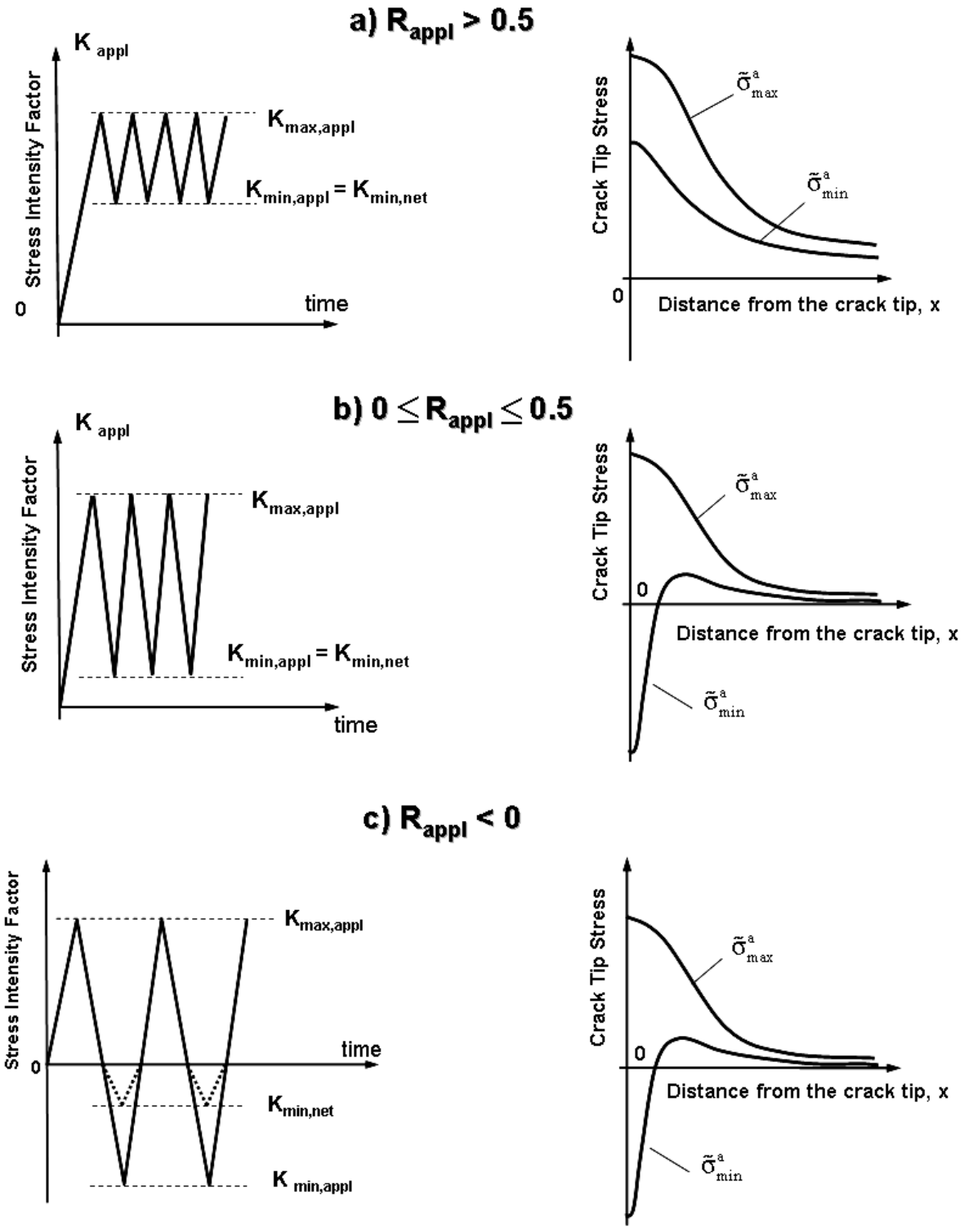

Figure 3-6: Approximate elastic-plastic crack tip stress distribution induced by cyclic loading; a) at high stress ratios R > 0.5, b) at low stress ratios $0 \leq R \leq 0.5$, c) at negative stress ratios R < 0.

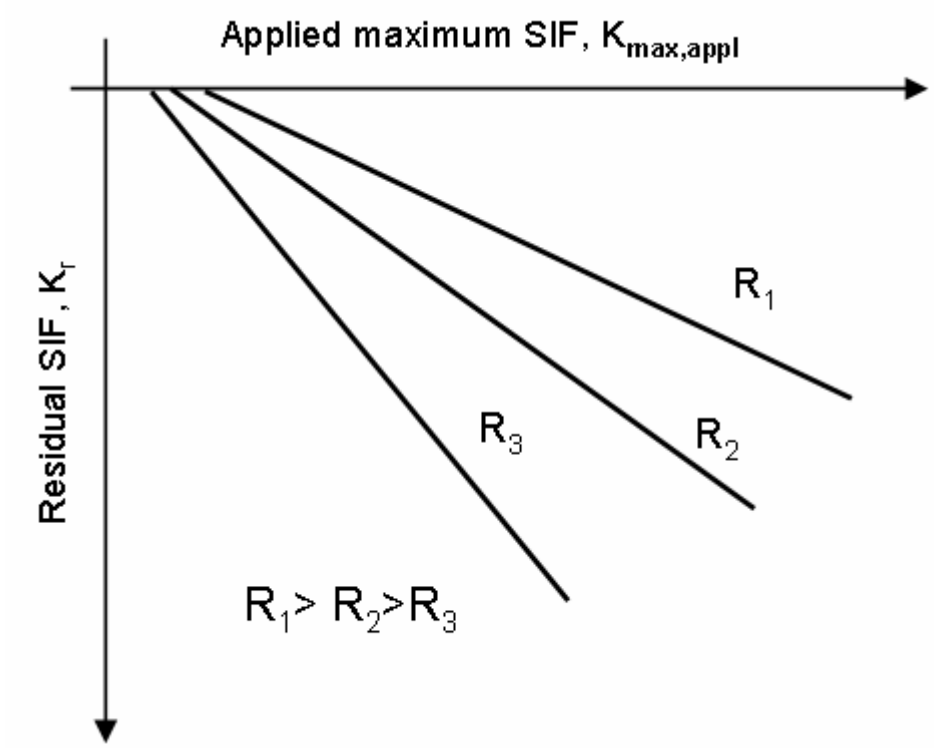

Figure 3-7: Typical linear plot of K_r vs. $K_{max,appl}$ at various stress ratios R.

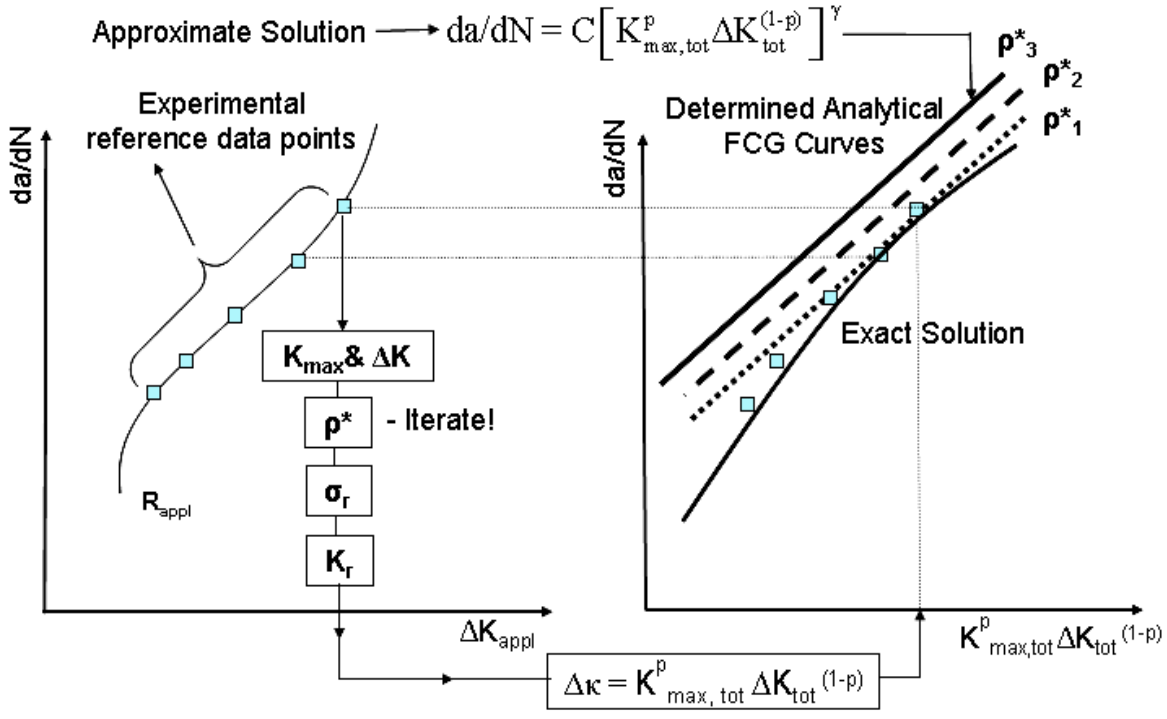

Figure 3-8: Schematic of the iterative determination of ρ* parameter using the high FCG data at arbitrary stress ratio R.

Chapter 4
Validation of the Proposed Model

4.1 Fatigue Crack Growth Prediction under Constant Amplitude Loading

The two-parameter fatigue crack growth driving forces, $K^{p}_{max,tot}\Delta K^{(1-p)}_{tot}$, $K^{0.5}_{max,tot}\Delta K^{0.5}_{tot}$ and $K^{p}_{max,tot}\Delta K^{0.5}_{tot}$, were used to model the effect of the stress ratio R on the fatigue crack growth under constant amplitude loading. The total stress intensity factors corrected for the residual stress effect were used to determine the magnitude of each driving force.

First, the experimental fatigue crack growth data are plotted in terms of each two-parameter driving force. Then, the "approximate" closed form solutions (Eqs. (3.52), (3.53), and (3.60)) and the "exact" numerical solution are also shown in the same diagrams to verify the proposed methodology for fatigue crack growth prediction. It should be noted that the "exact" solution can be obtained numerically by solving simultaneously the complete set of Eqs. (3.42) - (3.44), and (3.4). It can be noted that by increasing the ρ* parameter the predicted FCG rates decrease particularly in the near the threshold region. In other words, the near the threshold FCG data is very sensitive to the ρ* parameter.

Fatigue crack growth data for five materials were used for the validation of the model under constant amplitude loading: two steel alloys St-4340 and St-4140, two aluminum alloys Al 7075-T6 and Al 2024-T351, and one titanium alloy Ti-6Al-4V. The cyclic (3.1) and fatigue properties (3.2) for the materials are given in Table 4-1.

4.1.1 Modeling of Fatigue Crack Growth in Al 7075-T6 Alloy

To predict fatigue crack growth using the two-parameter FCG model, the material properties in the form of the cyclic stress-strain curve (3.1) and the fatigue strain-life

expression (3.2) need to be known. Linear regression analysis for the fatigue data [123] $\Delta\sigma/2$ vs. $\Delta\varepsilon_p/2$ are used to obtain the cyclic stress-strain material properties K´ and n´ in Eq. (3.1) with a coefficient of correlation r = 0.945. Similar linear regression analysis is used for the fatigue data $\Delta\varepsilon_e/2$ vs. $2N_f$ (with a coefficient of correlation r = -0.888) and $\Delta\varepsilon_p/2$ vs. $2N_f$ (with a coefficient of correlation r = -0.927) to obtain the stain-life fatigue properties σ'_f, b, ε'_f, and c in Eq. (3.2). The cyclic (3.1) and fatigue properties (3.2) can then be found in Table 4-1. The Ramberg-Osgood stress-strain curve and the Manson-Coffin fatigue curve for the 7075-T6 aluminum alloy are illustrated in Figure 4-1 and Figure 4-2, respectively.

Due to the availability of the near threshold data obtained at high stress ratios, the ρ^* parameter was determined from Eqs. (3.43), (3.44), and (3.72), as described in section 3.6 (Table 4-2). Based on the material cyclic stress-strain properties (Table 4-1) and the determined ρ^* parameter, the residual stress distribution ahead of the crack tip, σ_r, can be determined from Eq. set (3.25), as described in section 3.2.2. For example, for the loading condition ΔK_{appl} = 32.6 MPa$\sqrt{m}$ and R = 0 the residual stress distribution, σ_r, can be shown in Figure 4-3. After the residual stress distribution is properly determined, the residual stress intensity factor, K_r, can be calculated at the crack tip from Eq. (3.31), as described in section 3.3. Figure 4-4 shows the computed K_r corresponding to the applied load ΔK_{appl} = 32.6 MPa$\sqrt{m}$ (R=0). However, the value of K_r at the crack tip is calculated to determine the total stress intensity factors (Figure 4-4). The linear K_r-$K_{max,appl}$ relationship at different stress ratios for the Al 7075-T6 material is plotted in Figure 4-5.

Since the near threshold data is not so accurate, the ρ^* parameter was also determined by using the FCG data in the Paris regime. However, for the determination of the ρ^* parameter in this regime, the total stress intensity factors, $K_{max,tot}$ and ΔK_{tot}, must be used.

The evolution of the ρ* parameter determined from the applied SIFs, $K_{max,appl}$ and ΔK_{appl}, and also from the total SIFs, $K_{max,tot}$ and ΔK_{tot}, are plotted at two stress ratios of 0 and 0.5 for 7075-T6 aluminum alloy in Figure 4-6 and Figure 4-7, respectively. The magnitude of the ρ* parameter determined from the applied SIFs increases as fatigue crack growth rates increase (Figure 4-6). However, it is clear from Figure 4-7 that the variation of the ρ* parameter determined from the total SIFs at different FCG rates and also different stress ratios, R, is almost constant.

Based on the material data listed in Table 4-1 and the determined ρ* parameter, the constants of Eqs. (3.52), (3.53), and (3.60) can be calculated, Table 4-3. The stabilized fatigue damage parameter, Φ, can be determined from several iterations of Eq. (3.67) and is given in Table 4-2.

The fatigue crack growth data for the 7075-T6 aluminum alloy was found in [124, 125, 126]. The fatigue crack growth data sets were obtained at various stress ratios, R_{appl}, and are shown in Figure 4-8 as a function of the applied stress intensity factor range, ΔK_{appl}. The two-parameter fatigue crack growth driving forces, $K_{max,tot}^{p}\Delta K_{tot}^{(1-p)}$, $K_{max,tot}^{0.5}\Delta K_{tot}^{0.5}$, and $K_{max,tot}^{p}\Delta K_{tot}^{0.5}$, were used to model the effect of the stress ratio R on the fatigue crack growth under constant amplitude loading. The total stress intensity factors corrected for the residual stress effect were used to determine the magnitude of each driving force. It is seen (Figure 4-9) that in the high and medium FCG rate regimes, the "plastic" driving force, $K_{max,tot}^{p}\Delta K_{tot}^{(1-p)}$, was successful in correlating the fatigue crack growth data obtained at various stress ratios. The "elastic" driving force, $K_{max,tot}^{0.5}\Delta K_{tot}^{0.5}$, was the least successful one even in the near threshold region (Figure 4-10). It can be noted that the elastic driving force may be used only to consolidate FCG data at very low fatigue crack growth rates; therefore, it should

not be used for fatigue crack growth predictions away from the threshold. However, it was found (Figure 4-11) that the combination of the elastic and plastic stress-strain material behavior at the crack tip in the form of the "mixed" driving force, $K^{p}_{max,tot}\Delta K^{0.5}_{tot}$, could be used to correlate FCG data at various R-ratios for the FCG rates spanning from near threshold to the high growth rate regime.

The "approximate" closed solutions, in the form of Eqs. (3.52), (3.53), and (3.60) were attainable after neglecting the plastic or elastic terms in the Ramberg-Osgood and Manson-Coffin equations. Unfortunately, such solutions become inaccurate in the regions where both terms are equally important. However, numerical solutions to the complete set of Eqs. (3.42) - (3.44), and (3.4), i.e. without neglecting any terms, are possible. The final solution can not be derived in a closed form but it can be illustrated graphically. The numerical solution called as the "exact solution". The "exact" solutions accounting for the effect of stabilized fatigue damage accumulation, and result from solving the complete set of Eqs. (3.42) - (3.44), and (3.68). The "approximate" closed form solutions accounting for the effect of fatigue stabilized damage accumulation are obtained from Eq. (3.69).

Both the "exact" FCG curves and the approximate closed form solutions (Eqs. (3.52), (3.53) and (3.60)) are shown in Figure 4-9, Figure 4-10, and Figure 4-11, where the fatigue crack growth rate is shown as a function of the appropriate driving force $\Delta\kappa$. The exact FCG curves and the approximate closed form solutions (Eq. (3.69)) accounting for the effect of "stabilized" fatigue damage accumulation are plotted on the same figures with dashed curves. It can be seen from the figures that the effect of "stabilized" fatigue damage accumulation resulted in increasing the fatigue crack growth, which is more conservative for fatigue life prediction.

The best results in correlating the FCG under various stress ratios were obtained while using the "mixed" driving force in the form of $K^{p}_{max,tot}\Delta K^{0.5}_{tot}$. As shown in Figure 4-11, the exact numerical solution presented in terms of the mixed driving force had good agreement with the experimental data over the entire range of FCG data. However, the elasto-plastic approximate solution (Eq. (3.60)) agreed well only with the low FCG data. Therefore, it is recommended that in practice the two lines da/dN vs. $K^{p}_{max,tot}\Delta K^{0.5}_{tot}$ should be fitted to the existing FCG data for the determination of constants "C" and "γ" in Eq. (3.60), i.e. one line covering the near threshold FCG data and the other approximating the so-called Paris regime (Figure 4-12). The fitting parameters "C" and "γ" can be found in Table 4-3. The two power law curves characterized by two sets of constants (the exponent "γ" and the constant "C") can be subsequently used for FCG analyses.

4.1.2 Modeling of Fatigue Crack Growth in Al 2024-T351 Alloy

The fatigue crack growth data for the Al 2024-T351 aluminum alloy was found in [127, 128, 129]. The fatigue crack growth data sets were obtained at various stress ratios, R_{appl}, and are shown in Figure 4-13 as a function of the applied stress intensity factor range, ΔK_{appl}.

The cyclic (3.1) and fatigue properties (3.2) for the Al 2024-T351 aluminum alloy were obtained from reference [130], as listed in Table 4-1, but the same data can also be found on the Society of Automotive Engineers (SAE) web-site (fde.uwaterloo.ca) maintained by the Fatigue Design & Evaluation Committee. Due to the availability of the near threshold data obtained at high stress ratios, the ρ* parameter was determined from Eqs. (3.43), (3.44), (3.72), as described in section 3.6 (Table 4-2). Based on the material data listed in Table 4-1

and the determined ρ* parameter, the constants from Eqs. (3.52), (3.53), and (3.60) were calculated and are found in Table 4-3. The stabilized fatigue damage parameter, Φ, can be determined from several iterations of Eq. (3.67) and is given in Table 4-2 as well.

The two-parameter fatigue crack growth driving forces, $K_{max,tot}^{p}\Delta K_{tot}^{(1-p)}$, $K_{max,tot}^{0.5}\Delta K_{tot}^{0.5}$ and $K_{max,tot}^{p}\Delta K_{tot}^{0.5}$, were used to model the effect of the stress ratio R on the fatigue crack growth under constant amplitude loading. The total stress intensity factors corrected for the residual stress effect were used to determine the magnitude of each driving force. It is seen (Figure 4-14) that in the high and medium FCG rate regimes, the "plastic" driving force, $K_{max,tot}^{p}\Delta K_{tot}^{(1-p)}$, was successful in correlating the fatigue crack growth data obtained at various stress ratios. The "elastic" driving force, $K_{max,tot}^{0.5}\Delta K_{tot}^{0.5}$, was the least successful one even in the near threshold region (Figure 4-15). It can be noted that the elastic driving force may be used only to consolidate FCG data at very low fatigue crack growth rates; therefore, it should not be used for fatigue crack growth predictions away from the threshold. However, it was found (Figure 4-16) that the combination of the elastic and plastic stress-strain material behavior at the crack tip in the form of the "mixed" driving force, $K_{max,tot}^{p}\Delta K_{tot}^{0.5}$, could be used to correlate FCG data at various R-ratios for the FCG rates spanning from the near threshold to the high growth rate regime.

The "approximate" closed solutions, in the form of Eqs. (3.52), (3.53), and (3.60) were attainable after neglecting the plastic or elastic terms in the Ramberg-Osgood and the Manson-Coffin equations. Unfortunately, such solutions become inaccurate in the regions where both terms are equally important. However, numerical solutions to the complete set of

Eqs. (3.42) - (3.44), and (3.4), i.e. without neglecting any terms, are possible. The final solution can not be derived in a closed form but it can be illustrated graphically.

Both the "exact" FCG curves and the approximate closed form solutions (Eqs. (3.52), (3.60) and (3.53)) are shown as diagrams (Figure 4-14, Figure 4-15, and Figure 4-16) where the fatigue crack growth rate is shown as a function of the appropriate driving force $\Delta\kappa$.

The best results in correlating the FCG under various stress ratios were obtained while using the mixed driving force in the form of $K^{p}_{max,tot}\Delta K^{0.5}_{tot}$. As shown in Figure 4-16, the exact numerical solution presented in terms of the mixed driving force had good agreement with the experimental data over the entire range of FCG data. However, the elasto-plastic approximate solution (Eq. (3.60)) agreed well only with the low FCG data. Therefore, it is recommended that in practice the two lines da/dN vs. $K^{p}_{max,tot}\Delta K^{0.5}_{tot}$ should be fitted into the existing FCG data for the determination of constants "C" and "γ" in Eq. (3.60), i.e. one line covering the near threshold FCG data and the other approximating the so-called Paris regime (Figure 4-17). The fitting parameters "C" and "γ" can be found in Table 4-3. The two power law curves characterized by two sets of constants (the exponent "γ" and the constant "C") can be subsequently used for FCG analyses.

4.1.3 Modeling of Fatigue Crack Growth in 4340 Steel Material

The fatigue crack growth data for the 4340 steel alloy was found in [131, 132, 133, 134]. The fatigue crack growth data sets were obtained at various stress ratios, R_{appl}, and are shown in Figure 4-18 as a function of the applied stress intensity factor range, ΔK_{appl}.

The cyclic (3.1) and fatigue properties (3.2) for the 4340 steel alloy were obtained from reference [131] and are listed in Table 4-1. Due to the availability of the near threshold

data obtained at high stress ratios, the ρ* parameter was determined from Eqs. (3.43), (3.44), (3.72), as described in section 3.6 (Table 4-2). Based on the material data listed in Table 4-1 and the determined ρ* parameter, the constants of Eqs. (3.52), (3.53), and (3.60) can be calculated and found in Table 4-3. The stabilized fatigue damage parameter, Φ, can be determined from several iterations of Eq. (3.67) and is given in Table 4-2 as well.

The two-parameter fatigue crack growth driving forces, $K_{max,tot}^{p}\Delta K_{tot}^{(1-p)}$, $K_{max,tot}^{0.5}\Delta K_{tot}^{0.5}$ and $K_{max,tot}^{p}\Delta K_{tot}^{0.5}$, were used to model the effect of the stress ratio R on the fatigue crack growth under constant amplitude loading. The total stress intensity factors corrected for the residual stress effect were used to determine the magnitude of each driving force. It is seen (Figure 4-19) that in the high and medium FCG rate regimes, the "plastic" driving force, $K_{max,tot}^{p}\Delta K_{tot}^{(1-p)}$, was successful in correlating the fatigue crack growth data obtained at various stress ratios. The "elastic" driving force, $K_{max,tot}^{0.5}\Delta K_{tot}^{0.5}$, was the least successful one even in the near threshold region (Figure 4-20). It can be noted that the elastic driving force may be used only to consolidate FCG data at very low fatigue crack growth rates; therefore, it should not be used for fatigue crack growth predictions away from the threshold. However, it was found (Figure 4-21) that the combination of the elastic and plastic stress-strain material behavior at the crack tip in the form of the "mixed" driving force, $K_{max,tot}^{p}\Delta K_{tot}^{0.5}$, could be used to correlate FCG data at various R-ratios for the FCG rates spanning from the near threshold to the high growth rate regime.

The "approximate" closed solutions, in the form of Eqs. (3.52), (3.53), and (3.60) were attainable after neglecting the plastic or elastic terms in the Ramberg-Osgood and the Manson-Coffin equations. Unfortunately, such solutions become inaccurate in the regions

where both terms are equally important. However, numerical solutions to the complete set of Eqs. (3.42) - (3.44), and (3.4), i.e. without neglecting any terms, are possible. The final solution can not be derived in a closed form but it can be illustrated graphically.

Both the "exact" FCG curves and the approximate closed form solutions (Eqs. (3.52), (3.60) and (3.53)) are shown as diagrams (Figure 4-19, Figure 4-20, and Figure 4-21) where the fatigue crack growth rate is shown as a function of the appropriate driving force $\Delta\kappa$.

The best results in correlating the FCG under various stress ratios were obtained while using the mixed driving force in the form of $K^{p}_{max,tot}\Delta K^{0.5}_{tot}$. As shown in Figure 4-21, the exact numerical solution presented in terms of the mixed driving force had good agreement with the experimental data over the entire range of FCG data. However, the elasto-plastic approximate solution (Eq. (3.60)) agreed well only with the low FCG data. Therefore, it is recommended that in practice the two lines da/dN vs. $K^{p}_{max,tot}\Delta K^{0.5}_{tot}$ should be fitted into the existing FCG data for the determination of constants "C" and "γ" in Eq. (3.60), i.e. one line covering the near threshold FCG data and the other approximating the so-called Paris regime (Figure 4-22). The fitting parameters "C" and "γ" can be found in Table 4-3. The two power law curves characterized by two sets of constants (the exponent "γ" and the constant "C") can be subsequently used for FCG analyses.

4.1.4 Modeling of Fatigue Crack Growth in 4140 Steel Material

The fatigue crack growth data for the 4140 steel alloy was found in [72]. The fatigue crack growth data sets were obtained at various stress ratios, R_{appl}, and are shown in Figure 4-23 as a function of the applied stress intensity factor range, ΔK_{appl}.

The cyclic (3.1) and fatigue properties (3.2) for the 4140 steel alloy were obtained from reference [135] and are listed in Table 4-1. Due to the absence of the near threshold fatigue crack growth data at high stress ratios, the curve fitting method, as discussed in section 3.6, was used for estimating the ρ* parameter (Table 4-2). Based on the material data listed in Table 4-1 and the determined ρ* parameter, the constants of Eqs. (3.52), (3.53), and (3.60) can be calculated and found in Table 4-3. The stabilized fatigue damage parameter, Φ, can be determined from several iterations of Eq. (3.67) and is given in Table 4-2 as well.

The two-parameter fatigue crack growth driving forces, $K_{max,tot}^{p}\Delta K_{tot}^{(1-p)}$, $K_{max,tot}^{0.5}\Delta K_{tot}^{0.5}$ and $K_{max,tot}^{p}\Delta K_{tot}^{0.5}$, were used to model the effect of the stress ratio R on the fatigue crack growth under constant amplitude loading. The total stress intensity factors corrected for the residual stress effect were used to determine the magnitude of each driving force. It is seen (Figure 4-24) that in the high and medium FCG rate regimes, the "plastic" driving force, $K_{max,tot}^{p}\Delta K_{tot}^{(1-p)}$, was successful in correlating the fatigue crack growth data obtained at various stress ratios. The "elastic" driving force, $K_{max,tot}^{0.5}\Delta K_{tot}^{0.5}$, was the least successful one even in the near threshold region (Figure 4-25). It can be noted that the elastic driving force may be used only to consolidate FCG data at very low fatigue crack growth rates; therefore, it should not be used for fatigue crack growth predictions away from the threshold. However, it was found (Figure 4-26) that the combination of the elastic and plastic stress-strain material behavior at the crack tip in the form of the "mixed" driving force, $K_{max,tot}^{p}\Delta K_{tot}^{0.5}$, could be used to correlate FCG data at various R-ratios for the FCG rates spanning from the near threshold to the high growth rate regime.

The "approximate" closed solutions, in the form of Eqs. (3.52), (3.53), and (3.60) were attainable after neglecting the plastic or elastic terms in the Ramberg-Osgood and the Manson-Coffin equations. Unfortunately, such solutions become inaccurate in the regions where both terms are equally important. However, numerical solutions to the complete set of Eqs. (3.42) - (3.44), and (3.4), i.e. without neglecting any terms, are possible. The final solution can not be derived in a closed form but it can be illustrated graphically.

Both the "exact" FCG curves and the approximate closed form solutions (Eqs. (3.52), (3.60) and (3.53)) are shown as diagrams (Figure 4-24, Figure 4-25, and Figure 4-26) where the fatigue crack growth rate is shown as a function of the appropriate driving force $\Delta\kappa$.

The best results in correlating the FCG under various stress ratios were obtained while using the "mixed" driving force in the form of $K^{p}_{max,tot}\Delta K^{0.5}_{tot}$. As shown in Figure 4-26, the exact numerical solution presented in terms of the mixed driving force had good agreement with the experimental data over the entire range of FCG data. However, the elasto-plastic approximate solution (Eq. (3.60)) agreed well only with the low FCG data. Therefore, it is recommended that in practice the two lines da/dN vs. $K^{p}_{max,tot}\Delta K^{0.5}_{tot}$ should be fitted into the existing FCG data for the determination of constants "C" and "γ" in Eq. (3.60), i.e. one line covering the near threshold FCG data and the other approximating the so-called Paris regime (Figure 4-27). The fitting parameters "C" and "γ" can be found in Table 4-3. The two power law curves characterized by two sets of constants (the exponent "γ" and the constant "C") can be subsequently used for FCG analyses.

4.1.5 Modeling of Fatigue Crack Growth in Ti-6Al-4V Material

The fatigue crack growth data for the Ti-6Al-4V alloy was found in [136, 137]. The fatigue crack growth data sets were obtained at various stress ratios, R_{appl}, and are shown in Figure 4-28 as a function of the applied stress intensity factor range, ΔK_{appl}.

The cyclic (3.1) and fatigue properties (3.2) for the Ti-6Al-4V alloy were obtained from reference [131] and are listed in Table 4-1. Due to the availability of the near threshold data obtained at high stress ratios, the ρ* parameter was determined from Eqs. (3.43), (3.44), (3.72), as described in section 3.6 (Table 4-2). Based on the material data listed in Table 4-1 and the determined ρ* parameter, the constants of Eqs. (3.52), (3.53), and (3.60) can be calculated and found in Table 4-3. The stabilized fatigue damage parameter, Φ, can be determined from several iterations of Eq. (3.67) and is given in Table 4-2 as well.

The two-parameter fatigue crack growth driving forces, $K_{max,tot}^{p}\Delta K_{tot}^{(1-p)}$, $K_{max,tot}^{0.5}\Delta K_{tot}^{0.5}$ and $K_{max,tot}^{p}\Delta K_{tot}^{0.5}$, were used to model the effect of the stress ratio R on the fatigue crack growth under constant amplitude loading. The total stress intensity factors corrected for the residual stress effect were used to determine the magnitude of each driving force. It is seen (Figure 4-29) that in the high and medium FCG rate regimes, the "plastic" driving force, $K_{max,tot}^{p}\Delta K_{tot}^{(1-p)}$, was successful in correlating the fatigue crack growth data obtained at various stress ratios. The "elastic" driving force, $K_{max,tot}^{0.5}\Delta K_{tot}^{0.5}$, was the least successful one even in the near threshold region (Figure 4-30). It can be noted that the elastic driving force may be used only to consolidate FCG data at very low fatigue crack growth rates; therefore, it should not be used for fatigue crack growth predictions away from the threshold. However, it was found (Figure 4-31) that the combination of the elastic and plastic stress-strain material

behavior at the crack tip in the form of the "mixed" driving force, $K^{p}_{max,tot}\Delta K^{0.5}_{tot}$, could be used to correlate FCG data at various R-ratios for the FCG rates spanning from the near threshold to the high growth rate regime.

The "approximate" closed solutions, in the form of Eqs. (3.52), (3.53), and (3.60) were attainable after neglecting the plastic or elastic terms in the Ramberg-Osgood and the Manson-Coffin equations. Unfortunately, such solutions become inaccurate in the regions where both terms are equally important. However, numerical solutions to the complete set of Eqs. (3.42) - (3.44), and (3.4), i.e. without neglecting any terms, are possible.

The final solution can not be derived in a closed form but it can be illustrated graphically. Both the "exact" FCG curves and the approximate closed form solutions (Eqs. (3.52), (3.60) and (3.53)) are shown as diagrams (Figure 4-29, Figure 4-30, and Figure 4-31) where the fatigue crack growth rate is shown as a function of the appropriate driving force $\Delta\kappa$. The best results in correlating the FCG under various stress ratios were obtained while using the "mixed" driving force in the form of $K^{p}_{max,tot}\Delta K^{0.5}_{tot}$. However, for fatigue crack growth rates more than 2×10^{-5} mm/cycle, there are some discrepancies between the predicted and experimental curves, as shown in Figure 4-29 and Figure 4-31. Although two different sets of fatigue crack growth data were used for the comparisons, the "exact" FCG curves and the approximate closed form solutions were plotted using one set of cyclic and fatigue properties of the material. Probably, the Ti-6Al-4V material used to generate the fatigue crack growth data $da/dN > 2\times10^{-5}$ mm/cycle might have had slightly different cyclic $da/dN > 2\times10^{-5}$ mm/cycle and fatigue properties than the properties used in the analysis. Moreover, the change of mechanism in this material at the FCG rate of about 2×10^{-5} mm/cycle can probably be another reason for the discrepancies. The change of mechanism results in the

change of the material properties in the form of the cyclic stress-strain curve and the fatigue strain-life expression yielding two different exact solutions or two different approximate solutions.

As shown in Figure 4-31, the exact numerical solution presented in terms of the mixed driving force had good agreement with the experimental data over the entire range of FCG data. However, the elasto-plastic approximate solution (Eq. (3.60)) agreed well only with the low FCG data. Therefore, it is recommended that in practice the two lines da/dN vs. $K_{max,tot}^{p}\Delta K_{tot}^{0.5}$ should be fitted into the existing FCG data for the determination of constants "C" and "γ" in Eq. (3.60), i.e. one line covering the near threshold FCG data and the other approximating the so-called Paris regime (Figure 4-32). However, in this case, fitting one line into the experimental FCG data in the Paris regime is not possible mainly due to the change of mechanism in the material, as discussed in the previous paragraph. Therefore, it is recommended that two fitted lines be plotted in the Paris regime. The fitting parameters "C" and "γ" can be found in Table 4-3. The two power law curves characterized by two sets of constants (the exponent "γ" and the constant "C") can be subsequently used for FCG analyses.

4.2 Under a Single Overload

The proposed model was also used to predict the fatigue crack growth rate after application of a single tensile overload. The interaction effects which occur under variable amplitude loading can manifest themselves in a change of the magnitude of the total stress intensity factors and consequently the change of the fatigue crack growth rate. The crack growth rate, at each crack increment Δa_i, can be estimated by numerical solutions to the complete set of Eqs. (3.42) - (3.44), and (3.4), involving the total stress intensity factors.

Fatigue crack growth under variable amplitude loading can also be predicted from the "approximate" closed solutions, in the form of Eqs. (3.52), (3.53), and (3.60). However, in both cases, care should be taken for the calculation of the total SIFs after applying the overload. The numerical solution is termed further on as the "exact solution".

It can be assumed that the plastic zone induced by the constant amplitude loading just before applying the overload remains in the wake of the advancing crack tip. After applying the overload, the fatigue crack growth is influenced by the stresses induced by the overload plastic zone. A typical residual stress distribution used to calculate the residual stress intensity factors after the overload is shown in Figure 4-33. The residual stress field consists of two stress fields that are not symmetric: the first one created by the base constant amplitude loading remains in the wake of the advancing crack tip; the second one was created by a single overload. As the crack is penetrating into the overload plastic zone, the magnitude of the residual stress intensity factor increases, due to the increase of the compressive residual stress, and consequently the fatigue crack growth rate decreases. As soon as the magnitude of the residual SIF induced by the overload stress field is the same as that one induced by the subsequent constant amplitude base loading, the overload effect is assumed to cease. In other words, beyond this point the fatigue crack growth needs to be calculated by using the residual SIF induced by the post-overload or the current load fluctuations.

Experimental fatigue crack growth data obtained after the application of a single overload in the aluminum alloy 7075-T6, 4140 steel alloy and the titanium alloy Ti-6Al-4V were used for the verification of the model for the FCG analysis under variable amplitude loading.

4.2.1 Modeling of Variable Fatigue Crack Growth in the Al 7075-T6 Alloy

The experimental fatigue crack growth data after the application of a single overload to the Al 7075-T6 aluminum alloy specimens was found in reference [82]. The predicted and the experimental fatigue crack growth following a single tensile overload are shown in Figure 4-34 and Figure 4-35. The experimental post-overload FCG rate was measured [82] in load-controlled fatigue tests on the 7075-T6 aluminum alloy single-edge notched (SEN) specimens at R = 0.1 with the overload ratios of 1.5 and 1.8 and the base stress intensity range ΔK_{BL} = 11.4 MPa√m and ΔK_{BL} = 8.955 MPa√m, respectively. Both predicted fatigue crack growth rates, i.e. one based on the numerical "exact" and the other on "approximate" closed form solution (Eq. (3.60)) are shown in Figure 4-34 and Figure 4-35. It is felt that the discrepancy between the numerical "exact" solution and the experimental curve was due to the inaccuracy of the ρ* parameter. The ρ* parameter was estimated using one constant amplitude FCG data set from reference [124-126] and the predictions were carried out for another set of data borrowed from reference [82]. It is not certain whether the material properties of the two different sets of specimens tested in different laboratories and separated by at least a few years time span were exactly the same. However, in the case of using Eq. (3.60) (the constants "C" and "γ" in this equation is determined based on the curve fitting method) for FCG prediction, the discrepancy between the analytical "approximate" solution and the experimental curve was not so significant.

4.2.2 Modeling of Variable Fatigue Crack Growth in the Ti-6Al-4V Alloy

The experimental fatigue crack growth data obtained after the application of a single tensile overload from the Ti-6Al-4V alloy was found in reference [67]. The predicted and the experimental fatigue crack growth following a single tensile overload is shown in Figure

4-36. The experimental post-overload FCG rate was measured in load-controlled fatigue tests on the Ti-6Al-4V alloy center-cracked specimen at R = 0 with the overload ratio of 2 and the base stress intensity range of ΔK_{appl} = 16.33 MPa√m. Both predicted fatigue crack growth rates, i.e. one based on the numerical "exact" and the other on "approximate" closed form solution (Eq. (3.60)) are shown in Figure 4-36. It is felt that the discrepancy between the numerical "exact" solution and the experimental curve was due to the inaccuracy of the ρ* parameter. The ρ* parameter was estimated using one constant amplitude FCG data set from reference [136, 137] and the predictions were carried out for another set of data from reference [67]. It is not certain whether the material properties of the two different sets of specimens tested in different laboratories and separated by at least a few years time span were exactly the same. However, the fatigue crack growth can be predicted pretty well based on two fitted lines to the current experimental fatigue crack growth data, da/dN versus $K^{p}_{max,tot}\Delta K^{0.5}_{tot}$, as shown in Figure 4-36.

4.2.3 Modeling of Variable Fatigue Crack Growth and Fatigue Life in 4140 Steel

The experimental fatigue crack growth data and the fatigue life measurements after the application of a single overload for the 4140 steel was taken from reference [72]. The predicted and experimental fatigue crack growth following a single tensile overload is shown in Figure 4-37, Figure 4-38, and Figure 4-39. Furthermore, the predicted and the experimental fatigue lives in terms of number of cycles are also shown in Figure 4-40, Figure 4-41, and Figure 4-42. The tests were carried out for three different loading conditions: R = 0.1; ΔK_{BL} = 17.82 MPa√m, R = 0.5; ΔK_{BL} = 19.8 MPa√m and R = 0.1; ΔK_{BL} = 35.64 MPa√m

with the overload ratio of 2. The experimental post-overload FCG rates were measured in the K-controlled fatigue tests on 4140 steel CT specimens.

Both predicted fatigue crack growth rates (da/dN vs. “a”), i.e. one based on the numerical “exact” and the other on “approximate” closed form solution (Eq. (3.60)) are shown in Figure 4-37, Figure 4-38, and Figure 4-39 for the three different loading conditions. Moreover, both predicted fatigue lives, “a” vs. “N”, based on the numerical “exact” solution and the “approximate” closed form solution (Eq. (3.60)) are shown in Figure 4-40, Figure 4-41, and Figure 4-42. It should be noted that the “approximate” closed form solution was based on Eq. (3.60) in which the constants “C” and “γ” were determined by the curve fitting method.

Because the constant amplitude FCG data set and the predictions were carried out for similar specimens tested in the same laboratory, good comparison between the theoretical and experimental curves was obtained for both the fatigue crack growth rate prediction (da/dN vs. “a”) and fatigue life prediction (“a” vs. “N”).

Table 4-1: Material properties.

Material		Al 7075-T6	Al 2024-T351	St-4340	St-4140	Ti-6Al-4V
Monotonic material properties	E (MPa)	71700	70000	200000	205000	117000
	ν	0.32	0.32	0.3	0.3	0.3
	σ_{ys} (MPa)	468.85	403.46	889.32	645.65	1185
Cyclic stress-strain	K' (MPa)	737.81	751.5	1910	1640	1772
	n'	0.056	0.1	0.123	0.15	0.106
Strain -life curve	σ'_f (MPa)	729.62	909.48	1879	1530.7	2030
	b	-0.059	-0.1	-0.0859	-0.087	-0.104
	ε'_f	0.2638	0.36	0.64	0.63	0.841
	c	-0.802	-0.65	-0.636	-0.58	-0.688
Reference		[123]	[130]	[131]	[135]	[131]

Table 4-2: The elementary material block size (crack tip radius) ρ*.

Material	Al 7075-T6	Al 2024-T351	St-4340	St-4140	Ti-6Al-4V
$\rho^*(m)$	4×10^{-6}	8×10^{-6}	2×10^{-6}	4×10^{-6}	8×10^{-6}
Φ	0.69	0.75	0.75	0.78	0.73

Table 4-3: Parameters and constants of the two-parameter fatigue crack growth model.

Material		Al 7075-T6	Al 2024-351	St-4340	St-4140	Ti-6Al-4V
Plastic	γ	2.32	2.67	2.77	3	2.53
	p	0.05	0.09	0.11	0.13	0.096
	C $\frac{\text{mm/cycle}}{(\text{MPa}\sqrt{\text{m}})^m}$	6.1×10^{-9}	9.13×10^{-10}	4.25×10^{-11}	1.64×10^{-11}	1×10^{-10}
Elastic	γ	16.95	10	11.64	11.49	9.62
	p	0.5	0.5	0.5	0.5	0.5
	C $\frac{\text{mm/cycle}}{(\text{MPa}\sqrt{\text{m}})^m}$	2.61×10^{-14}	5.43×10^{-13}	5.25×10^{-15}	2.81×10^{-15}	4.67×10^{-16}
Elastic – Plastic	γ	16.95	10	11.64	11.49	9.62
	p	0.05	0.09	0.11	0.13	0.096
	C $\frac{\text{mm/cycle}}{\left(\text{MPa}^{(0.5+p)}\sqrt{\text{m}}\right)^m}$	1.63×10^{-12}	8.72×10^{-12}	1.83×10^{-13}	7.22×10^{-14}	1.88×10^{-13}
Fitted Line (Paris Regime)	γ	7	6.2	4.1	4.9	5 5.8
	p	0.05	0.09	0.11	0.13	0.096
	C $\frac{\text{mm/cycle}}{\left(\text{MPa}^{(0.5+p)}\sqrt{\text{m}}\right)^m}$	1.5×10^{-10}	8×10^{-11}	6×10^{-8}	9×10^{-12}	7×10^{-11} 5×10^{-12}
Fitted Line (Near Threshold)	γ	90	90	40	90	100
	p	0.05	0.09	0.11	0.13	0.096
	C $\frac{\text{mm/cycle}}{\left(\text{MPa}^{(0.5+p)}\sqrt{\text{m}}\right)^m}$	63×10^{-19}	3×10^{-29}	9×10^{-23}	3×10^{-43}	3×10^{-44}

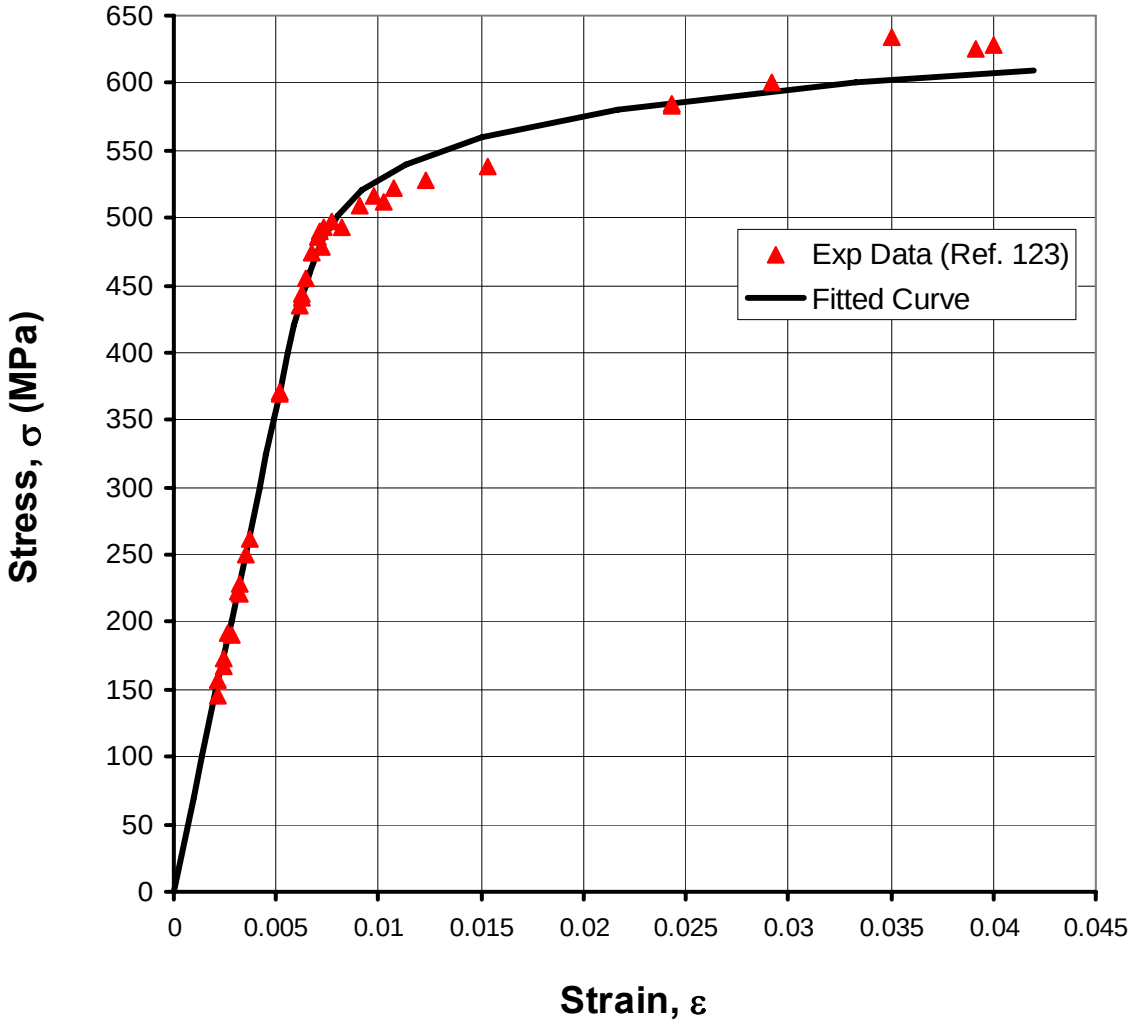

Figure 4-1: The Ramberg-Osgood stress-strain material curve, 7075-T6 Al alloy.

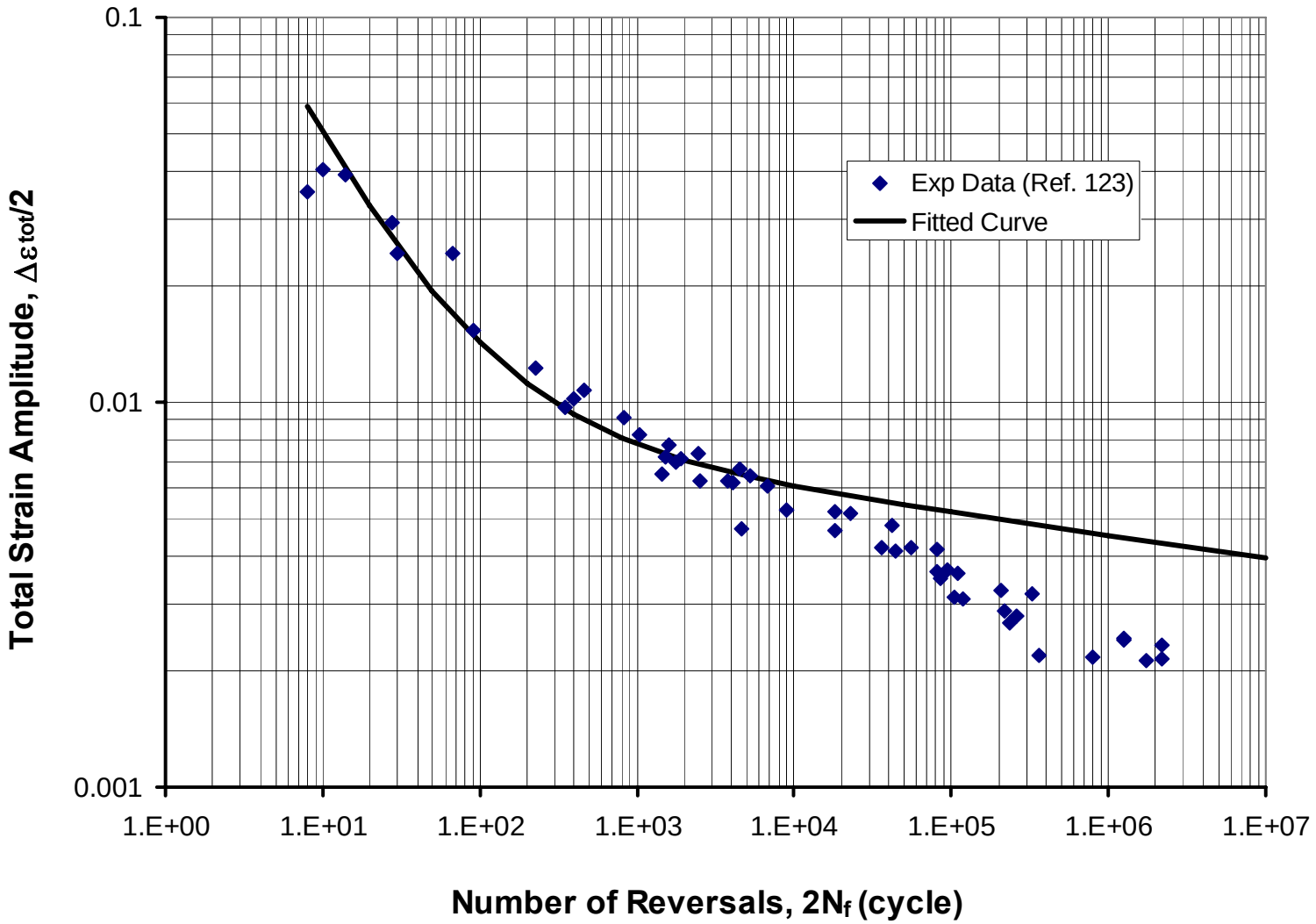

Figure 4-2: The Manson-Coffin fatigue curve, 7075-T6 Al alloy.

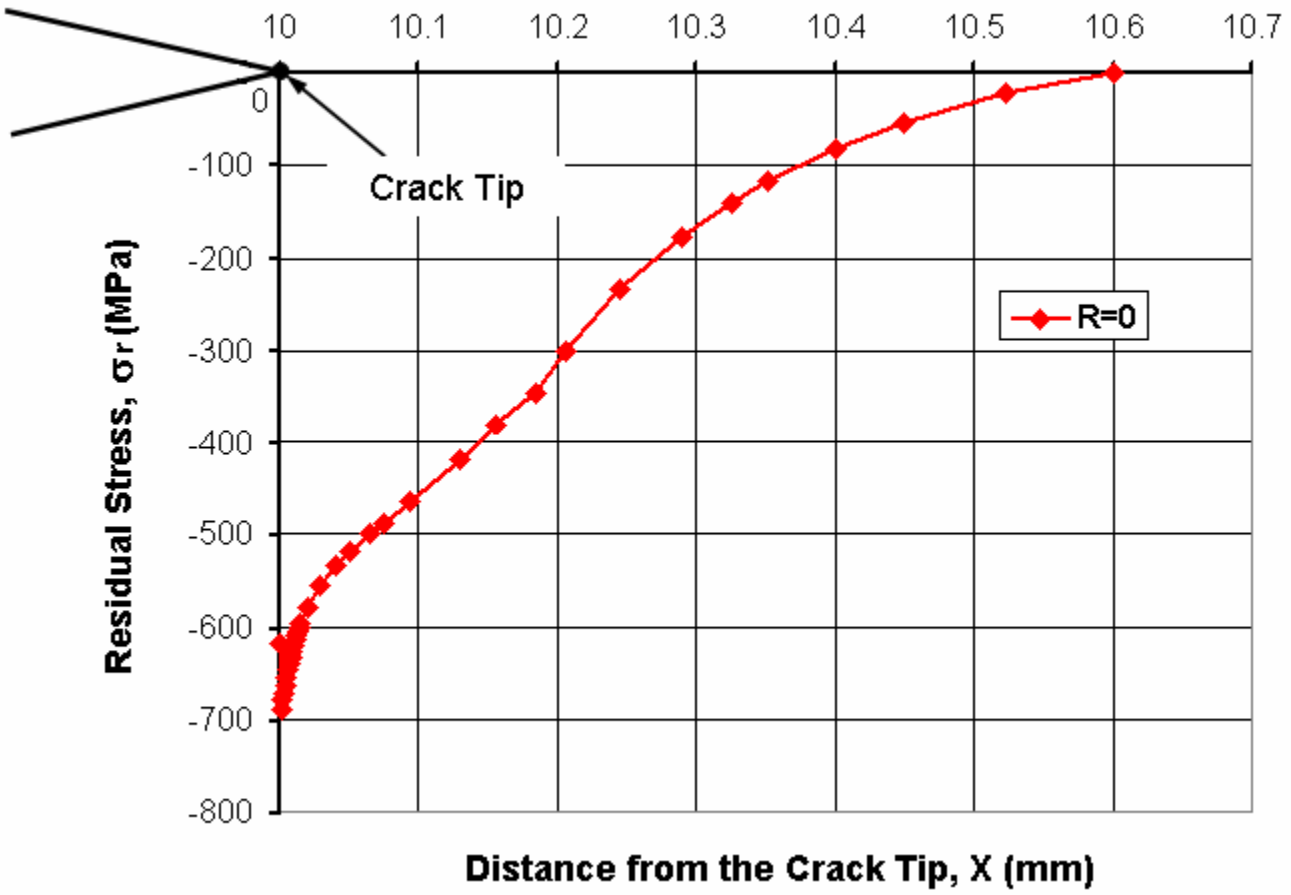

Figure 4-3: Distribution of compressive residual stress ahead of the crack tip induced by the applied load ΔK_{appl} = 32.6 MPa√m & R = 0, 7075-T6 Al alloy.

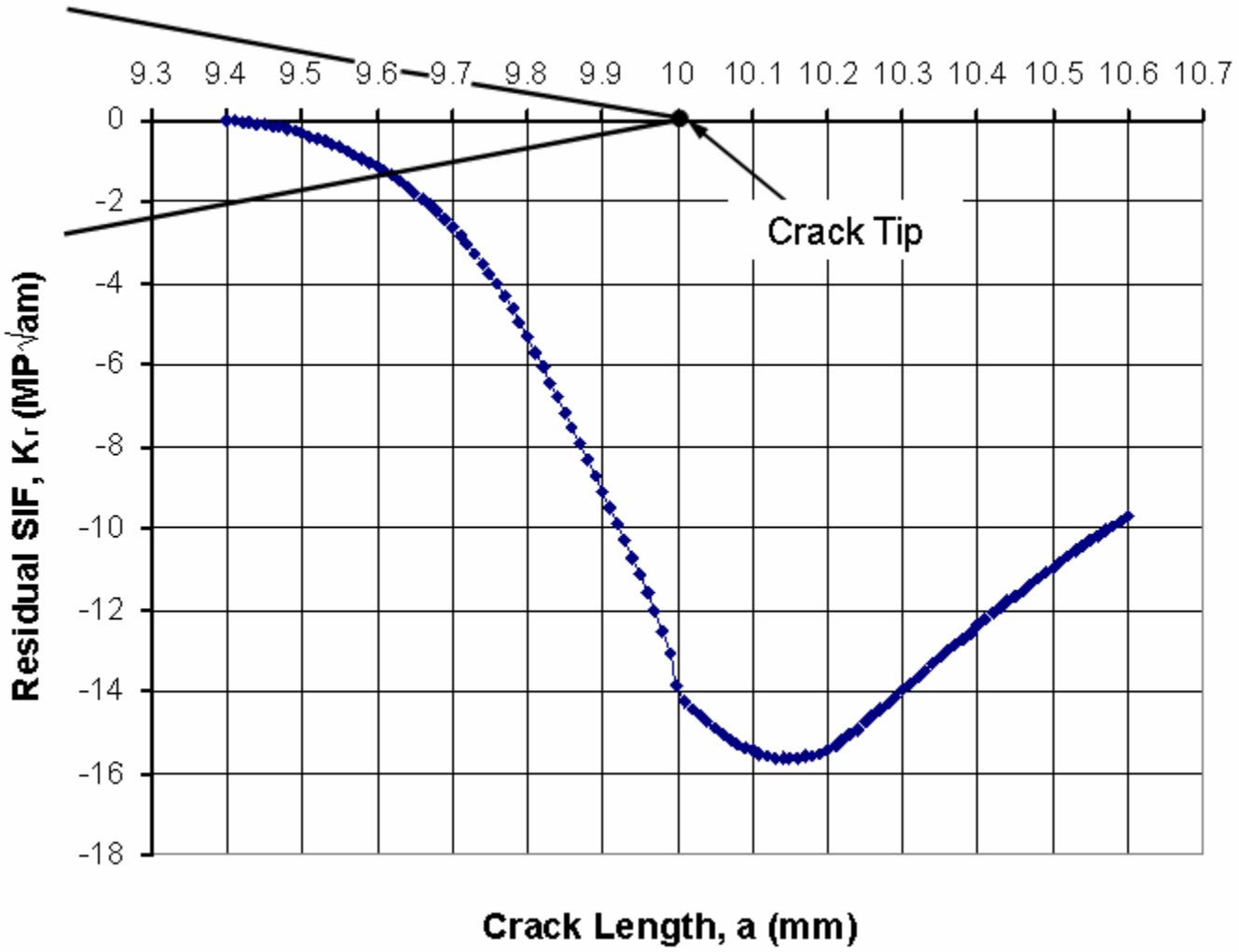

Figure 4-4: Residual stress intensity factor versus crack length for the applied load ΔK_{appl} = 32.6 MPa√m & R = 0, 7075-T6 Al alloy.

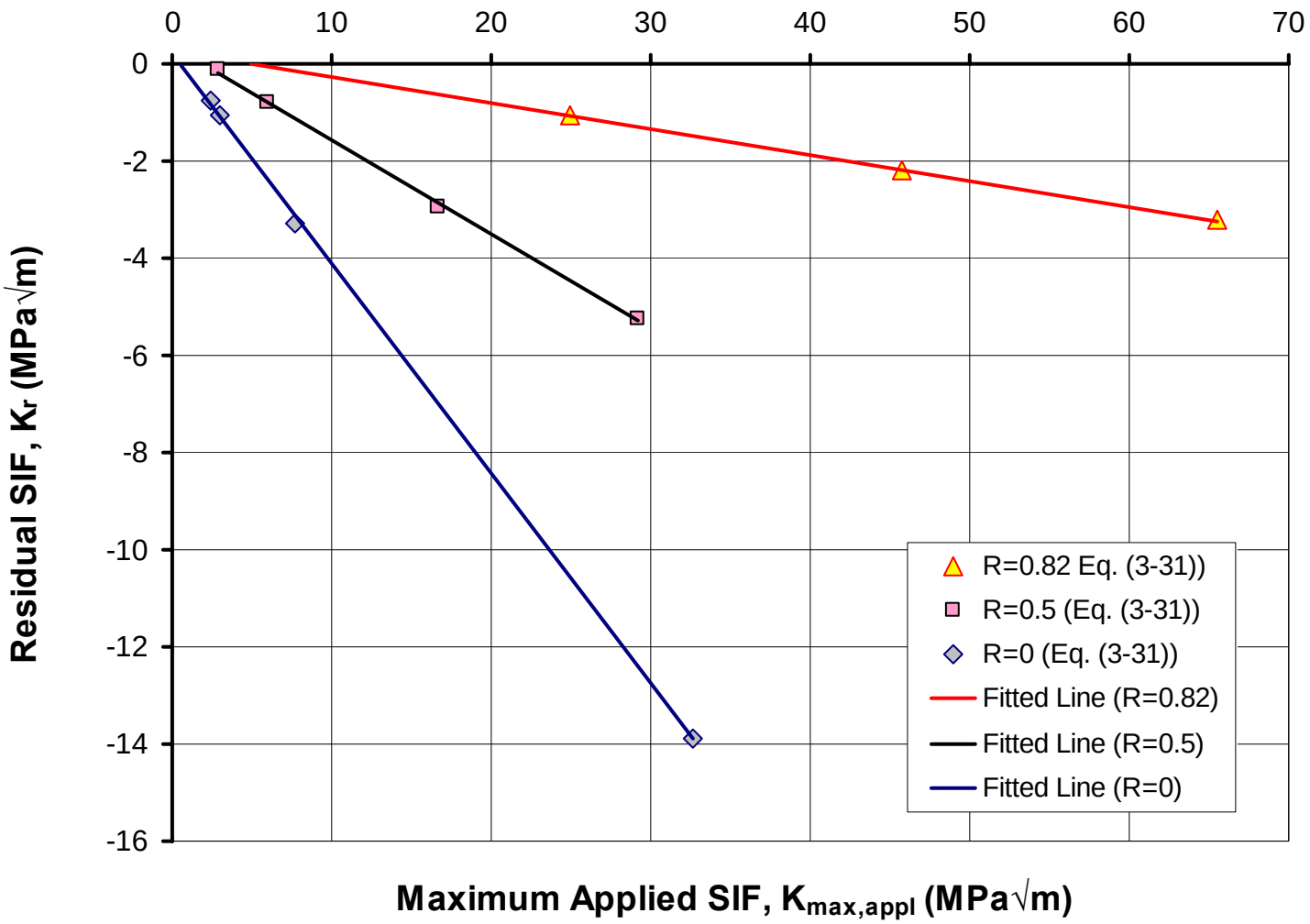

Figure 4-5: Linear interpolation of the residual stress intensity factor, 7075-T6 Al alloy.

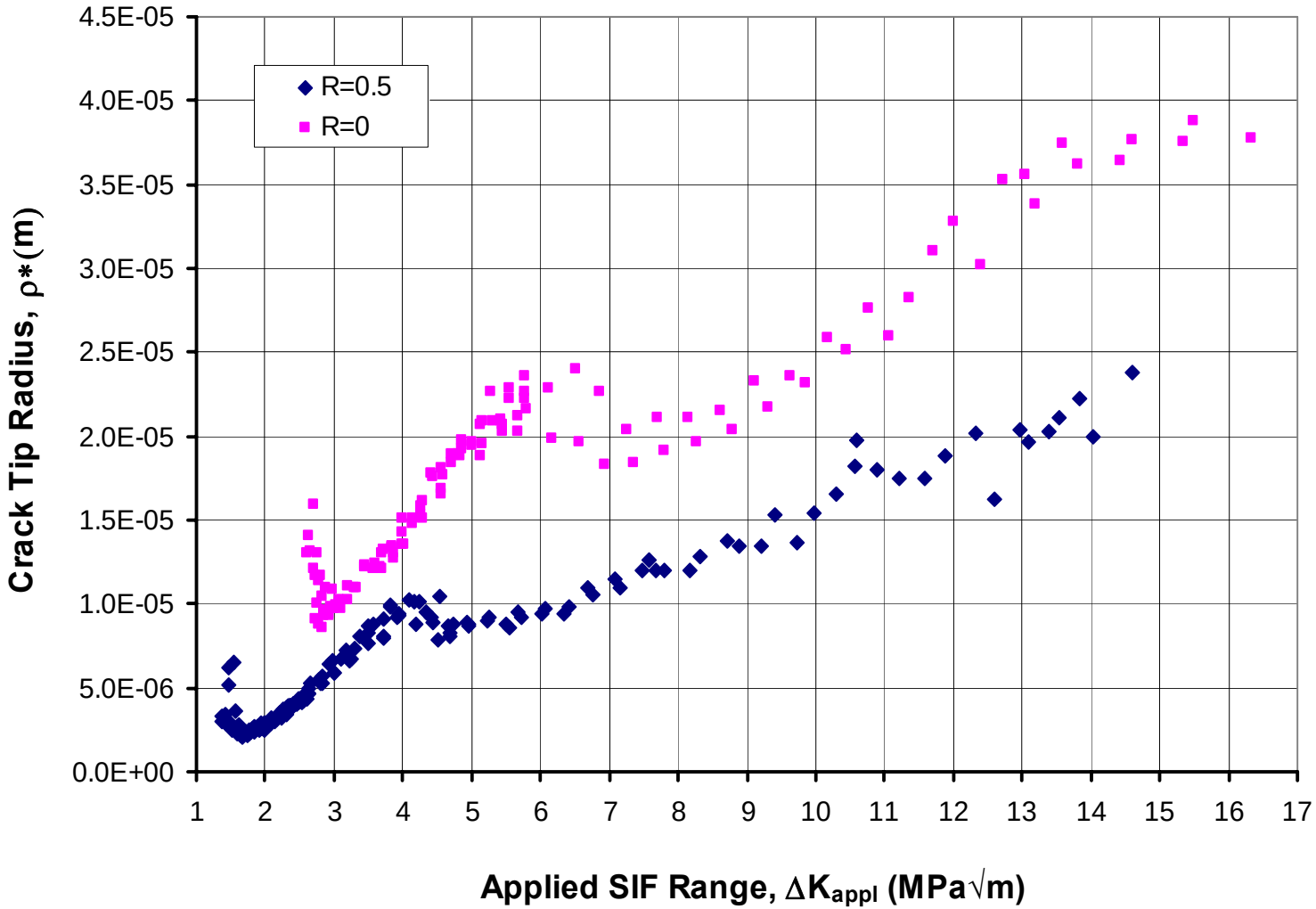

Figure 4-6: Evolution of the ρ* parameter determined from the "applied" stress intensity range, 7075-T6 Al alloy.

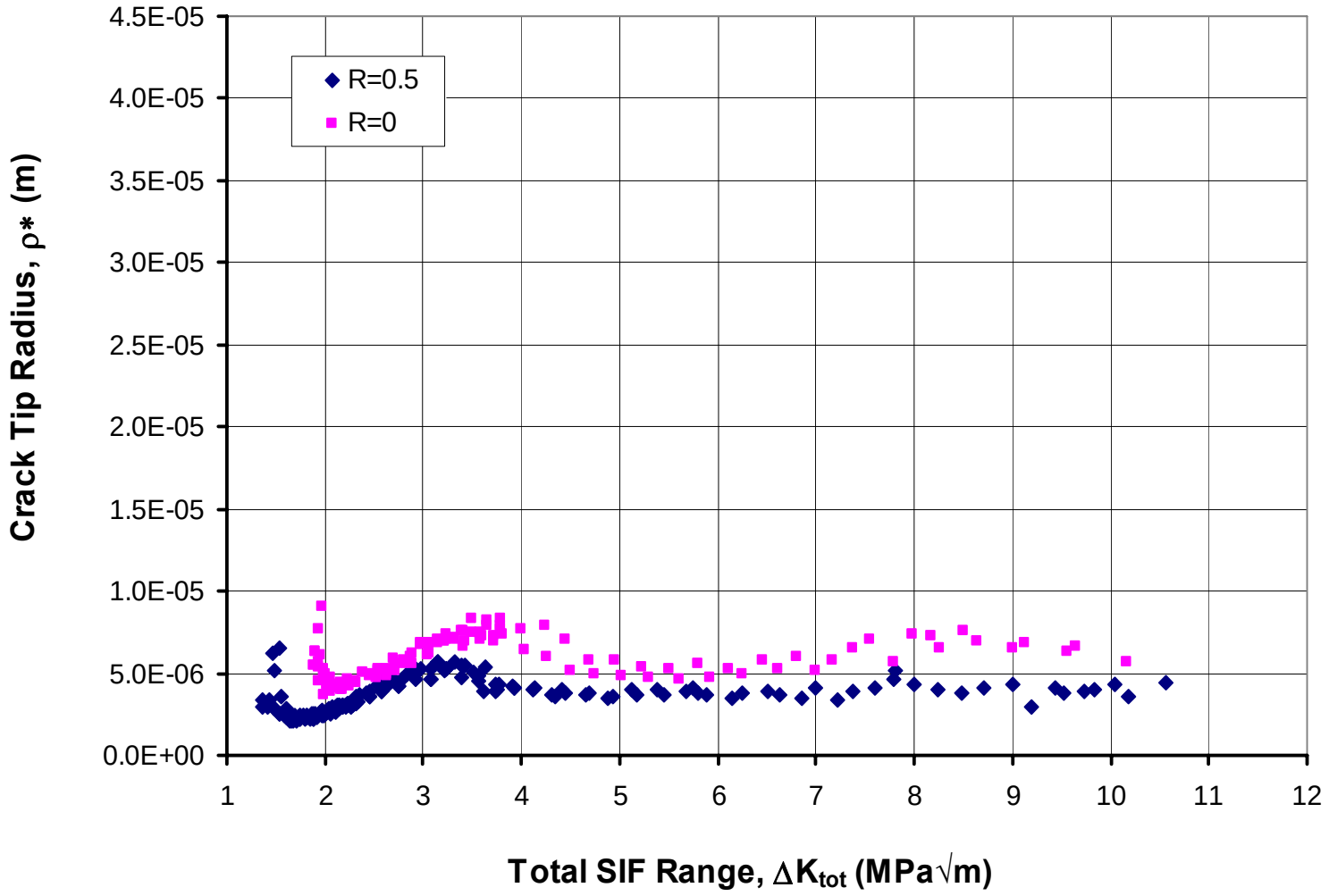

Figure 4-7: Evolution of the ρ* parameter determined from the "total" stress intensity range, 7075-T6 Al alloy.

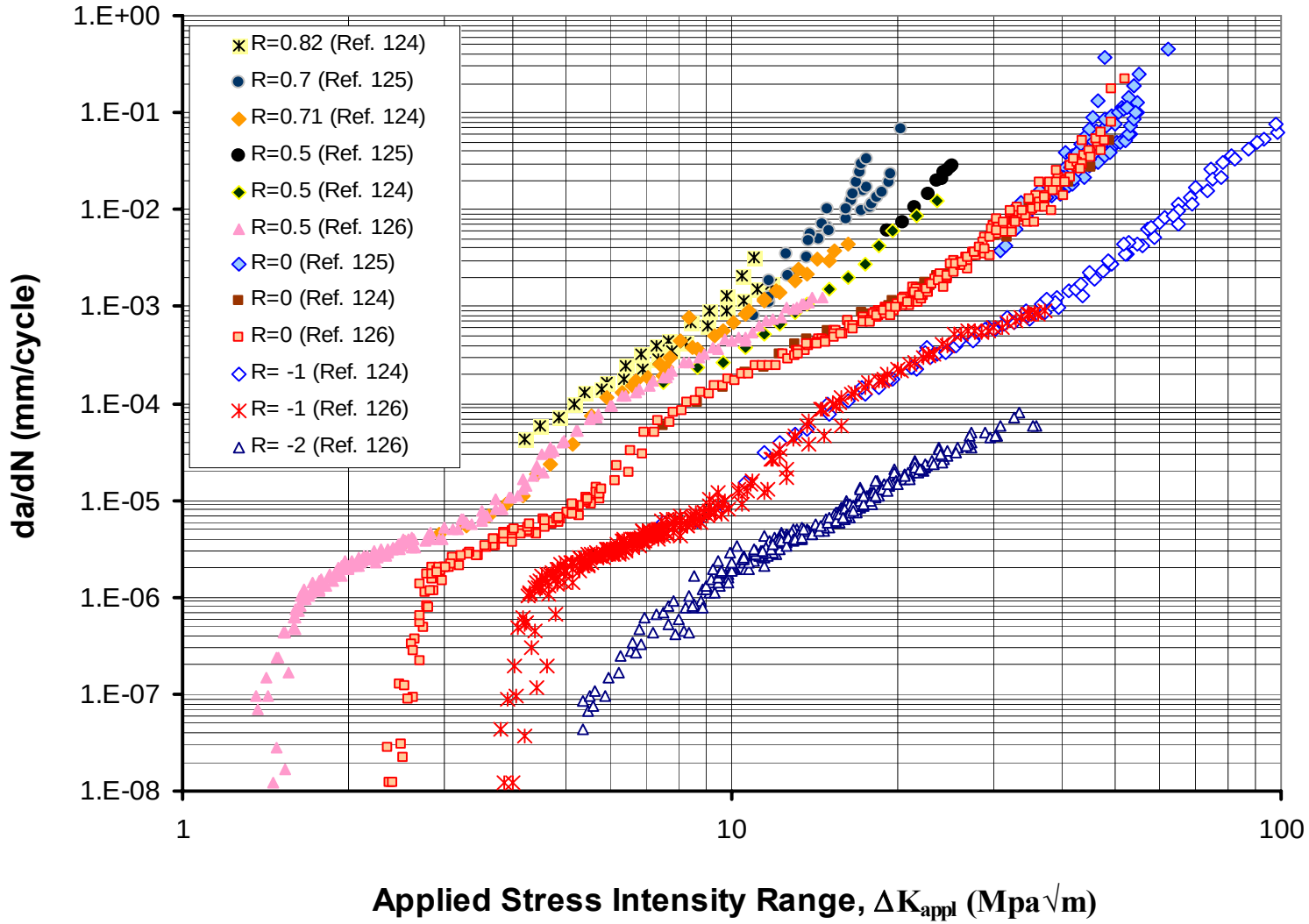

Figure 4-8: Fatigue crack growth data for 7075-T6 aluminum alloy obtained at stress ratios $-2 \leq R \leq 0.82$ [124-126].

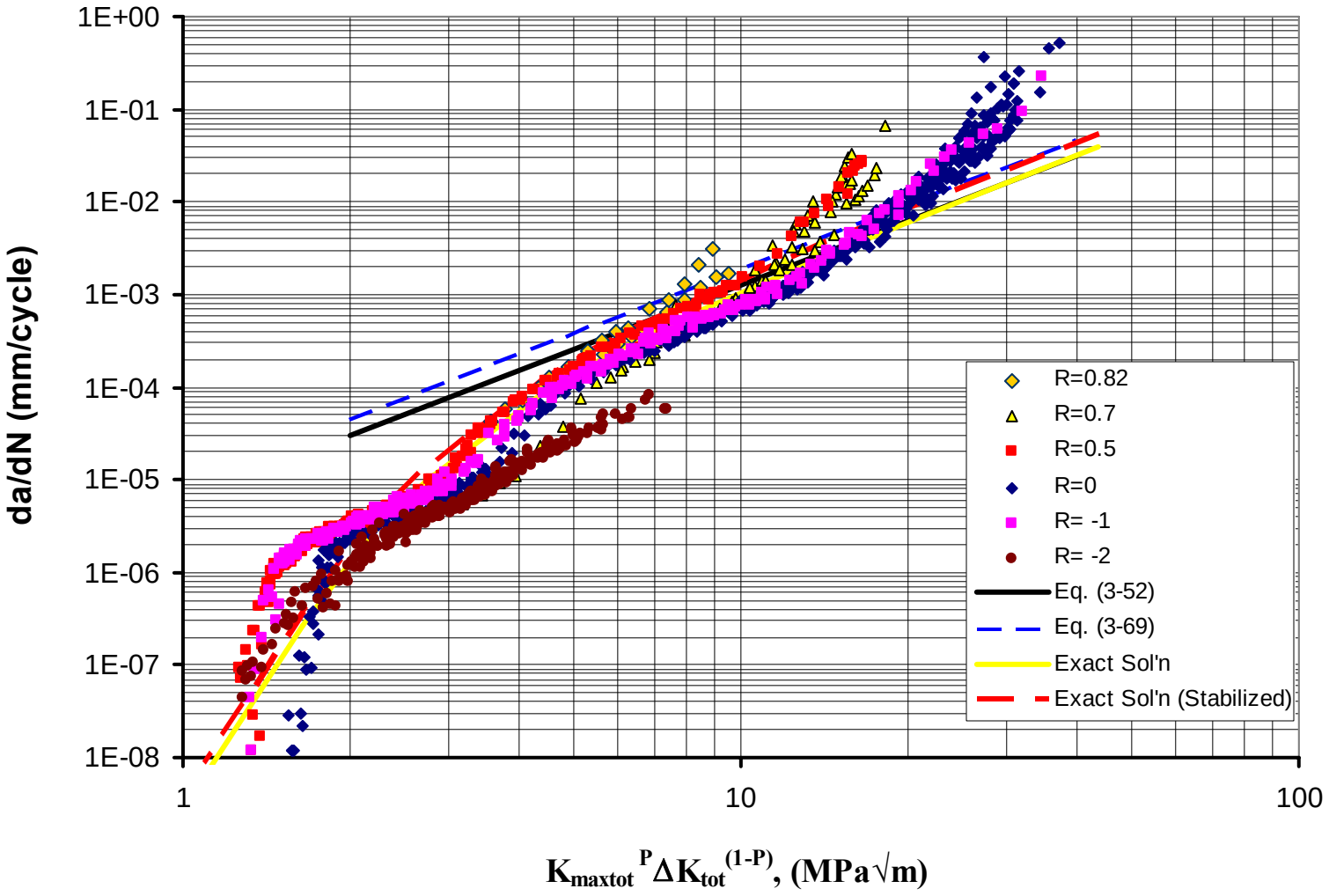

Figure 4-9: Fatigue crack growth as a function of the "plastic" two parameter driving force, $K_{max,tot}{}^{p}\Delta K_{tot}{}^{(1-p)}$, 7075-T6 Al alloy.

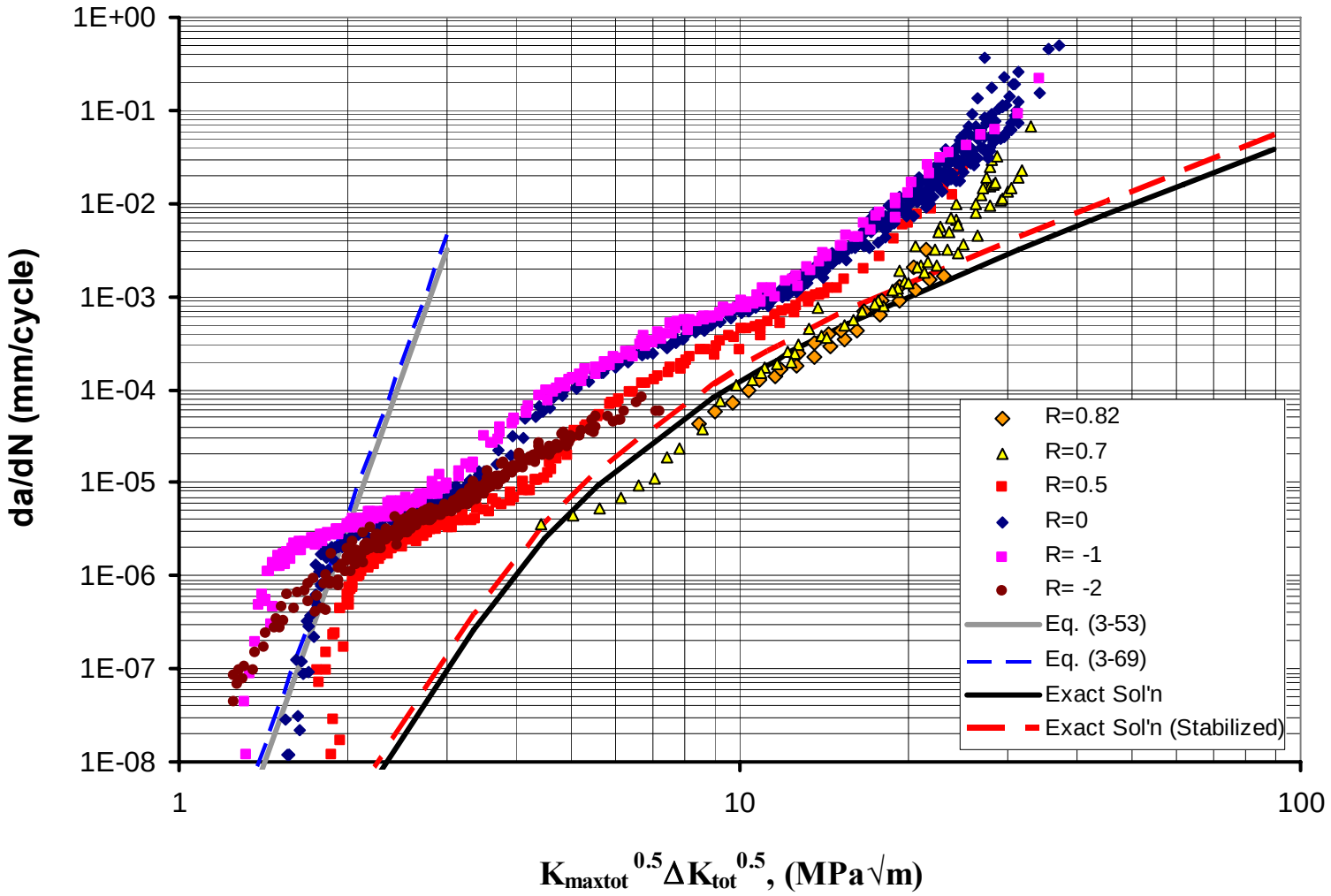

Figure 4-10: Fatigue crack growth as a function of the "elastic" two parameter driving force, $K_{max,tot}^{0.5}\Delta K_{tot}^{0.5}$, 7075-T6 Al alloy.

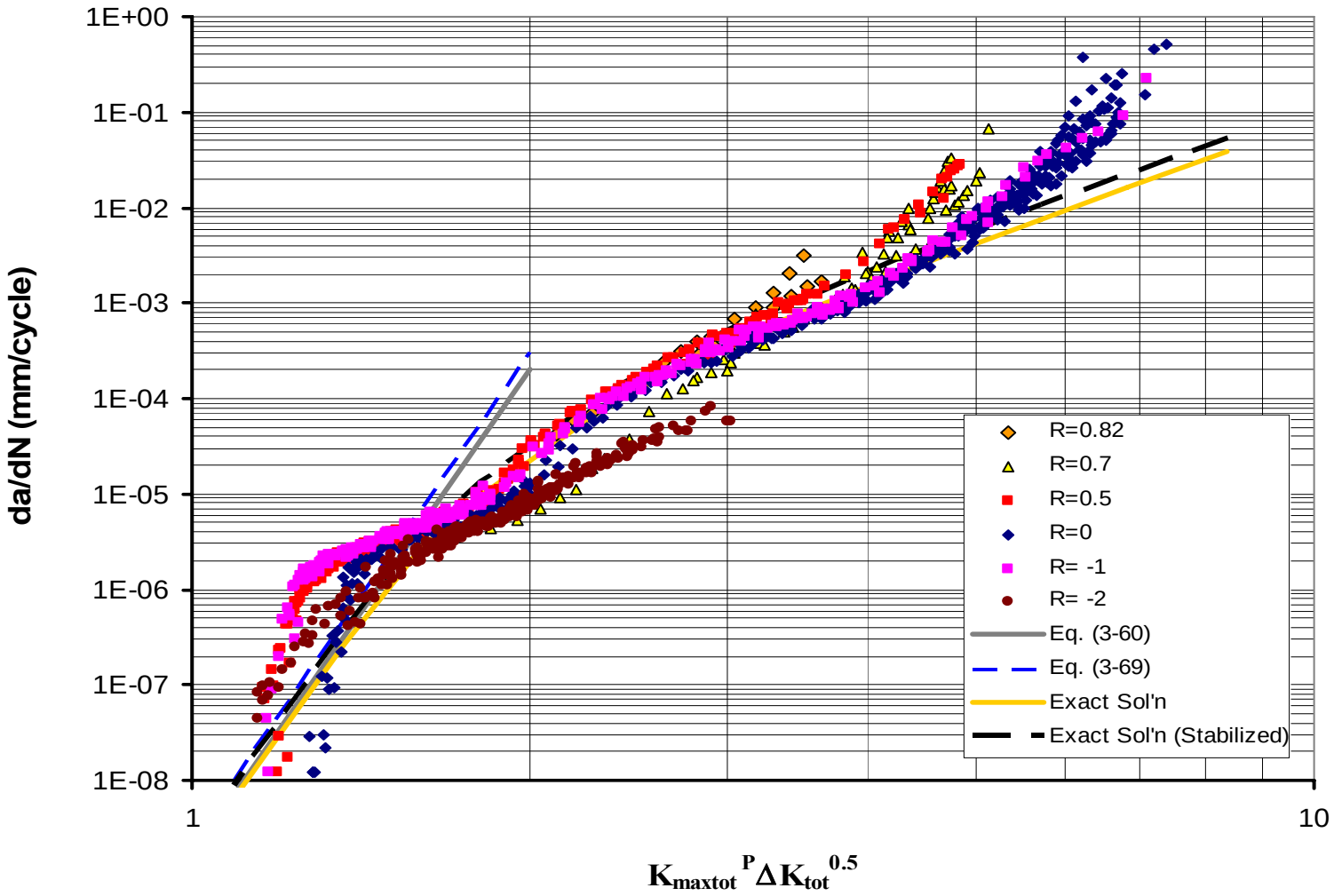

Figure 4-11: Fatigue crack growth as a function of the "mixed" two parameter driving force, $K_{max,tot}{}^{p}\Delta K_{tot}{}^{0.5}$, 7075-T6 Al alloy.

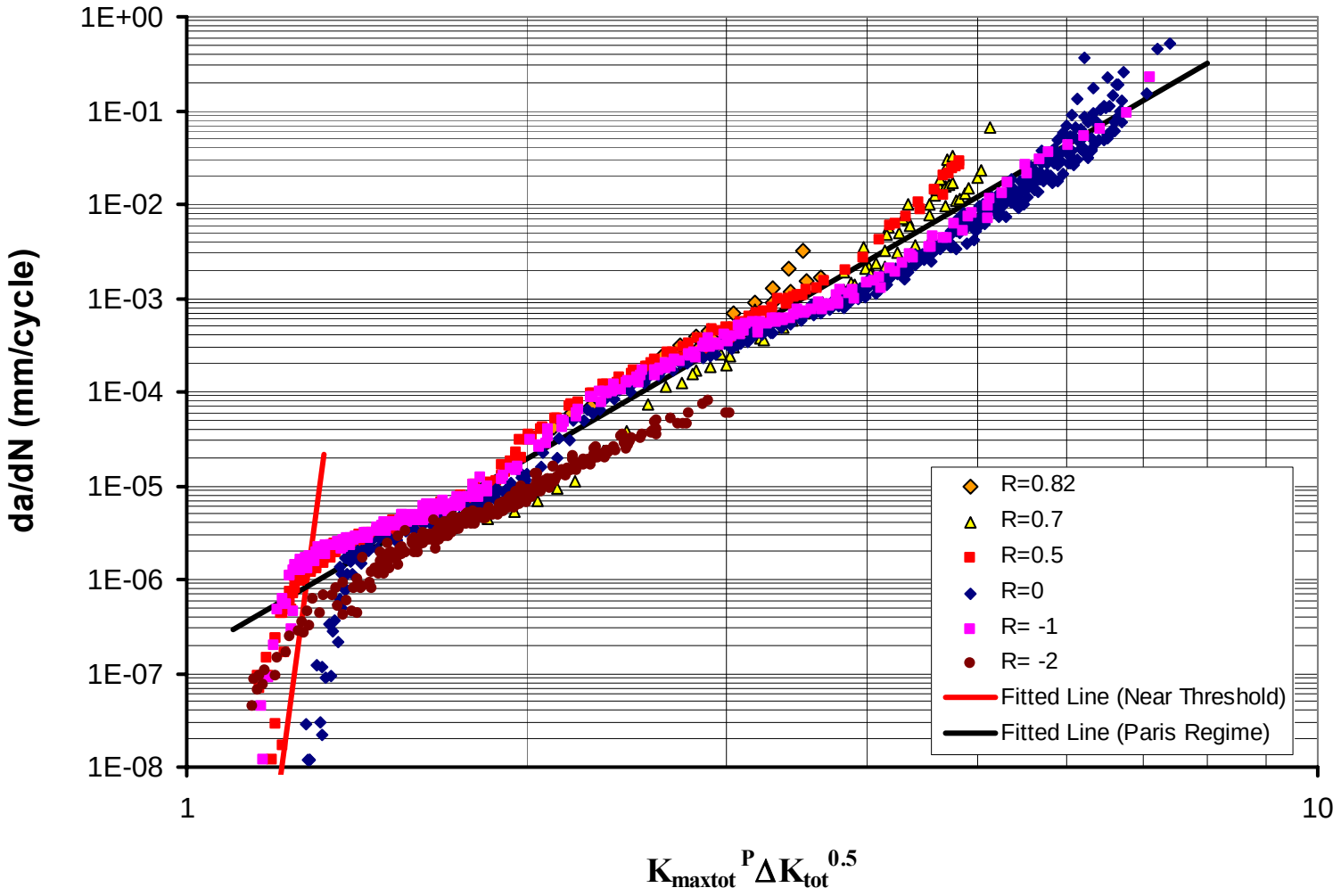

Figure 4-12: Two lines fitted into the experimental FCG as a function of the "mixed" two parameter driving force, $K_{max,tot}{}^{P}\Delta K_{tot}{}^{0.5}$, 7075-T6 Al alloy

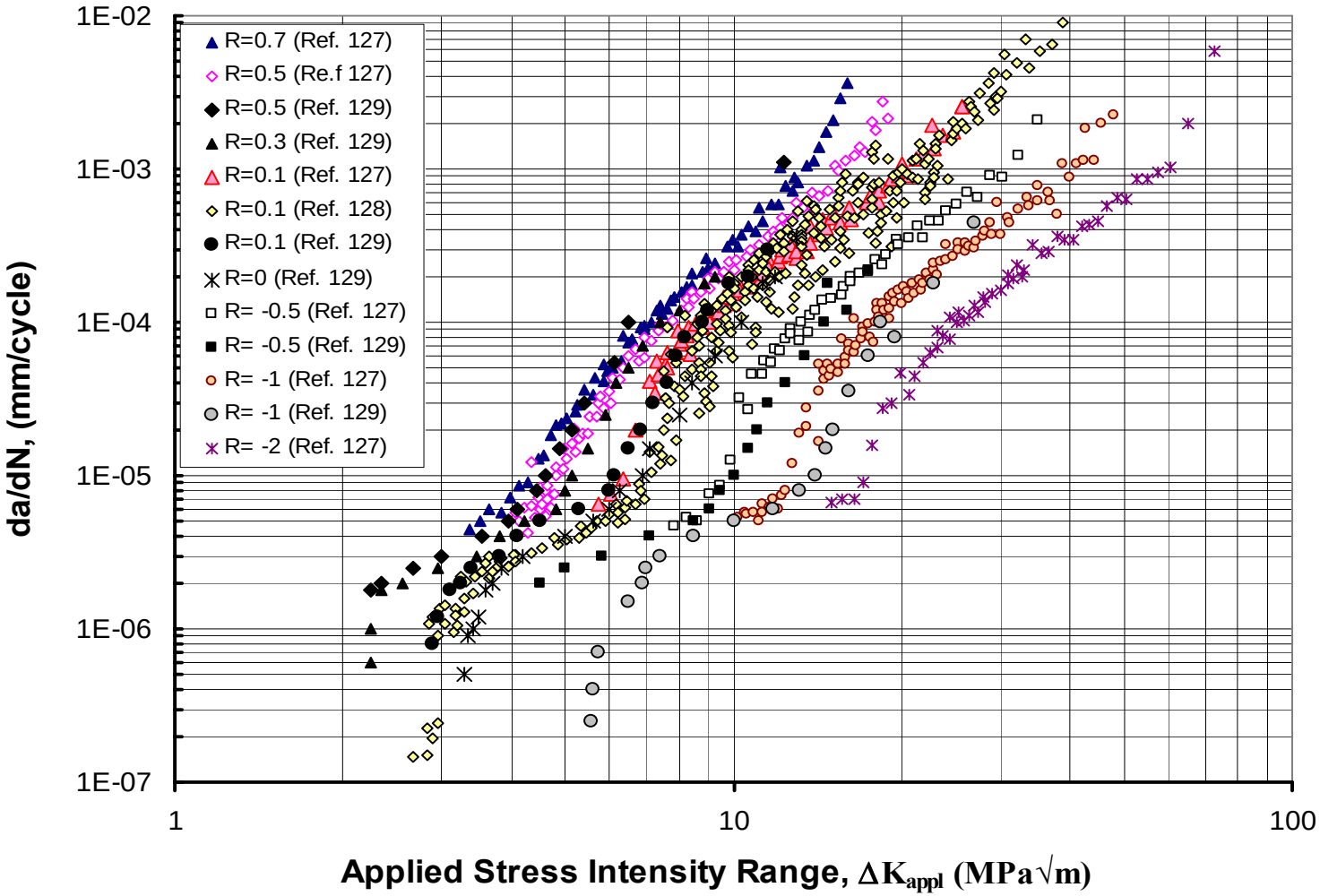

Figure 4-13: Fatigue crack growth data for 2024-T351 aluminum alloy obtained at stress ratios $-1 \leq R \leq 0.7$ [127-129].

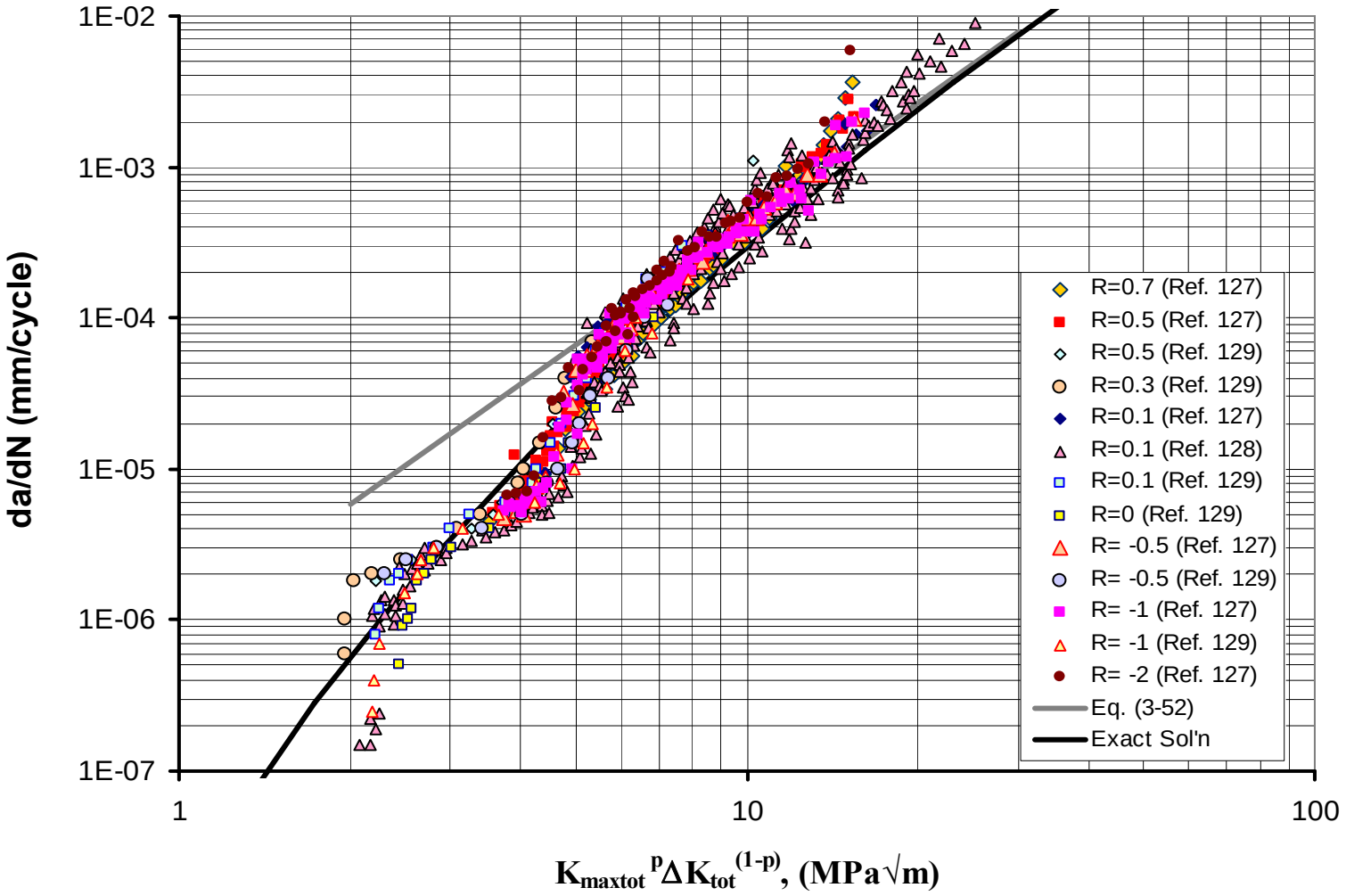

Figure 4-14: Fatigue crack growth as a function of the "plastic" two parameter driving force, $K_{max,tot}\,{}^{p}\Delta K_{tot}{}^{(1-p)}$, 2024-T351 Al alloy.

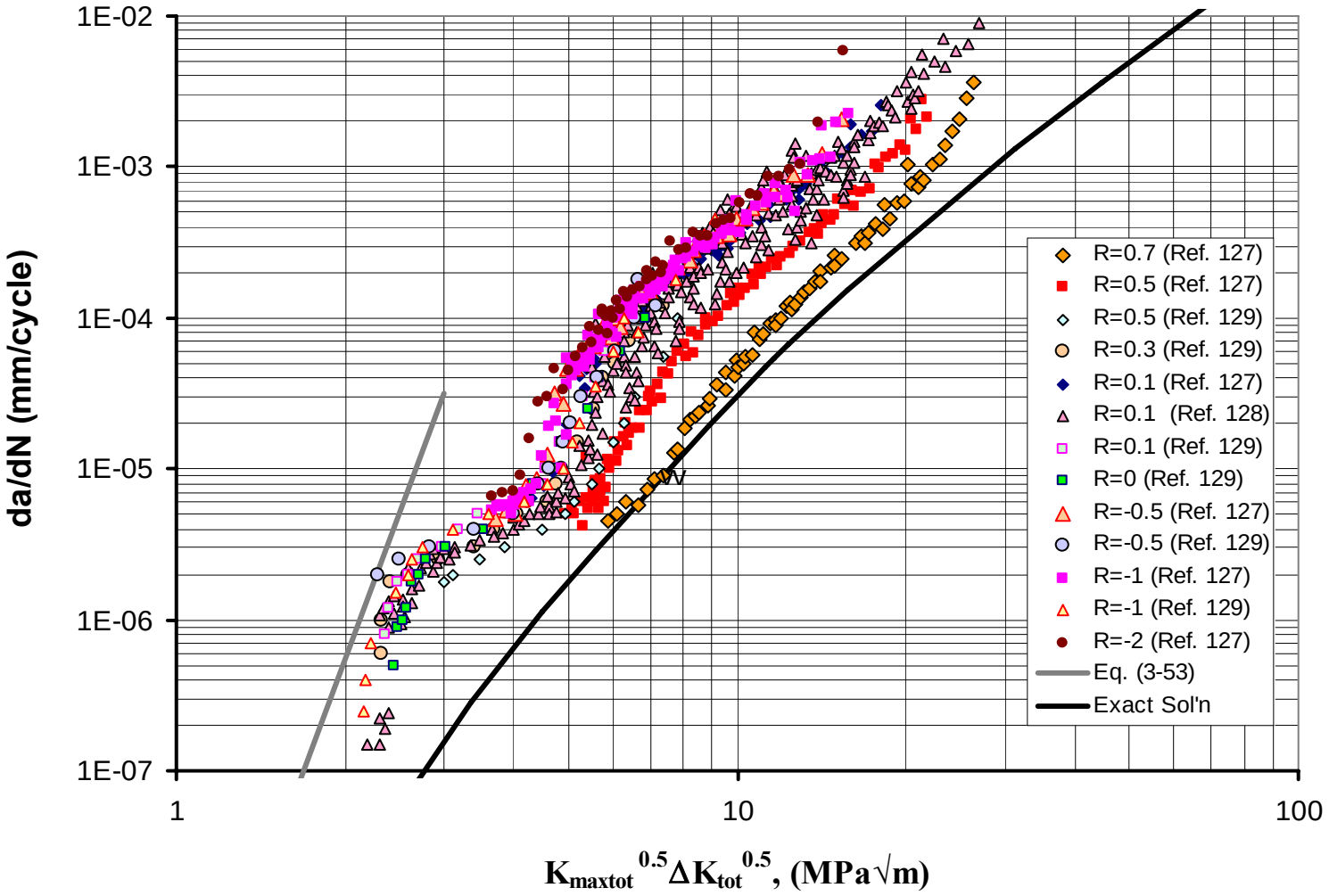

Figure 4-15: Fatigue crack growth as a function of the "elastic" two parameter driving force, $K_{max,tot}^{0.5}\Delta K_{tot}^{0.5}$, 2024-T351 Al alloy.

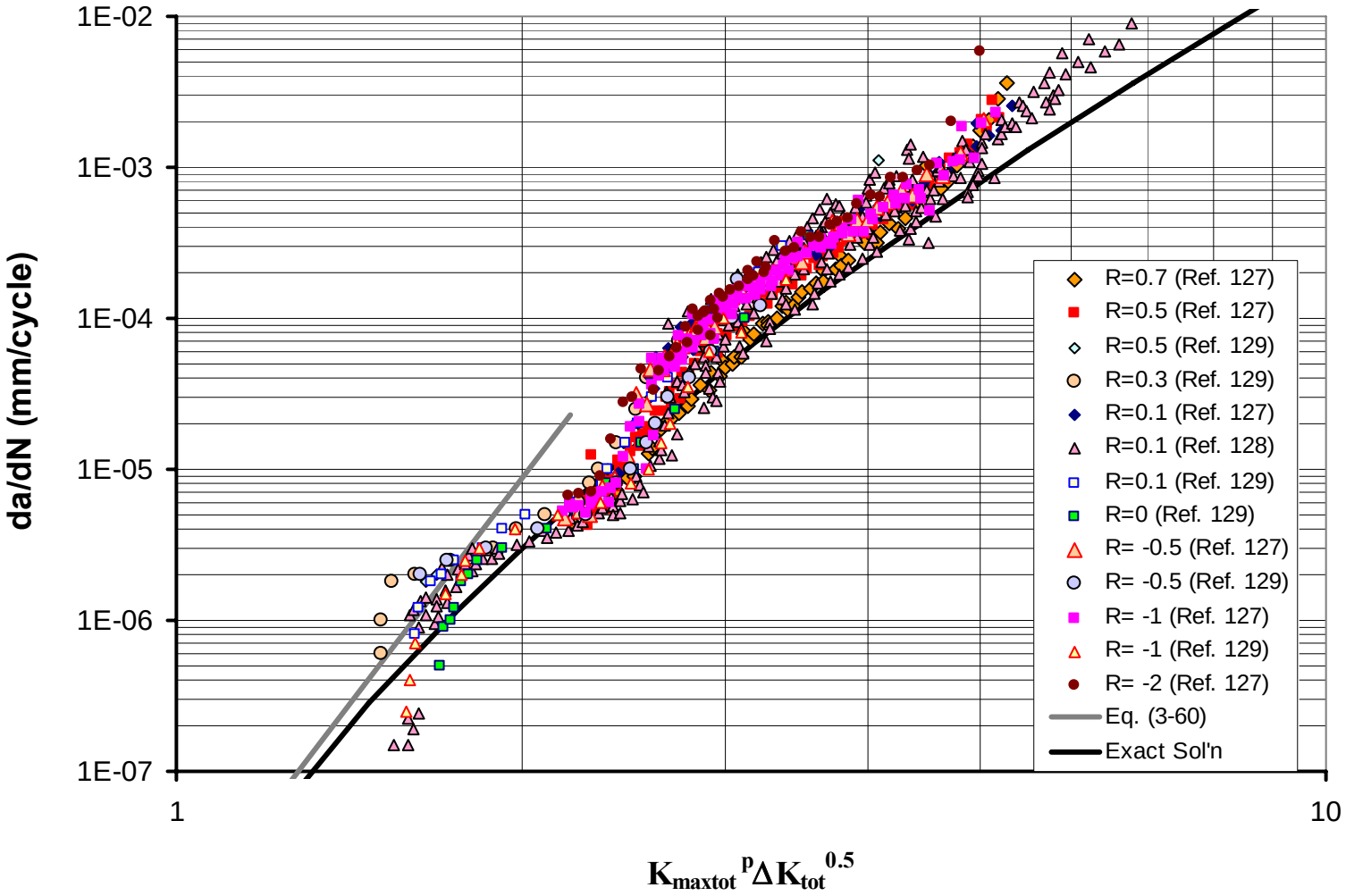

Figure 4-16: Fatigue crack growth as a function of the "mixed" two parameter driving force, $K_{max,tot}{}^{p}\Delta K_{tot}{}^{0.5}$, 2024-T351 Al alloy.

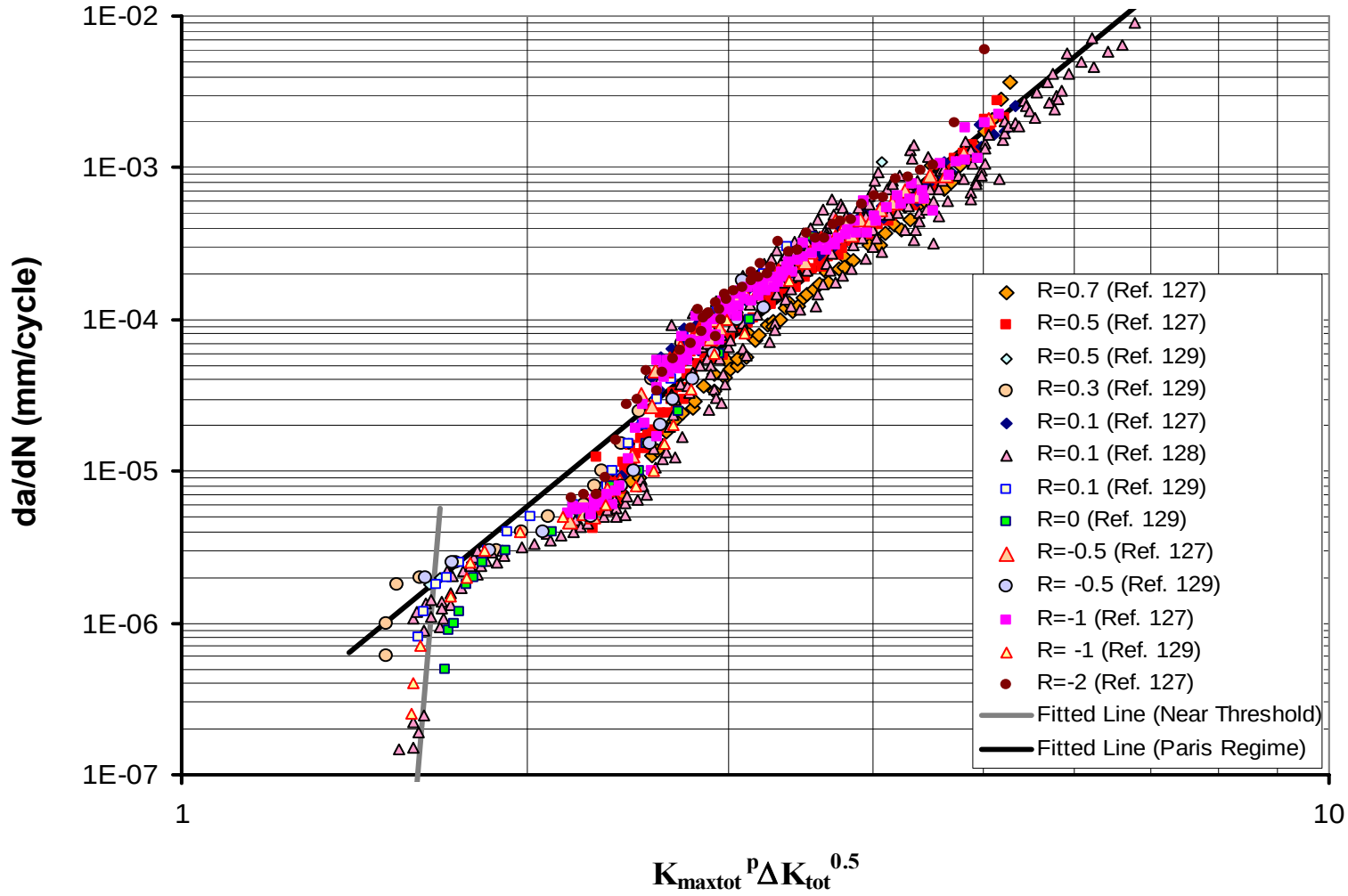

Figure 4-17: Two lines fitted into the experimental FCG as a function of the "mixed" two parameter driving force, $K_{max,tot}{}^{p}\Delta K_{tot}{}^{0.5}$, 2024-T351 Al alloy.

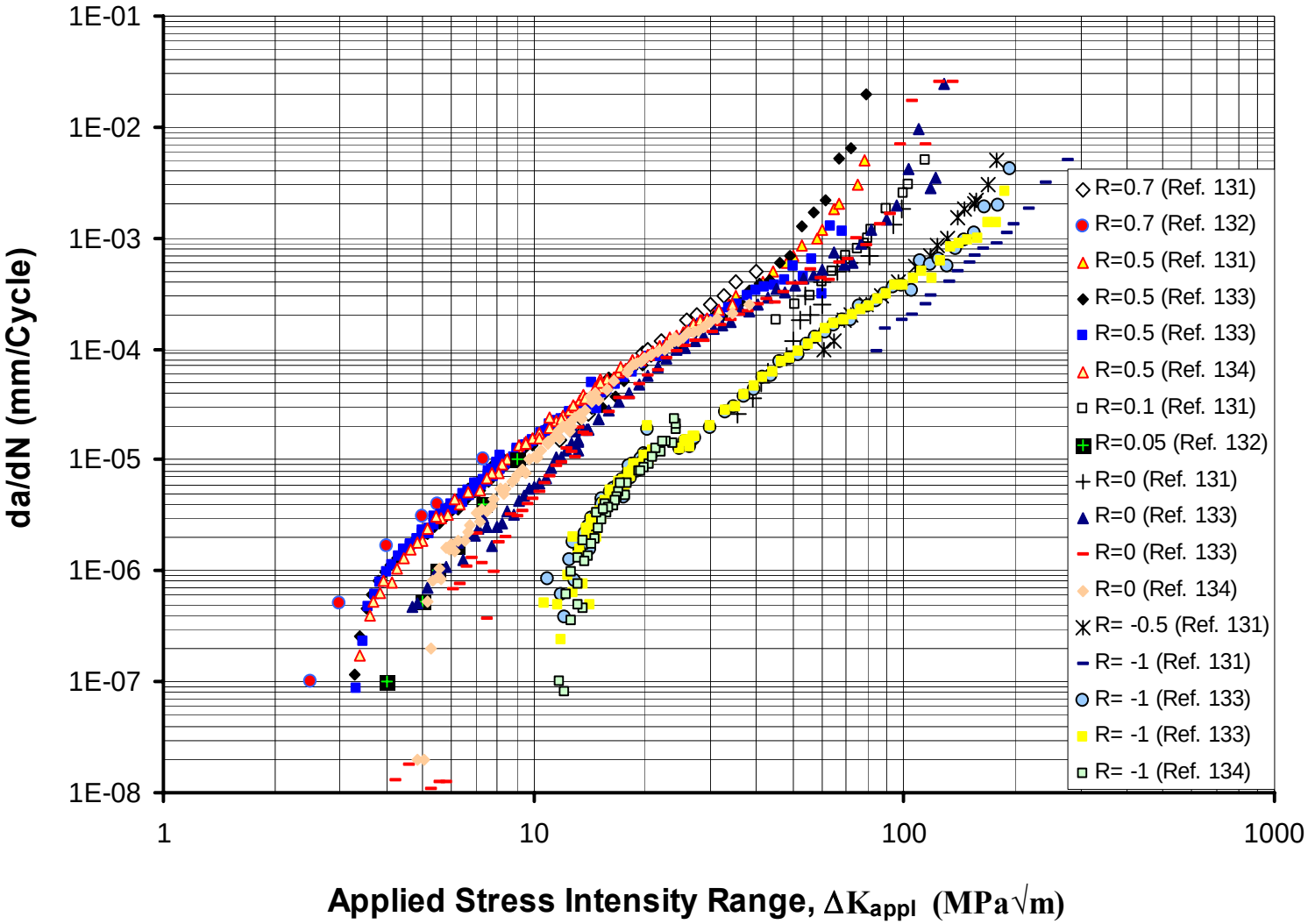

Figure 4-18: Fatigue crack growth data for 4340 steel obtained at stress ratios $-1 \leq R \leq 0.7$ [131-134].

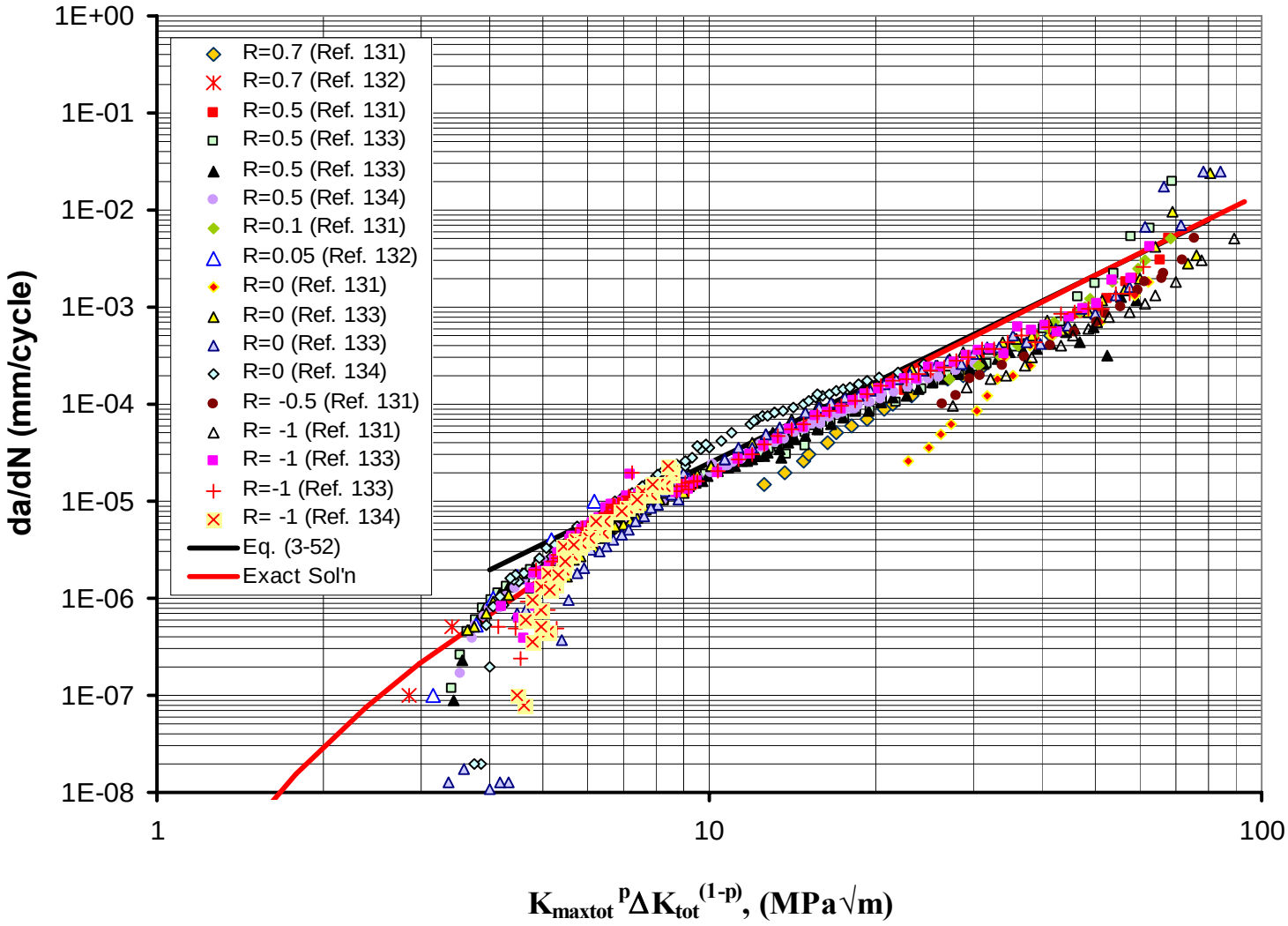

Figure 4-19: Fatigue crack growth as a function of the "plastic" two parameter driving force, $K_{max,tot}{}^{p}\Delta K_{tot}{}^{(1-p)}$, 4340 steel.

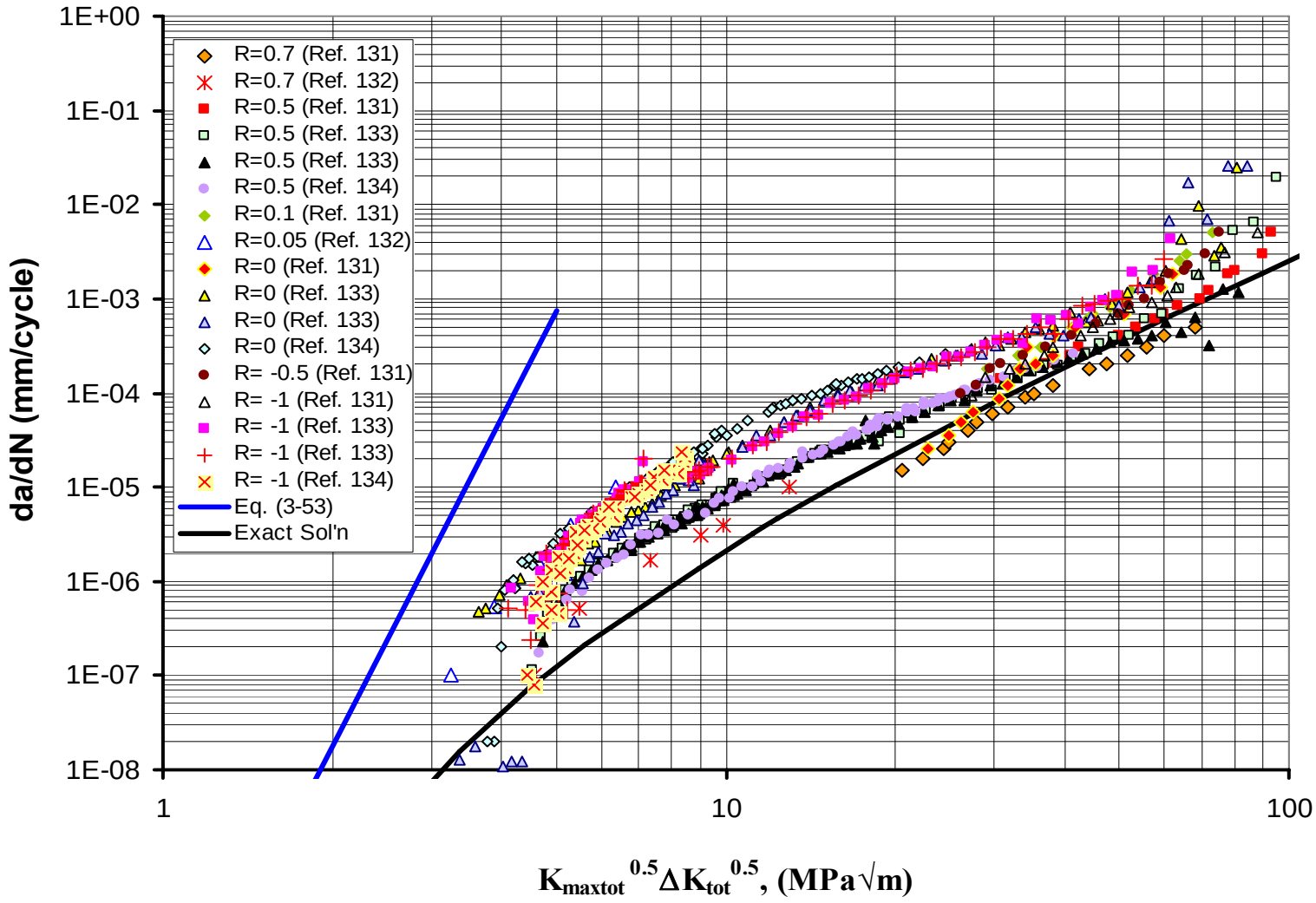

Figure 4-20: Fatigue crack growth as a function of the "elastic" two parameter driving force, $K_{max,tot}^{0.5}\Delta K_{tot}^{0.5}$, 4340 steel.

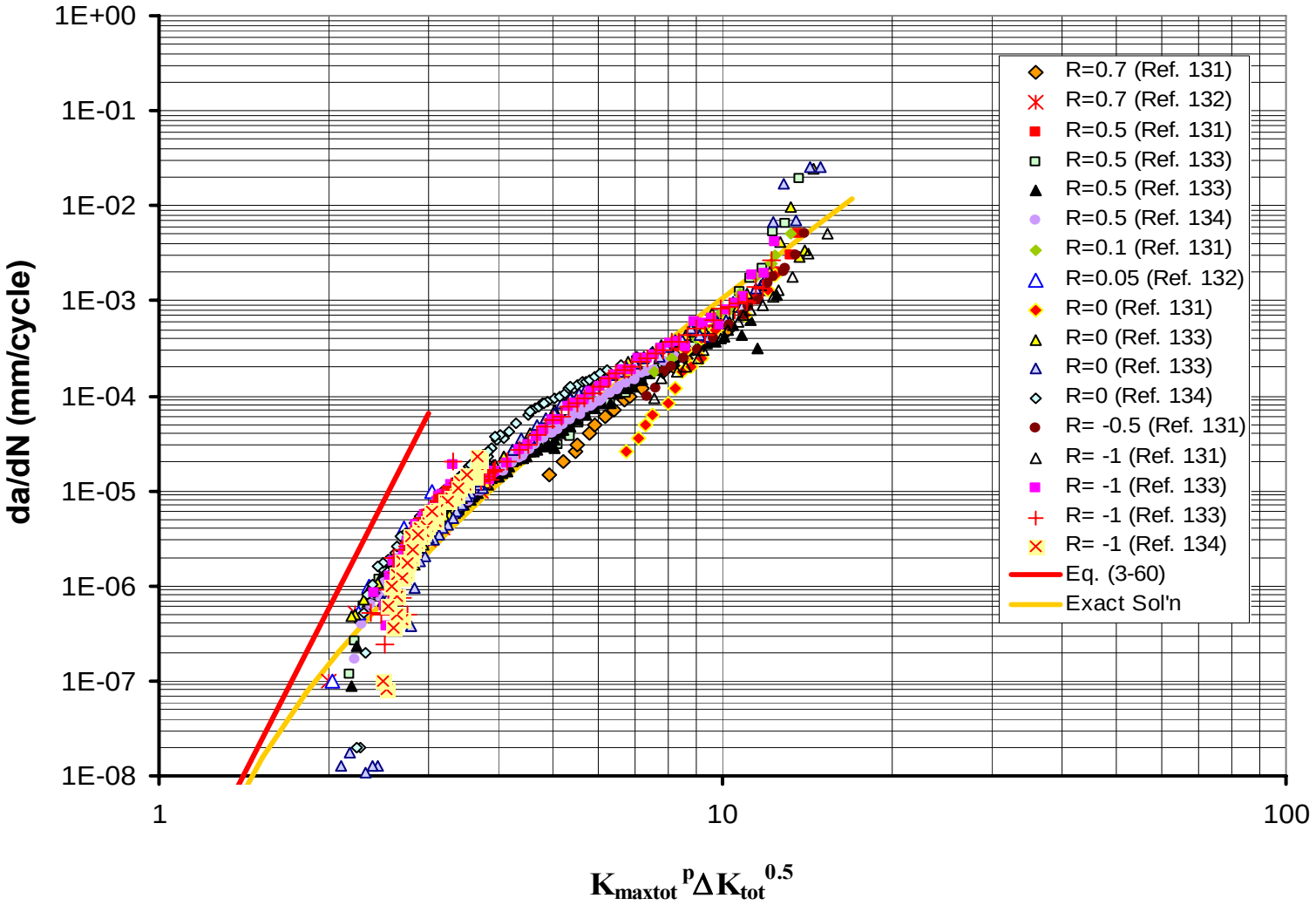

Figure 4-21: Fatigue crack growth as a function of the "mixed" two parameter driving force, $K_{max,tot}{}^{p}\Delta K_{tot}{}^{0.5}$, 4340 steel.

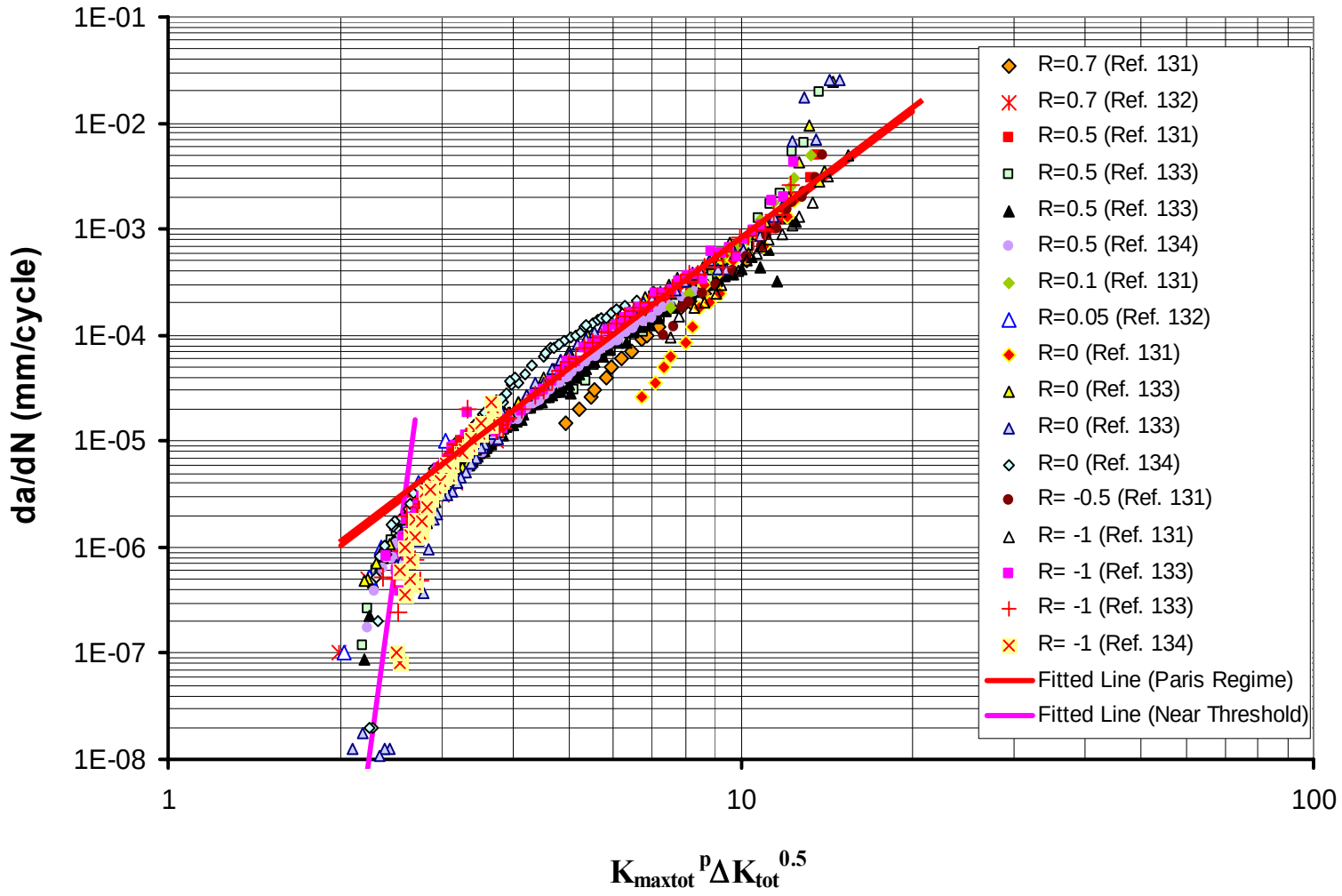

Figure 4-22: Two lines fitted into the experimental FCG as a function of the "mixed" two parameter driving force, $K_{max,tot}{}^{p}\Delta K_{tot}{}^{0.5}$, 4340 steel.

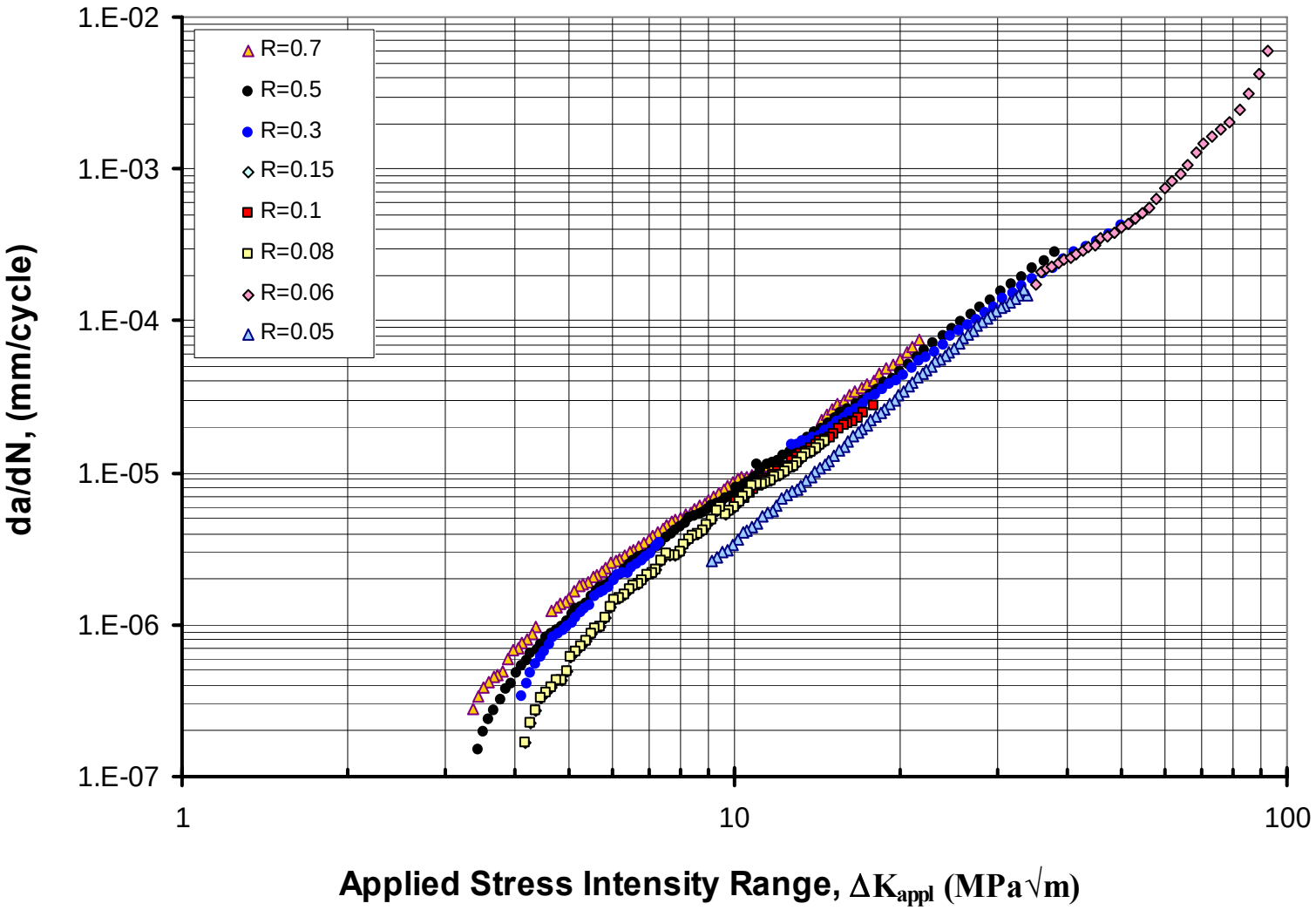

Figure 4-23: Fatigue crack growth data for 4140 steel obtained at stress ratios $-1 \leq R \leq 0.7$ [72].

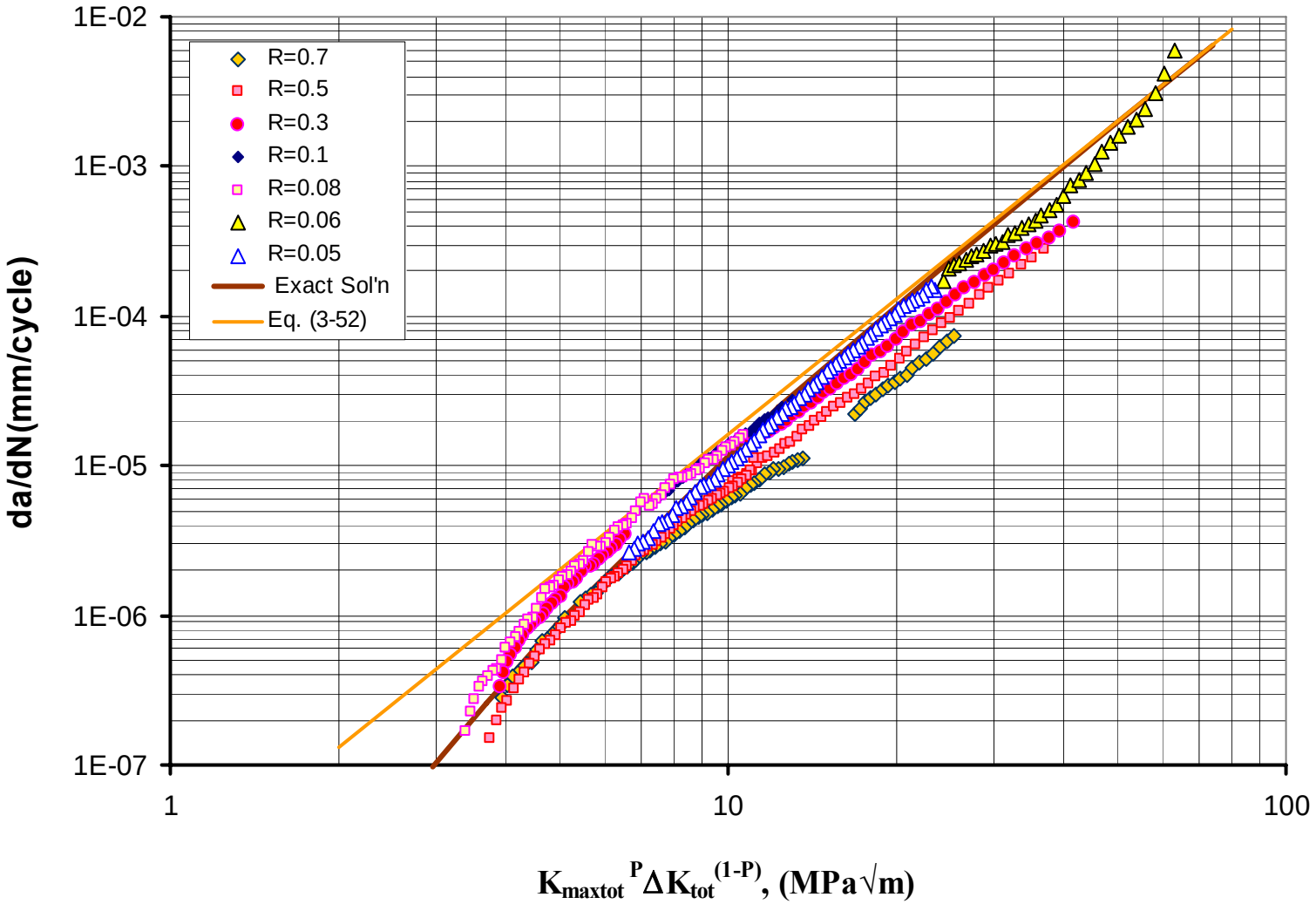

Figure 4-24: Fatigue crack growth as a function of the "plastic" two parameter driving force, $K_{max,tot}{}^{P}\Delta K_{tot}{}^{(1-p)}$, 4140 steel.

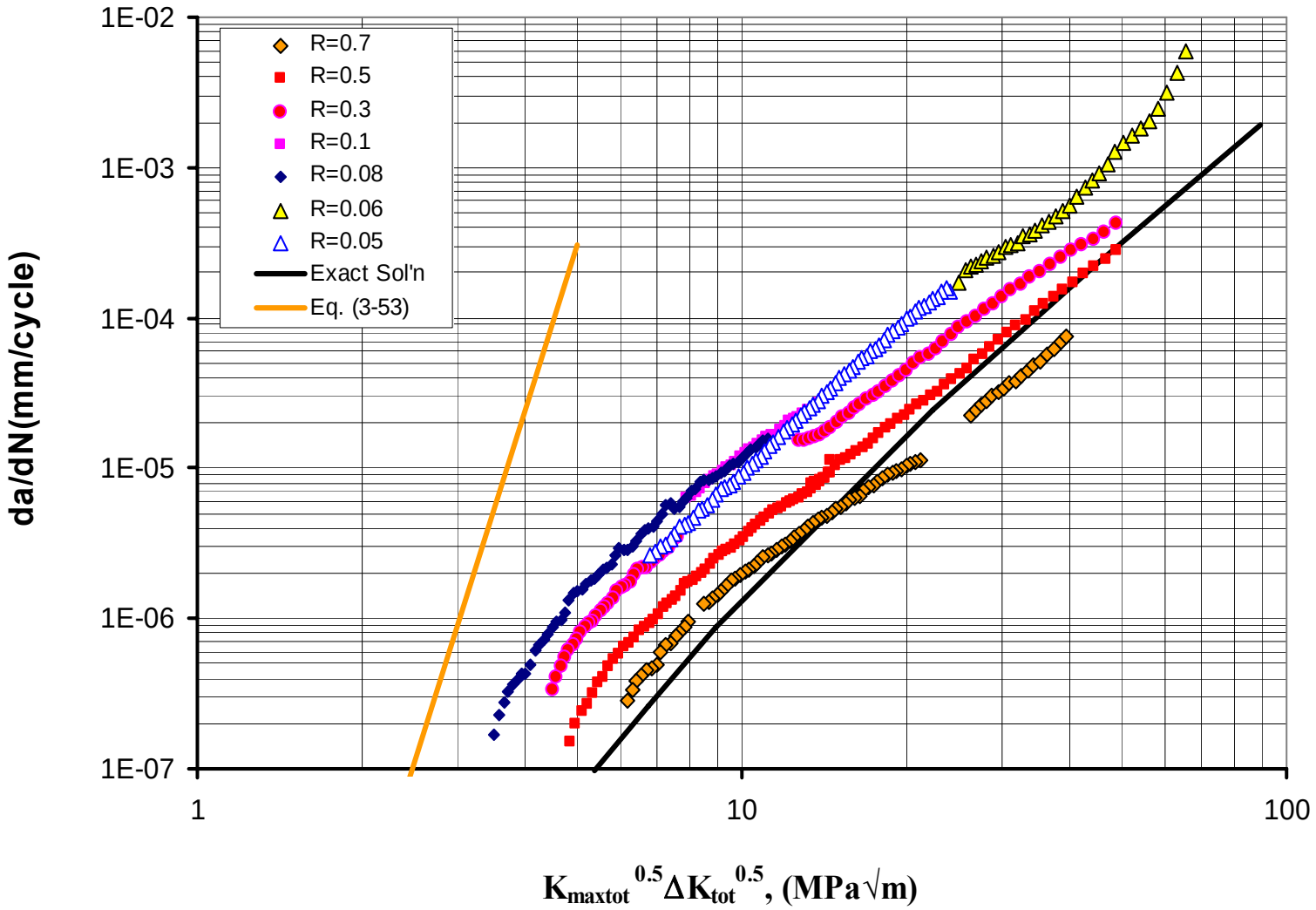

Figure 4-25: Fatigue crack growth as a function of the "elastic" two parameter driving force, $K_{max,tot}^{0.5}\Delta K_{tot}^{0.5}$, 4140 steel.

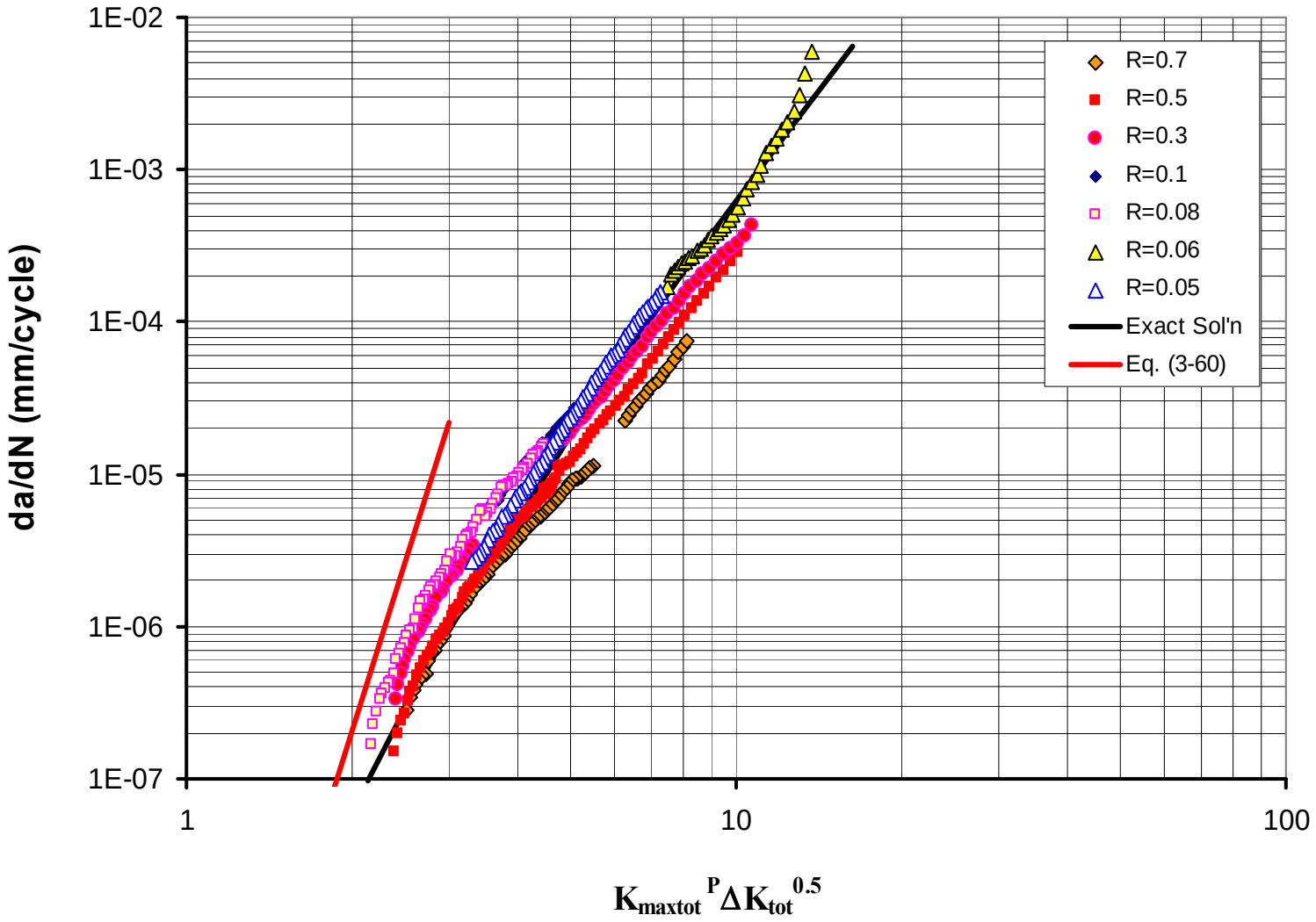

Figure 4-26: Fatigue crack growth as a function of the "mixed" two parameter driving force, $K_{max,tot}{}^{p}\Delta K_{tot}{}^{0.5}$, 4140 steel.

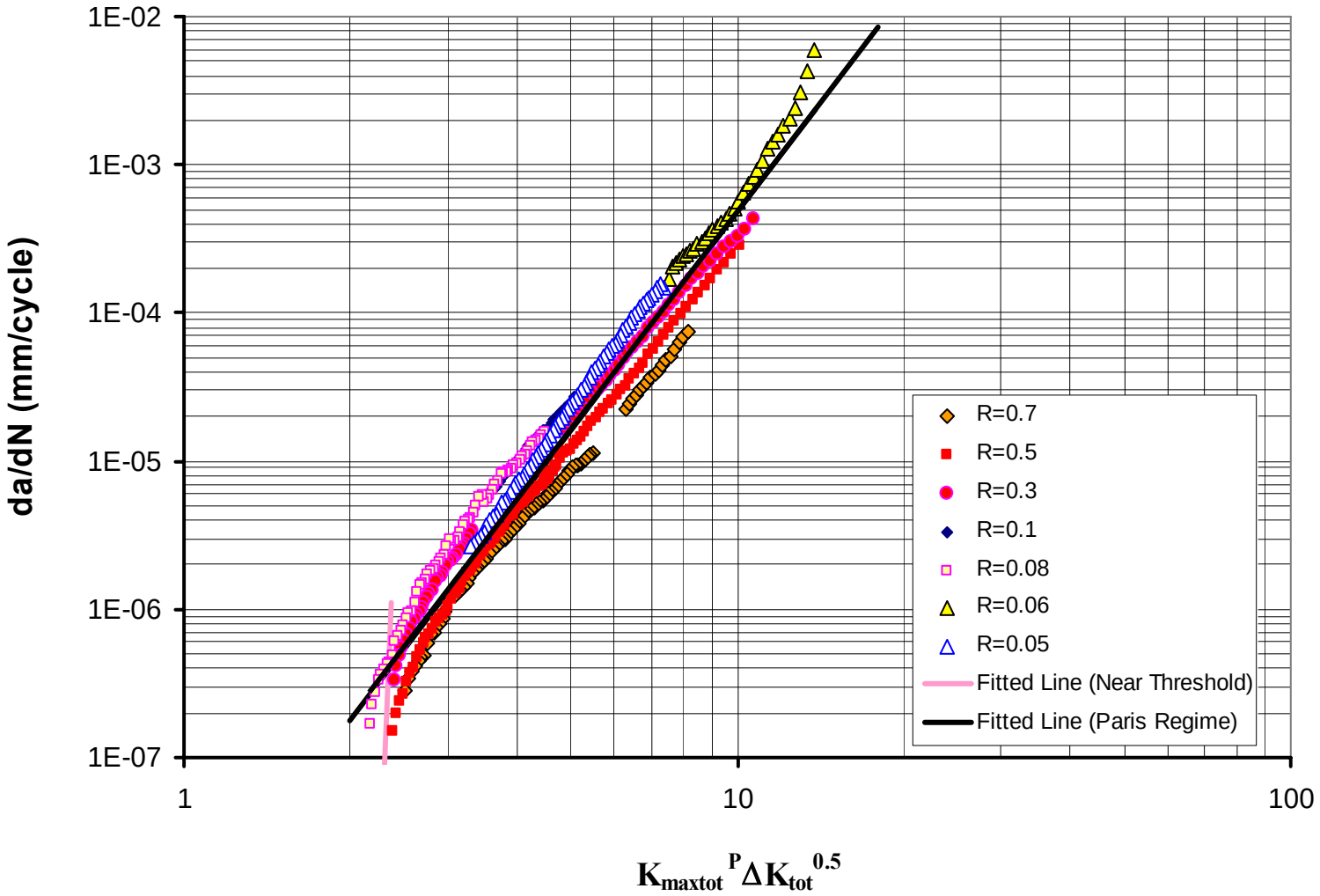

Figure 4-27: Two lines fitted into the experimental FCG as a function of the "mixed" two parameter driving force, $K_{max,tot}{}^{p}\Delta K_{tot}{}^{0.5}$, 4140 steel.

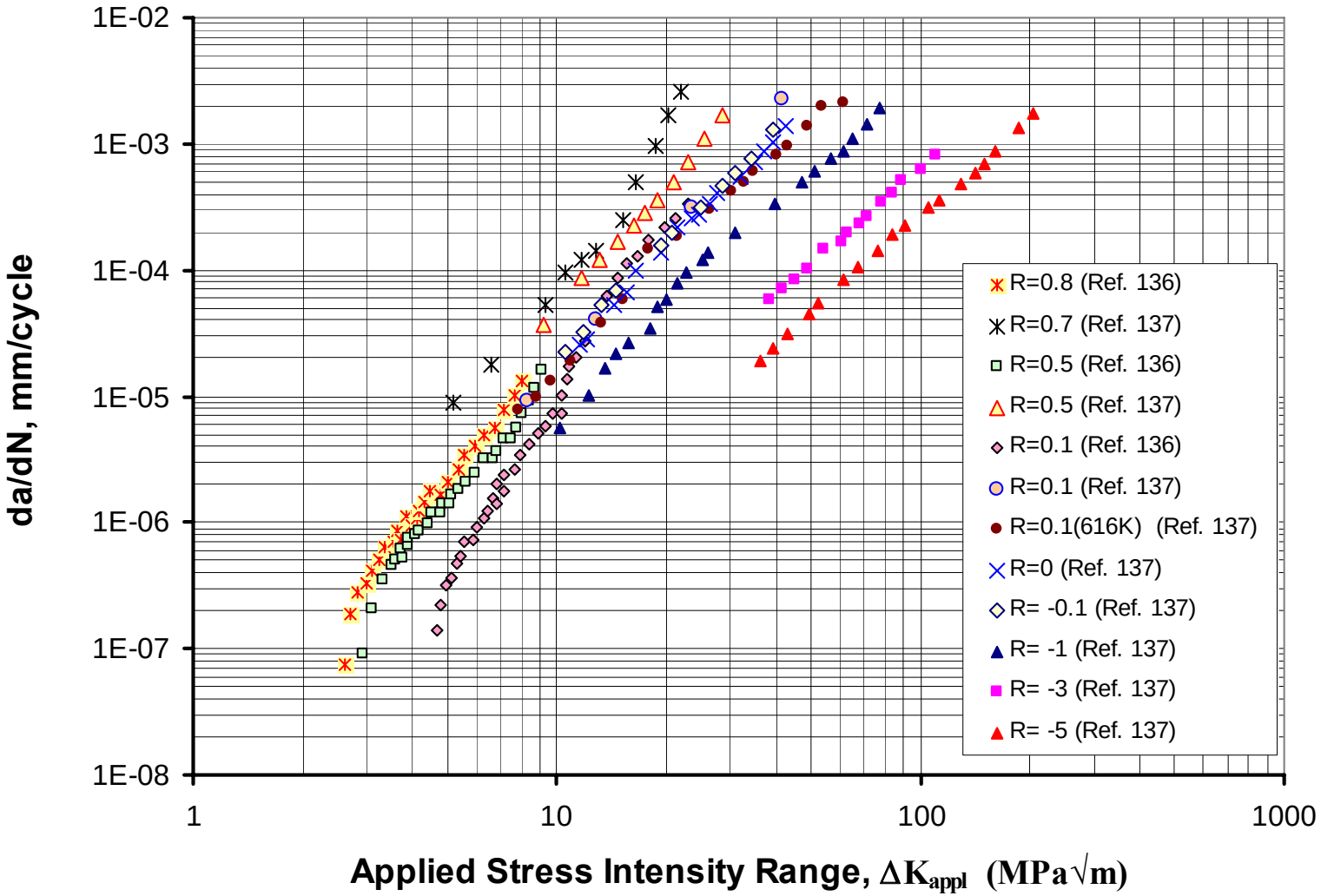

Figure 4-28: Fatigue crack growth data for Ti-6Al-4V alloy obtained at stress ratios $-5 \leq R \leq 0.8$ [136, 137].

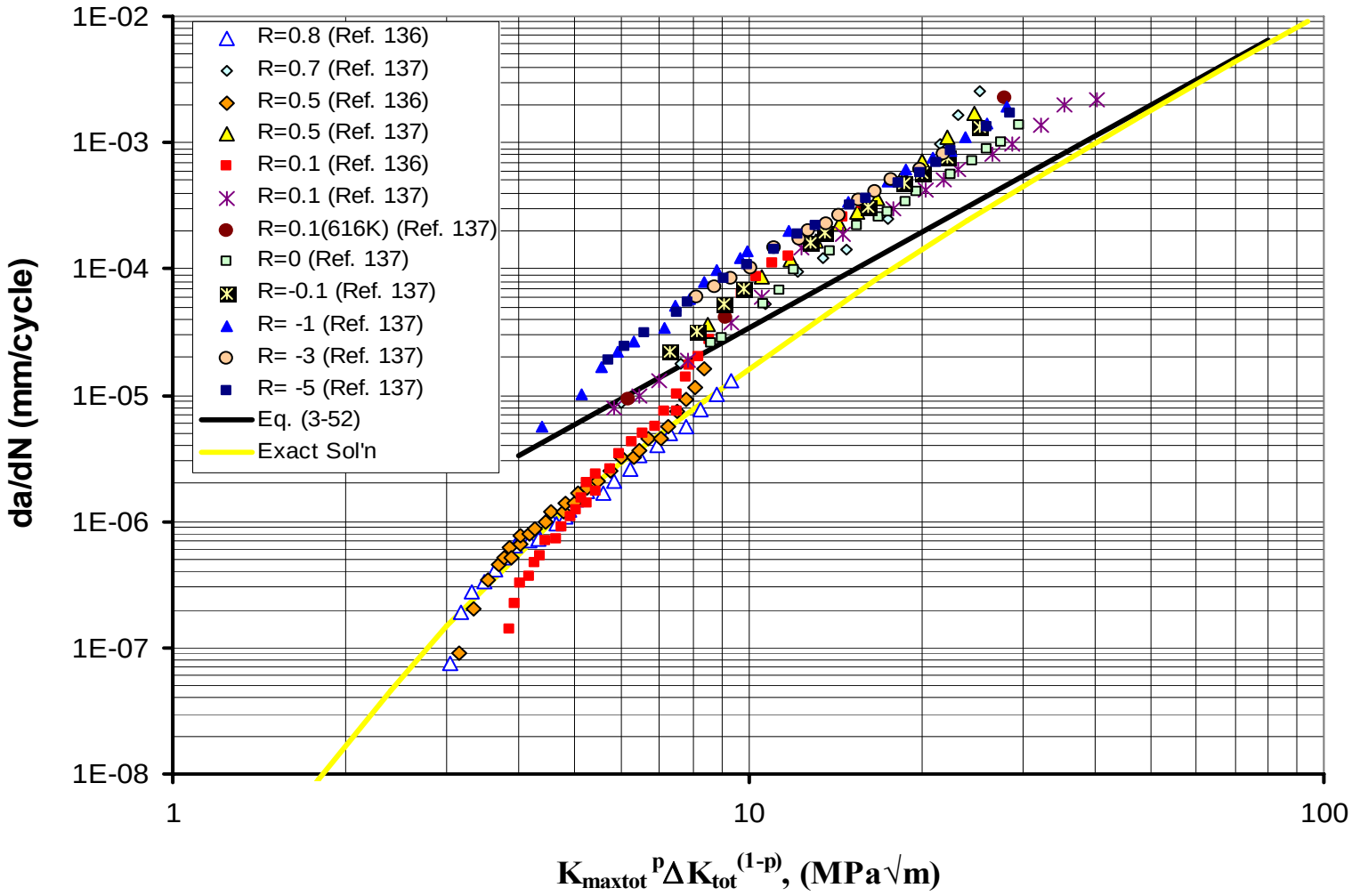

Figure 4-29: Fatigue crack growth as a function of the "plastic" two parameter driving force, $K_{max,tot}{}^{p}\Delta K_{tot}{}^{(1-p)}$, Ti-6Al-4V alloy.

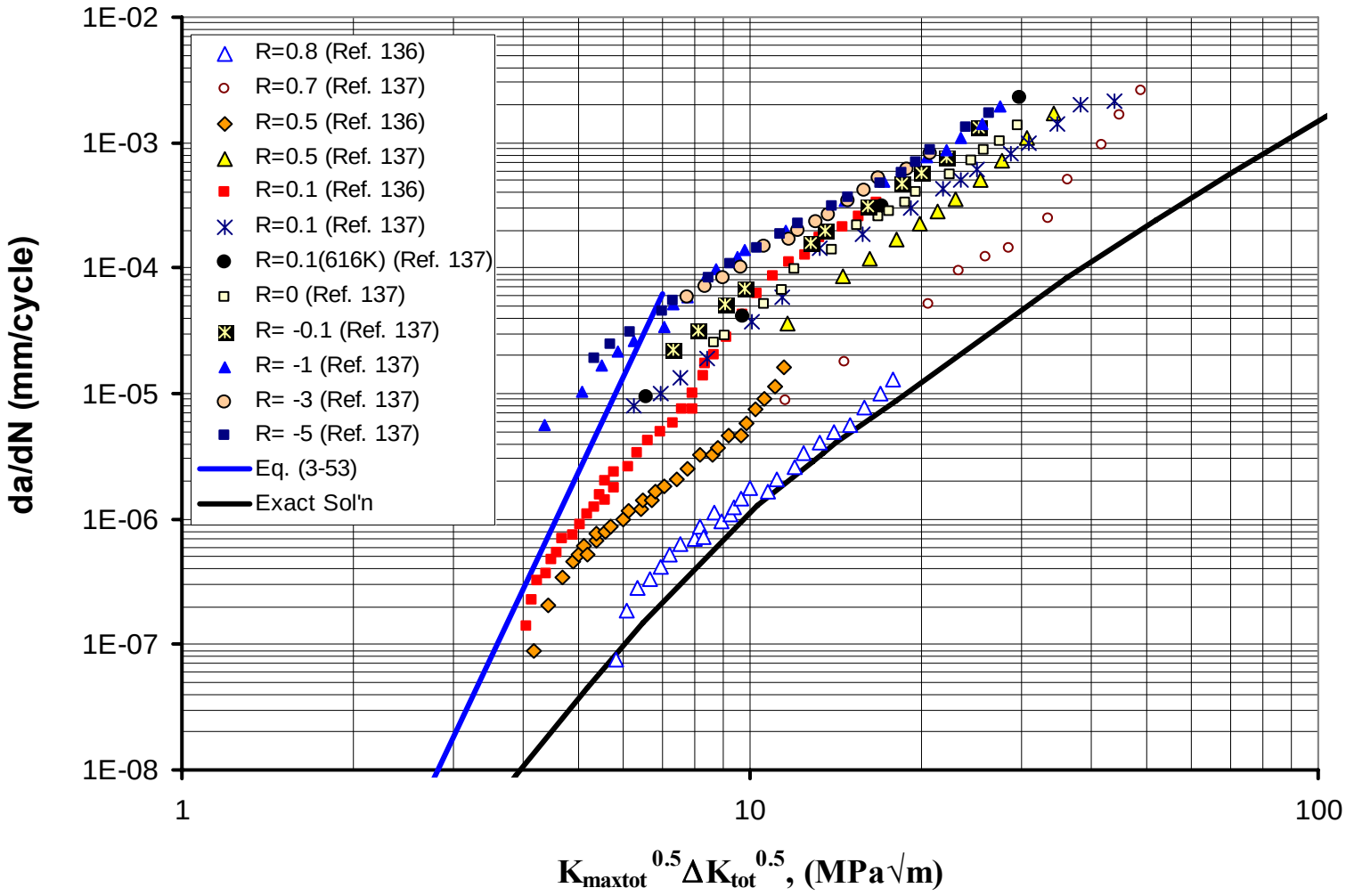

Figure 4-30: Fatigue crack growth as a function of the "elastic" two parameter driving force, $K_{max,tot}^{0.5}\Delta K_{tot}^{0.5}$, Ti-6Al-4V alloy.

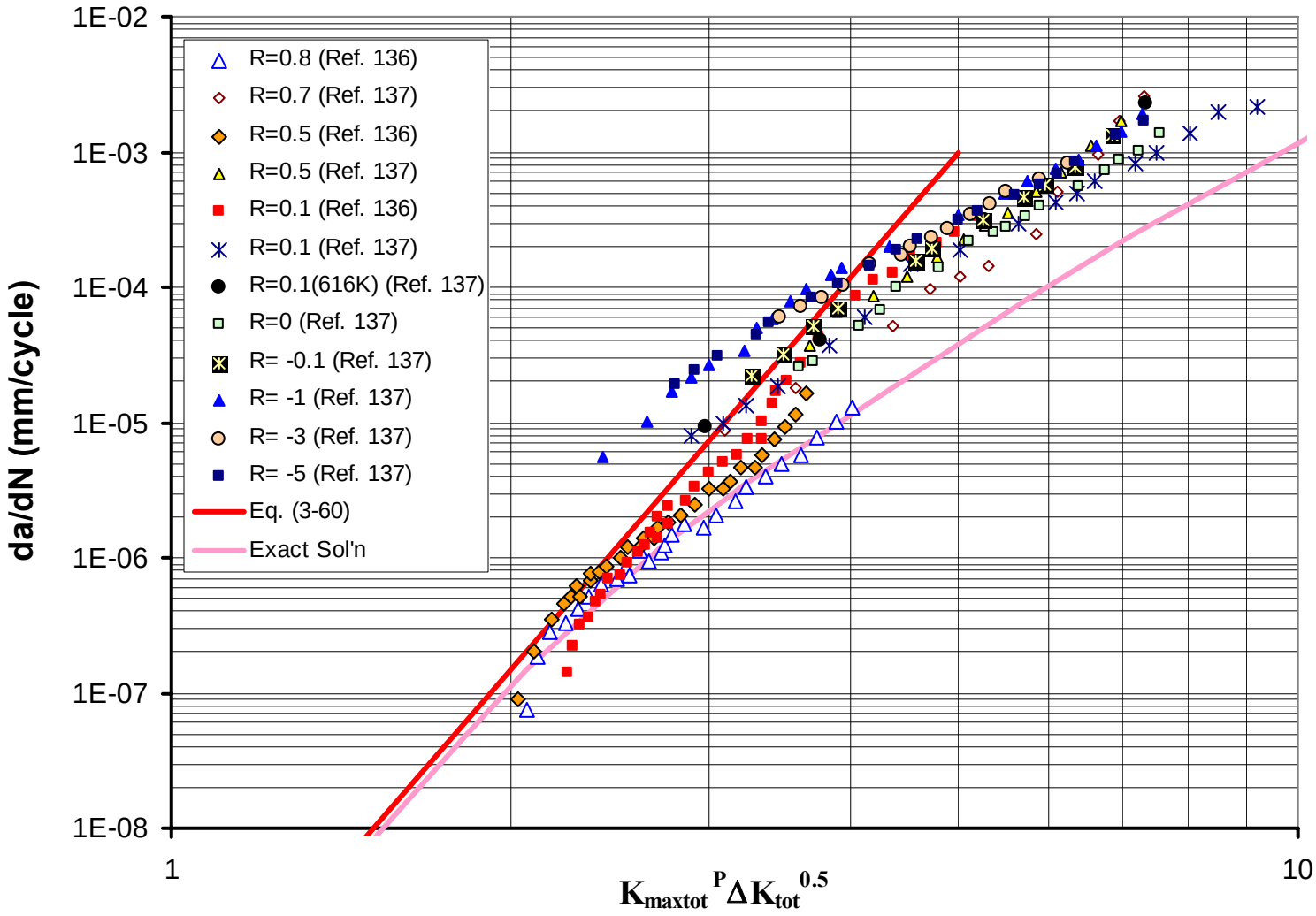

Figure 4-31: Fatigue crack growth as a function of the "mixed" two-parameter driving force, $K_{max,tot}{}^{P}\Delta K_{tot}{}^{0.5}$, Ti-6Al-4V alloy.

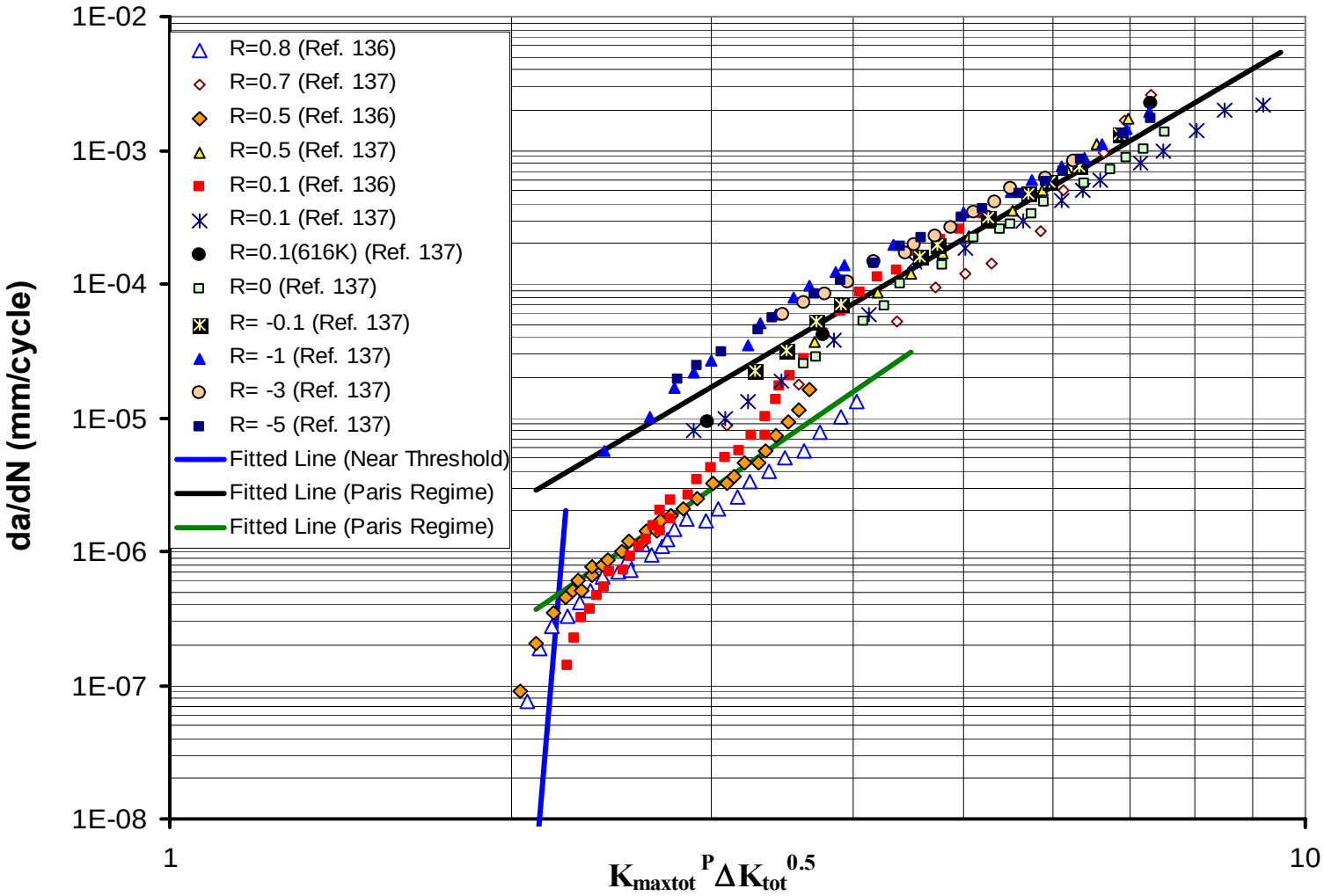

Figure 4-32: Two lines fitted into the experimental FCG as a function of the "mixed" two parameter driving force, $K_{max,tot}{}^{P}\Delta K_{tot}{}^{0.5}$, Ti-6Al-4V alloy.

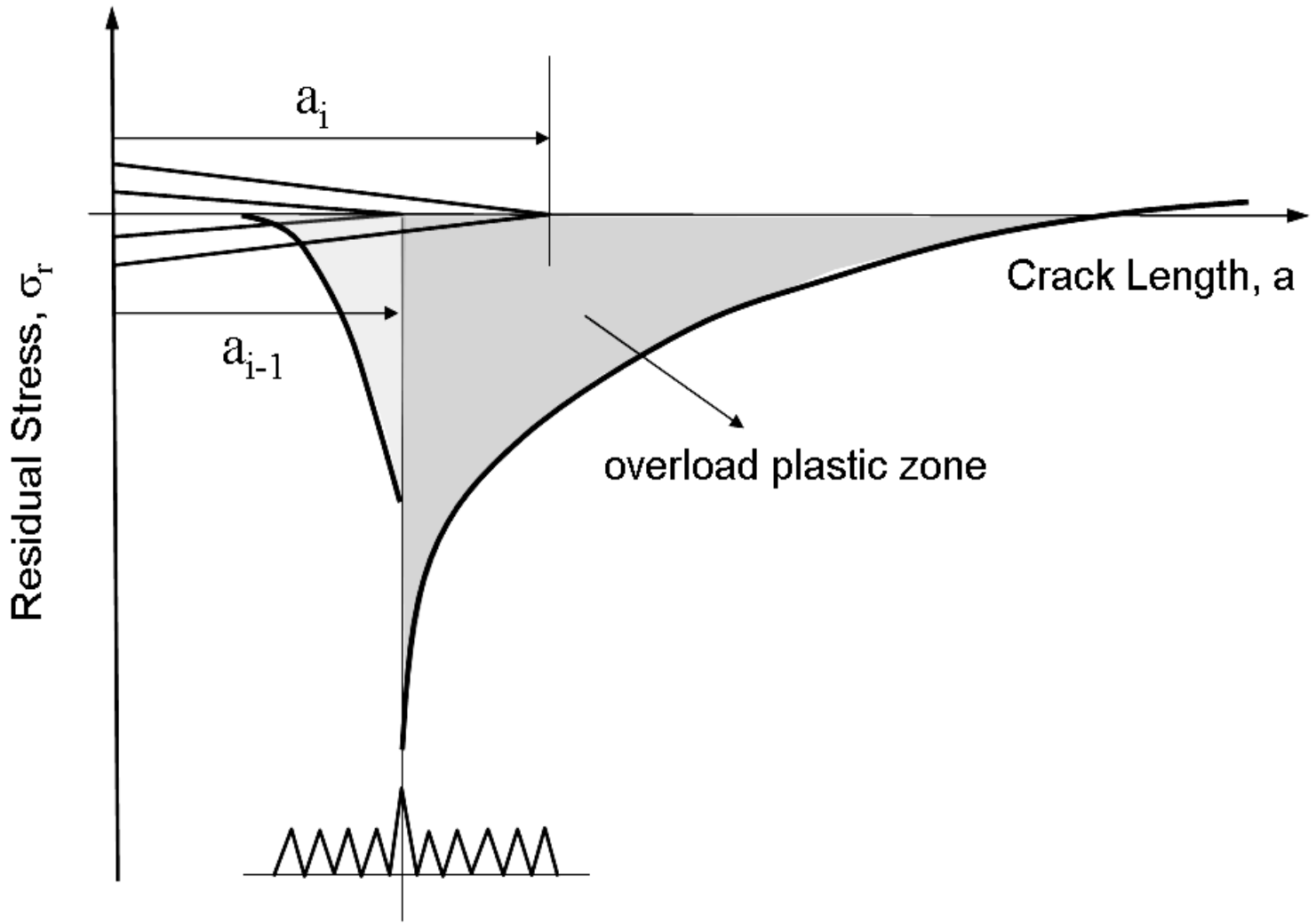

Figure 4-33: Schematic of residual stress distribution used for the calculation of residual stress intensity factors after an overload.

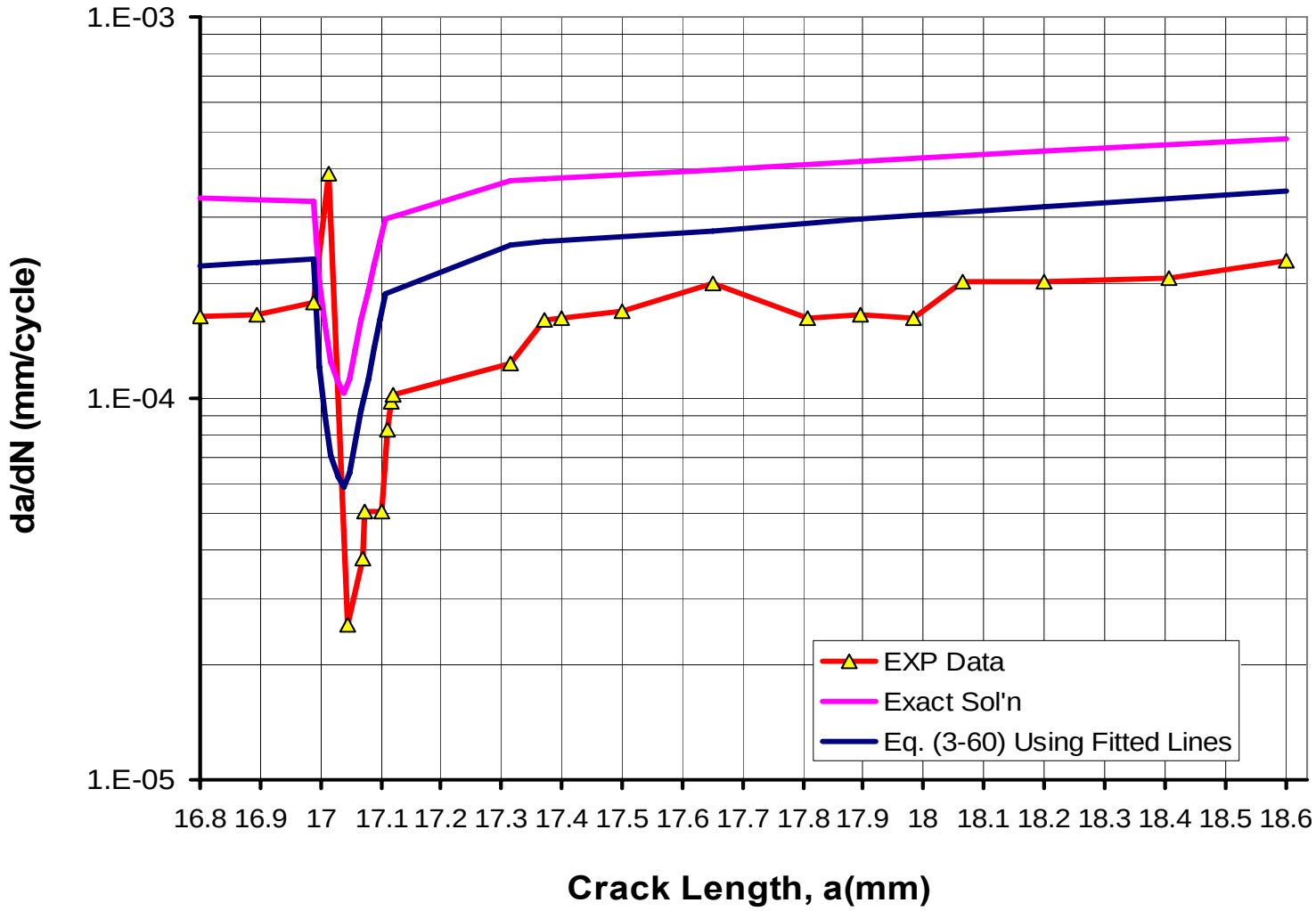

Figure 4-34: Experimental and predicted fatigue crack growth rates after 50 percent overload (7075-T6 Al alloy, ΔK_{BL}=11.4 MPa$\sqrt{m}$).

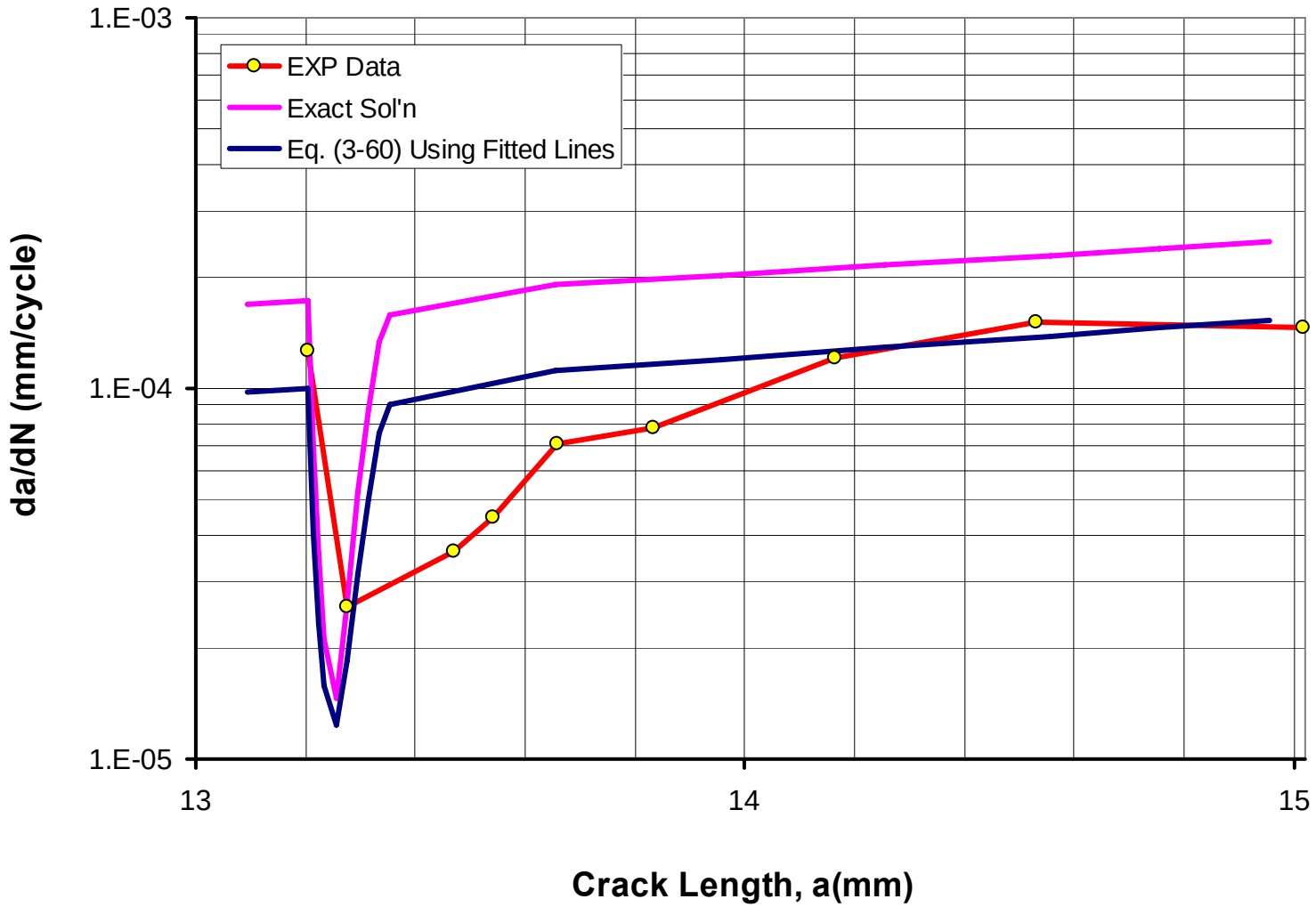

Figure 4-35: Experimental and predicted fatigue crack growth rates after 80 percent overload (7075-T6 Al alloy, ΔK_{BL}=8.955 MPa$\sqrt{m}$).

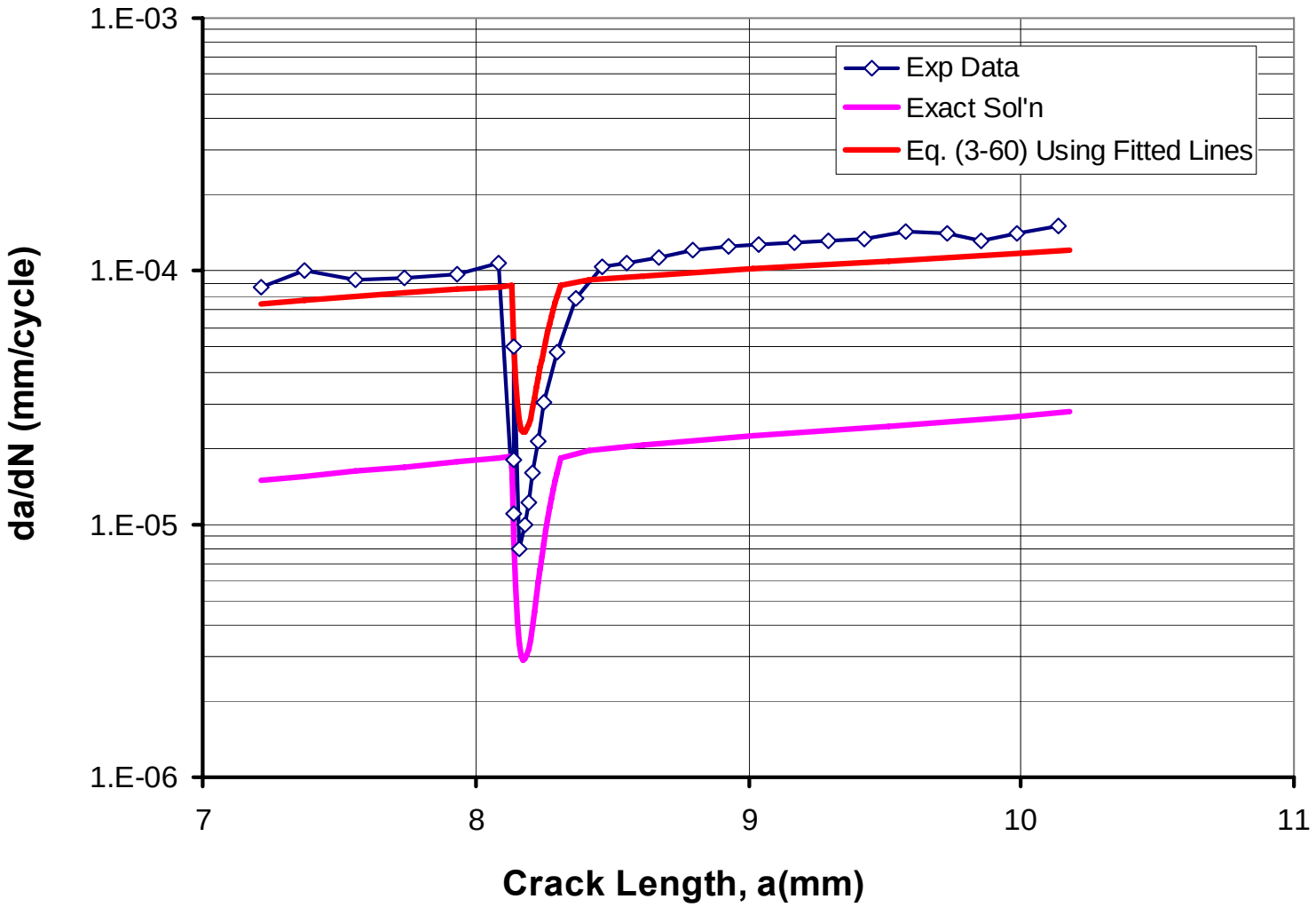

Figure 4-36: Experimental and predicted fatigue crack growth rates after 100 percent overload (Ti-6Al-4V alloy, ΔK_{BL}=16.33 MPa$\sqrt{m}$).

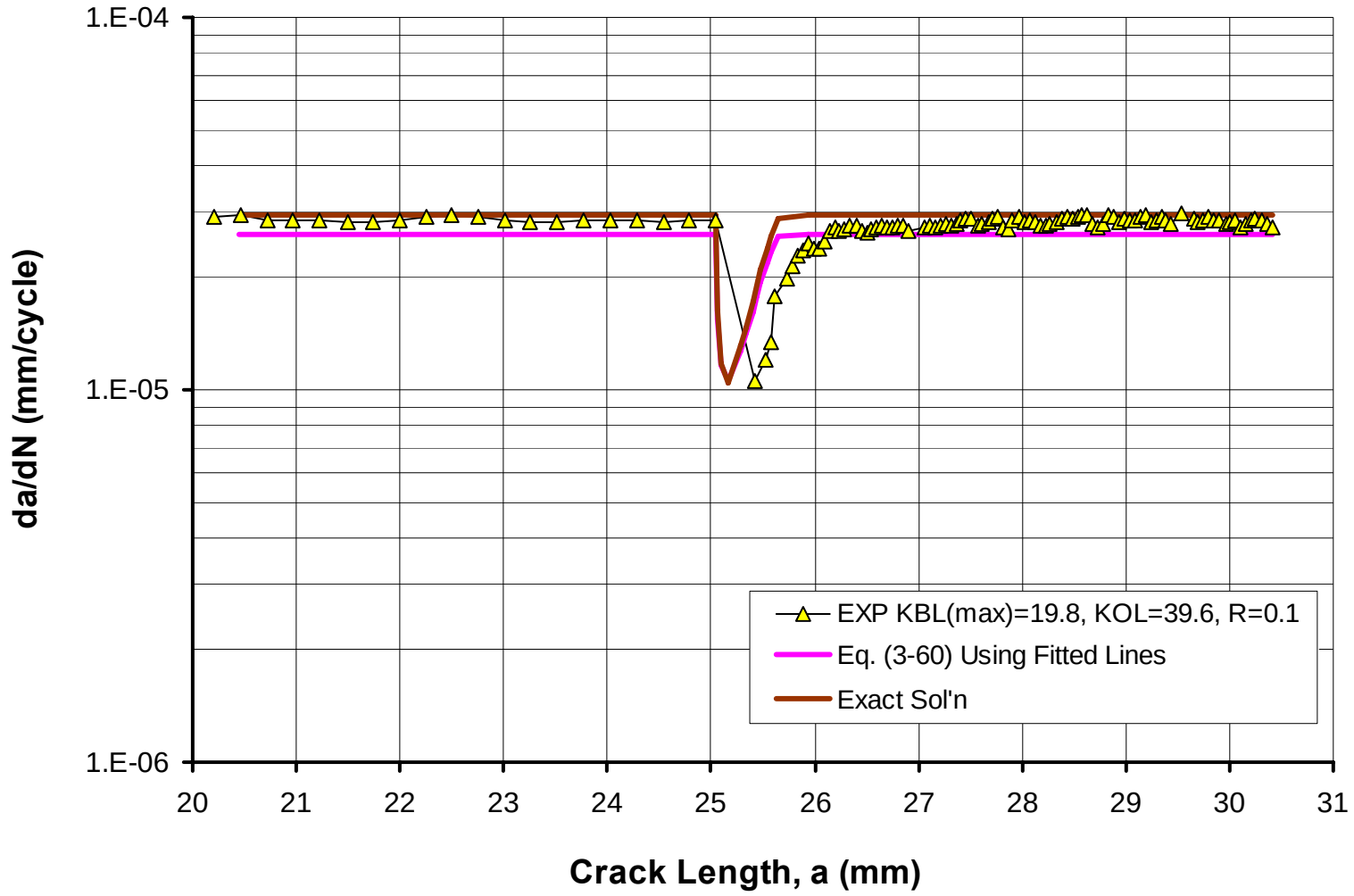

Figure 4-37: Experimental and predicted fatigue crack growth rates after 100 percent overload (4140 steel, ΔK_{BL}=17.82 MPa√m).

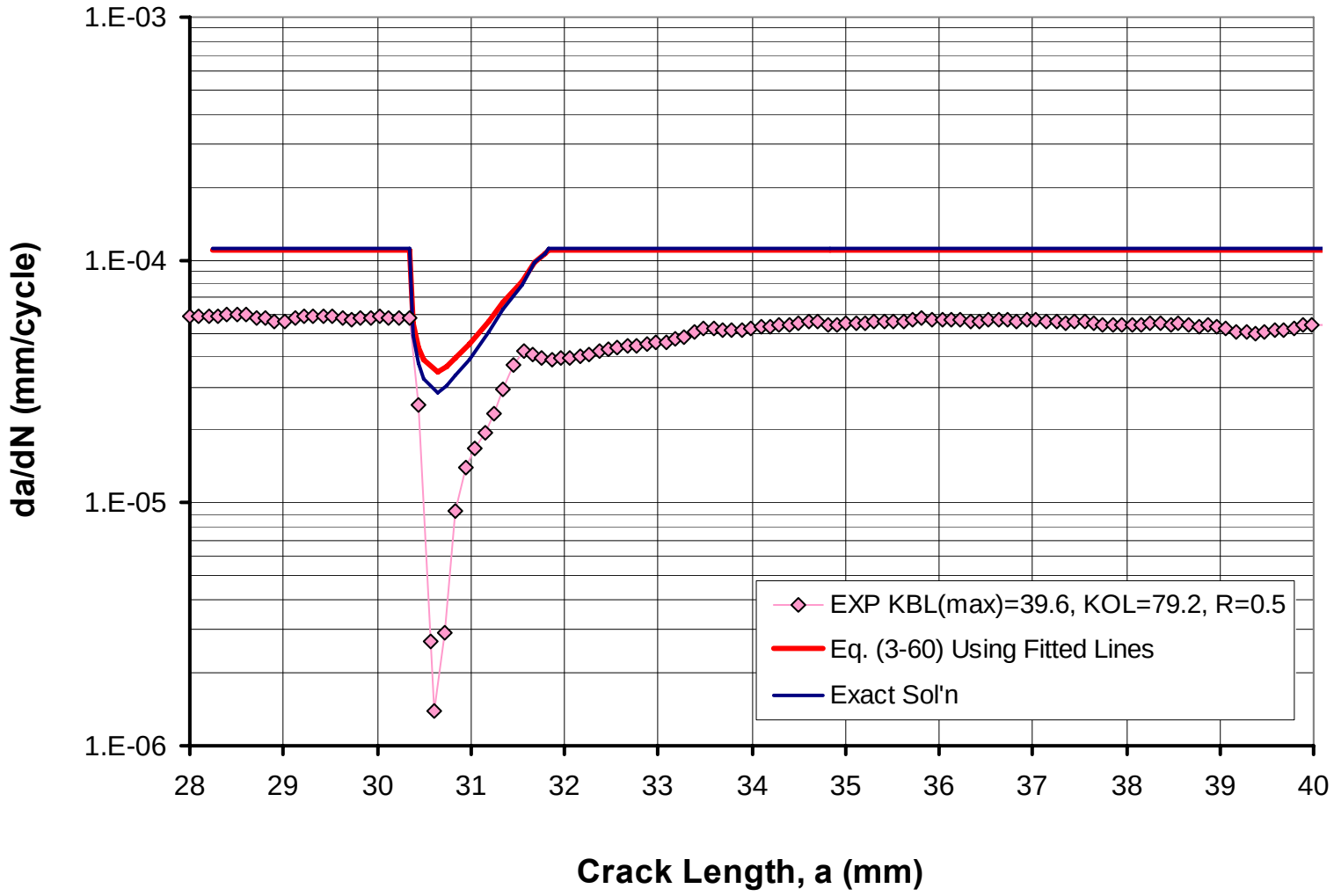

Figure 4-38: Experimental and predicted fatigue crack growth rates after 100 percent overload (4140 steel, ΔK_{BL}= 19.8 MPa$\sqrt{m}$).

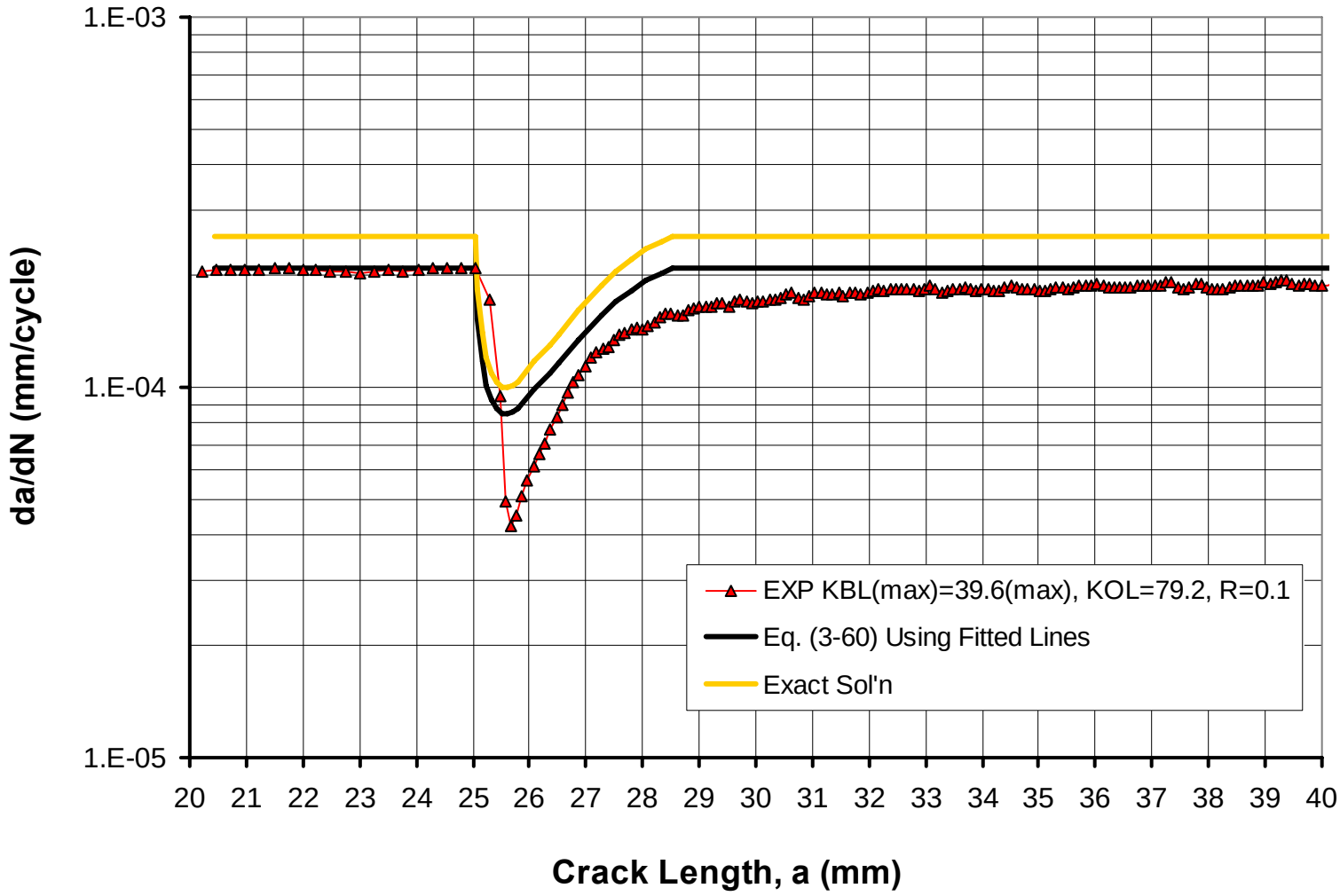

Figure 4-39: Experimental and predicted fatigue crack growth rates after 100 percent overload (4140 steel, ΔK_{BL}=35.64 MPa√m).

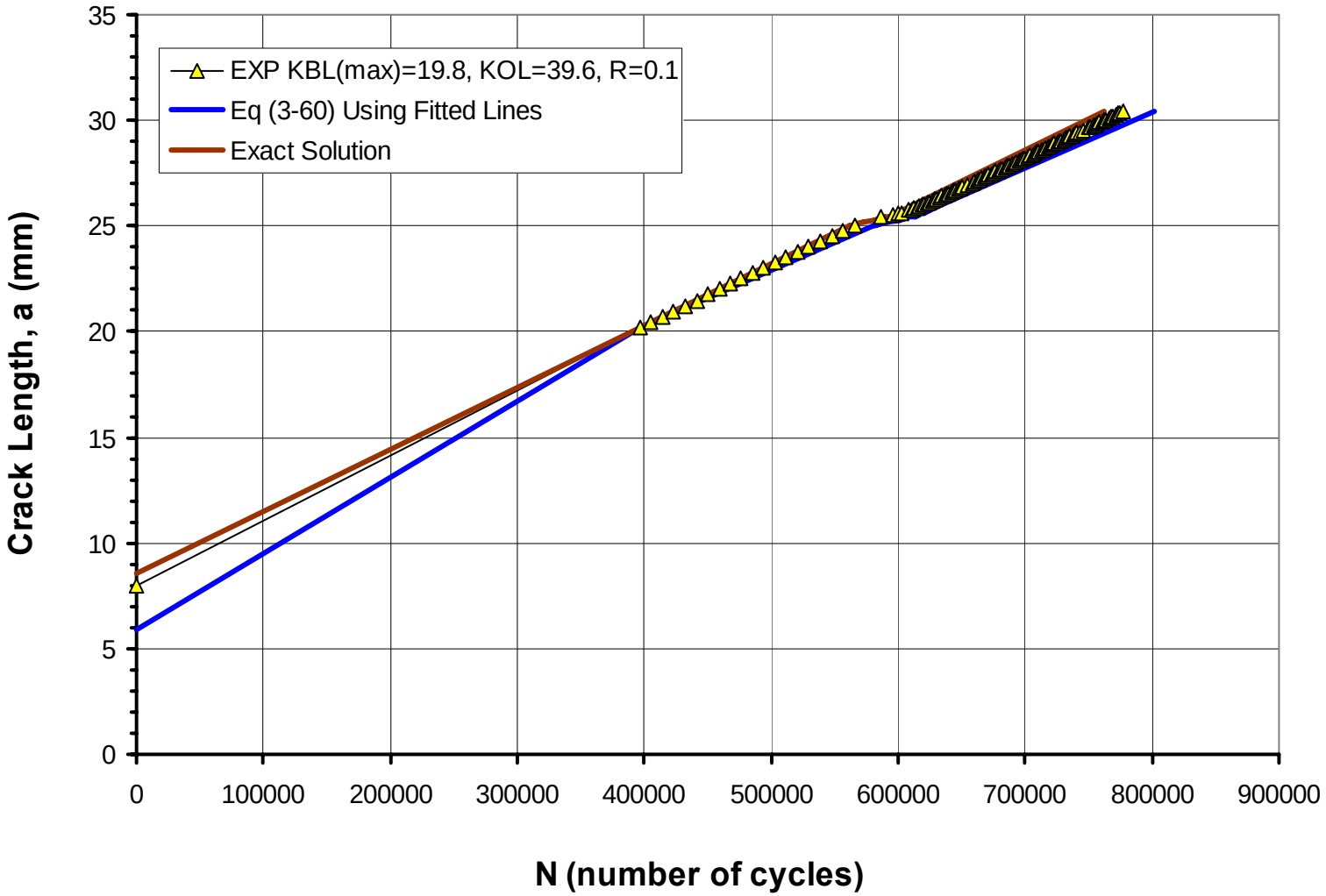

Figure 4-40: Experimental and predicted fatigue crack propagation life after 100 percent overload (4140 steel, ΔK_{BL}=17.82 MPa√m).

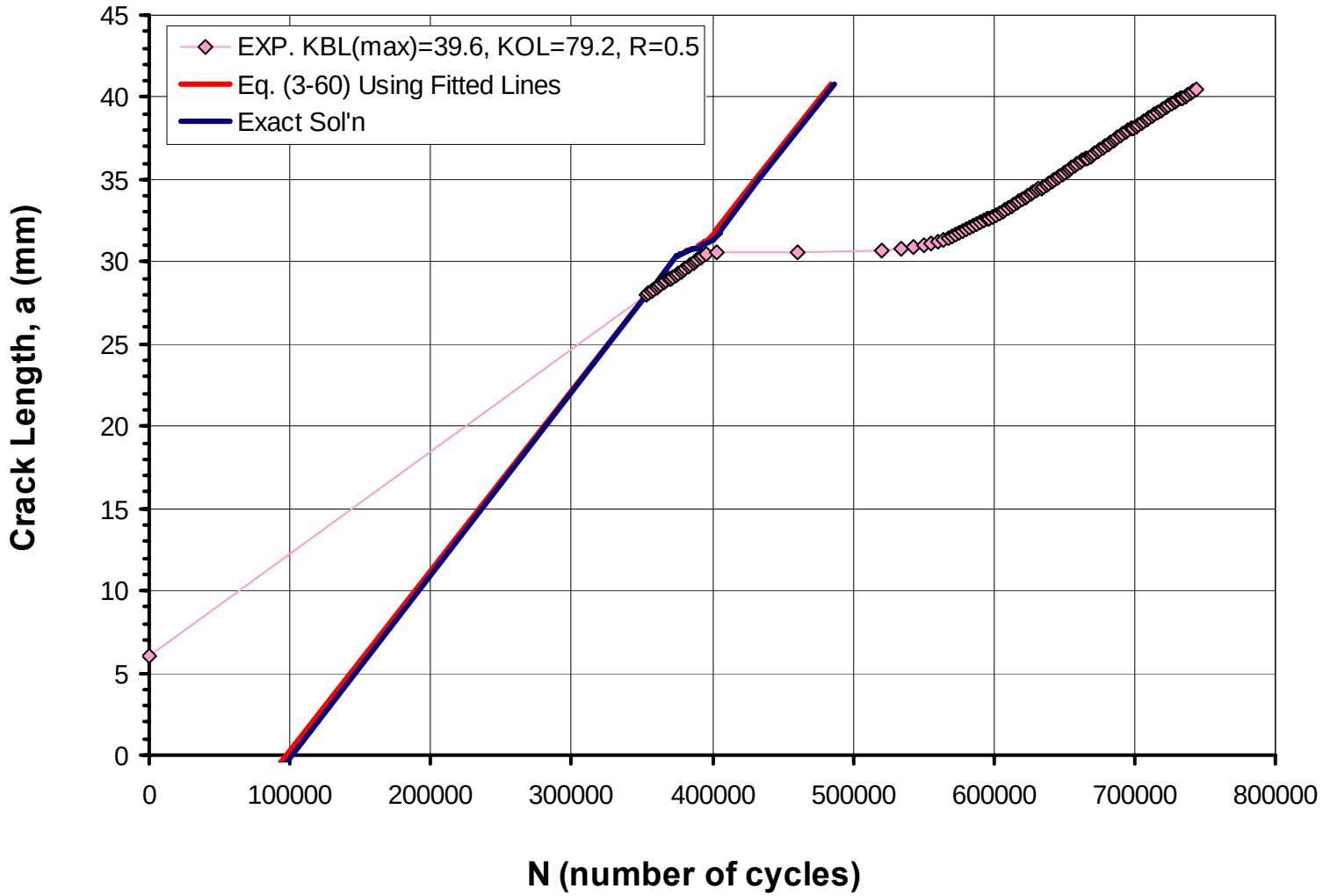

Figure 4-41: Experimental and predicted fatigue crack propagation life after 100 percent overload (4140 steel, ΔK_{BL}= 19.8 MPa$\sqrt{m}$).

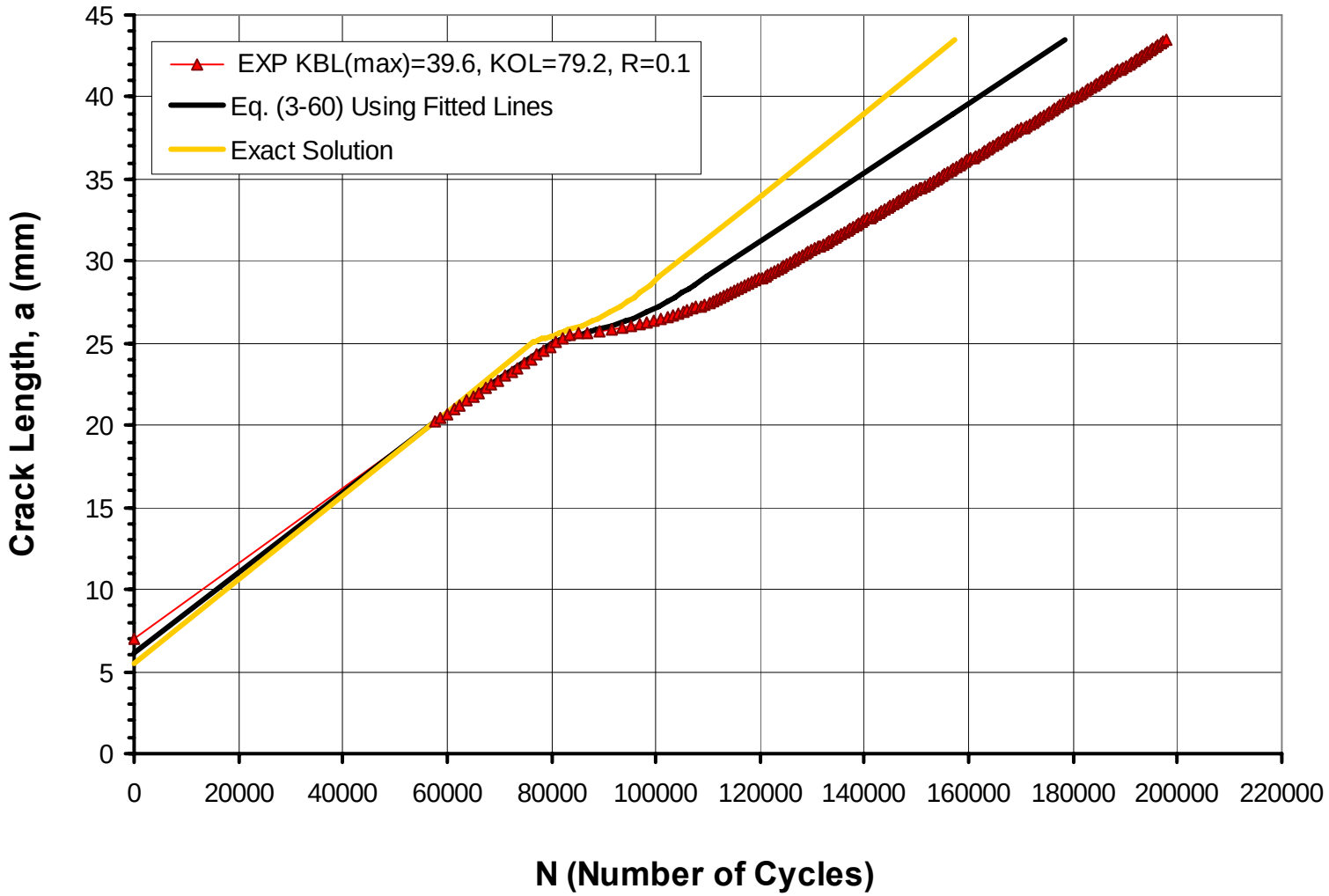

Figure 4-42: Experimental and predicted fatigue crack propagation life after 100 percent overload (4140 steel, ΔK_{BL}=35.64 MPa$\sqrt{m}$).

Chapter 5
Conclusions and Recommendations

A fatigue crack growth model based on the simulation of the elastic-plastic stress-strain response at the crack tip has been proposed. It was assumed that the crack can be modeled as a deep notch with tip radius ρ*. The analysis was carried out as for a classical notch without the necessity of introducing the concept of the crack closure behind the crack tip. It was found that the simulated crack tip stress-strain history and the Smith-Watson-Topper fatigue damage parameter made it possible to derive fatigue crack growth expressions analogous to previously proposed empirical fatigue crack growth equations accounting for the mean stress effect. Application of the model resulted in the derivation of a two parameter driving force combining the effect of the maximum stress intensity factor and the stress intensity range. It was shown that after correcting the applied stress intensity factors for the effect of the plasticity induced residual stresses near the crack tip it was possible to derive one master fatigue crack growth curve valid for a wide range of stress ratios. It was also possible to predict the fatigue crack growth rate based on the Ramberg-Osgood stress-strain material curve and the fatigue strain-life Manson-Coffin equation obtained from smooth material specimens tested under constant amplitude strain control loading.

Three forms of fatigue crack driving force were derived, $K_{max,tot}^{p}\Delta K_{tot}^{(1-p)}$, $K_{max,tot}^{0.5}\Delta K_{tot}^{0.5}$ and $K_{max,tot}^{p}\Delta K_{tot}^{0.5}$, depending on the simplifications used while solving the basic set of equations. It was shown that the driving force in the form of $K_{max,tot}^{p}\Delta K_{tot}^{0.5}$ was able to correlate FCG data for a wide range of stress ratios and FCG rates. The driving force $K_{max,tot}^{p}\Delta K_{tot}^{(1-p)}$ could only be used for predicting high FCG rates. The driving force

$K_{max,tot}^{0.5}\Delta K_{tot}^{0.5}$ was not good for FCG predictions, even in the near threshold region. The model was also able to account for the beneficial effect of the compressive part of a loading cycle. It was found that the relative contribution of the compressive part of the stress reversal was relatively small and depended on the crack tip radius, ρ*, and the actual crack size, a. It was also noted that modeling the crack tip as a circular hole might be non-conservative as far as the effect of applied compressive stresses is concerned. Furthermore, the model was also able to predict the fatigue crack growth after a single tensile overload.

The Creager-Paris solution used in the analysis is only valid for long cracks with $a \gg \rho^*$. Therefore, the proposed model does not apply to short cracks whose lengths are relatively short compared to the elementary material block size ρ*. The classical notch stress-strain analysis (instead of Creager-Paris solution) has the potential to handle short crack problems.

It was assumed and validated that the effects of the residual stress and plastic zone manifest themselves through the decrease in the resultant maximum stress intensity factor, $K_{max,tot}$, without significant changes in the resultant minimum stress intensity factor, $K_{min,tot}$. It is recommended that the local stresses and strains ahead of the crack tip be measured, or calculated by finite element analysis, for each loading reversal. This recommendation would improve the assumptions for the correction of the applied stress intensity factors, $K_{max,appl}$ and ΔK_{appl}.

The proposed model can also be used to predict the corrosion effect on fatigue crack growth. The ρ* parameter depends on the fatigue crack growth data. Changing the ρ* parameter depending on the environment allows the model to account for the environmental effects.

The model can be potentially applied to analyses of fatigue crack growth under spectrum loading providing that additional elements involving the load interaction and memory effects are added.

Appendix A The Derivation of Correction Factor C_p

The equivalent stresses can be related in Eq. (A.1), see Figure A-1.

$$\left.\begin{aligned}\sigma_{eq,C}\times C_p &= \sigma_{eq,B}\\ \sigma_{eq,B} &= \sigma_{eq,A} = \sigma_{ys}\end{aligned}\right\} \Rightarrow \sigma_{eq,C}\times C_p = \sigma_{eq,A} = \sigma_{ys} \tag{A.1}$$

By substituting the equivalent stresses at points A and C, which are calculated from Eq. (2.13), into Eq. (A.1) the following equations can be obtained.

$$\frac{K_I}{\sqrt{2\pi\left(r_p+\Delta r_p\right)}}\sqrt{1+\frac{3}{4}\left(\frac{\rho^*}{r_p+\Delta r_p}\right)^2}\times C_p = \frac{K_I}{\sqrt{2\pi r_p}}\sqrt{1+\frac{3}{4}\left(\frac{\rho^*}{r_p}\right)^2} = \sigma_{ys} \tag{A.2}$$

or

$$\sigma_{ys} = \frac{C_p\times K_I}{\sqrt{2\pi\left(\lambda_p\right)}}\sqrt{1+\frac{3}{4}\left(\frac{\rho^*}{r_p+\Delta r_p}\right)^2} = \frac{K_I}{\sqrt{2\pi\lambda_p^*}}\sqrt{1+\frac{3}{4}\left(\frac{\rho^*}{r_p}\right)^2} \tag{A.3}$$

The relationship between plastic zone sizes is resulted from Figure A-1:

$$\frac{\lambda_p}{\lambda_p^*} = \frac{r_p+\Delta r_p}{r_p} \tag{A.4}$$

The general form of Eq. (A.4) can be expressed in the form of:

$$\lambda^* = r\frac{r_p}{r_p+\Delta r_p} \tag{A.5}$$

The general form of Eq. (A.3) can then be expressed in the form of:

$$\frac{C_p\times K_I}{\sqrt{2\pi r}}\sqrt{1+\frac{3}{4}\left(\frac{\rho^*}{r}\right)^2} = \frac{K_I}{\sqrt{2\pi\lambda^*}}\sqrt{1+\frac{3}{4}\left(\frac{\rho^*}{\lambda^*}\right)^2} \tag{A.6}$$

Substituting Eq. (A.5) into Eq. (A.6), the correction factor "C_p" can be calculated as follow:

$$\frac{C_p \times K_I}{\sqrt{2\pi r}}\sqrt{1+\frac{3}{4}\left(\frac{\rho^*}{r}\right)^2} = \frac{K_I}{\sqrt{2\pi r\dfrac{r_p}{r_p+\Delta r_p}}}\sqrt{1+\frac{3}{4}\left(\frac{\rho^*}{r\dfrac{r_p}{r_p+\Delta r_p}}\right)^2} \qquad \text{(A.7)}$$

$$\Rightarrow \qquad C_p = \sqrt{1+\frac{\Delta r_p}{r_p}} \times \sqrt{\frac{1+\frac{3}{4}\left[\frac{\rho^*}{r}\times\left(1+\frac{\Delta r_p}{r_p}\right)\right]^2}{1+\frac{3}{4}\left(\frac{\rho^*}{r}\right)^2}} \qquad \text{(A.8)}$$

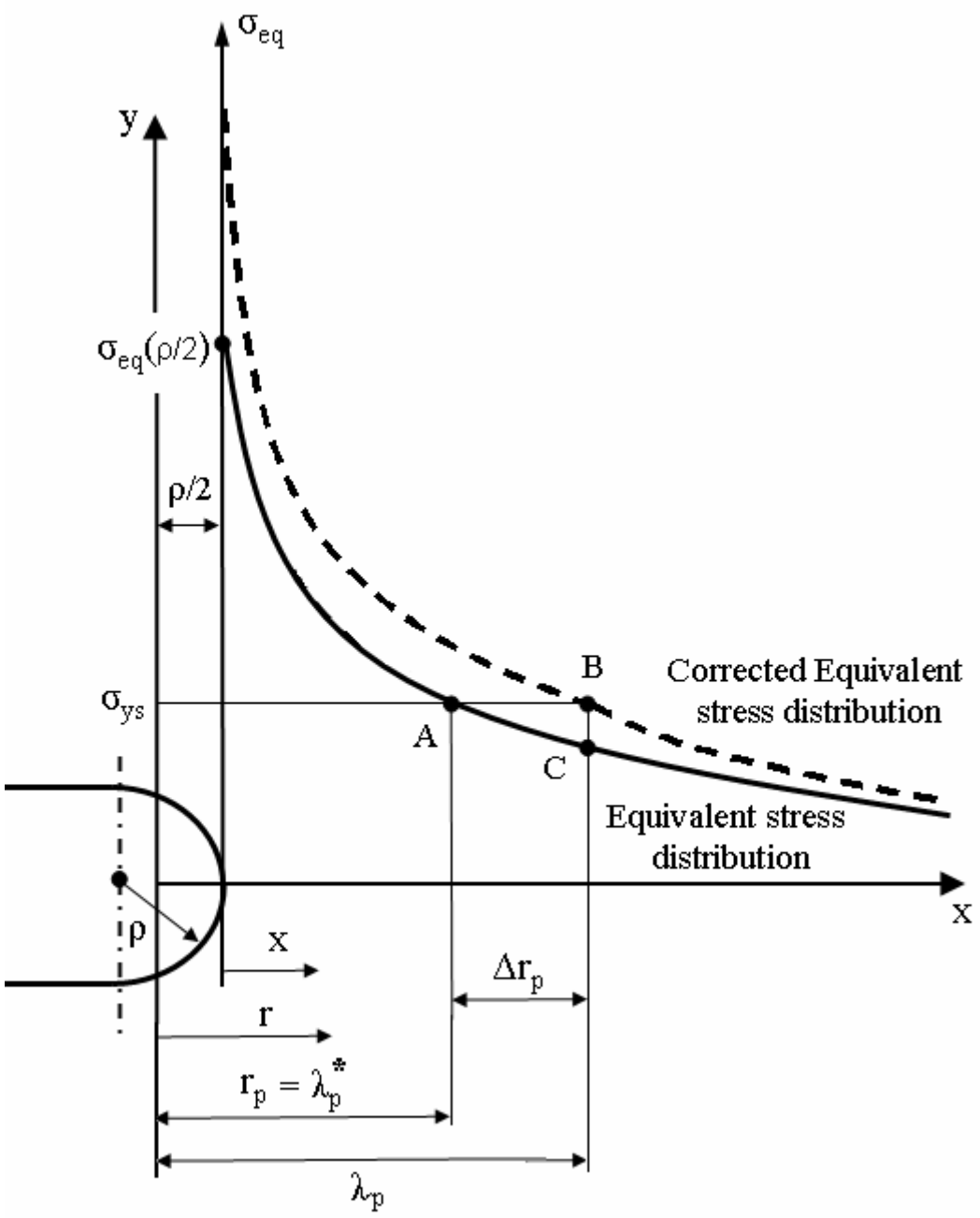

Figure A-1 : The original and the corrected equivalent stress distribution.

Appendix B Parameters M_i for Weight Functions m(x,a)

Parameters M_1, M_2, and M_3 for an edge crack in a plate of the finite width "w". See Figure B-1(a) for the nomenclatures.

$$M_1 = 0.0719768 - 1.51346\left(\frac{a}{w}\right) - 61.1001\left(\frac{a}{w}\right)^2 + 1554.95\left(\frac{a}{w}\right)^3 - 14583.8\left(\frac{a}{w}\right)^4 + 71590.7\left(\frac{a}{w}\right)^5$$
$$-205384\left(\frac{a}{w}\right)^6 + 356469\left(\frac{a}{w}\right)^7 - 368270\left(\frac{a}{w}\right)^8 + 208233\left(\frac{a}{w}\right)^9 - 49544\left(\frac{a}{w}\right)^{10}$$

$$M_2 = 0.246984 + 6.47543\left(\frac{a}{w}\right) + 176.457\left(\frac{a}{w}\right)^2 - 4058.76\left(\frac{a}{w}\right)^3 + 37303.8\left(\frac{a}{w}\right)^4 - 181755\left(\frac{a}{w}\right)^5$$
$$+520551\left(\frac{a}{w}\right)^6 - 904370\left(\frac{a}{w}\right)^7 + 936863\left(\frac{a}{w}\right)^8 - 531940\left(\frac{a}{w}\right)^9 + 127291\left(\frac{a}{w}\right)^{10}$$

$$M_3 = 0.529659 - 22.3235\left(\frac{a}{w}\right) + 532.074\left(\frac{a}{w}\right)^2 - 5479.53\left(\frac{a}{w}\right)^3 + 28592.2\left(\frac{a}{w}\right)^4 - 81388.6\left(\frac{a}{w}\right)^5$$
$$+128746\left(\frac{a}{w}\right)^6 - 106246\left(\frac{a}{w}\right)^7 + 35780.7\left(\frac{a}{w}\right)^8$$

Parameters M_1, M_2, and M_3 for a central through crack in a finite width plate subjected to symmetric loading. See Figure B-1(b) for the nomenclatures.

$$M_1 = 0.06987 + 0.40117\left(\frac{a}{w}\right) - 5.5407\left(\frac{a}{w}\right)^2 + 50.0886\left(\frac{a}{w}\right)^3 - 200.699\left(\frac{a}{w}\right)^4 + 395.552\left(\frac{a}{w}\right)^5$$
$$-377.939\left(\frac{a}{w}\right)^6 + 140.218\left(\frac{a}{w}\right)^7$$

$$M_2 = -0.09049 - 2.14886\left(\frac{a}{w}\right) + 22.5325\left(\frac{a}{w}\right)^2 - 89.6553\left(\frac{a}{w}\right)^3 + 210.599\left(\frac{a}{w}\right)^4 - 239.445\left(\frac{a}{w}\right)^5$$
$$+111.128\left(\frac{a}{w}\right)^6$$

$$M_3 = 0.427216 + 2.56001\left(\frac{a}{w}\right) - 29.6349\left(\frac{a}{w}\right)^2 + 138.40\left(\frac{a}{w}\right)^3 - 347.255\left(\frac{a}{w}\right)^4 + 457.128\left(\frac{a}{w}\right)^5$$
$$-295.882\left(\frac{a}{w}\right)^6 + 68.1575\left(\frac{a}{w}\right)^7$$

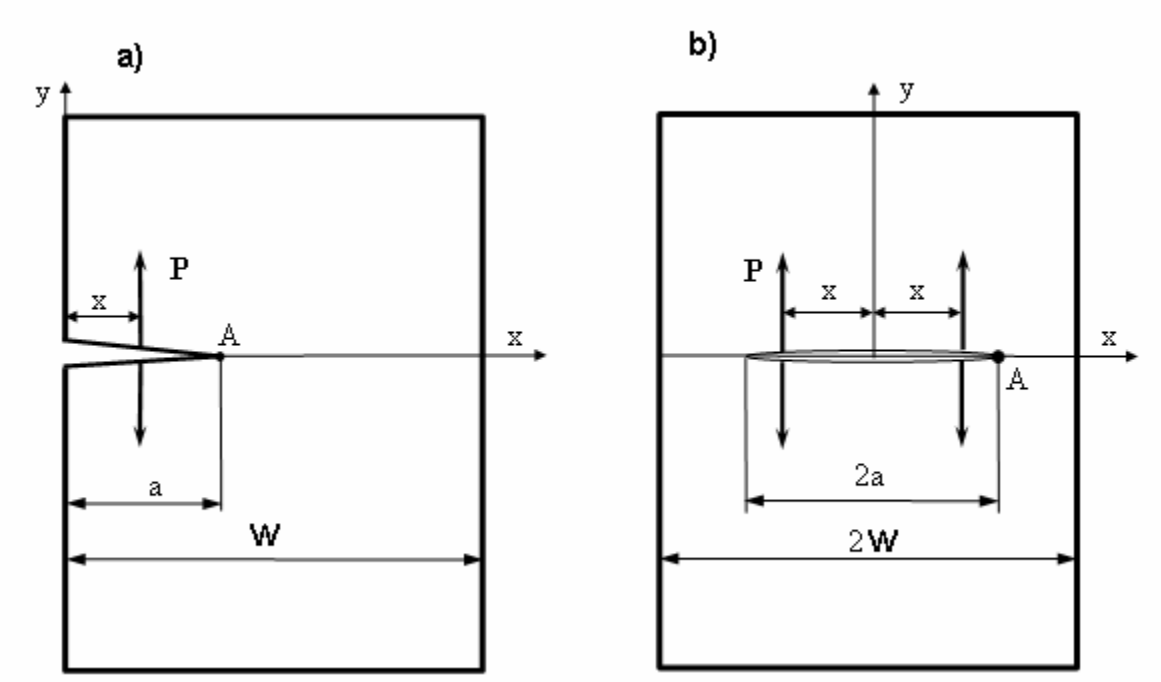

Figure B-1 : The system of coordinates and nomenclature for the universal weight function; a) edge crack in a finite thickness plate, b) through central crack in a finite width plate.

References

[1] Paris P.C. and Erdogan F., A Critical Analysis of Crack Propagation Laws, Journal of Basic Engineering, ASME, Vol. 85, pp. 528-534, 1960.

[2] Elber W., The Significance of Fatigue Crack Closure, in Damage Tolerance in Aircraft Structure, ASTM STP 486, American Society for Testing and Materials, Philadelphia, pp. 230-242, 1971.

[3] Aliaga D., Davy A. and Schaff H., A Simple Crack Closure Model for Predicting Fatigue crack Growth under Flight Simulation Loading, In: Durability and Damage Tolerance in Aircraft Design, Proceedings of 13th ICAF Symposium in Pisa, Editors: Salvetti A. and Cavallini G., EMAS Warley, pp. 605-630, 1985.

[4] Baudin G. and Robert M., Crack Growth Life Time Prediction under Aeronautical Type Loading, Proceedings of 5th European Conference on Fracture, Lisbon, pp. 779-792, 1984.

[5] De Köning A.U., A Simple Crack Closure Model for Prediction of Fatigue Crack Growth Rates under Variable-Amplitude Loading. In: Fracture Mechanics, Editor: Roberts R., ASTM STP 743, American Society for Testing and Materials, Philadelphia, pp. 63-85, 1981.

[6] Newman J.C., A Crack Closure Model for Prediction Fatigue Crack Growth under Aircraft Spectrum Loading, in Methods and Models for Predicting Fatigue Crack Growth under Random Loading, ASTM STP 748, J.B. Chang and C.M. Hudson: Editors, American Society for Testing and Materials, Philadelphia, pp.53-84, 1981.

[7] Newman J.C., Prediction of Fatigue Crack Growth under Variable-Amplitude and Spectrum Loading Using a Closure Model, ASTM STP 761, P.R. Abelkis and C.M. Hudson: Editors, American Society for Testing and Materials, Philadelphia, pp.255-277, 1982.

[8] Macha D.E., Corby D.M. and Jones J.W., On the Variation of fatigue-Crack-Opening Load with Measurement Location, Experimental Mechanics, Vol. 19, No. 6, pp. 207-213, 1979.

[9] Shin C.S. and Smith R.A., Fatigue Crack Growth from Sharp Notches, International Journal of Fatigue, Vol. 7, pp. 87-93, 1985.

[10] Fleck N. A., Influence of Stress State on Crack Growth Retardation, Basic Questions in Fatigue, Editors: Fong J. T. and Fields R. J., ASTM STP 924, pp. 157-183, 1988.

[11] Vasudevan A.K., Sadanada K. and Louat N., A Review of Crack Closure, Fatigue Crack Threshold and Related Phenomena, Materials Science and Engineering, A188, No. (1-2), pp. 1-22, 1994.

[12] Walker E.K., The Effect of Stress Ratio During Crack Propagation and Fatigue for 2024-T3 and 7076-T6 Aluminum, In: Effect of Environment and Complex Load History on Fatigue Life, ASTM STP 462, pp. 1-14, 1970.

[13] Kujawski D., A new $(\Delta K^{+} K_{max})^{0.5}$ Driving Force Parameter for Crack Growth in Aluminum Alloys, International Journal of Fatigue, Vol. 23, No. 8, pp. 733-740, 2001.

[14] Dinda S. and Kujawski D., Correlation and Prediction of Fatigue Crack Growth for Different R-ratios Using K_{max} and ΔK^{+} parameters, Engineering Fracture Mechanics, Vol. 71, No. 12, pp. 1779-1790, 2004.

[15] Donald K. and Paris P.C., An Evaluation of ΔK_{eff} estimation procedure on 6061-T6 and 2024-T3 aluminum alloys. International Journal of Fatigue, Vol. 21, No. S1, pp. 47-57, 1999.

[16] Smith K.N., Watson P., and Topper T.H., A Stress-Strain Function for the Fatigue of Metals, Journal of Materials., Vol. 5, No. 4, pp. 767-778, 1970.

[17] Irwin G.R., "Fracture Dynamics", In Fracturing of Metals, Transaction of the ASME, Vol. 40A, pp.147-166, 1948.

[18] Glinka G., Lecture Notes of Fatigue and Fracture Mechanics Analysis and Design, University of Waterloo, 2004.

[19] Creager M. and Paris P.C., Elastic Field Equations for Blunt Cracks with Reference to Stress Corrosion Cracking, International Journal of Fracture Mechanics, Vol.3, No. 4, pp. 247-252, 1967.

[20] Irwin G.R. Plastic Zone near a Crack and Fracture Toughness, Foundations of Linear Elastic Fracture Mechanics, Sanford R.J. Editor, University of Maryland, College Park, Department of Mechanical Engineering, 1997.

[21] Dugdale D.S., Yielding of Steel Sheets Containing Slits, Journal of the Mechanics and Physics and Solid , Vol. 8, pp. 100-104, 1960.

[22] Barenblatt G.I., The Mathematical Theory of Equilibrium Cracks in Brittle Fracture, Advances in Applied Mechanics, Dryden H.L. and Von Karman Th. Editors, Vol. VII, Academic Press, pp.55-129, 1962.

[23] Peeker E., Extended Numerical Modeling of Fatigue Behavior, PhD Thesis, Swiss Federal Institute of Technology, Lausanne, Department of Civil Engineering, 1997.

[24] Tada H., Paris P.C. and Irwin G.R., The Stress Analysis of Cracks Handbook, Second Edition, Paris Production Inc., St. Louis, Missouri, 1985.

[25] Aliabadi M.H. and Rooke D.P., Numerical Fracture Mechanics, Kluwer Academic Publishers, 1991.

[26] Glinka G., Calculation of Inelastic Notch-Tip Strain-Stress History Under Cyclic Loading, Engineering Fracture Mechanics, Vol. 22, No. 5, pp. 839-854, 1985.

[27] Irwin G.R., Linear Fracture Mechanics, Fracture Transition and Fracture Control, Engineering Fracture Mechanics, Vol. 1, pp. 241-257, 1968.

[28] Glinka G., Unpublished Data, 2002.

[29] Seeger T., Beste A. and Amsutz A., Elastic-Plastic Stress-Strain Behavior of Monotonic and Cyclic Loaded Notched Plates, Fracture 1977, Proceeding 4th International Conference on Fracture ICF4 (Edited by D.M.R. Taplin), pp. 943-951, University of Waterloo Press, Ontario, 1977.

[30] Neuber H., Theory of Stress Concentration for Shear-Strained Prismatic Bodies with Arbitrary Nonlinear Stress-Strain Law, ASME Journal of Applied Mechanics, Vol. 28, No. 4, pp. 544-551, 1961.

[31] Barkey M.E., Socie D.F. and Hisa K.J., A Yield Surface Approach to the Estimation of Notch Strains for Proportional and Non-Proportional Cyclic Loading, ASME Journal of Engineering Material and Technology, Vol. 116, pp. 173-180, 1994.

[32] Seeger T. and Heuler P., Generalized Application of Neuber's Rule, Journal of Testing and Evaluation, ASME, Vol. 8, pp. 199-204, 1980.

[33] Conle A. and Nowack H., Verification of a Neuber-Based Notch Analysis by Companion Specimen Method, Experimental Mechanics, Vol. 17, pp. 57-63, 1977.

[34] Molski K. and Glinka G., A Method of Elastic Plastic Stress and Strain Calculation at a Notch Root, Material Science and Engineering, Vol. 50, No. 1, pp. 93-100, 1981.

[35] Paris P.C., Gomez M.P and Anderson W.P., A Rational Analytic Theory of Fatigue, The Trend in Engineering, Vol. 13, pp. 9-14, 1961.

[36] Rolfe S.T. and Barsom J.M., Fracture and Fatigue Control in Structures, Prentice-Hall, Englewood Cliffs, N.J., 1977.

[37] Barsom J.M., Fatigue-Crack Propagation in Steels of Various Yield Strength, Transaction of The ASME, Journal of Engineering for Industry, Vol. B73, No.4, pp. 1190, 1971.

[38] Throop J.F. and Miller G.A., Optimum Fatigue Crack Resistance, In Achievement of High Fatigue Resistance in Metals and Alloys, ASTM STP 467, American Society for Testing and Material, Philadelphia, pp. 154, 1970.

[39] Padmadinata U.H., Investigation of Crack-Closure Prediction Models for Fatigue in Aluminum Alloy Sheet Under Flight-Simulation Loading, PhD-thesis, Delft University of Technology, Faculty of Aerospace Engineering, 1990.

[40] Schijve J., Some Formulas for The Crack Opening Stress Level, Engineering Fracture Mechanics, Vol. 14, pp. 461-465, 1981.

[41] Suresh S. and Ritchie R.O., Propagation of Short Fatigue Cracks, International Metallurgical Reviews, Vol. 29, pp. 445-476, 1984.

[42] Suresh S., Fatigue of Materials, Cambridge University Press, Cambrige, 1991.

[43] Gary G.T., Williams J.C. and Thompson A.W., Roughness Induced Crack Closure an Explanation for Micro-Structurally Sensitive Fatigue Crack Growth, Metallurgical Transactions, Vol. 14, pp. 421-433, 1983.

[44] Ling M.R. and Schijve J., The Effect of Intermediate Heat Treatments and Overload Induced Retardations During Fatigue Crack Growth In an Al-Alloy, Fracture of Engineering Materials and Structures, Vol. 15, pp. 421-430, 1992.

[45] Josefson B.L., Svensson T., Ringsberg J.W., Gustafsson T. and De Mare J., Fatigue Life and Crack Closure in Specimens Subjected to Variable Amplitude Loads Under Plain Strain Conditions, Engineering Fracture Mechanics, Vol. 66, pp. 587-600, 2000.

[46] Garrett G.G. and Knott J.F., On the Effect of Crack Closure on the Rate of Fatigue Crack Propagation, International Journal of Fracture, Vol. 13, pp. 101-104, 1977.

[47] Meggiolaro M.A. and De Castro J.T.P, On the Dominant Role of Crack Closure on Fatigue crack Growth Modeling, International Journal of Fatigue, Vol. 25, pp. 843-854, 2003.

[48] Wei L.W. and James M.N., A Study of Fatigue Crack Closure in Polycarbonate CT Specimens, Engineering Fracture Mechanics, Vol. 66, pp. 223-242, 2000.

[49] Paris P.C., Tada H. And Donald J.K., Service Load Fatigue Damage ---- A Historical Perspective, International Journal of Fatigue, Vol. 21, pp. S35-S46, 1999.

[50] Garz R.E. and James M.N., Observations on Evaluating Fatigue Crack Closure from Compliance Traces, International Journal of Fatigue, Vol.11, pp. 437-440, 1989.

[51] Parida B.K. and Nicholas T., Effect of Stress Ratio on Fatigue Crack Growth in a Titanium Aluminide Alloy, International Journal of Fracture, Vol.52, p. R51-R54, 1991.

[52] Shih T.T. and Wei R.P., A Study of Crack Closure in Fatigue, Engineering Fracture Mechanics, Vol. 6, pp. 19-32, 1974.

[53] FitzGerald J. and Wei R.P., Test procedure for Determining the Influence of Stress Ratio on Fatigue Crack Growth, Journal of Testing & Evaluation, ASTM, Vol. 2, pp. 67-70,1973.

[54] Clerivet A. and Bathias C., Study of Crack Tip Opening Under Cyclic Loading Taking into Account the Environment and R-ratio, Engineering Fracture Mechanics, Vol. 12, pp. 599-611, 1979.

[55] Kirby B.R. and Beevers C.J., Slow Fatigue Crack Growth and Threshold Behavior in Air and Vacuum of Commercial Aluminum Alloys, Fatigue of Engineering Materials and Structures, Vol. 1, No. 2, pp. 203-215, 1979.

[56] Shercliff H. R. and Fleck N. A., Effect of Specimen Geometry on Fatigue Crack Growth in Plane Strain—II. Overload Response, Fatigue and Fracture of Engineering Materials and Structures, Vol. 13, No. 3, pp. 297-310, 1990.

[57] Anderson T.L., Fracture Mechanics Fundamental and Applications, 2nd Edition, Chapter 2, 1994.

[58] Forman R.G., Kearney V.E. and Engle R.M., Numerical Analysis of Crack Propagation in Cyclic-loaded Structures, Journal of Basic Engineering., Transaction of The ASME, Vol. 89, pp. 459-464, 1967.

[59] Weertman J., Rate of Growth of Fatigue Cracks Calculated from the Theory of Infinitesimal Dislocations Distributed on a Plane, International Journal of Fracture Mechanics, Vol. 2, pp. 460-467, 1966.

[60] Klesnil M. and Lukas P., Influence of Strength and Stress History on Growth and Stabilization of Fatigue Cracks, Engineering Fracture Mechanics, Vol. 4, pp. 77-92, 1972.

[61] Donahue R.J., Clark H.M., Atanmo P., Kumble R. and McEvily A.J., Crack opening Displacement and the Rate of Fatigue Crack Growth, International Journal of Fracture Mechanics, Vol. 8, pp. 209-219, 1972.

[62] McEvily A.J., On Closure in Fatigue Crack Growth, ASTM STP 982, American Society for Testing and Materials, Newman J.C. and W. Elber: Editors, Philadelphia, pp. 35-43, 1988.

[63] Skorupa K., Load Interaction Effects during Fatigue Crack Growth under Variable Amplitude Loading—A Literature Review. Part I: Empirical Trends, Fatigue and Fracture of Engineering Materials and Structures, Vol. 21, No. 8, pp. 987-1006, 1998.

[64] Skorupa K., Load Interaction Effects during Fatigue Crack Growth under Variable Amplitude Loading—A Literature Review. Part II: Qualitative Interpretation, Fatigue and Fracture of Engineering Materials and Structures, Vol. 22, No. 10, pp. 905-926, 1999.

[65] Stephens R., Chen D.K. and Hom B.W., Fatigue Crack Growth with Negative Stress Ratio Following Single Overloads in 2024-T3 and 7075-T6 Aluminum Alloys, In: Fatigue Crack Growth under Spectrum Loads, Editors: Wheeler J.B., Hoersch H.M., DeFranco C.E. and McGlinchey E.J., ASTM STP 595, American Society for Testing and Materials, Philadelphia, Pa, pp. 27-40, 1976.

[66] Otto Buck, Frandsen J.D. and Marcus H.L., Spike Overload and Humidity Effects on Fatigue Crack Delay in Al 7075-T651, In: Fatigue Crack Growth under Spectrum Loads, Editors: Wheeler J.B., Hoersch H.M., DeFranco C.E. and McGlinchey E.J., ASTM STP 595, American Society for Testing and Materials, Philadelphia, Pa, pp. 101-112, 1976.

[67] Jacoby G.H., Nowack H. and Van Lipzig H.T.M., Experimental Results and A Hypothesis for Fatigue Crack Propagation under Variable-Amplitude Loading, In: Fatigue Crack Growth under Spectrum Loads, Editors: Wheeler J.B., Hoersch H.M., DeFranco C.E. and McGlinchey E.J., ASTM STP 595, American Society for Testing and Materials, Philadelphia, Pa, pp. 172-183, 1976.

[68] McMaster F.J. and Smith D.J., Effect of Load Excursions and Specimen Thickness on Crack Closure Measurements, In: Advances in Fatigue Crack Closure Measurement and Analysis, Editors: McClung R.C. and Newman J.C., ASTM STP 1343, American Society for Testing and Materials, Philadelphia, PA, pp. 246-264, 1997.

[69] McMaster F.J. and Smith D.J., Predictions of Fatigue Crack Growth in Aluminum Alloy 2024-T351 using Constraint Factors, International Journal of Fatigue, Vol. 23, No. S1, pp. 93-101, 2001.

[70] Schijve J., Skorupa M., Skorupa A., Machniewicz T., and Gruszczynski P., Fatigue Crack Growth in the Aluminum Alloy D16 under Constant and Variable Amplitude Loading, International Journal of Fatigue, Vol. 26, No. 1, pp.1-15, 2004.

[71] Gallagher J.P. and Hughes T.F., The Influence of Yield Strength on Overload Affected Fatigue Crack Growth Behavior in 4340 Steel, AFFDL-TR-74-27, Air Force Flight Dynamics Laboratory, Wright-Patterson AFB, Ohio, 1974.

[72] Naval Research Laboratory Data.

[73] Skoupa M., Skorupa A., Schijve J., Machniewicz T. and Korbut P., Fatigue Crack Growth Behavior of 18G2A Steel under Constant Amplitude Loading and Following a Single Overload, Archiwum Budowy Maszyn (Archives of Mechanical Engineering), Vol. 47, pp.139-163, 2000.

[74] Bernard P.J., Lindley T.C. and Richards C.E., Mechanisms of Overload Retardation during Fatigue Crack Propagation, In: Fatigue Crack Growth under Spectrum Loads, Editors: Wheeler J.B., Hoersch H.M., DeFranco C.E. and McGlinchey E.J., ASTM STP 595, American Society for Testing and Materials, Philadelphia, PA, pp. 78-97, 1976.

[75] Mills W.J., Hertzberg R.W. and Roberts R., Load Interaction Effects on Fatigue Crack Growth in A514F Steel Alloy, In: Cyclic Stress-Stain and plastic Deformation Aspects of Fatigue Crack Growth, ASTM STP 637, American Society for Testing and Materials, Philadelphia, PA, pp. 192-208, 1977.

[76] Stephens R.R., Stephens R.I., Lemm D.E., Berge S.G., Liknes H.O. and Cousins C.J., Role of Crack Closure Mechanisms on Fatigue Crack Growth of Ti-62222 under Constant-Amplitude and Transient Loading at 54, 25, and 175ºC, In: Advances in Fatigue Crack Closure Measurement and Analysis, Editors: McClung R.C. and Newman J.C., ASTM STP 1343, American Society for Testing and Materials, Philadelphia, PA, pp. 224-245, 1997.

[77] Yildirim N. and Vardar O., Effect of Single Overload in FCP, Engineering Fracture Mechanics, Vol. 30, No. 3, pp. 329-335, 1988.

[78] Alzos W.X., Skat A.C. and Hillberry B.M., Effect of Single Overload/Underload Cycles on Fatigue Crack Propagation, In: Fatigue Crack Growth under Spectrum Loads, Editors: Wheeler J.B., Hoersch H.M., DeFranco C.E. and McGlinchey E.J., ASTM STP 595, American Society for Testing and Materials, Philadelphia, PA, pp. 41-60, 1976.

[79] Chen G.L. and Roberts R., Delay Effects in AISI 1035 Steel, Engineering Fracture Mechanics, Vol. 22, No. 1, pp. 201-212, 1985.

[80] Shin C.S. and Hsu S.H., On the Mechanisms and Behavior of Overload Retardation in AISI 304 Stainless Steel, International Journal of Fatigue, Vol. 15, No. 3, pp. 181-192, 1993.

[81] Damri D. and Knott J.F., Transient Retardation in Fatigue Crack Growth Following a Single Peak Overload, Fatigue and Fracture of Engineering Materials and Structures, Vol. 14, No. 7, pp. 709-719, 1991.

[82] Chanani G.R., Retardation of Fatigue-Crack Growth in 7075 Aluminum, Metals Engineering Quarterly, Vol. 15, No. 1, pp. 40-48, 1975.

[83] Tsukuda A., Ogiyama H. and Shiraishi T., Transient Fatigue Crack Growth Behavior Following Single Overloads at High Stress Ratios, Fatigue and Fracture of Engineering Materials and Structures, Vol. 19, No. 7, pp. 879-891, 1996.

[84] Ward-Close C.M., Blom A.F. and Ritchie, Mechanisms Associated with Transient Fatigue Crack Growth under Variable-Amplitude Loading: An Experimental and

Numerical Study, Engineering Fracture Mechanics, Vol. 32, No. 4, pp. 613-638, 1989.

[85] Vecchio R.S., Hertzberg R.W. and Jaccard R., On the Overload Induced Fatigue Crack Propagation Behavior in Aluminum and Steel Alloys, Fatigue of Engineering Materials and Structures, Vol. 7, No. 3, pp. 181-194, 1984.

[86] Petit J., Tintillier R., Ranganathan N., Ait Abdeddaim M. and Chalant G., Influence of Microstructure and Environment of Fatigue Crack propagation Affected by Single or Repeated Overloads in a 7075 Alloy, In: Fatigue Crack Growth under Variable Amplitude Loading, Editors: Petit J., Davidson D.L., Suresh S. and Rabbe P., Elsevier Science Publishers Ltd, England, pp. 162-179, 1988.

[87] Venkateswara Rao K.T. and Ritchie R.O., Micromechanisms of Transient fatigue Crack Growth Behavior in Aluminum-Lithium Alloys Following Single Tensile Overloads, In: Fatigue Crack Growth under Variable Amplitude Loading, Editors: Petit J., Davidson D.L., Suresh S. and Rabbe P., Elsevier Science Publishers Ltd, England, pp. 134-145, 1988.

[88] Shuter D.M. and Geary W., Some Aspects of Fatigue Crack growth Retardation Behavior Following Tensile Overloads in a Structural Steel, Fatigue and Fracture of Engineering Materials and Structures, Vol. 19, No. 2/3, pp. 185-199, 1996.

[89] Yildirim N. and Vardar O., Study of Periodic Overloads at a Fixed Overload Ratio, Engineering Fracture Mechanics, Vol. 36, No. 1, pp. 71-76, 1990.

[90] Tür Y.K. and Vardar O., Periodic Tensile Overloads in 2024-T3 Al-Alloy, Engineering Fracture Mechanics, Vol. 53, No. 1, pp. 69-77, 1996.

[91] Yildirim N. and Vardar O., Crack Growth Retardation due to Intermittent Overloads, International Journal of Fatigue, Vol. 12, No. 4, pp.283-287, 1990.

[92] Mills W.J. and Hertzberg R.W., Load Interaction Effects on fatigue Crack Propagation in 2024-T3 Aluminum Alloy, Engineering Fracture Mechanics, Vol. 8, pp. 657-667, 1976.

[93] Wheeler O.E., Spectrum Loading and Crack Growth, Journal of Basic Engineering, ASME, Vol. 94, No. 1, pp. 181-186, 1972.

[94] Willenborg J., Engle R.M. and Wood H.A., A Crack Growth Retardation Model Using an Effective Stress Concept, AFFDL TM-71-1, Air Force Flight Dynamic Laboratory, Wright Patterson Air Force Base, 1971.

[95] Bannantine J., Fundamentals of Metal Fatigue Analysis, Prentice-Hall Inc., USA, 1990.

[96] Irwin G.R., Analysis of Stresses and Strains Near the End of a Crack Traversing a Plate, Transactions ASME, Journal of Applied Mechanics, Vol. E24, pp. 361-364, 1957.

[97] Hutchinson J.W., Singular Behaviour at the End of a Tensile Crack in a Hardening Material, Journal of the Mechanics and Physics of Solids, Vol.16, pp. 13-31, 1968.

[98] Lal D.N. and Weiss V., A Notch Analysis of Fracture Approach to Fatigue Crack Propagation, Metallurgical Transactions, Vol. 9A, pp. 413-420, 1978.

[99] Kaisand L.R. and Mowbray D.F., Relationships between Low-Cycle Fatigue and Fatigue Crack Growth-Rate Properties, Journal of Testing and Evaluation, Vol. 7, No. 5, pp. 270-280, 1979.

[100] Glinka G., A Notch Stress-Strain Analysis Approach to Fatigue Crack Growth, Engineering Fracture Mechanics, Vol. 21, No. 2, pp. 245-261, 1985.

[101] Neuber H., Kerbspannugslehre, Springer Verlag, Berlin, 1985.

[102] Bowles C.Q., The Role of Environment, Frequency, and Shape During Fatigue Crack Growth in Aluminum Alloys, Doctoral Dissertation, Delft University, The Netherlands, 1978.

[103] Zhang J.Z., A Shear Band Decohesion Model for Small Fatigue Crack Growth in an Ultra-Fine Grain Aluminium Alloy, Engineering Fracture Mechanics, Vol. 65, pp. 665-681, 2000.

[104] Pommier S., A study of the Relationship Between Variable Level Fatigue Crack Growth and the Cyclic Constitutive Behaviour of Steel, International Journal of Fatigue, Vol.23, No. S1, pp. 111-118, 2001.

[105] Sander M. and Richard H.A., Lifetime Prediction for Real Loading Situations-Concepts and Experimental Results of Fatigue Crack Growth, International Journal of Fatigue, Vol. 25, No. 9-11, pp. 999-1005, 2003.

[106] Forsyth P.J.E., Unified Description of Micro and Macroscopic Fatigue Crack Behaviour, International Journal of Fracture, Vol. 5, pp. 3-14, 1983.

[107] Landgraf R.W., Morrow J. and Endo T., Determination of the Cyclic Stress-Strain Curve, Journal of Materials, Vol. 4, No. 1, pp. 176, 1969.

[108] Technical Report on Low Cycle Fatigue Properties: Ferrous and Non-ferrous Metals. SAE Standard No. J1099, Society of Automotive Engineers (SAE), Warrendale, Pennsylvania, 1998.

[109] Moftakhar A., Buczynski A. and Glinka G., Calculation of Elasto-Plastic Strains and Stresses in Notched Under Multi-Axial Loading, International Journal of Fracture, Vol. 70, No. 3, pp. 357-373, 1995.

[110] Glinka G. and Buczynski A., Multi-axial Stress-Strain Notch Analysis. In: Multi-axial Fatigue and Deformation, editors: Kalluri S, et al. ASTM STP 1387, Philadelphia: American Society for Testing and Materials, pp. 82-98, 2000.

[111] Skrzypek J.J. and Hetnarski R.B., Plasticity and Creep: Theory, Examples and Problem, CRC Press, Boca Raton, 1993.

[112] Burdekin F.M., and Stone D.E.W., The Crack Opening Displacement Approach to Fracture Mechanics in Yielding Materials, Journal of Strain Analysis, Vol. 1, pp. 145-153, 1966.

[113] Bueckner H.F, A Novel Principle for the Computation of Stress Intensity Factors, Zeitschrift Angewandte Mathematik und Mechanik, Vol. 50, pp. 529-546, 1970.

[114] Glinka G. and Shen G., Universal Features of Weight Functions for Cracks in Mode I, Engineering Fracture Mechanics, Vol. 40, No. 6, pp. 1135-1146, 1991.

[115] Shen G. and Glinka G., Determination of Weight Functions from Reference Stress Intensity Factor, Theoretical and Applied Fracture Mechanics, Vol. 15, No. 3, pp. 237-245, 1991.

[116] Wang X., Lambert S. and Glinka G., Approximate Weight Functions for Embedded Elliptical Cracks, Engineering Fracture Mechanics, Vol. 59, No.3, pp. 381-392, 1998.

[117] Moftakhar A. and Glinka G., Calculation of Stress Intensity Factors by Efficient Integration of Weight Functions, Engineering Fracture Mechanics, Vol. 43, No. 5, pp.749-756, 1992.

[118] Glinka G., Ott W. and Nowack H., Elastoplastic Plane Strain Analysis of Stresses and Strains at the Notch Root, Journal of Engineering Materials and Technology, Vol. 110, No. 3, pp. 195-204, 1988.

[119] Nie H., and Shaobo L., Biaxial Stress Fatigue Life Prediction by the Local Strain Method, International Journal of Fatigue, Vol. 19, No. 6, pp. 517-522, 1997.

[120] Palmgren A., The Fatigue Life of Ball- Bearings, Zeitschrift des Vereins Deutscher Ingenieure, Vol. 68, pp. 339-341, 1924.

[121] Miner M.A., Cumulative damage in Fatigue, Journal of Applied Mechanics, Vol. 12, pp. 159-164,1945.

[122] Kitagawa H. and Takahashi S., Applicability of Fracture Mechanics to Very Small Cracks in the Early Stage, In: Processing of the Second International Conference on

Mechanical Behaviour of Materials, Metals Park, American Society for Metals, pp. 627-631, 1976.

[123] Jiang Y., Unpublished Experimental Data, Department of Mechanical Engineering, University of Nevada, Reno, 2005.

[124] Hudson C.M., Effect of Stress Ratio on Fatigue Crack Growth in 7075-T6 and 2024-T3 Aluminum Alloy Specimens, NASA TN D-5390, 1969.

[125] Dubensky R.G., Fatigue Crack Propagation in 2024-T3 and 7075-T6 Aluminum Alloys at High Stress, NASA CR-1732, 1971.

[126] Newman JC. Wu XR. Venneri SL. and Li CG., Small-Crack Effects in High Strength Aluminum Alloys, Report No. A NASA/CAE Cooperative Program, NASA Reference Publication 1309, 1994.

[127] Liu A.F., Structural Life Assessment Methods, ASM International, Materials Park, OH, USA, 1998.

[128] Wanhill R.J.H., Damage Tolerance Engineering Property Evaluation of Aerospace Aluminum Alloys with Emphasis on Fatigue Crack Growth, National Research Laboratory NLR, Amsterdam, Technical Publication NLR TP 94177 U, 1994.

[129] Pang C-M. and Song J-H., Crack Growth and Closure Behaviour of Short Fatigue Cracks, Engineering Fracture Mechanics, Vol. 47, No. 3, pp. 327-343, 1994.

[130] Leis B., Cyclic Inelastic Deformation Behaviour of Thin Notched Plates, Master Thesis, University of Waterloo, Department of Civil Engineering, 1972.

[131] Dowling N.E., Mechanical Behaviour of Materials, Prentice Hall, New Jersey, 1999.

[132] Taylor D. A., Compendium of Fatigue Threshold and Growth Rates, EMAS Ltd., Warley, U.K., 1985.

[133] Swain M.H., Everett R.A., Newman J.C. and Phillips E.P., The Growth of Short Cracks in 4340 Steel and Aluminum-Lithium 2090, AGARD R-767, Editors: Edwards P.R. and Newman J.C., pp. 7.1-7.30, 1990.

[134] Wanhill R.J.H., Private Communication from Newman J.C., 2005.

[135] Naval Research Laboratory Data.

[136] Ritchie R.O., Boyce B.L., Campbell J.P., Roder O., Thompson A.W. and Milligan W.W., Threshold for High-Cycle Fatigue in a Turbine Engine Ti-6Al-4V Alloy, International Journal of Fatigue, Vol. 21, pp. 653-662, 1999.

[137] Yuen A., Hopkins S.W., Leverant G.R. and Rau C.A., Correlations between Fracture Surface Appearance and Fracture Mechanics Parameters for Stage II Fatigue Crack Propagation in Ti-6Al-4V, Metallurgical Transactions, Vol. 5, pp. 1833-1842, 1974.